UNIVERSITÀ degli STUDI di CASSINO e del LAZIO MERIDIONALE

COLLANA SCIENTIFICA

Elio Sacco – Michela Monaco (Editors)

Mechanics of Masonry Construction

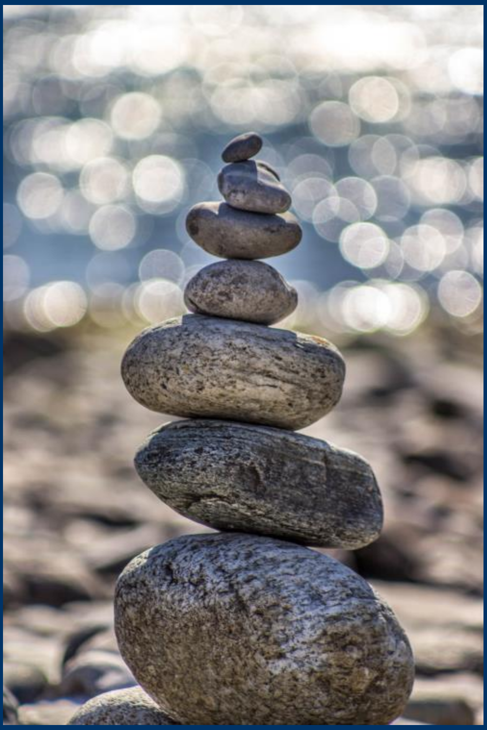

EDIZIONI UNIVERSITA' DI CASSINO
2017

Centro Editoriale di Ateneo
Palazzo degli Studi
Località Folcara, Cassino (FR), Italia
ISBN 978-88-8317-155-0

The cover picture is by Deniz Altindas on Unsplash (https://unsplash.com/)

EDIZIONI UNIVERSITÀ DI CASSINO

Mechanics of Masonry Construction

dedicated to Antonio Ercolano

Elio Sacco – Michela Monaco (Editors)

Authors

Daniela Addessi
Claudio Alessandri
Maurizio Angelillo
Nicola M. Auciello
Valentina P. Berardi
Giuseppe Brando
Bruno Calderoni
Mario Como
Emilia Angela Cordasco
Valentina Corlito
Emanuela Criber
Gianfranco De Matteis
Mariella De Piano
Luciana Di Gennaro
Fernando Fraternali
Giorgio Frunzio
Marcello Fulgione
Maria Teresa Guadagnuolo
Vincenzo Mallardo
Francesco Marmo
Ida Mascolo
Daniele Mase
Daniele Masi
Vincenzo Minutolo
Gaetana Pacella
Mario Pasquino
Luciano Rosati
Giuseppe Rocchetta
Eugenio Ruocco
Elio Sacco
Paolo Simoniello

Preface

Masonry structures represent a large part of the constructions in the World. Old masonry buildings, historical towns and monumental constructions characterize the heritage of the Countries. This important heritage deserves to be saved, maintained, preserved, protected and restored. Thus, the formulation of reliable and efficient procedures for evaluating the structural response of masonry constructions is a challenging research in civil engineering field. Indeed, the development of accurate stress analyses is fundamental not only to verify the stability of existing masonry constructions, but also to properly design effective strengthening and repairing interventions.

The analysis of masonry structural response is a quite complex task. In fact, masonry material is characterized by strong nonlinear mechanical behavior, even for low deformation levels, with anisotropy both in the linear and nonlinear range. Furthermore, masonry structures often require 2D or 3D modeling approaches, i.e. more complex structural schemes compared with those usually used for concrete or steel framed structures. For these reasons, the research on the Mechanics of Masonry Constructions is still a very active research field. This is demonstrated by the large amount of scientific papers published on specialized journals. It should be remarked the great contribution of the Italian scientific community in the research activities in the Mechanics of Masonry field. Many conferences, workshops, minisymposia concerning the thematic of safety and strengthening of masonry constructions are indeed organized in Italy, or by Italian researchers.

In this context, the Workshop “MCM2016: Mechanics of Masonry Constructions” was held at the University of Cassino and Southern Lazio (Italy) on July 4, 2016. The workshop was dedicated to the memory of Antonio Ercolano, who spent large part of his scientific life at the University of Cassino performing researches on the Mechanics of Masonry as well. His studies in this field started at the beginning of ’90, developing computational models and numerical techniques for the analysis of masonry structures.

This book collects the papers presented during the MCM2016, where scientists interested in the study of masonry structures discussed the results of their recent work. Several papers cite the works developed and published by Antonio Ercolano.

During the workshop a commemoration of the colleague and friend Antonio was held. Antonio was a researcher and a teacher outside the box; he was not interested in publishing great numbers of papers, but more in studying and in understanding interesting scientific questions. He always had very good personal relationships with all the colleagues because of his smart ability to find something beautiful, intriguing and fun in everything. He had also a special relation with all the students, sharing the "panettone" with them in Christmas.

This book is dedicated to his memory and to his beautiful family.

to Mariella, Valeria, Arianna and Chiara

Table of contents

Thrust evaluations of masonry domes. An application to the St. Peter's Dome

Mario Como[1]

[1] University of Rome "Tor Vergata", Department of Civil Engineering and Computer Science
Engineering, via del Politecnico 1,
00133, Rome (RM), Italy
como@uniroma2.it

Abstract. The research of the thrust of the St. Peter's dome has a long history that goes up to Poleni (1748) and to the so-called Three Mathematicians (1742) which, in the first half of the eighteenth century, were engaged to study the damaged dome and to provide its strengthening and restoration. The paper recalls this history and in the framework of some developments of Limit Analysis applied to masonry bodies, gives an evaluation of the thrust of the St. Peter's dome in Rome by using the Kinematical approach.

Keywords: Masonry constructions, dome, thrust force.

1 Introduction

A masonry dome, loaded by its own weight, cracks as soon as the hoop stresses near the springing reach the masonry's weak tensile strength. The initial membrane equilibrium of the rotational shell (Flugge, 1962; Heyman, 1977) is thereby lost and meridian cracks take place and spread along the dome (Figure 1).

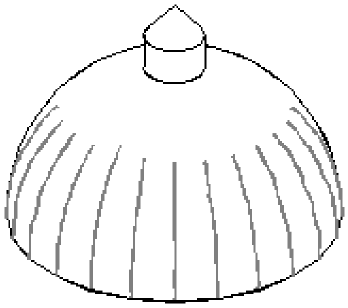

Fig. 1 – Typical meridian cracks in a masonry dome (Heyman, 1995)

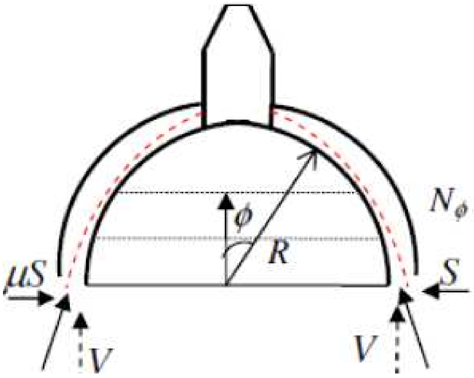

Fig. 2 – The pressure line in the slices and the insurgence of the thrust (Como, 2010; Como, 2016)

Consequently, the dome breaks up into slices that behave as independent pairs of semi-arches leaning on each other.

Cracking brings a significant change in the Statics of the dome. The hoop forces N_θ in the cracked zone vanish and the meridian forces N_ϕ, acting along the slices centrelines, are no longer able to ensure equilibrium. The pressure curve thus tilts towards the horizontal and deviates away from the central surface of the dome. A small cap at the top of each slice will be subjected to the thrusting action transmitted by the other slices, which will be transmitted all the way to the springings. Figure 2 shows a rough sketch of the pressure curve of a cracked hemispherical dome. The dotted line shows the position of this curve, which inclines towards the horizontal at the springings. The horizontal component of the reaction of the supports represents the thrust S per unit length of the base circumference of the dome.

The emergence of the thrust in the dome represents the most consequential outcome of meridian cracking in typical masonry round domes.

The assumed rigid in compression masonry model can give a plain description of the stress state of the cracked dome. Loaded by the dome's thrust, the sustaining structures (e.g., the drum and the underlying piers), settle and splay. The dome slices, no longer restrained from deforming by rings, bends under the loads and can form a mechanism. Consequently, the dome thrust takes the minimum value (Heyman, 1966; Heyman, 1995; Como, 1996; Como, 1998; Coccia, 2016). The weight of a particularly heavy lantern, for example, could even cause the dome to fail on cracking.

In the settled state, the pressure curve passes through the extrados at the key section of the slices and then runs within their interior, skimming over the intrados of the dome. In the arch composed by two opposite slices, hinges of the settlement mechanism occur at the key and at the haunches. Domes with lanterns have a top ring to sustain it. Thus, instead of a single hinge, two symmetric hinges will form at the extrados of the section connecting the slice with the top ring.

The minimum thrust S_{min} can be obtained via the static, as well as via the kinematic approach, (Como, 1996; Como, 1998).

The static approach calls for tracing the statically admissible funicular curves of the loads. In this case, we can neglect the small hooped cap situated at the top, near the zenith of the dome. The thrust S of the settled dome is transmitted along the pressure curve passing through these hinges and corresponds to the minimum value S_{min} of all thrusts S_{stat} of the statically admissible pressure lines s, i.e. wholly contained within the slice. Thus, following the static approach, we must identify, from among all the statically admissible pressure lines (Gesualdo *et al.*, 2017), the one that releases the minimum thrust at the dome springing:

$$S_{stat}(s) \ge S = \min[S(s)]\ ,\ \forall\ s \text{ statically admissible} \tag{1}$$

The kinematic approach is dual with respect to the static one. Let us consider any kinematically admissible settlement mechanism *v*, describing the adjustment of the dome to the side deformation of its sustaining structures, and define the kinematic thrust $S_{kin}(v)$ as:

$$S_{kin}(v) = \frac{<g,v>}{\Delta(v)} \tag{2}$$

In Eq. (2) the term $<g,v>$ represents the work, undoubtedly positive, of the dead loads *g* for the vertical displacements of the mechanism *v*, and $\Delta(v)$ is the radial widening of the dome at its base, produced by the mechanism *v*. The settlement mechanisms are obtained releasing the slices positioning hinges to allow the horizontal sliding of the dome at its springings. Thus the hinges must be positioned:

- at the extrados, in the section linking the central closing ring with the slice;
- at the intrados, at the haunches, as shown in Figure 3. The position *K* of this hinge is unknown and is indicated by the angle σ.

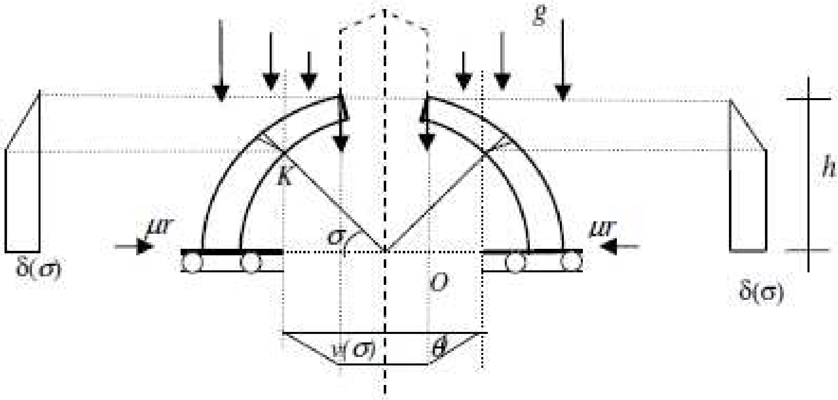

Fig. 3 – The settlement mechanism of the slice following the widening of the drum top

According to this approach the minimum thrust can be evaluated as the maximum of all kinematic thrusts $S_{kin}(v)$, (Como, 1996; Como, 1998):

$$S_{kin}(v) \leq S = \max[S(v)], \ \forall \ v \text{ kin. adm. settlement mechanism} \qquad (3)$$

Consequently, the minimum value of the thrust force can be evaluated as:

$$S_{\min} = \max[S_{kin}(v)] = \max\left[\frac{< g, v >}{\Delta(v)}\right] \qquad (4)$$

where v varies in the set of all kinematically admissible settlement mechanisms.

Figure 3 shows a typical mechanism produced by the dome springing widening. In this mechanism, the position of the internal hinge *K* is unknown. The set of all these kinematically admissible mechanisms is described by varying the position of the hinge *K* between the springing and the key section of the slice. Identifying the maximum of the function, by varying the position of hinge *K*, enables us to obtain the sought-for thrust. The minimum thrust is thus included between the kinematically and statically admissible ones, (Como, 1996; Como, 1998):

$$S(v) \leq \max[S(v)] = S = \min[S(s)] \leq S(s) \qquad (5)$$

This approach will be further extensively applied to the thrust evaluation of the St. Peter's Dome in Rome.

2 St. Peter's Dome by Michelangelo. The static restoration by Poleni and Vanvitelli

2.1 Dome geometry

The history of the dome planned by Michelangelo for St. Peter's Basilica in Rome is well known, (Mainstone, 1999; Mainstone, 2003, Benvenuto, 1990; Di Stefano, 1980).

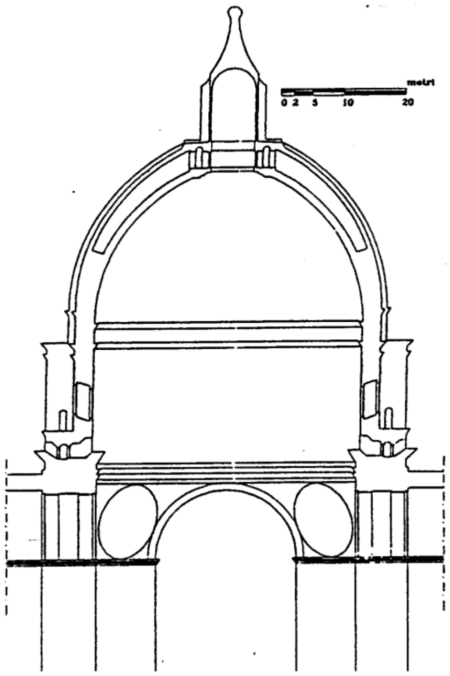

Fig. 4 – Dome longitudinal section (L. Vanvitelli, in Di Stefano, 1980)

The large structure of the dome is similar to the Brunelleschi's one in Florence. It is in fact made up of two interconnected shells, stiffened by 16 ribs. The section of the dome, as sketched by Vanvitelli and reported in Poleni (1748), is shown in Figure 4.

The main measures defining the geometry of the dome and of the supporting drum have been obtained directly from Vanvitelli's drawings (Figure 4 and Figure 5). The thicknesses of the internal and external shells are respectively 2.00 m and 1.00 m, while the total thickness of the composite dome varies between 3.00 m at the springing and about 5.00 m at the crown. The overall arrangement of the entire dome is that of an ogival spherical vault. The internal diameter of the dome at its base measures 42.70 m. A 3.00 m thick cylindrical wall, with an internal radius of 21.35 m, composes the drum. The dome is stiffened by sixteen 3.00 m thick radial buttresses, arising from the drum for a length of about 4.50 m and a height of 14.50 m.

The masonry used for the dome is made up of bricks, travertine blocks and mortar beds, and it was laid with the support of wood scaffolds and centrings. The two shells were built up between the ribs. Two iron ties encircling the dome were placed by Della Porta, (Di Stefano, 1980).

It is interesting to point out that the so-called Rules of C. Fontana (1694), followed in late 17th century Roman constructions, would have called for the drum to be thicker than the actual 3.00 m. However, the rules refer to domes without buttresses.

2.2 The damage

Many years after the dome's completion cracks began to develop and grow gradually over time. The first signs of damage were detected as far back as 1631 and more and more cracks appeared over the following years. In the mid-18th century, about 150 years after its completion, the dome exhibited widespread, serious damage and debates spread throughout the scientific community. Various descriptions and experts judgments were forthcoming, amongst which the dire account of Saverio Brunetti (Book II of Poleni, 1748): *«… the entire wall of the drum and the attic, together with the columns and buttresses, have rotated outwards, dilating the dome and lowering the lantern ... ».*

This description corresponds to the cracking pattern detected by L. Vanvitelli between 1742 and 1743 in an exquisite set of drawings published by Poleni in his *"Stato dei difetti"* (e.g., Plate XV shown in Figure 5). In this figure, long meridian cracks are clearly visible running along the dome intrados. They arise from the drum nearly up to the height of the ring connecting the crown to the lantern. The sixteen buttresses were hard-pressed to contrast the thrusting action of the attic and drum: their effort is evidenced by large, diffuse sloping cracks across them. At the time, sheets of lead covered the exterior of the outer shell and cracks could therefore be visible on the dome’s extrados.

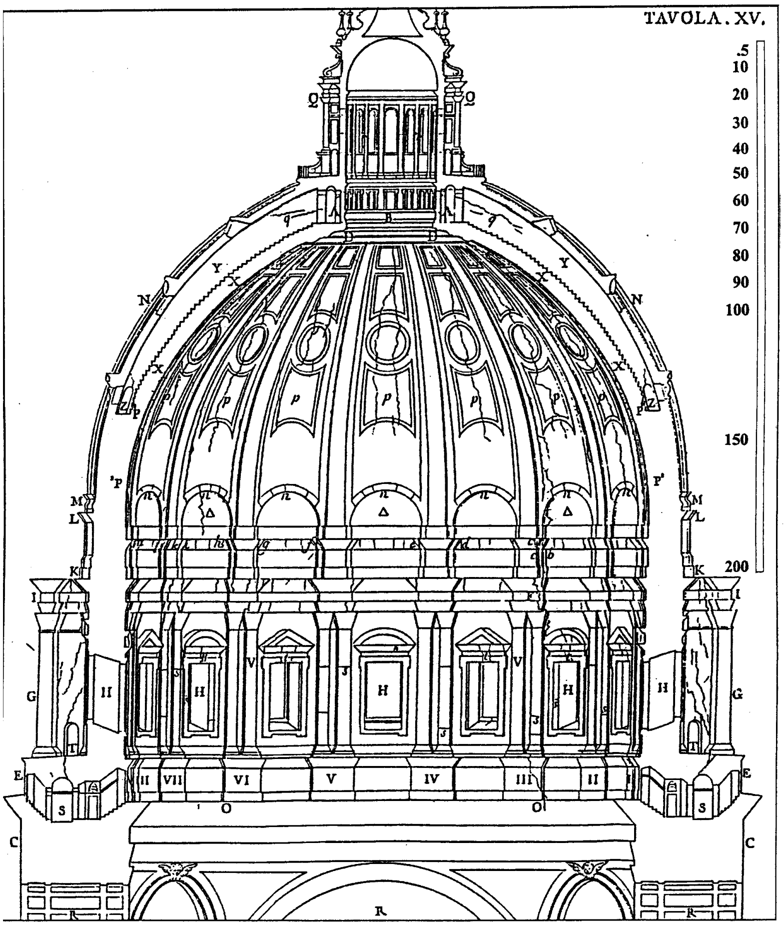

Fig. 5 – Cracking detected by L. Vanvitelli (from Poleni, 1748)

A membrane stress state, with hoop tensile stresses acting along the lower rings, occurred first in the original undamaged dome. Nevertheless, the friction strength between the bricks rings, compressed along the meridians, slowly faded, probably because of humidity penetrating into the masonry mass. The behavior of the dome gradually shifted from that of a rigid shell, stiffened by hoop stresses, towards that of a pushing dome, partitioned by long meridian cracks.

Alarm grew in Europe and in 1742 Pope Benedict XIV appointed a committee of scientists, known as *"The Three Mathematicians"*, composed by T. Le Seur, F. Jacquier and R.G. Boscovich, to report on the condition of the dome.

The Three Mathematicians' initial assessment, published as the *"Parere"* (1742) - i.e. opinion - was that the dome was seriously damaged and that its reparation would require extensive reinforcement operations. A later report by the same authors, the so-called *"Riflessioni"*, confirmed their initial estimation.

However, other scholars collaborating in the analysis dissented from their opinion. To settle this dispute, Benedict XIV decided to seek the advice of a brilliant Italian scholar, Giovanni Poleni.

In the Poleni manuscript, published as the *"Memoirs"* (1748), the author reported the results of a static analysis of the dome performed in his laboratory in Padua. This analysis was conducted in the wake of some recent results on the Statics of masonry arches obtained by R. Hooke, (1675). Poleni presented his proposal for the restoration. The *Memoirs* were received favorably by the Pope, who then entrusted Poleni with carrying out the dome restoration in collaboration with L. Vanvitelli, the architect of the *"Opera di San Pietro"*.

2.3 Analysis

According to historical accounts, the two discordant opinions regarding the dome's state and safety were heatedly debated (Mainstone, 2003; Benvenuto, 1990; Como, 1997; Como, 2008). The Three Mathematicians (1742), backed by many other scholars, believed that the dome's failure was imminent and its restoration, involving significant architectonic changes to the entire monument, was required with the utmost urgency. Poleni, instead, sustained that the dome's state of safety was much less threatening.

Moreover, Poleni was convinced that the so-called defects of the great dome could be repaired without any modifications to its architecture.

The Three Mathematicians' *Parere*, assessed that the dome was in danger of failure. They, using a simple mechanical model, viewed the cracking pattern as the starting point of the collapse mechanism. This model, drawn from a plate of their *Parere*, is sketched out in Figure 6 and considers the combination of the dome with the attic and the drum, together with the adjacent buttress. They reduced the complex system composed by the dome, the attic/drum and the buttress to the simple mechanism illustrated in the scheme of Figure 6. The system was modelled as an inclined beam *HT*, whose top point *T* was free to move along the vertical direction and whose base point *H* could move along the horizontal direction. The horizontal segment *AD* of the section shown in Figure 6 represents the drum base and the adjacent buttress, while the segment *AF* refers to the external edge of the vertical buttress. The buttress and the drum/attic were very weakly bound together, so that the Three Mathematicians reasonably considered the buttress to have been detached from the drum wall. Their mechanism describes the deformation of the damaged dome, with the drum and the attic rotating externally, and the dome slices counter-rotating inward, with the lowering of the lantern and the dilatation of the dome. According to this mechanism, the whole dome slice *HMNI* rotates inward around the hinge *H* and produces counter-rotation of the drum/attic/ buttress around *A* and *C*.

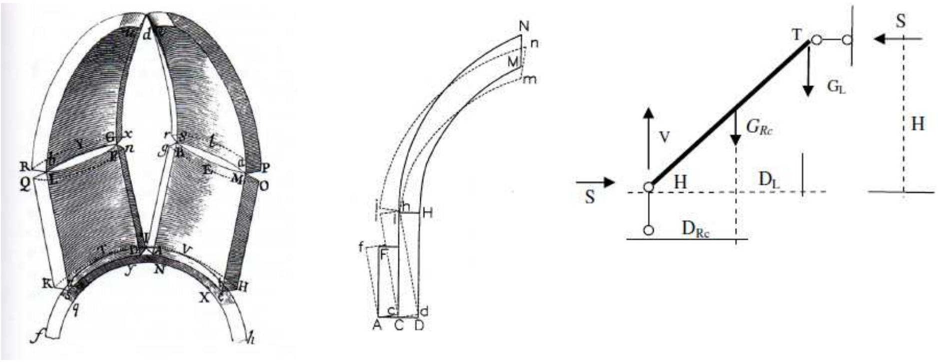

Fig. 6 – The Three Mathematicians' model and the corresponding failure mechanism

By applying the kinematic approach to this scheme, the Three Mathematicians evaluated the thrust of the dome. The restoration operations proposed by the Three Mathematicians were quite extensive: in addition to encircling the dome with new iron ties, they also wanted to thicken the buttresses and place new heavy statues on the top of them.

Poleni (1748), on the contrary, did not accept the conclusions of the Three Mathematicians: in his opinion, there was no correlation between the cracking of the dome and the one of the attic and drum. He instead attributed the damage solely to defects in construction and to the use of poor masonry. Poleni's firm conviction stemmed from the results of a static analysis that he himself developed and performed. This analysis, though incomplete, proved to him that the dome was still safe, despite its defects. Poleni's analytical procedure was inspired by Hooke's (1745) theorem of the inverted chain. Accordingly, Poleni divided the dome into fifty slices, each subdivided into thirty-two "wedges", whose position and weight he evaluated. He then constructed a detailed scale model of a dome slice in his Padua laboratory. He knew, in fact, the proportionality rule that holds for the no tension masonry-like constructions, (Como, 2014).

Poleni considered two thin chains: one of equal small-sized rings (an ideal catenary), and another composed of thirty-two small lead balls, whose weights modeled the weights of the thirty-two wedges constituting a single dome slice, including the top wedge's share of the weight of the lantern atop the dome. The length of the chains was fixed so that their end sections could pass through the centers of the sections at the springing and the crown of the slice.

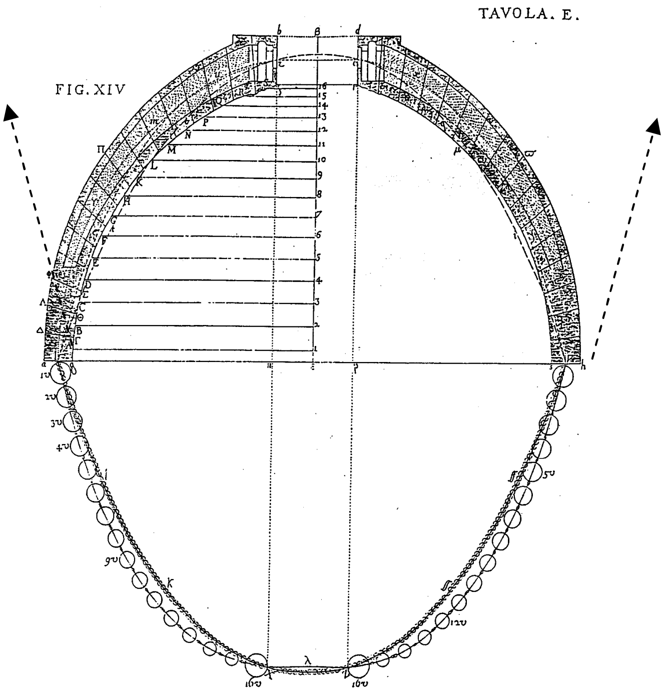

Fig. 7 – Poleni's static check (from G. Poleni, 1748)

The first step in the procedure was the determination of the equilibrium curve of the chains. Then, by inverting these curves and marking them on the slice model, Poleni was able to verify their positions with respect to the curve of the wedges centers. Figure 7 shows three curves in the slice: the first is the wedge centers curve, the second is the inverted catenary and the third is the inverted funicular of the wedges weights. This last curve runs over the inverted catenary but at the haunches, together with the catenary, runs near the intrados of the slice.

The position of the curve of the homogeneous catenary differed considerably from the curve of the wedge centers. The chain of lead balls, on the other hand, was contained within the slice and maintained a position quite close to the curve of the centers.

Poleni, thus, concluded that the equilibrium within the slice was certainly admissible, because compression stresses alone should be able to sustain the loads. Figure 7 shows the famous Poleni model with a sketch of his determination of the funicular curves with the vectors R tangent to the funicular at the springing. The horizontal component of R gives the pull of the chain and, consequently, according to the inverted chain model, the thrust in the dome. It is clear that Poleni's attention was focused exclusively on the equilibrium of the dome. In this way, Poleni was able to verify that the geometry of the meridian curve of the dome was actually admissible. Notwithstanding, Poleni believed that the dome of St. Peter was not at risk of failure and that the model proposed by the Three Mathematicians had to be flawed.

The dome was thus repaired and reinforced according to Poleni's recommendations and under the technical supervision of L. Vanvitelli. The cracks in the dome were patched through the procedure known as "*scuci e cuci*" (literally,"unstitch and stitch"), which is still commonly used today. However, the most important intervention was encircling the dome with six iron ties, which were able to counterbalance the static deficiency of both drum and buttresses.

3 The actual minimum thrust

In order to verify the real state of safety of the dome/buttresses system, it is necessary to evaluate the actual thrust of the dome. With this aim, it is convenient to follow Poleni's partitioning and the corresponding weight evaluations of the thirty-two wedges of the slice. In doing so, we shall refer to Figure 8 from Poleni's *Memoirs* (1748), where the various wedges are denoted as *A*, *B*, *C*, etc.

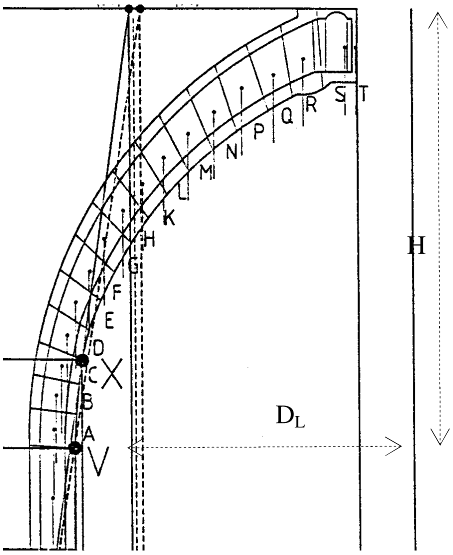

Fig. 8 – Wedge weights and centres positions, 1 cm corresponds to 4.75 m (Poleni, 1748)

The corresponding wedges weights are evaluated using the same unit of weight of Poleni, the pound [lb]. The slice to be considered is 1/50 of the entire dome. In Figure 8, 1 cm corresponds to 4.75 m. According to Poleni, the weight of the lantern slice G_{slL}, corresponding to 1/50 of the round angle, is $81.6\cdot 10^3$ lb. The weight of the entire lantern G_L thus equals $G_L = 50\cdot G_{slL} = 50\cdot 81.6\cdot 10^3$ lb $= 4080\cdot 10^3$ lb. The weight of the dome slice G_{sl} includes a share of the weight of the rib and the corresponding band of the outer and inner shells. Table 1 shows the weights of the various wedges:

Table 1. Weights of the various wedges

Wedge	**Weight [lb·10^3]**	**Wedge**	**Weight [lb·10^3]**
A	89	K	66
B	88	L	60
C	87	M	54
D	85	N	48
E	82	P	41
F	79	Q	34
G	75	R	27
H	71	S	18

Summing up all the weights of the wedges, the weight G_{sl} of the slice is equal to $1004\cdot 10^3$ lb. The weight G_{slL} of the slice, including the weight of the lantern slice, is 1085.6 lb.

The horizontal axis shown in Figure 8 and passing through the point V, indicates the head of the drum/attic, i.e. the level of the dome base. The vertical alignment passing through the point T of Figure 8 is the vertical line passing through the centre of the section joining the dome with the lantern, along which the load G_{slL} conveys.

The following distances are considered:

- D_L = 17.85 m is the distance between the vertical line passing through the drum's internal edge (V in Figure 8) and the alignment T;
- D_{sl} is the distance between the slice's centre and the alignment T;
- D_{slL} is the distance between the slice centre, including the share of the lantern weight, and the alignment T;
- D_{DslL} is the distance between the drum internal edge and the slice centre, through which the weight G_{slL} passes;
- H = 28.20 m is the height of the extrados of the section joining the dome with the lantern with respect to the dome base.

The moments of the wedges weights around the point T (placed at the intrados of the dome-to-lantern connection section) are shown in Table 2:

Table 2. Moments of the wedges weights around the point *T*

Wedge	**Moment [lb·m·10^3]**
A	$89\cdot4.15=369.35$
B	$88\cdot4.14=364.32$
C	$87\cdot4.05=374.10$
D	$85\cdot3.95=335.75$
E	$82\cdot3.85=315.70$
F	$79\cdot3.65=288.35$
G	$75\cdot3.45=262.50$
H	$71\cdot3.20=227.20$

Wedge	**Moment [lb·m·10^3]**
K	$66\cdot2.95=194.70$
L	$60\cdot2.65=159.00$
M	$54\cdot2.30=124.20$
N	$48\cdot1.95=93.60$
P	$41\cdot1.60=65.60$
Q	$34\cdot1.15=39.10$
R	$27\cdot0.75=20.25$
S	$18\cdot0.15=2.70$

The moment of the weight of the lantern slice is equal to $81.6 \cdot 10^3$ lb·0.0 m = 0.00 lb·m. The total moment M is thus equal to $3210.92 \cdot 10^3$ lb·4.75 m = 15251.87 lb·m.

The distance of the slice centre from the alignment T is $D_{sl}=M/G_{sl}=15.19$ m. The distance of the slice centre (including the share of the lantern weight) from the alignment T is $D_{slL}=M/G_{slL}=14.05$ m. The distance of the slice centre (including the share of the lantern weight) from the internal edge of the drum $D_{DslL}=17.85 - 14.05 = 3.80$ m.

Figure 9a sketches the outline of a typical mechanism v of a dome slice, whose base undergoes a slight broadening. The point O indicates the position of the internal hinge. When the point O falls on the intrados of the dome springing section, this mechanism corresponds to the one envisioned by the Three Mathematicians. Figure 9b shows all involved quantities. The work done by the loads g is given by:

$$< g, v >= \theta \cdot \sum_i G_i (D^* - x_i) \tag{6}$$

where D^* indicates the horizontal distance of the hinge O from the alignment T and x_i the distance of each single force G_i from the same alignment, as shown in Figure 9.

Finally, we have:

$$\Delta(v) = \theta \cdot H^* \tag{7}$$

where H^* is the vertical distance between the internal hinge O and the extrados of the section where the dome joins the lantern.

The vertical displacements v_i of the application points of the loads G_i, representing the weights of the various wedges, are then given by:

$$v_i = (D^* - x_i) \cdot \theta \tag{8}$$

Thus, we have:

$$S_{kin}(v) = \frac{\sum_i G_i (D^* - x_i)}{H^*} \tag{9}$$

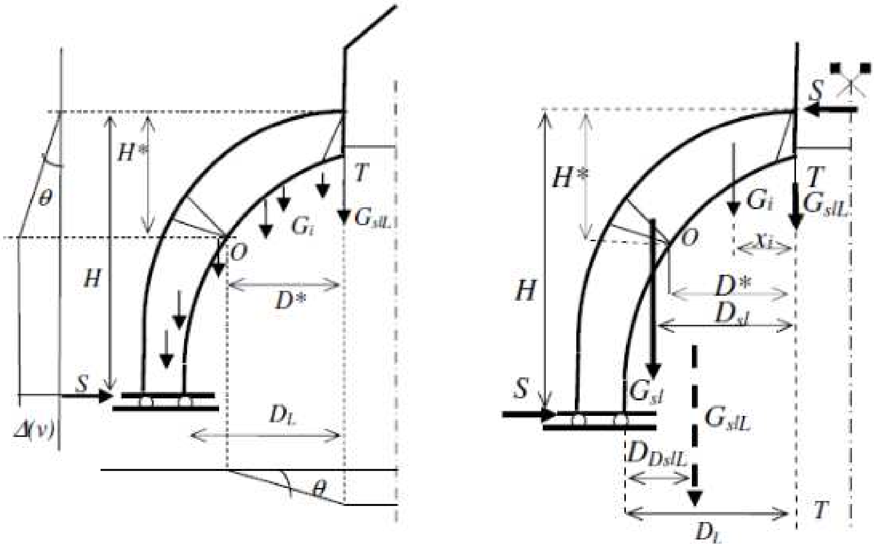

(a) (b)

Fig. 9 – The minimum thrust evaluated via the kinematic procedure

The maximum kinematic thrust $S_{kin}(v)$ is found by varying the position of the internal hinge *O* along the intrados curve of the slice. In the following, five different mechanisms, numbered from (0) to (4), are considered and the corresponding kinematic thrust $S_{kin}(v)$ is evaluated for each one of them. The highest value among all values of $S_{kin}(v)$ turns out to be the one obtained considering the mechanism (4).

Mechanism (0) – The mechanism of the Three Mathematicians

- Position of the internal hinge *O*: point *V* shown in Figure 8, located at the intrados of the dome springing, at the height of the top of the attic/drum;

- The work of the loads includes the weights G_i running from the wedge *A* to the wedge *S*, in addition to the corresponding share of the lantern weight;
- Horizontal distance D^* of the hinge *O* from the alignment *T*: $D^{*}=D_L$=17.85 m;
- Vertical distance H^* of the hinge *O* from the extrados of the section where the dome joins the lantern: $H^* = H$ = 28.20 m.
- Total work L_{tot} of the loads G_i, including the work of the lantern slice, on the assumed mechanism: L_{tot}=1615.67 tm·θ;
- Work performed by the thrust: $S_{kin} \cdot H \cdot \theta = S_{kin} \cdot 28.20 \cdot \mathrm{m} \cdot \theta$;
- S_{kin} = 57.29 t = 126.3·10^3 lb.

Mechanism (1)

- Position of the internal hinge *O*: point *X* shown in Figure 8. According to this mechanism, the weights of the wedges *A*, *B* and *C* do no work;
- Horizontal distance D^* of the hinge (1) from the alignment *T*: D^*=17.56 m;
- Vertical distance H^* of the hinge (1) from the extrados of the joining section of the dome to the lantern: H^* = 22.325 m;
- Total work of the loads G_i, including the work of the lantern slice, along the assumed mechanism: L_{tot} = 1579.556·θ tm;
- Work performed by the thrust: $S_{kin} \cdot H \cdot \theta = S_{kin} \cdot 22.325 \text{ m} \cdot \theta$;
- S_{kin} =70.75 t = 155.98·10^3 lb.

Mechanism (2)

- Position of the internal hinge *O*: point located between the wedges *H* and *K* in Figure 8. According to this mechanism, the weights of the wedges from *H* to *A* do no work;
- Distance D^* of the hinge (2) from the alignment *T*: D^* =13.53 m;
- Distance H^* of the hinge (2) from the extrados of the joining section of the dome to the lantern: H^* =13.3 m;
- S_{kin} = 78.51 t = 173.08·10^3 lb.

Mechanism (3)

- Position of the internal hinge O: point located between the wedges E and F in Figure 8. According to this mechanism, the weights of the wedges from E to A do no work;
- Distance D^* of the hinge (3) from the alignment T: $D^* = 16.62$ m;
- Distance H^* of the hinge (3) from the extrados of the joining section of the dome to the lantern: $H^* = 18.52$ m;
- $S_{kin}\cdot 18{,}52\ \mathrm{m}\cdot \theta = 1444.78\cdot \theta$;
- $S_{kin} = 78\ \mathrm{t} = 171.96\cdot 10^3$ lb.

Mechanism (4)

- Position of the internal hinge O: point located between the wedges D and E in Figure 8. According to this mechanism, the weights of the wedges from D to A do no work;
- Distance D^* of the hinge (4) from the alignment T: $D^* = 17.81$ m;
- Distance H^* of the hinge (4) from the extrados of the joining section of the dome to the lantern: $H^* = 20.42$ m;
- Total work of the weights of the wedges and of the lantern slice: $L_{tot} = 1715.40\cdot \theta$;
- Work performed by the thrust: $S_{kin}\cdot H^*\cdot \theta = S_{kin}\cdot 20.42\ \mathrm{m}\cdot \theta$;
- $S_{kin}\ 20.425\ \mathrm{m}\cdot \theta = 1715.40\cdot \theta$;
- $S_{kin} = 84\ \mathrm{t} = 185.19\cdot 10^3$ lb.

Other mechanisms, with internal hinges located elsewhere on the intrados of the slice, do not furnish larger thrust values than the one corresponding to mechanism (4). Thus, the maximum kinematic thrust value corresponds to mechanism (4) and the minimum thrust of all statically admissible states therefore corresponds to the kinematic thrust that results by positioning the hinge O between the wedges D and E, namely $225.77\cdot 10^3$ lb. A slice having a width equal to 1/50 of the dome's round angle transmits this thrust. Given an average drum diameter of 45.70 m, and an average circumference of $45.70\cdot\pi=143.57$ m, the length of the arc corresponding to the assumed slice is 143.57/50 = 2.87 m. The thrust of 84 t is thus transmitted along a length of 2.87 m, and the thrust per unit length of the drum equals 84 t/2.87 m =29.26 t/m. Comparing the various thrust values and making reference to Eq. (5) we have:

$$S_{ThreeMat} = 57.29t < \max[S(v)] = 84t = \min[S(s)] < S_{Poleni} = 87.4t \tag{10}$$

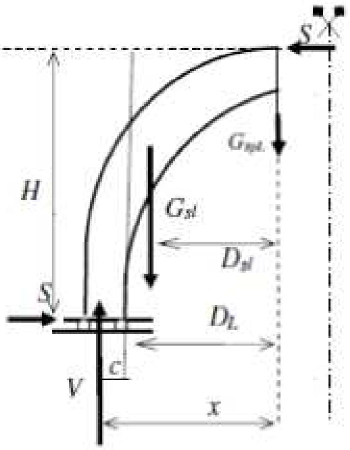

Fig. 10 – Equilibrium of the slice

With reference to Figure 10, the vertical load transmitted by the slice equals the total weight of the slice, V=108.6·10^3 lb. The position of the vertical force V at the base of the slice can be obtained by considering the equilibrium of the slice. Let x be the distance of the force V from the alignment T (Figure 10). The condition of null moment of all forces around the point of intersection of the dome extrados with the section of the dome connection with the lantern gives:

$$Vx - G_{sl}D_{sl} - SH = 0 \tag{11}$$

whence we obtain x = 19.9 m.

Thus, the distance of the force V from the inner edge of the drum is:

$$c = (19.85 - 17.85)m = 2.0m \qquad (12)$$

The mechanism assumed by the Three Mathematicians was very far from the mechanism corresponding to the settlement state that requires a circumferential hinge at the intrados in the haunches of the dome.

The thrust evaluated by Poleni, by means of an extraordinary application of the Hooke Theorem, is, on the contrary, only a bit larger than the minimum thrust.

4 Safety Assessment of the Dome/Buttresses System

Poleni, on the other hand, neglected to consider the effects of the thrust on the supporting structures as the drum and the sixteen buttresses. An accurate analysis of the statics of the buttresses, on the contrary, has shown that they were very near to fail, (Como, 1997; Como, 2008). By way of definition, the quantities shown in Figure 11 are:

- S_{domT}, the thrust transmitted directly by the dome slice, acting at a height of about 18.00 m from the drum base;
- V, the vertical load due to the weight of the dome slice;
- C_3, the weight of the slice of the attic/drum, having thickness equal to the dome base;
- c = 2.0 m, the distance of the vertical force V, taken from the internal edge of the drum, as previously evaluated;
- h_1, the height of the strip of the attic/drum, equal to 18.00 m.

The dotted arrow shown in Figure 11 represents the counter-thrust of the buttress, which was not considered in the foregoing analysis. Previous calculations gave us S_{domT}=84 t and V=403.84 t. The total weight of the drum and the attic, according to Poleni, is equal to 17.861 t and the corresponding weight of the slice is C_3=17.861·1/50 = 357.22 t, as illustrated in Figure 11. Let us consider the base section of this slice of the drum/attic, which is 1/50 of the round angle: this base is found at the height of the passageway floor through the buttress, as shown in Figure 5. The total moment of all vertical forces acting on the centre of this base section, having thickness equal to 3.00 m, is:

$$M_{tot} = 84 \cdot 18 + 403.84 \cdot 0.55 = 1734.1 tm \tag{13}$$

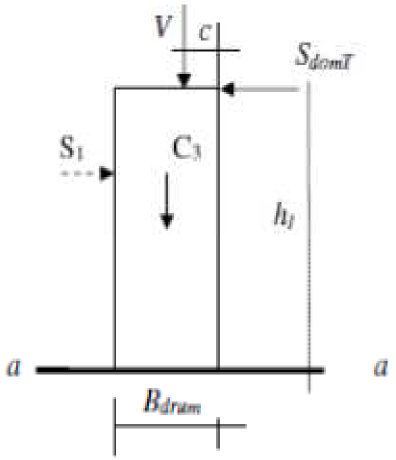

Fig. 11 – Check of the vertical strip of the drum

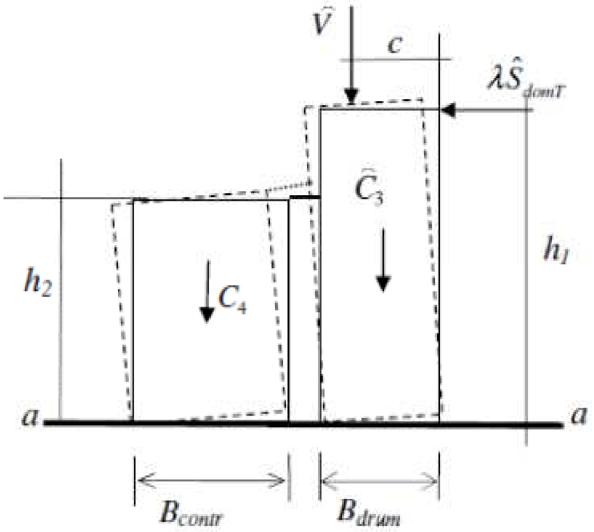

Fig. 12 – Check of the drum strip including the buttress

It should be recalled that, in the first analysis, the possible counter-thrust of the buttress was not taken into account. The section, having a width of 2.87 m, equal to the arc length of the slice, bears the axial load N:

$$N = 403.84 + 357.2 = 761.04t \tag{14}$$

with an eccentricity e equal to:

$$e = 1734.1 / 761 = 2.28m > B / 2 = 1.50m \tag{15}$$

The resultant of the axial force N and of the bending moment M thus turns out to be outside the base section of the slice. The effects of the buttress counter-thrust must therefore be taken into account. Indeed, it is the composite system drum/attic, coupled with the buttresses, of height h_2, that represents the structure resisting the dome thrust (Figure 12). Failure of this system could occur via the mechanism foreseen by the Three Mathematicians, through equal rotations of the sliced drum/attic and buttresses, as in Figure 6. Instead, we now consider the thrust λS_{domT} as shown in Figure 12.

Given that the buttresses around the drum are sixteen in number, we must take 1/16 of the round angle as the width of the drum/attic slice associated to a single buttress. The values of the corresponding weight and thrust considered above must now be multiplied by the factor 50/16 =3.125. These values of the weight and thrust will be respectively indicated as $\hat{C}_3$ and $\hat{S}_{domT}$, to distinguish them from the other values corresponding to 1/50 of the round angle. The weight of the buttress, indicated as C_4 in Figure 12, is very difficult to evaluate because of its complex geometry. As a rough estimation, averaging its transverse section, we have C_4=2.3·14.50·3.60·5.60=672 t, to account for the greater weight from the marble elements, the presence of large cornices, and so forth. The thrust load multiplier λ is, thus, obtained by equating the resistant and pushing works done by the various forces along the mechanism:

$$\left[\hat{C}_3 \frac{B_{drum}}{2} + C_4 \frac{B_{contr}}{2} + \hat{V}(B_{drum} - c)\right]\theta = \lambda\theta\hat{S}_{domT} h_1 \qquad (16)$$

whence:

$$\lambda = \frac{\hat{C}_3 \frac{B_{drum}}{2} + C_4 \frac{B_{contr}}{2} + \hat{V}(B_{drum} - c)}{\hat{S}_{domT} h_1} \approx 1.00 \qquad (17)$$

Another simplified analysis, performed by Como (1997), yielded a safety factor λ of 1.06, only slightly higher than the determined value of 1.02.

Note that we have assumed the drum to be cracked along its entire height. Such an assumption leads to a picture of the static condition of the dome that is considerably more pessimistic than its actual condition. In any event, the cracking pattern detected by Vanvitelli included severe diagonal cracks in the buttresses (Figure 5).

The resisting buttresses were seriously stressed by the dome and the equilibrium was extremely precarious. The particular geometry of the buttresses, with their external columns practically detached from the masonry wall, indicates that they were not originally designed as resistant elements to the dome’s thrust. Despite the imprecision of the performed rough estimation, it can nonetheless be concluded that the static conditions of the dome were actually quite critical, even close to failure.

5 Conclusions

To sum up, the attic/drum and buttresses were too weak to support the dome, given the nearly semicircular profile of its meridian section and the presence of the heavy lantern above. In particular, the rather frail geometry of the buttresses contributed little to its static stability, something probably overlooked by Michelangelo.

The Three Mathematicians realized the static inadequacy of the drum, albeit through a too simplified kinematic model. However, their proposed repairing and restoration intervention was too invasive and it would have modified the monument's architecture. Poleni, on the other hand, never understood the actual static precariousness of the dome's state. However, although his static analysis was flawed, he, with the invaluable help of L. Vanvitelli, had installed six iron hoops to encircle the dome, which, in the end, were able to counterbalance the static deficiency of both drum and buttresses.

In brief, Poleni and Vanvitelli's restoration, carried out in full respect of the monument's architecture, turned out to be a great success indeed. To this day, not only the wondrous Vatican dome is still standing, but it has retained its original architecture.

References

1. Benvenuto, E. (1990). *An Introduction in the History of Structural Mechanics*. Part II, Vaulted Structures and Elastic Systems. New York, USA: Springer Verlag.
2. Coccia, S., Como, M., Di Carlo, F. (2016). Minimum thrust and minimum thickness of hemispherical masonry domes. *Acta Mechanica.* vol. 227 (*9*), pp. 2415-2425.
3. Como, M. (1996). On the role played by Settlements in the Statics of masonry Structures. *Int. Conf. Geotechnical Engin. for the Preservation of Monuments and Historic Sites*. Naples, Italy, 3-4 Oct. 1996, Rotterdam, Netherlands: A.A. Balkema.
4. Como, M. (1997). Un antico restauro statico della cupola di S. Pietro a Roma. In C. Conforti (Ed.), *Lo specchio del cielo*. Milano, Italy: Electa.
5. Como, M. (1998). Minimum and maximum thrust states in Statics of ancient masonry buildings. Proc. *2nd International Arch Bridge Conference.* Venice, Italy, 6–9 Oct. 1998, Rotterdam, Netherlands: A.A. Balkema.
6. Como, M. (2008). Sulla storia del restauro statico della cupola di S. Pietro in Roma eseguito da Poleni e Vanvitelli. *Convegno Nazionale di Storia dell'Ingegneria*, Napoli, Italy: Cuzzolin Ed..
7. Como, M. (2010). *Statica delle Costruzioni Storiche in Muratura*, Roma, Italy: Ed. Aracne.
8. Como, M. (2016). *Statics of Historic Masonry Constructions*. Heidelberg, Germany: Springer.
9. Como, M. (2014). The Theory of Proportions in the History of Architecture and Engineering. In: S. D'Agostino, G. Fabricatore (eds.) *Proc. Intern. Conf. "History of*

Engineering". May 19-20, 2014, Napoli, Italy: Cuzzolin Ed.

10. Di Stefano, R. (1980). *La cupola di S. Pietro – Storia della Costruzione e dei Restauri*, Napoli , Italy: Edizioni Scientifiche Italiane.
11. Fontana, C. (1694). *Il tempio vaticano e sua origine*. Roma.
12. Flügge, W. (1962). *Stresses in shells*. Berlin , Germany: Springer Verlag.
13. Gesualdo, A., Cennamo, C., Fortunato, A., Frunzio, G., Monaco, M., Angelillo, M. (2017). Equilibrium formulation of masonry helical stairs, *Meccanica*, vol. 52 (*8*), pp. 1963-1974.
14. Heyman, J. (1966). The stone skeleton. *Intern. Journal of Solids and Structures*, vol. 2 (*2*), pp. 249-256.
15. Heyman, J. (1977). *Equilibrium of shell structures*. Oxford, UK: Oxford University Press.
16. Heyman, J. (1995). *The stone skeleton*, Cambridge, UK: Cambridge University Press.
17. Hooke, R. (1675). *A description of helioscopes and some other instruments*. London.
18. Mainstone, R. (1999). The Dome of St. Peter: Structural Aspects of its Design and Conservation. Inquiries into its Stability. In *Structure and Architecture History*, Design and Innovation. Ashgate, Variorum Collected Studies Series.
19. Mainstone, R. (2003). Saving the dome of St. Peter's. *Construction History,* vol. 19.
20. Poleni, G. (1748). *Memorie istoriche della gran cupola del tempio vaticano e de' danni di essa, e de' ristoramenti loro*. Padova. Included: Breve Parere di Vanvitelli L. Roma: Reprint of the Faculty of Architecture of University of Rome Sapienza.
21. Three Mathematicians, Le Seur, T., Jacquier, F., Boscovich, R.G. (1742). Parere di tre matematici sopra i danni che si sono trovati nella cupola di S. Pietro sul fine dell'anno 1742, dato per ordine di N.S. Benedetto XIV, Roma. Reprint of the Faculty of Architecture of University of Rome Sapienza, Roma.

An enriched 2D finite element for the nonlinear analysis of masonry walls

Daniela Addessi[1], Elio Sacco[2]

[1] Sapienza University of Rome, Via Eudossiana 18
00184 Roma (RM), Italy
daniela.addessi@uniroma1.it
[2] University of Cassino and Southern Lazio, Via G. Di Biasio 43
03043 Cassino (FR), Italy
sacco@unicas.it

Summary. This paper presents a kinematic enriched finite element model for the nonlinear analysis of brick masonry walls loaded in their plane. The finite element accounts for the transversal deformation of the wall and permits to reproduce the mortar-brick interaction in the direction of wall thickness. Nonlocal constitutive relationships are considered both for mortar and bricks, adopting a damage-friction law for the mortar and an isotropic damage model for the bricks, both accounting for tensile failure mechanisms. A numerical procedure is developed for the evaluation of the damage and friction evolution in the mortar and brick materials. Numerical applications are presented, comparing the results obtained by the proposed finite element with the experimental outcomes.

Keywords: finite element, enriched kinematics, damage, friction, masonry.

1 Introduction

The formulation of accurate and efficient numerical models for the nonlinear analysis of masonry structures is a relevant topic in civil engineering. A wide variety of approaches has been proposed, which differ in the modeling scale and in the adopted constitutive laws (Addessi *et al.*, 2015). Among these, micromechanical models are the most accurate, as these describe in detail geometry, arrangement and constitutive behavior of the masonry constituents, bricks, mortar and interfaces. This approach has been adopted by Ercolano in a series of papers (Ercolano, 1994 and 1995;

Auciello and Ercolano, 1997) describing the masonry as a texture of superimposed rigid blocks in unilateral contact each other in static and dynamic framework.

The micromechanical models can be developed including also the cohesive response of the mortar joints and the friction plasticity mechanisms for both bricks and mortar and/or interfaces (Guinea *et al.*, 2000; Zucchini and Lourenço, 2009; Aref and Dolatshahi, 2013). A number of two-dimensional (2D) models has been developed, instead of full three-dimensional approaches, usually based on the plane stress or plane strain assumptions. Nevertheless, these approaches can lead to strong approximations and fail in correctly describing the actual transversal tensile failure of the masonry wall, when this is subjected to in-plane compression (Hilsdorf, 1969). Some attempts to improve the 2D models can be found, introducing generalized plane state assumptions (Anthoine, 1997; Massart *et al.*, 2005), which can be a suitable method to evaluate the effect of the mortar-brick interaction in the thickness direction. Following a different approach, in recent works (Addessi and Sacco, 2014, 2016a and 2016b) the authors presented a 2D linear elastic model, standing on an enriched kinematic formulation, which considers also the out-of-plane strain and stress components.

In this paper, the new finite element EKQFE (Enriched Kinematics Quadrilateral Finite Element) is developed, accounting for the nonlinear constitutive laws of the masonry constituents, bricks and mortar.

A coupled damage-friction model is considered for the mortar, while an isotropic damage law is proposed for the bricks, based on the assumption that damage mechanisms are governed only by the tensile strains.

To overcome the localization problems and the mesh-dependency of the FE solution, due to the considered constitutive laws with strain-softening, the damage evolution is assumed to be driven by nonlocal equivalent strains. These are defined on the basis of the nonlocal integral technique.

A numerical procedure is developed to solve the evolution problems of the damage and plastic variables at each Gauss integration point, by means of a predictor-corrector technique. The algorithm is implemented in the FE code

FEAP (Taylor, 2011), used to perform the analyses on the masonry elements.

An experimental masonry wall under a diagonal concentrated vertical load is analyzed to validate the proposed nonlinear model and the implemented FE numerical procedure. Moreover, the numerical study of a masonry unit cell response under simple loading conditions is shown.

2 2D finite element with enriched kinematics

Let Ω denote the three-dimensional region occupied by a masonry wall. In Fig. **1**, a wall characterized by a classical regular texture (running bond) is shown. The Cartesian coordinate system (x_1, x_2, x_3) is introduced, with $x_1 - x_2$ located in the wall mid-plane denoted by S and x_3 in the thickness direction. The wall thickness is indicated by t, so that $\Omega = S \times (-t/2, t/2)$. Next, Voigt notation is adopted for the stress and strain measures.

The objective of this work is to investigate the response of the masonry wall subjected to in-plane loadings. Thus, it is assumed that the surface S is loaded by body forces $\mathbf{b} = \{b_1 \; b_2 \; 0\}^T$ (force per unit surface), acting on the mid-plane of the wall and by contact forces $\mathbf{p} = \{p_1 \; p_2 \; 0\}^T$ (force per unit length), applied to the mid-plane boundary.

A new displacement-based finite element is presented. This is a 4-node quadrilateral element based on an enriched kinematics, called EKQFE (enriched kinematics quadrilateral finite element). Denoting with $\mathbf{u} = \{u_1 \; u_2 \; u_3\}^T$ the displacement vector, it is assumed that the displacement components are approximated in the wall thickness direction as:

$$\begin{array}{lcl} u_1(\mathbf{x}) & = & U_{11}(x_1, x_2) + x_3^2 U_{12}(x_1, x_2) \\ u_2(\mathbf{x}) & = & U_{21}(x_1, x_2) + x_3^2 U_{22}(x_1, x_2), \\ u_3(\mathbf{x}) & = & x_3 e_1(x_1, x_2) + x_3^3 e_2(x_1, x_2) \end{array} \tag{1}$$

where $\mathbf{x} = \{x_1 x_2 x_3\}^T$, U_{11} and U_{21} are the in-plane displacement components, evaluated at the mid-plane of the wall, while U_{12} and U_{22} are additional components enriching the in-plane displacement description; e_1 and e_2 represent the out-of-plane displacement components.

Note that the enrichment of the in-plane displacement components is expressed in function of an even power of the thickness coordinate x_3, due to the expected symmetry of the wall in-plane response with respect to its mid-plane. Instead, the enrichment of the out-of-plane components is given by an odd power of x_3, due to the skew-symmetric out-of-plane response of the wall with respect to its mid-plane.

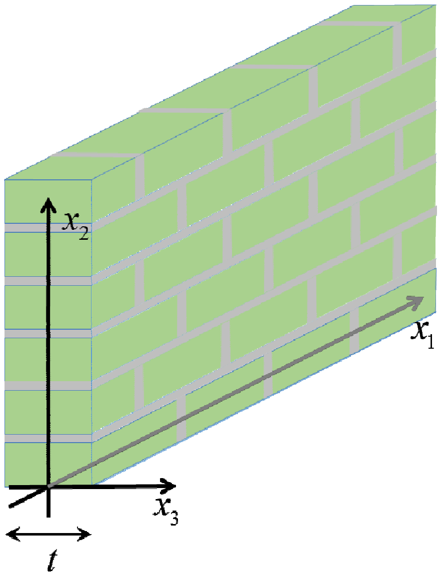

Fig. 1 - Schematic of the masonry wall characterized by regular (running bond) texture.

Concerning the in-plane approximation, Lagrangian interpolation functions of the displacement components $U_{11}(x_1,x_2)$, $U_{12}(x_1,x_2)$, $U_{21}(x_1,x_2)$, $U_{22}(x_1,x_2)$, $e_1(x_1,x_2)$ and $e_2(x_1,x_2)$ are adopted for the EKQFE. Bilinear interpolation functions are used and, on the basis of Equation (1), 6 degrees of freedom are defined at each FE node.

Denoting with $\mathbf{s}^e = \left\{U_{11}^1\, U_{12}^1\, U_{21}^1\, U_{22}^1\, e_1^1\, e_2^1 \ldots\ldots U_{11}^4\, U_{12}^4\, U_{21}^4\, U_{22}^4\, e_1^4\, e_2^4\right\}^T$ the vector containing all the $6 \times 4 = 24$ nodal kinematic degrees of freedom of the FE and following a standard procedure, the displacement vector $\mathbf{u}(\mathbf{x}) = \{u_1\ u_2\ u_3\}^T$, whose components are defined in Equation (1), is approximated as:

$$\mathbf{u}(\mathbf{x}) = \left(\mathbf{N}_0 + x_3\mathbf{N}_1 + x_3^2\mathbf{N}_2 + x_3^3\mathbf{N}_3\right)\mathbf{s}^e, \tag{2}$$

where $\mathbf{N}_0(x_1, x_2)$, $\mathbf{N}_1(x_1, x_2)$, $\mathbf{N}_2(x_1, x_2)$, $\mathbf{N}_3(x_1, x_2)$ are 3×24 matrices, containing the bilinear interpolation functions.

On the basis of expression (2), the strain vector results as:

$$\boldsymbol{\varepsilon}(\mathbf{x}) = \left(\mathbf{B}_0 + x_3\mathbf{B}_1 + x_3^2\mathbf{B}_2 + x_3^3\mathbf{B}_3\right)\mathbf{s}^e, \tag{3}$$

where $\mathbf{B}_0(x_1, x_2), \mathbf{B}_1(x_1, x_2), \mathbf{B}_2(x_1, x_2), \mathbf{B}_3(x_1, x_2)$ are the compatibility operators, with evident meaning of the symbols.

Once the strain vector is known at each Gauss integration point of the FE, the equilibrium equations are derived for the single FE using the virtual displacement work theorem:

$$\begin{aligned}
0 &= \int_{-t/2}^{t/2}\int_{S_e} \delta\boldsymbol{\varepsilon}^T\boldsymbol{\sigma}\, dx_1 dx_2\, dx_3 - \int_{S_e} \delta\mathbf{u}^T\mathbf{b}\, dx_1 dx_2 - \int_{\partial S_e} \delta\mathbf{u}^T\mathbf{p}\, ds \\
&= \delta\left(\mathbf{s}^e\right)^T \left[\int_{S_e} \left(\mathbf{B}_0{}^T\mathbf{N} + \mathbf{B}_1{}^T\mathbf{M} + \mathbf{B}_2{}^T\mathbf{P} + \mathbf{B}_3{}^T\mathbf{Q}\right) dx_1 dx_2 \right. \\
&\qquad \left. - \int_{S_e} \mathbf{N}_0{}^T\mathbf{b}\, dx_1 dx_2 - \int_{\partial S_e} \mathbf{N}_0{}^T\mathbf{p}\, ds \right]
\end{aligned} \tag{4}$$

where S_e is the area of the FE and the stress resultants are defined as:

$$\mathbf{N} = \int_{-t/2}^{t/2} \boldsymbol{\sigma}\, dx_3 \quad \mathbf{M} = \int_{-t/2}^{t/2} x_3\boldsymbol{\sigma}\, dx_3 \quad \mathbf{P} = \int_{-t/2}^{t/2} x_3^2\boldsymbol{\sigma}\, dx_3 \quad \mathbf{Q} = \int_{-t/2}^{t/2} x_3^3\boldsymbol{\sigma}\, dx_3 \tag{5}$$

The constitutive equations are introduced in the next section.

3 Masonry constitutive model

Masonry is a heterogeneous medium composed by the assemblage of bricks joined by mortar. Both brick and mortar are cohesive materials, characterized by softening mechanical response, due to the onset and growth of micro-cracks that evolve and coalesce leading to the formation of macro-cracks. During the masonry failure process, mortar joints are subjected to progressive damage caused by the presence of tensile (opening mechanism) and shear (friction-sliding mechanism) stresses. The unilateral response of the mortar joints, due to the opening and re-closure of the micro-cracks, and the friction-sliding, occurring when the compressed joint is damaged because of the presence of shear stresses, play a relevant role in masonry element response.

The damaging process of the brick is mainly due to the tensile failure mechanism, due to the mortar-brick interaction in a masonry wall subjected to compressive stresses, which induce compression in mortar and tension in the brick along the thickness direction [14]. Because of the damaging effects, the response of both mortar and bricks are characterized by the presence of softening branches, so that nonlocal constitutive laws are required to avoid strain and damage localization and strong mesh dependency of the FE results.

A constitutive model which accounts for damage, friction and unilateral contact is considered for the mortar. The model proposed in (Sacco, 2009; Addessi *et al.*, 2010) is able to describe the overall response of the system made of mortar joint and interfaces, connecting the mortar to the adjacent bricks. A local coordinate system (x_T, x_N) is introduced in the typical mortar joint, with T and N denoting the directions parallel and orthogonal to the joint, respectively. The stress at the typical point of the joint is expressed by the relation:

$$\boldsymbol{\sigma} = \mathbf{C}^m \left(\boldsymbol{\varepsilon} - \boldsymbol{\pi}\right), \tag{6}$$

where $\boldsymbol{\pi} = D^m \left(\mathbf{c} + \mathbf{p}\right)$ is the inelastic strain vector, collecting all the inelastic effects, i.e. damage, unilateral contact and friction sliding. Indeed, in

Equation (6) $\mathbf{C}^m$ is the isotropic elasticity matrix of the mortar, D^m is the scalar damage parameter defined in the mortar joints, while $\mathbf{c}$ and $\mathbf{p}$ are the strain vectors accounting for the unilateral opening effect and for the friction sliding, respectively. The components of the inelastic strain vectors $\mathbf{c}$ and $\mathbf{p}$ are:

$$\begin{aligned} \mathbf{c} &= h(\varepsilon_N)\{\varepsilon_T \quad \varepsilon_N \quad \varepsilon_{33} \quad 0 \quad \gamma_{N3} \quad \gamma_{T3}\}^T, \\ \mathbf{p} &= \qquad \{0 \quad 0 \quad 0 \quad \gamma_{NT}^p \quad 0 \quad 0\}^T, \end{aligned} \tag{7}$$

where $h(\varepsilon_N)$ is the Heaviside function, being $h(\varepsilon_N)=0$ if $\varepsilon_N \leq 0$ and $h(\varepsilon_N)=1$ if $\varepsilon_N > 0$.

The friction effect is modeled as a classical plasticity problem. The evolution law of the inelastic slip strain component γ_{NT}^p is governed by the Coulomb yield function:

$$\varphi(\boldsymbol{\sigma}^d, \zeta) = \mu(\zeta)\sigma_N^d + \left|\tau_{NT}^d\right|, \tag{8}$$

where $\boldsymbol{\sigma}^d = \mathbf{C}^m(\boldsymbol{\varepsilon} - (\mathbf{c}+\mathbf{p}))$ is the so-called contact stress, μ is the friction parameter, evolving according to the following exponential law:

$$\mu(\zeta) = (\mu_f - \mu_i)(1 - e^{-\omega\zeta}) + \mu_i, \tag{9}$$

being μ_i and μ_f the initial and final friction values, respectively, ω the exponential rate parameter and ζ the accumulated plastic slip strain, defined as:

$$\zeta = \int_0^\theta |\dot{\gamma}_{NT}^p| d\tau. \tag{10}$$

A non-associative flow rule is considered for the slip:

$$\dot{\gamma}_{NT}^p = \dot{\lambda}\frac{\tau_{NT}^d}{\left|\tau_{NT}^d\right|}, \tag{11}$$

with the following loading-unloading Kuhn-Tucker conditions:

$$\dot{\lambda} \geq 0 \quad \varphi\left(\boldsymbol{\sigma}^d\right) \leq 0, \quad \dot{\lambda}\,\varphi\left(\boldsymbol{\sigma}^d\right) = 0, \tag{12}$$

where λ is the inelastic multiplier.

A model accounting for the coupling of the fracture mode I and II is considered to evaluate the damage parameter D^m. The two quantities η_N and η_{NT}, which depend on the first cracking strains $\varepsilon_{N,0}$ and $\gamma_{NT,0}$, on the peak values of the stresses $\sigma_{N,0}$ and $\tau_{NT,0}$ and on the fracture energies G_{cI} and G_{cII}, respectively, are introduced in the form:

$$\eta_N = \frac{\varepsilon_{N,0}\sigma_{N,0}}{2G_{cI}}, \qquad \eta_{NT} = \frac{\gamma_{NT,0}\tau_{NT,0}}{2G_{cII}}. \tag{13}$$

The equivalent strain measures Y_N and Y_{NT} are defined as:

$$Y_N = \left(\left\langle \varepsilon_N \right\rangle_+\right)^2, \quad Y_{NT} = \left(\gamma_{NT}\right)^2, \tag{14}$$

where the operator $\left\langle \bullet \right\rangle_+$ evaluates the positive part of the number.

To overcome the localization problems related to the strain-softening constitutive behavior, the nonlocal definition $\bar{Y}_{N/NT}$ of the equivalent strain measures $Y_{N/NT}$, defined in Equations (14), is introduced as:

$$\bar{Y}_{N/NT}(\mathbf{x}) = \frac{1}{\int_{\Omega^m} \psi(\mathbf{y})\, d\Omega} \int_{\Omega^m} \psi(\mathbf{x}-\mathbf{y})\, Y_{N/NT}(\mathbf{y})\, d\Omega, \tag{15}$$

where Ω^m and ψ denote the mortar volume and the weighting function, respectively. The weighting function measures the influence on the analyzed point $\mathbf{x}$ of the point $\mathbf{y}$, lying in its neighborhood Ω^m, and is set as:

$$\psi(\mathbf{x}-\mathbf{y}) = e^{-\left(\frac{\|\mathbf{x}-\mathbf{y}\|}{\rho^m}\right)^2}, \tag{16}$$

ρ^m being the material characteristic length of the mortar, also called nonlocal radius.

Then, the following quantities are determined on the basis of the nonlocal equivalent strain measures:

$$\eta = \frac{1}{N^2}\left(\overline{Y}_N\ \eta_N + \overline{Y}_{NT}\ \eta_{NT}\right), \quad Y = \sqrt{\frac{\overline{Y}_N}{\varepsilon_{N,0}^2} + \frac{\overline{Y}_{NT}}{\gamma_{NT,0}^2}}, \quad N = \sqrt{\overline{Y}_N + \overline{Y}_{NT}}. \qquad (17)$$

Finally, the damage is evaluated according to the following law:

$$D^m = \max_{history}\left\{0, \min_{history}\left\{\tilde{D}^m, 1\right\}\right\} \qquad \text{with } \tilde{D}^m = \frac{Y-1}{(1-\eta)Y}, \qquad (18)$$

inducing a linear softening stress-strain response for monotonic loading histories of pure mode I or mode II, or for monotonic mixed loading histories.

An isotropic elastic-damage model is considered for the bricks. The adopted stress-strain relationship is written in the form:

$$\boldsymbol{\sigma} \ = \left(1 - D^b\right)\mathbf{C}^b\boldsymbol{\varepsilon}, \qquad (19)$$

where $\mathbf{C}^b$ is the 6×6 isotropic elastic constitutive matrix of the brick and D^b is the damage variable, with $0 \le D^b \le 1$.

A failure criterion, which is a slightly modified form of that presented in [2], is adopted. The following equivalent strain measure is introduced:

$$\varepsilon_{eq} = \sqrt{\left\langle \sum_{i=1}^{3}\left\langle \varepsilon_i + \varepsilon_o \right\rangle_+^2 - \kappa \sum_{i=1}^{3}\sum_{j=1}^{3}\frac{\left(1-\delta_{ij}\right)}{2}\left\langle \varepsilon_i \right\rangle_- \left\langle \varepsilon_j \right\rangle_- \right\rangle_+} - \varepsilon_o, \qquad (20)$$

where $\langle \bullet \rangle_{+/-}$ denotes the positive/negative part of the variable and δ_{ij} is the Kronecker's symbol. In formula (20), the compressive principal strains play the beneficial effect of confinement of the cohesive material, reducing the equivalent strain measure. The material parameter κ governs the reduction of the equivalent tensile strain due to the presence of compressive strains, while ε_o is a small regularization-like parameter, which ensures the convexity of the elastic domain. Once the equivalent strain ε_{eq} is defined, the nonlocal associated measure $\overline{\varepsilon}_{eq}$ is evaluated as:

$$\bar{\varepsilon}_{eq}(\mathbf{x}) = \frac{1}{\int_{\Omega^b} \psi(\mathbf{y}) d\Omega} \int_{\Omega^b} \psi(\mathbf{x}-\mathbf{y}) \varepsilon_{eq}(\mathbf{y}) d\Omega, \tag{21}$$

where Ω^b denotes the brick volume and the weighting function ψ is defined as in (16), by introducing the nonlocal radius ρ^b, which is the material characteristic length of the brick.

The yield limit function is defined as:

$$F = \bar{\varepsilon}_{eq} - \varepsilon_t, \tag{22}$$

where ε_t is the tensile strain threshold, as schematically illustrated in Fig. **2**, where typical uniaxial tensile and compressive responses of the brick material are illustrated.

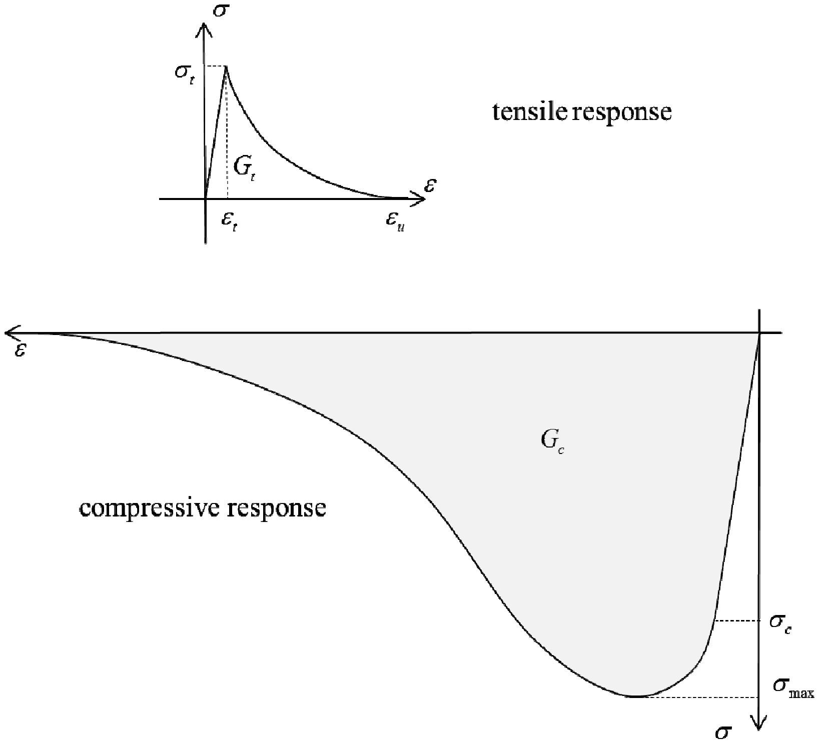

Fig. 2 – Tensile and compressive response for the brick material.

In Fig. **3** the limit function F is plotted in the principal strain plane $\varepsilon_1-\varepsilon_2$ (a) and in the principal stress plane $\sigma_1-\sigma_2$ (b), in both cases under the plane stress assumption $\sigma_3=0$. The material parameters contained in Table 1 are adopted.

Table 1. Model parameters adopted for the brick material.

$E^b=1850$ MPa	$\nu^b=0.15$	$\varepsilon_t=9.0\times10^{-4}$
$\varepsilon_u=1.8\times10^{-2}$	$\kappa=0.03$	$\varepsilon_o=1.0\times10^{-5}$

It can be remarked that the equi-biaxial compressive limit stress does not depend, for the considered cases, on the compressive limit strain, as the material failure is due to the reached tensile limit strain in the transversal direction, i.e. in the direction of the stress $\sigma_{33}=0$.

The damage evolution is governed by an exponential law, expressed as:

$$D^b=\max_{history}\left\{0,\min_{history}\left\{\tilde{D}^b,1\right\}\right\}, \tag{23}$$

with

$$\tilde{D}^b=1-\frac{1}{\bar{\varepsilon}_{eq}\left(\varepsilon_u-\varepsilon_t\right)^3}e^{-\beta\left(\bar{\varepsilon}_{eq}-\varepsilon_t\right)}\left(\bar{\varepsilon}_{eq}-\varepsilon_u\right)^2\left(\bar{\varepsilon}_{eq}\varepsilon_u+\bar{\varepsilon}_{eq}\varepsilon_t-2\varepsilon_t^2\right). \tag{24}$$

where $\bar{\varepsilon}_{eq}$ is the nonlocal strain measure evaluated on the basis of formula (21).

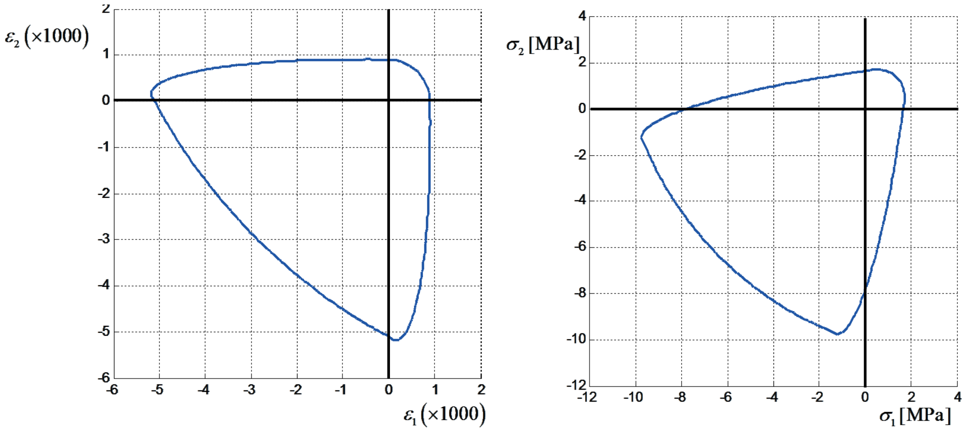

(a) (b)

Fig. 3 - Damage limit function F in the principal strain plane $\varepsilon_1 - \varepsilon_2$ (a) and stress plane $\sigma_1 - \sigma_2$ (b) under the assumption of plane stress state.

In formula (24), the quantity ε_u is the ultimate value of the equivalent strain corresponding to the full damage, i.e. $D^b = 1$, as reported in Fig. **2**. The parameter β governs the softening branch of the stress-strain relationship, which is assumed to be related to the value of the first strain invariant I_1 as:

$$\beta = \beta_t + \frac{1}{1+\exp\left(\alpha\left(I_1 - I_{1m}\right)\right)}\left(\beta_c - \beta_t\right), \tag{25}$$

with β_c and β_t denoting the values of β for a mostly contracted or elongated strain state, respectively. The parameter α governs the rate of the variation of β from β_c to β_t and vice-versa, while I_{1m} is the value of the strain first invariant, corresponding to $\beta = \left(\beta_c + \beta_t\right)/2$. Thanks to the choice of the damage law governed by Equations (23)-(25), a failure mechanism more brittle in tension than in compression is considered.

The value of β_t is determined enforcing that the damage energy is equal to G_t. Concerning the compressive response, once the value of ε_t is fixed, the compressive elastic stress σ_c, represented in Fig. **2**, is also given;

moreover, the value of β_c is determined as function of the compressive damage energy G_c. Finally, the parameter α rules the rate of the variation of β from β_t to β_c and vice-versa and has to be numerically determined by means of biaxial tests.

4 Numerical procedure

The time integration of the nonlinear constitutive relationships for the mortar and brick materials is performed in the framework of a quasi-static incremental/iterative solution procedure, adopting a backward-Euler implicit algorithm.

A step-by-step solution technique is used and the evolution problem is solved in a typical step $[\theta_n, \theta_{n+1}]$, being $\theta_{n+1} > \theta_n$. To ease notation, the subscript n denotes the quantities evaluated at the time θ_n, while subscript is omitted for all quantities evaluated at the time θ_{n+1}.

The time-discrete constitutive equations of the mortar and brick are solved at the Gauss quadrature points of the FE discretization, adopting a predictor-corrector algorithm and a strain-driven formulation. To simplify the model, the damage is evaluated in the mid-plane of the wall and it is assumed constant in the thickness direction.

Concerning the evolution of the mortar inelastic mechanisms, once the strain field is determined, the nonlocal equivalent strain measures $\bar{Y}_N$ and $\bar{Y}_{NT}$ are evaluated at the typical point $\mathbf{x} = \{x_1, x_2, 0\}$ of the mid-plane, by using the classical Gauss quadrature formula, as:

$$\bar{Y}_{N/NT}(\mathbf{x}) = \frac{1}{\Psi^m} \sum_q \psi^m(\mathbf{x} - \mathbf{y}_q) w_q Y_{N/NT}(\mathbf{y}_q), \tag{26}$$

where Ψ^m is the integral over the mortar domain of the function ψ^m, $\mathbf{y}_q$ is a Gauss integration point located on the wall mid-plane and w_q is the Gauss weight at the point $\mathbf{y}_q$. Note that the sum in Equation (26) is extended to the whole mortar domain. Then, applying formulas (13)-(18), the quantity $\tilde{D}^m$

is determined at $\mathbf{x}$. The damage is computed by Equation (18), which assumes the specific form:

$$D^m = \max_{history}\left\{D_n^m, \min_{history}\left\{\tilde{D}^m, 1\right\}\right\}. \tag{27}$$

If D^m is greater than zero at the typical point of the mortar joint, the contact and friction effects have to be evaluated. To this end, the normal strain ε_N is computed and the value of the Heaviside function $h(\varepsilon_N)$ is determined, so that the vector $\mathbf{c}$ can be evaluated by the first of the expressions (7).

Note that, because of the first of (7) and expression (3), the components of the unilateral contact vector $\mathbf{c}$ are expressed as polynomial functions of the x_3 coordinate, when $\varepsilon_N < 0$. In this case, the mortar joint is compressed in the normal direction and its components are equal to the components of the strain vector $\boldsymbol{\varepsilon}$, except for c_{NT}, which is always equal to zero. This implies that the unilateral strain vector $\mathbf{c}$ can be written as:

$$\mathbf{c}(\mathbf{x}) = \mathbf{c}_0(x_1, x_2) + x_3\mathbf{c}_1(x_1, x_2) + x_3^2\mathbf{c}_2(x_1, x_2) + x_3^3\mathbf{c}_3(x_1, x_2). \tag{28}$$

To evaluate the shear sliding strain γ_{NT}^p contained in the vector $\mathbf{p}$ given by the second of Equations (7), a plasticity problem is solved. This inelastic strain is computed in the wall mid-plane and, for the sake of simplicity, it is assumed constant along the x_3 coordinate.

Initially, the value of the trial solution is introduced setting $\mathbf{p} = \mathbf{p}_n$ and $\zeta = \zeta_n$. The trial stress $\boldsymbol{\sigma}_{el}^d$ is determined as:

$$\boldsymbol{\sigma}_{el}^d = \mathbf{C}^m\left[\boldsymbol{\varepsilon} - (\mathbf{c} + \mathbf{p}_n)\right], \tag{29}$$

and the value of the Coulomb limit function $\varphi\left(\boldsymbol{\sigma}_{el}^d, \zeta_n\right)$ is computed using formula (8). If $\varphi < 0$, then $\mathbf{p} = \mathbf{p}_n$, $\zeta = \zeta_n$ and $\boldsymbol{\sigma}^d = \boldsymbol{\sigma}_{el}^d$; otherwise, the inelastic strain $\mathbf{p}$ and, as a consequence, the total plastic slip strain ζ have to be updated, computing a new value for γ_{NT}^p. This is evaluated by solving the time-discretized expressions of Equations (8), (9) and (10), written in the following residual form:

$$R_{\varphi} = \left[\left(\mu_f - \mu_i\right)\left(1 - e^{-\omega(\zeta_n + \Delta\lambda)}\right) + \mu_i\right]\sigma_{N\,el}^{d} + \left|\tau_{NT\,el}^{d}\right| - \Delta\lambda C_{44}^{b} = 0. \tag{30}$$

The value of $\Delta\lambda$ is determined by solving Equation (30), by means of a Newton-Raphson algorithm. Then, the updated value of the sliding strain γ_{NT}^{p} is computed from Equation (11) as:

$$\gamma_{NT}^{p} = \gamma_{NT\,n}^{p} + \Delta\lambda \frac{\tau_{NT\,el}^{d}}{\left|\tau_{NT\,el}^{d}\right|}. \tag{31}$$

Finally, the strain vector $\boldsymbol{\pi} = D^{m}\left(\mathbf{c} + \mathbf{p}\right)$ is determined, assuming the following representation form in the finite element formulation:

$$\boldsymbol{\pi}\left(\mathbf{x}\right) = \boldsymbol{\pi}_0\left(x_1, x_2\right) + x_3\boldsymbol{\pi}_1\left(x_1, x_2\right) + x_3^2\boldsymbol{\pi}_2\left(x_1, x_2\right) + x_3^3\boldsymbol{\pi}_3\left(x_1, x_2\right), \tag{32}$$

with $\boldsymbol{\pi}_0 = D^{m}\left(\mathbf{c}_0 + \mathbf{p}\right), \boldsymbol{\pi}_1 = D^{m}\mathbf{c}_1, \boldsymbol{\pi}_2 = D^{m}\mathbf{c}_2, \boldsymbol{\pi}_3 = D^{m}\mathbf{c}_3$.

The damage is also determined in the wall mid-plane for the brick and it is assumed constant in the thickness direction. The nonlocal equivalent strain $\bar{\varepsilon}_{eq}$ is computed at the point $\mathbf{x} = \{x_1\ x_2; 0\}$, as:

$$\bar{\varepsilon}_{eq}\left(\mathbf{x}\right) = \frac{1}{\Psi^{b}}\sum_{q}\psi^{b}\left(\mathbf{x} - \mathbf{y}_q\right)w_q\,\varepsilon_{eq}\left(\mathbf{y}_q\right), \tag{33}$$

where Ψ^{b} is the integral over the brick domain of the function ψ^{b}.

Applying formulas (23) and (24), the brick damage D^{b} is determined at the point $\mathbf{x}$. As a consequence, by the constitutive equations (6) and (19) the stress vectors in the mortar and the brick are evaluated. In both cases, the stress vector admits the following polynomial representation:

$$\boldsymbol{\sigma}\left(\mathbf{x}\right) = \boldsymbol{\sigma}_0\left(x_1, x_2\right) + x_3\boldsymbol{\sigma}_1\left(x_1, x_2\right) + x_3^2\boldsymbol{\sigma}_2\left(x_1, x_2\right) + x_3^3\boldsymbol{\sigma}_3\left(x_1, x_2\right). \tag{34}$$

Taking into account the variational equilibrium equation (4) with the definitions (5), the element equilibrium equation in residual form becomes:

$$
\begin{aligned}
\mathbf{R}^e = \int_{S_e} \Bigg[\bigg[& \left(t\mathbf{B}_0 + \frac{t^3}{12}\mathbf{B}_2 \right)^T \boldsymbol{\sigma}_0 + \left(\frac{t^3}{12}\mathbf{B}_1 + \frac{t^5}{80}\mathbf{B}_3 \right)^T \boldsymbol{\sigma}_1 \\
& + \left(\frac{t^3}{12}\mathbf{B}_0 + \frac{t^5}{80}\mathbf{B}_2 \right)^T \boldsymbol{\sigma}_2 + \left(\frac{t^5}{80}\mathbf{B}_1 + \frac{t^7}{448}\mathbf{B}_3 \right)^T \boldsymbol{\sigma}_3 \bigg] dx_1 dx_2 \\
& - \int_{S_e} \mathbf{B}_0{}^T \mathbf{b}\, dx_1 dx_2 - \int_{\partial S_e} \mathbf{B}_0{}^T \mathbf{p}\, ds \Bigg]
\end{aligned}
\tag{35}
$$

The presented FE formulation has been implemented in the FE program FEAP (Taylor, 2011).

5 Numerical applications

Aiming at validating the proposed EKQFE, two numerical applications are performed, concerning:

1. the diagonal compression test of a masonry panel;
2. the overall response of a unit cell of a periodic masonry wall.

The diagonal compression test is widely used to evaluate the shear strength of masonry panels (Gabor *et al.*, 2006; Calderini *et al.*, 2010). Herein, the square panel in Fig. **4**, experimentally analyzed in (Kalali and Kabir, 2010), is studied. This is made up of 14 courses of bricks and mortar, arranged in Flemish bond. The side of the panel is 560 mm and its thickness is 105 mm. The size of the bricks, specially produced for the experimental test to be one-half scale of the original ones, is $105\times50\times28\ \text{mm}^3$ and the thickness of the mortar is approximately 10 mm for the bed joints and 6 mm for the head joints. In the experimental setup two loading shoes were located to the upper and lower corners to apply the hydraulic jack load on a corner, performing a displacement-controlled procedure and to restraint the other corner. The applied load and the compressive strain of the diagonal were measured.

The load was monotonically increased until the specimen collapse. A mesh made of 1935 FEs is used for the computations, adopting for the materials the mechanical parameters contained in Table 2 for the bricks and in Table **3** for the mortar, as reported in (Kalali and Kabir, 2010 and 2012). The brick tensile and compressive strengths are equal to 1.6 MPa and 11.6 MPa, respectively.

The nonlocal radius is set equal to $\rho_b = 20\text{ mm}$ for the bricks and $\rho_m = 15\text{ mm}$ for the mortar.

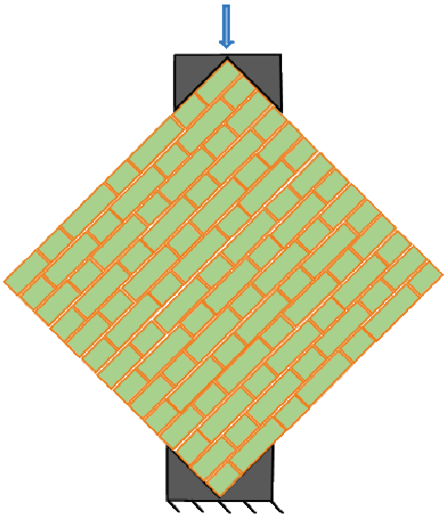

Fig. 4 - Diagonal compression test: schematic of masonry panel.

Table 2 - Diagonal compression test: material parameters adopted for bricks.

$E^b = 2000\text{ MPa}$	$\nu^b = 0.15$	$\varepsilon_t = 8.0\times10^{-4}$
$\varepsilon_u = 8.0\times10^{-3}$	$\kappa = 0.03$	$\varepsilon_o = 1.0\times10^{-5}$
$\beta_t = 7000$	$\beta_c = 200$	$\alpha = 8000$

In Fig. **5** the global response curves are shown, depicting the applied load versus the deformation along the compressed diagonal. The solid lines refer to the experimental outcomes, obtained by the analysis of two specimens.

The diamond symbols indicate the numerical results derived by the FE analysis.

Table 3 - Diagonal compression test: material parameters adopted for mortar.

$E^m = 700\ \text{MPa}$	$\nu^m = 0.2$	$\varepsilon_{N,0} = 5.0\times10^{-4}$
$\gamma_{NT,0} = 1.9\times10^{-3}$	$G_{cI} = 4.37\times10^{-4}\ \text{MPa}$	$G_{cII} = 2.63\times10^{-3}\ \text{MPa}$
$\mu_i = 0.58$	$\mu_f = 0.58$	$\omega = 3.0$

The results in Fig. **5** show that the EKQFE model is able to satisfactorily reproduce the experimental response of the panel. It can be remarked that, for this kind of application, failure is mainly due to shear collapse of the mortar, while no compressive collapse occurs in the brick. The proposed damage-friction constitutive model is able to reproduce the occurring failure mechanism. On the other hand, as the compressive failure mechanism is not activated, unless in limited zones around the boundary constraints, the out-of-plane effect is not significantly involved in the collapse of the masonry wall. The proposed EKQFE finite element is also adopted to derive the overall response of the masonry material, performing a micromechanical and homogenization analysis. In particular, a running bond regular masonry texture is considered for the unit cell (UC), as illustrated in Fig. **6**.

The UC is firstly subjected to a vertical macroscopic strain $E_{22} = c$, then to a macroscopic shear strain Γ_{12} cyclic history, as reported in

Table 4. To study the effect of the vertical compression load on the UC shear response, three different values are selected for the parameter $c = 0, -2.0\times10^{-4}, -4.0\times10^{-4}$.

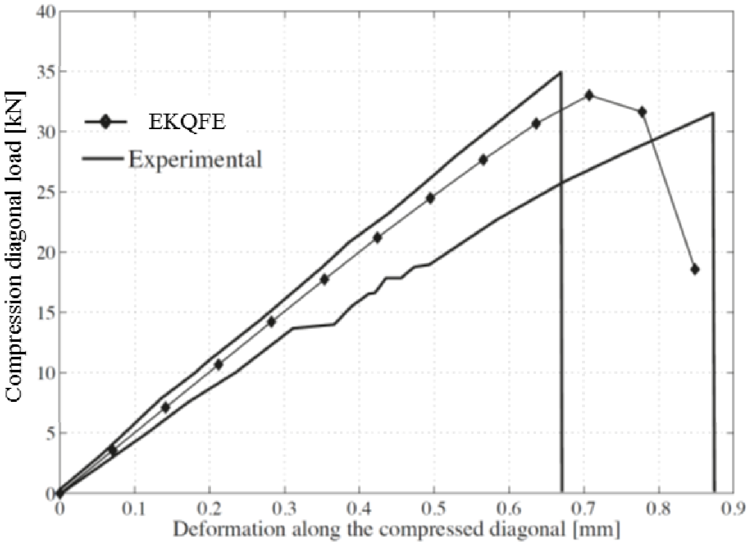

Fig. 5 - Diagonal compression test: global response curves.

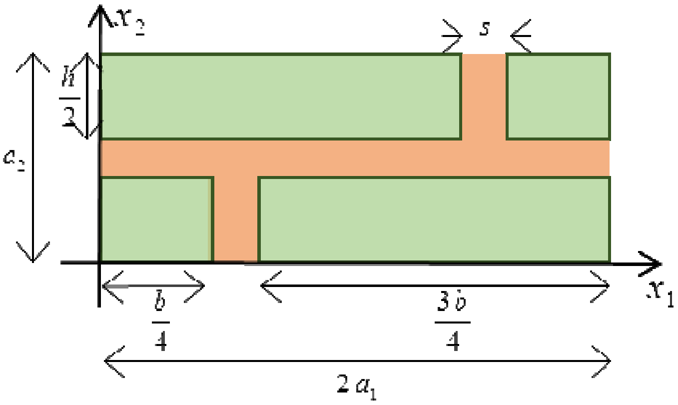

Fig. 6 - Unit cell for the running bond regular masonry texture.

Table 4 - Loading history for the UC.

time	0	1	2	3	4
E_{22}	0	c	c	c	c
Γ_{12}	0	0	1.5×10^{-3}	-1.0×10^{-3}	0

In Fig. **7** the homogenized macroscopic shear stress Σ_{12} versus the applied macroscopic shear strain Γ_{12} is plotted, for the three different values of the vertical macroscopic strain E_{22}.

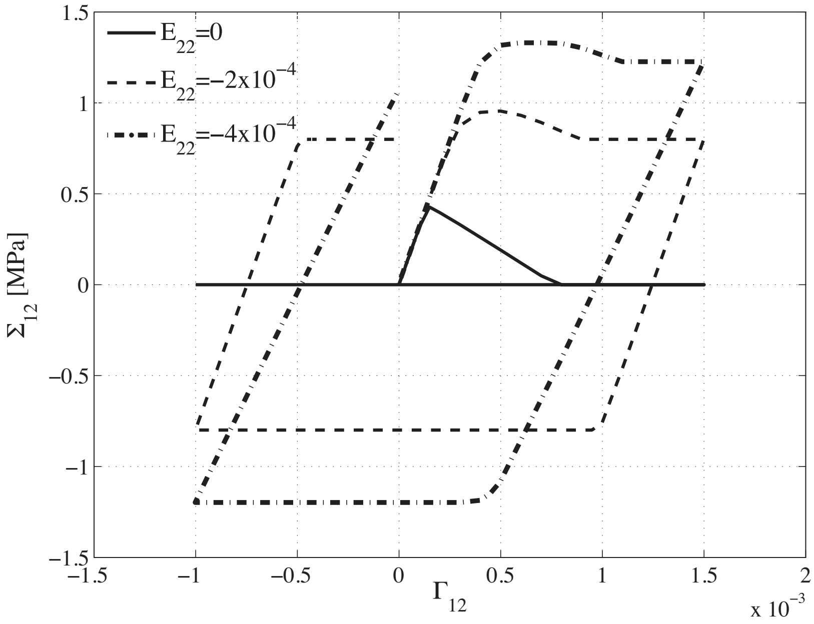

Fig. 7 - Shear response of the pre-stressed UC for $E_{22} = 0$ (solid line), $E_{22} = -2.0\times10^{-4}$ (dashed line), $E_{22} = -4.0\times10^{-4}$ (dashed-dot line).

Higher values of the limit shear strength are obtained in presence of the vertical pre-stress. Also, the post-peak behavior is modified, as the damaging mechanisms exhibited by bricks and mortar change with the value of the pre-stress. The solid line in Fig. **7** shows the pure shear response of the UC, characterized by the onset and evolution of damage only in the bed joint. When this is completely damaged, the shear strength vanishes. The dashed line, corresponding to the lowest value of $c = -2.0 \times 10^{-4}$, is also characterized by damage mainly in the bed mortar joints. In this case, the presence of the vertical stress causes the activation of the friction-plastic flow, too. Indeed, when the bed joints reach the maximum value of the damage, differently from the previous case, a residual shear strength remains. As the value of E_{22} grows (dashed-dot line), the damage also starts and evolves in the bricks, since the higher compression state induces tensile strains in the thickness direction, causing a degrading post-peak behavior until the residual strength is reached.

6 Conclusions

A new finite element EKQFE, characterized by an enriched kinematics, for the nonlinear analysis of masonry walls subjected to in-plane loading conditions has been developed. A damage-friction failure criterion has been adopted for the mortar joints, which can be regarded as an extension of the damaging Mohr-Coulomb law. As for the bricks, an isotropic damage model has been introduced, assuming that the degrading process of the material is governed only by the tensile strains. The developed FE has been implemented in the FEAP code and a numerical procedure has been developed.

The proposed model allows to correctly account for the mortar-brick interaction. Indeed, adopting the proposed formulation it is possible to describe the classical failure modes of the masonry composite material, as the sliding of the mortar joints and the tensile failure of the brick, when masonry experiences a compressive stress state.

A masonry panel, experimentally analyzed, has been studied to validate the proposed numerical procedure, obtaining a very good agreement with the experimental results in terms of global response curves. Moreover, the overall response of a UC subjected to prescribed 2D macro-strain histories, shows the effectiveness of the proposed approach.

References

1. Addessi, D., Marfia, S., Sacco, E., Toti, J. (2015). Modeling approaches for masonry structures. *The Open Civil Engineering Journal*, vol. 8 (*1*), pp. 288-300.
2. Addessi, D., Sacco, E. (2014). A kinematic enriched plane state formulation for the analysis of masonry panels. *European Journal of Mechanics - A/Solids*, vol. 44, pp. 188-200.
3. Addessi, D., Sacco, E. (2016a). Nonlinear analysis of masonry panels using a kinematic enriched plane state formulation. *International Journal of Solids and Structures*, vol. 90, 194–214.
4. Addessi, D., Sacco, E. (2016b). Enriched plane state formulation for nonlinear homogenization of in-plane masonry wall. *Meccanica*, vol. 51 (*11*), pp. 2891-2907.
5. Addessi, D., Sacco, E., Paolone, A. (2010). Cosserat model for periodic masonry deduced by nonlinear homogenization. *European Journal of Mechanics - A/Solids*, vol. 29, pp. 724-737.
6. Anthoine, A. (1997). Homogenization of periodic masonry: plane stress, generalized plane strain or 3d modelling? *Communications in Numerical Methods in Engineering*, vol. 13 (*5*), pp. 319-326.
7. Aref, A.J., Dolatshahi, K.M. (2013). A three-dimensional cyclic meso-scale numerical procedure for simulation of unreinforced masonry structures. *Computers & Structures*, vol. 120, pp. 9-23.
8. Auciello, N.M., Ercolano, A. (1997). Numerical simulation of masonry panels. *Engineering Transactions,* vol. 45(*3-4*), pp. 375-394.
9. Calderini, C., Cattari, S., Lagomarsino, S. (2010). The use of the diagonal compression test to identify the shear mechanical parameters of masonry. *Construction and Building Materials*, vol. 24 (*5*), pp. 677-685.
10. Ercolano, A. (1994). On a rigid-elastic model for monumental block structures, *Proc. XI Congreso Nacional De Ingenieria De Mecanica*, November 1994, Valencia, Espana.
11. Ercolano, A. (1995). Simulazioni di strutture murarie. *Proceedings of XII Congresso Nazionale dell'Associazione Italiana di Meccanica Teorica ed Applicata*, (AIMETA), vol. 1, pp. 377-382, Naples, October 3-5, 1995.
12. Gabor, A., Bennani, A., Jacquelin, E., Lebon, F. (2006). Modelling approaches of the in-plane shear behaviour of unreinforced and FRP strengthened masonry panels. *Composite Structures*, vol. 74 (*3*), pp. 277-288.
13. Guinea, G.V., Hussein, G. Elices, M. Planas, J. (2000). Micromechanical modeling of brick-masonry fracture. *Cement and Concrete Research*, vol. 30 (*5*), pp. 731-737.
14. Hilsdorf, H.K. (1969). *Investigation into the failure of brick masonry loaded in axial compression*. Houston, Texas: F.B. Johnson ed., Gulf Publishing, pp. 34-41.
15. Kalali, A., Kabir, M.Z. (2010). Modeling of unreinforced brick walls under in-plane shear and compression loading. *Structural Engineering and Mechanics*, vol. 36 (*3*), pp. 247-278.

16. Kalali, A., Kabir, M.Z. (2012). Experimental response of double-wythe masonry panels strengthened with glass fiber reinforced polymers subjected to diagonal compression tests. *Engineering Structures*, vol. 39, pp. 24-37.
17. Massart, T.J., Peerlings, R.H.J., Geers, M.G.D., Gottcheiner ,S. (2005). Mesoscopic modeling of failure in brick masonry accounting for three-dimensional effects. *Engineering Fracture Mechanics*, vol. 72 (*8*), pp.1238-1253.
18. Sacco, E. (2009). A nonlinear homogenization procedure for periodic masonry. *European Journal of Mechanics - A/Solids*, vol. 28, pp. 209-222.
19. Taylor, R.L. (2011). *FEAP-A finite element analysis program, Version 8.3*. Department of Civil and Environmental Engineering, University of California at Berkeley, California.
20. Zucchini, A., Lourenço P.B. (2009). A micro-mechanical homogenisation model for masonry: Application to shear walls. *International Journal of Solids and Structures*, vol. 46 (*3-4*), pp. 871-886.

Some laser-scanner applications in structural analysis

Claudio Alessandri[1], Vincenzo Mallardo[2]

[1] Department of Engineering, University of Ferrara, via Saragat 1, 44121 Ferrara, Italy
[2] Department of Architecture, University of Ferrara, via Quartieri 8, 44121 Ferrara, Italy
{ale, mlv}@unife.it

Summary. In the present work the authors intend to describe some recent experiences in the application of the laser scanner technique to the structural analysis. Three main examples are provided, the former involves a typical Renaissance Palace in Ferrara, the second one is developed in the framework of the damage analysis carried out for the Nativity Church in Bethlehem, and the latter deals with the nondestructive testing of a common historical masonry building in Ferrara. In such examples the laser scanner data acquisition is mainly aimed at investigating the structural behavior and not at the geometrical representation. The contribution ends with some comments on the current open issues.

Keywords: Laser scanner, data acquisition, structural analysis, structural monitoring.

1 Introduction

Most of the applications of the laser scanner technique to the civil engineering field is mainly focused on the acquisition of the geometry of the structure. Such an acquisition requires plenty of post-processing “extra” work before being suitably adopted in a readable format. Surface reconstruction, three-dimensional modelling, horizontal and vertical sections plotting are some of the steps that are to be carried out in order to provide clear drawings. Even more difficult, currently very hard, is the extra work that is necessary to import the data into any structural analysis software or simulation (Auciello and Ercolano, 1997). The issue is complicated by the assumption that, at present, the laser scanner allows the acquisition of the external skin of the structure, and, thus, the cloud of points is spoiled by non-structural elements (such as walls in reinforced concrete buildings, plaster, cornices, tiles, etc.). This is the reason why most of the applications in the literature refers to masonry structures, where at least the vertical bearing elements may be given by visible masonry walls, the horizontal slabs are, often, supported by visible wood beams and the vaults may be free of lining and characterized by complex curvatures.

In (Lubowiecka *et al.*, 2009) the terrestrial laser scanner was used to document and analyse some historical masonry bridges in Galicia, a region in Northwest Spain. One bridge was analysed in the paper. It has five pointed arches with the longest span of 11.5 m and the laser scanning was first set to 2 cm of resolution in order to provide its complex geometry. In (Wittich *et al.*, 2015) a broad field survey of 24 human-form statues was carried out. Geometric data was acquired with image-based processes and laser-scanning processes and the 3D digital reconstructions compared; a resolution of around 6mm was set and six-seven scans per statue were performed. In (Manfredi *et al.*, 2013) the geometric survey of a vaulted structures was carried out using a help-assisted total station with cylindrical targets. The data was referred to a highly damaged XVIII century building complex in the city of Nola (near Naples) in the South of Italy. The cloud of points was deeply post-processed in order to extract horizontal and vertical sections from which a 3D structural model might be built independently. In (Barbieri *et al.*, 2013) the exact geometry of a historic masonry building in Mantua (Italy) was detected by some laser scanner measurement campaigns carried out in two years with a high resolution ranging between 2.0 and 4.0 millimeters. The scanning was mostly concentrated to the main façades of the building. In (Bednarz *et al.*, 2014) the whole interior of an historical presbytery church in Poland was detected by a High-Definition Surveying 3D laser scan. In (Chellini *et al.*, 2014) a 3D outer and inner model of a Church in Barcelona (Spain) was obtained by performing a 4-mm accuracy laser scanning.

All the above contributions use the geometrical survey obtained by laser scanner to perform some structural numerical analyses, and all the authors underline the difficulties to carry out such a task. Alignment, cleaning and segmentation, triangulation and so on, are first performed to obtain clear drawings, usually in CAD format. The construction of the 2D or 3D structural (FEM) model is usually carried out manually. Even if recent developments allow the automatic conversion of the cloud-of-point model into a NURBS-based structural mesh model (see Beer, 2015 for instance) both in FEM (see Cotrell *et al.*, 2009) and in BEM (see Beer *et al.*, 2017), the issue has not been automatised so far and it is still open.

Last but not least, the work by Gordon and Derek (2007) is worthy of being mentioned as the laser scanner was involved to measure the vertical displacement of beams undergoing controlled loading. Therefore, this work can be considered an application aimed at non-destructive structural monitoring and not at geometry acquisition. A similar goal was pursued in (Barbieri *et al.*, 2013) where the laser scanner data was used to monitor the magnitude of the inclination of the longitudinal walls.

On the basis of some recent experiences carried out by the authors (see Mallardo *et al.*, 2008, Alessandri and Mallardo, 2012, Alessandri *et al.*, 2012, 2015), the present work intends to present some applications of the laser scanner technique both to the structural analysis and to the non-destructive structural monitoring.

2 Laser scanner as first step of structural analysis

A 3D laser scanner survey was carried out by the authors on a typical Renaissance historical Palace in Ferrara (see Mallardo *et al.*, 2008). A digital survey was carried out by using a 3D laser scanner equipment, that is Leica HDS Cyrax 3000, based on a time-of-flight technology supplying 1000-1800 points per second with the precision of 5-6 millimeters and viewing ranges of up to 360°x270°.

The data acquisition was mainly focused on the main façade of the Palace in order to obtain the geometry representation as well as any important structural information (lack of verticality, presence of holes, etc.). Some of the results from the 3D survey campaign are shown in Figure 1. The scan of the façade was carried out by means of three stations (located at the centers of each third of the façade length) and with a two-fold accuracy (5 x5 cm and 2.5 x 2.5 cm grids). The façade is 70 m long and 12 m high.

Fig. 1 – Dot clusters of the courtyard (right) and of the main façade (left)

The 3D-laser-scanner output needed to be processed iteratively in order to provide a 3D CAD geometrical model to be used in the F.E. context. The issue was more simple when the main façade was investigated. In fact, it was easier to build a plane model from the laser scanner output.

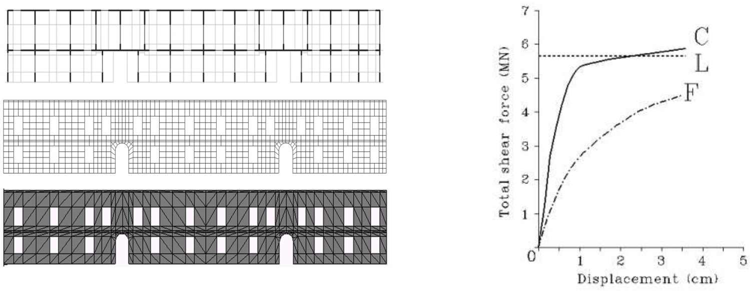

Fig. 2 – (Left from the top): Equivalent frame model (F), Adina 2D mesh (C), Homogenized limit analysis discretization (L). (Right): Global structural response.

A seismic analysis was then carried out on the wall to measure its vulnerability. Three approaches were used: equivalent frame model (F), inelastic plane stress model (C) and a homogenized limit analysis (L). Mesh adopted and global numerical results are depicted in Figure 2.

It must be pointed out that both steps, from laser scanner data to CAD format and from CAD format to the structural analysis, required many men-hours to be carried out as classical discretisation strategies were adopted.

A similar approach was carried out in the analysis of the Nativity Church in Bethlehem in the years 2009-2012 (see Alessandri and Mallardo, 2012 and Alessandri *et al.*, 2012). Such a study was mainly aimed at investigating the structural safety level of the Church with special attention to its seismic vulnerability and to the roof wooden trusses, the latter deeply damaged by copious rainwater infiltrations.

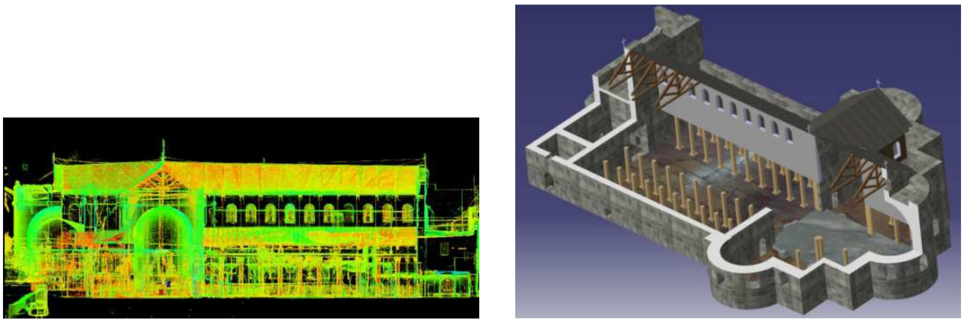

Fig. 3 – (Left): Snapshot of the laser scanner survey. (Right): Three-dimensional view of the Church obtained by the laser scanner survey.

The laser scanning survey (see Figure 3) was useful to obtain a detailed measurement of the geometry of the main wall, that is the wall bearing the roof and transferring its weight to the columns below, the precise acquisition of the dimensions of the roof wooden elements (see Figure 4-left), and the accurate survey of the complex system of underground grottoes. The whole data were obtained by selecting 110 different scanner positions and by using a 3D High Definition Laser Scanner Leica, model HDS3000 (grid varying from 5x5 to 10x10 cm, with some focus of 2.5x2.5 on special areas).

The above data allowed to get the correct value of the structural safety level of the wooden beams as it was enriched by any area variation along the main axis and by the presence of defects and knots. Such an analysis allowed to design a less invasive intervention solution as the geometry definition had no uncertainties, thus minimising the wood parts to be replaced.

The laser scanner data acquired from the main wall (with a grid of 2.5 x 2.5 cm and two different stations on each side of the wall) produced the description of the out-of-plane effects on the internal surfaces depicted in Figure 4-right. It was thus possible to measure the amplitude of the out-of-plane difference between the top and the bottom, that is 26 cm, and to keep such a difference into account in the structural safety analysis of the seismic out-of-plane mechanisms. The out-of-plane leaning was around 3.3% of the height of the wall (8 m), but more than a half was concentrated in the first top 4 meters thus providing a slope of around 5%. It is worthy to observe that a similar approach was carried out in Barbieri *et al.*, 2013 to investigate the magnitude of the inclination of the longitudinal walls of a historic masonry building in Italy.

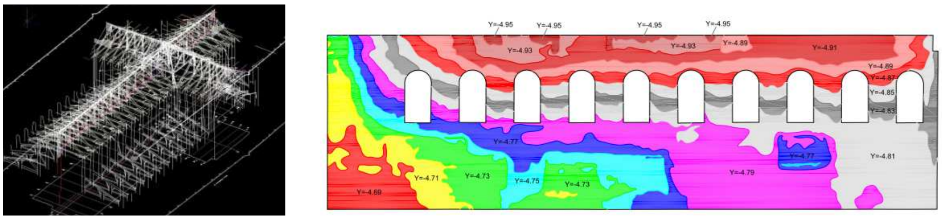

Fig. 4 – (Left): Snapshot of the laser scanner survey of the roof beams. (Right): Contour plot of the y-position. South wall as seen from the nave.

The laser scanning survey found its best application in the survey of the underneath grottoes (see Figure 5). The absence of finings and the well-known high complexity in the alternative manual mapping, make the laser scanning an excellent alternative. The output data were obtained with 25 different stations and a grid of 10x10 cm as the required detail was rather coarse.

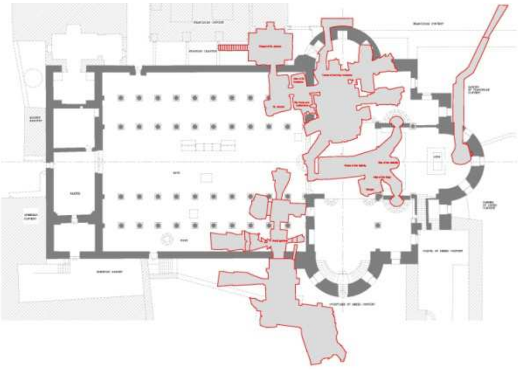

Fig. 5 –Plan of the grottoes under the Church.

The data were useful to perform the structural analysis of some meaningful 2-D sections of the grottoes and to provide a more realistic measure of the safety level in the areas of the Church subjected to the highest crowding of pilgrims.

3 Laser scanner as nondestructive monitoring tool

Most of the work dealing with the intersection between laser scanning and structural analysis is focused on the geometry acquisition and on the procedures to carry out to import the data in any structural software. As a matter of fact, structural monitoring would benefit from a long-term laser scanner acquisition, but the applications of laser scanning to structural monitoring are very few.

In (Bednarz *et al.*, 2014), for instance, three scans of the interior of a presbytery church were generated in three different years (2009, 2011 and 2013) but at the same day and at similar temperature/humidity conditions. The merging of the three scans provided a basis for analysis of the direction of displacement of vault and walls. In (Barbieri *et al.*, 2013) some (laser-scanner) measurement campaigns were carried out between 2005 and 2007 to monitor the inclination of some longitudinal walls.

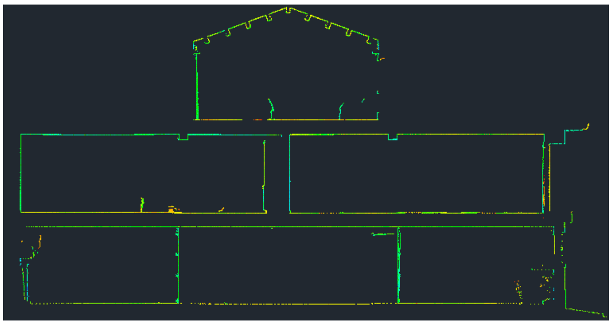

Fig. 6 –A vertical section provided by the laser scanner acquisiton system.

A very recent application of the authors had a similar objective. The issue was to provide shape and amplitude of the vertical displacement of some horizontal plates in a typical two-floor masonry building in Ferrara. These horizontal plates were designed to bear their weight (tiles, mortar, etc.) and the live load. They were formed by a system of one-direction wooden beams (70 cm spacing) supporting a reinforced (6 mm steel net) concrete slab (6 cm thickness) connected to the beams by bolted triangle trusses.

Some visible crack lines had occurred in the tiles of the horizontal slab and the goal of the investigation was to focus on the causes of such cracks, i.e. if related to the structural deflection or to the incorrect laying of tiles and/or underneath substrate.

A laser scanner survey was performed in all the rooms of the building and the acquired data were merged in order to provide meaningful vertical sections (see an example in Figure 6). The cloud of points was first amplified (see Figure 7-top) and then averaged in order to replace them with lines (see Figure 7-bottom). The final drawing represented the actual position of the bottom external surface of the beams bearing the slab. As the wooden beams were supported at their extremes by thick masonry walls (in Figure 7 located at the intersection with the vertical line), such lines provided a visual representation of the typical vertical deflection of simply-supported beams.

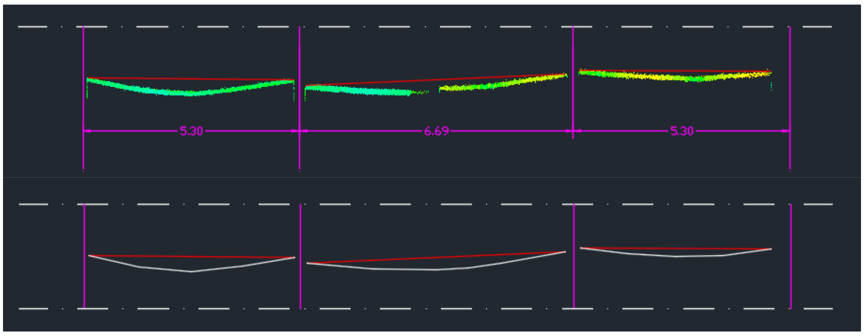

Fig. 7 – Amplification and lining of the vertical section.

The same procedure was also applied to the upper surface of the slabs. The final lines were able to give the exact vertical position of the tiles along more sections and, thus, to provide some suggestions on the influence of the tile laying phase on the crack occurrence.

4 Conclusions

Nowadays the laser scanner is a geometry acquisition tool that has been experienced many times in conjunction with the structural analysis. Some applications of the authors were described and commented. Still much work is necessary to improve the filtering steps between the cloud of points and the final structural model. A recent step forward has been carried out thanks to the isogeometric approach that would optimize the CAD-CAE step, but no recent breakthrough can be recalled to sort the cloud-olf-point-CAD step out. On the contrary, the technique may have interesting developments in structural monitoring and nondestructive testing. Some experiences of the authors in this field were also presented.

References

1. Alessandri, C., Garutti, M., Mallardo, V., Milani, G. (2015). Crack patterns induced by foundation settlements: Integrated analysis on a Renaissance masonry Palace in Italy. *International Journal of Architectural Heritage*, vol. 9 (*2*), pp. 111-129.
2. Alessandri, C., Mallardo, V. (2012). Structural assessments of the Church of the Nativity in Bethlehem. *Journal of Cultural Heritage*, vol. 13 (*4*), pp. e61-e69.
3. Alessandri, C., Mallardo, V., Pizzo, B., Ruocco, E. (2012). The roof of the Church of the Nativity in Bethlehem: Structural problems and intervention techniques. *Journal of Cultural Heritage*, vol. 13 (*4*), pp. e70-e81.
4. Auciello, N.M., Ercolano, A. (1997). Numerical simulation of masonry panels. *Engineering Transactions*, vol. 45 (*3-4*), pp. 375-394.
5. Barbieri, G., Biolzi, L., Bocciarelli, M., Fregonese, L., Frigeri, A. (2013). Assessing the seismic vulnerability of a historical building. *Engineering Structures*, vol. 57, pp. 523-535.
6. Bednarz, L.J., Jasienko, J., Rutkowski, M., Nowak, T.P. (2014). Strengthening and long-term monitoring of the structure of an historical church presbytery. *Engineering Structures*, vol. 81, pp. 62-75.
7. Beer, G. (2015). *Advanced Numerical Simulation Methods. From CAD data directly to simulation results*. London, UK: CRC Press Taylor & Francis Group.
8. Beer, G., Mallardo, V., Ruocco, E., Marussig, B., Zechner, J., Dunser, C., Fries, T.-P. (2017). Isogeometric boundary element analysis with elasto-plastic inclusions. Part 2: 3-D problems. *Computer Methods in Applied Mechanics and Engineering*, vol. 315, pp. 418-433.
9. Chellini, G., Nardini, L., Pucci, B., Salvatore, W., Tognaccini, R. (2014). Evaluation of seismic vulnerability of Santa Maria del Mar in Barcellona by an integrated approach based on terrestrial laser scanner and finite element modeling. *International Journal of Architectural Heritage*, vol. 8 (*6*), pp. 795-819.
10. Cottrell, J.A., Hughes, T.J.R., Bazilevs, Y. (2009). *Isogeometric analysis. Toward integration of CAD and FEA*. Chichester, UK: John Wiley and Sons, Ltd. Publication.
11. Gordon, S.J., Derek, D.D. (2007). Modeling terrestrial laser scanner data for precise structural deformation mesurement. *Journal of Surveying Engineering ASCE*, vol. 133 (*2*), pp. 72-80.
12. Lubowiecka, I., Armesto, J., Arias, P., Lorenzo, H. (2009). Historic bridge modelling using laser scanning, ground penetrating radar and finite element methods in the context of structural dynamics. *Engineering Structures*, vol. 31 (*11*), pp. 2667-2676.
13. Mallardo, V., Malvezzi, R., Milani, E., Milani, G. (2008). Seismic vulnerability of historical masonry buildings: A case study in Ferrara. *Engineering Structures*, vol. 30 (*8*), pp. 2223-2241.

14. Manfredi, G., Lignola, G.P., Voto, S. (2013). Military Quarters in Nola, Italy – Caserma Principe Amedeo: Damage assessment and reconstruction of a partially collapsed XVIII century complex. *International Journal of Architectural Heritage*, vol. 7 (*2*), pp. 225-246.
15. Wittich, C.E., Hutchinson, T.C., Wood, R.L., Seracini, M., Kuester, F. (2015). Characterization of full-scale, human-form, culturally important statues: Case study. *Journal of Computing in Civil Engineering*, vol. 30 (*3*), 05015001.

The model of Heyman and the statical and kinematical problems for masonry structures

Maurizio Angelillo[1]

[1] Università degli Studi di Salerno,
Fisciano (SA) Italy
mangelillo@unisa.it

Abstract. The study of masonry mechanics and the modelling of masonry structures requires a methodological approach radically different from the ones used for metallic and concrete structures. The main criteria adopted for the design of the latter, such as strength, stiffness and elastic stability, have a minor role when dealing with masonry structures. Even if this peculiar behaviour, confirmed though a careful historical critique by several authors, such as Heyman with his seminal work of 1966, followed in the 80's and 90' by Di Pasquale, Como, Benvenuto, Huerta, is rather evident, this point of view is far from manifesting itself among structural architects and engineers. Indeed the theory of Heyman, giving a modern turn to the old approach to masonry design by means of clear cut simplifications, is in sharp contrast with the sophisticated constitutive theories made possible by Finite Element methods and the use of super-computers. In these notes, the basic ingredients of a new method based on unilateral equilibrium and rigid block kinematics, which may allow the implementation of Heyman's model for masonry on a computer, is introduced. In particular we describe a simple method based on energy minimization allowing the evaluation of the combined effect of loads and settlements on real masonry structures.

Key words: masonry structures, unilateral constraints, unilateral materials, multi-body structures, contact and friction.

1 Introduction

The work of Antonio Ercolano. The scientific work of Antonio Ercolano, dedicated mainly to structures subjected to unilateral constraints

[1], or composed of unilateral materials [2], structures composed of rigid blocks in mutual unilateral contact among each other, in static conditions [3], and to the modelling of unilateral block dynamics [4], belongs to the research branch on masonry structures put forward, in the 80’ and 90’ by a group of researchers of the Neapolitan school of structural mechanics, among which it had a stimulating and inspiring role. The present work, in which a simple energy approach to the study of the statical and kinematical problem for masonry structures is introduced, touches three out of the four above mentioned topics, namely: unilateral constraints and structures, unilateral materials, rigid blocks in mutual unilateral contact.

Peculiarities of masonry behaviour. In the last decades, the study of the old technical literature and an attentive reconsideration of the old construction techniques and design rules, allowed to rediscover an almost lost code of conduct for masonry constructions. In this respect, the individuals which gave the more important contribution to this rediscovering were Jaques Heyman, with a series of works originating from the seminal paper [5] of 1966, whose title is “The stone skeleton” (and later, with the monography [6] by the same title), and Santiago Huerta, with a number of works originating from his doctoral thesis of 1992, and among which the cutting paper [7] by the provoking title “Galileo was wrong”, stands out. The main message of Heyman’s theory is that masonry structures are essentially unilateral and that the theorems of limit analysis can be used to assess their stability.

Although in the more historical and theoretical restoration literature a constant growth of sensibility toward less invasive and more attentive technics and procedures for masonry retrofitting can be acknowledged, in most of practical applications, still an inertia in recognizing and accepting the diversity of masonry behaviour still persists. Also building codes (such as the Eurocodes) often appear imprisoned by the schematism of the elastic approach, proposing models which appear as simply translated from framed structures of concrete and steel to masonry.

The original structural approach here proposed, following in the steps of Heyman and Huerta, has been the object of study of a group of researchers of the University of Salerno and Napoli, among which I played a leading part (see for example [8], [9], [10] and the references therein). The main object of the research of this group is the implementation of numerical methods based on the unilateral model for masonry, through computer codes allowing to predict the effect of forces and settlements, and assess the safety of real structures.

Quality of masonry. It is worth pointing out that Heyman's model applies to structures composed of masonry elements having the *quality* of masonry, that is built with the rules of art and whose building blocks have a sufficient integrity. Indeed masonry is not a bunch of blocks arranged randomly, but rather a collection of well-organized elements (bricks, stones, voussoirs) disposed in such a way to avoid sliding. There are essentially two tricks to obtain this goal: **friction** and **interlocking**.

Friction precludes sliding on planar joints where large compressive forces are present (horizontal planes in solid walls).

Interlocking prevents sliding on interfaces where there are feeble or no compressive forces (vertical planes in solid walls).

Such tricks are those allowing for the construction of vertical walls and pillars and guarantee the applicability of the theorems of limit analysis.

If we make stupid masonry structures (say a wall with vertical joints or with scarce interlocking) they may collapse even if a compressive equilibrium state exists, that is, for them, the theorems of limit analysis do not apply.

Heyman's model. Once the quality of the structure, namely the correct execution of the masonry apparatus, is granted, it is possible to proceed to the analysis of such masonry structure as composed of macro-elements, on adopting a simplified model based on Heyman's assumptions: masonry has no tensile strength, it is infinitely resistant in compression and does not slide along fracture lines. This model can catch the essential aspects of masonry behaviour and, overcoming the difficulties connected with the mechanical description of brittleness and friction (on introducing the no-tension/no-sliding assumptions), allows for the application of the theorems of limit analysis, bringing back the study of masonry structures within a consolidated framework.

2 Statics of rigid No-Tension bodies

2.1 Constitutive restrictions

The model of Heyman can be generalized to 2d continua, on introducing unilateral material restrictions on the stress and convenient assumptions on the latent strain, that is on the anelastic deformation necessary to sustain the unilateral constraint on stress.

A 2d masonry structure S, is modelled as a continuum occupying the region Ω of the Euclidean space $\mathcal{E}^2$. The stress inside Ω is denoted $\boldsymbol{T}$ and the displacements of material points $\boldsymbol{x}$ belonging to Ω is denoted $\boldsymbol{u}$. Restricting to the case of small displacements and strains, the infinitesimal strain $\boldsymbol{E}$ is adopted as the strain measure.

The so-called Normal Rigid No-Tension (NRNT) material is defined by the following restrictions:

$$\boldsymbol{T} \in Sym^{-} \ , \ \boldsymbol{E} \in Sym^{+} \ , \ \boldsymbol{T} \cdot \boldsymbol{E} = 0 \ , \tag{1}$$

Sym^{-} ,Sym^{+} being the mutually polar cones of negative semidefinite and positive semidefinite symmetric tensors.

Restrictions (1) are equivalent to the following conditions (called normality conditions):

$$\boldsymbol{T} \in Sym^{-} \ , \ (\boldsymbol{T} - \boldsymbol{T}^{*}) \cdot \boldsymbol{E} \geq 0 \ , \ \forall \, \boldsymbol{T}^{*} \in Sym^{-} \ , \tag{2}$$

and, dually, to the conditions, called dual normality conditions, listed below

$$\boldsymbol{E} \in Sym^{+} \ , \ (\boldsymbol{E}-\boldsymbol{E}^{*}) \cdot \boldsymbol{T} \geq 0 \ , \ \forall \, \boldsymbol{E}^{*} \ \in Sym^{+} \ . \tag{3}$$

The restrictions defining the NRNT material in the particular form (2), are the essential ingredients for the application of the theorems of Limit Analysis (see [11], [12]).

2.2 The boundary value problem

The equilibrium of a 2d masonry structure, modelled as a continuum composed of NRNT material subject to given loads and settlements, can be formulated as a Boundary Value Problem (BVP), in the following form.

“Find a displacement field $\boldsymbol{u}$, the associated deformation $\boldsymbol{E}$, and a stress field $\boldsymbol{T}$ such that

$$\boldsymbol{E} = \frac{1}{2}(\nabla \boldsymbol{u} + \nabla \boldsymbol{u}^{T}) \ , \ \boldsymbol{E} \in Sym^{+} \ , \ \boldsymbol{u} = \bar{\boldsymbol{u}} \ \ on \ \partial\Omega_{D} \ \ , \tag{4}$$

$$div \, \boldsymbol{T} + \boldsymbol{b} = 0 \ \ , \ \ \boldsymbol{T} \in Sym^{-} \ \ , \ \ \boldsymbol{Tn} = \bar{\boldsymbol{s}} \ \ on \ \partial\Omega_{N} \ \ , \tag{5}$$

$$\boldsymbol{T} \cdot \boldsymbol{E} = 0 \ \ , \tag{6}$$

where $\boldsymbol{n}$ is the unit outward normal to the boundary and $\partial\Omega$, and $\partial\Omega_{D}\, , \partial\Omega_{N}$ is a fixed partition of the boundary into the constrained and loaded parts.
On introducing the set $\mathcal{K}$ of kinematically admissible displacements, and the set $\mathcal{H}$ of the statically admissible stresses, defined as follows:

$$\mathcal{K} = \left\{ \boldsymbol{u} \in S \ / \ \boldsymbol{E} = \frac{1}{2}(\nabla \boldsymbol{u} + \nabla \boldsymbol{u}^{T}) \in Sym^{+} \ \& \ \ \boldsymbol{u} = \bar{\boldsymbol{u}} \ \ on \ \partial\Omega_{D} \right\} \ , \tag{7}$$

$$\mathcal{H} = \{ \boldsymbol{T} \in S' \ / \ div\boldsymbol{T} + \boldsymbol{b} = 0 \ \ , \ \ \boldsymbol{T} \in Sym^{-} \ \ , \ \boldsymbol{Tn} = \bar{\boldsymbol{s}} \ \ on \ \partial\Omega_{N} \ \} \ , \tag{8}$$

in which S, S' are two suitable function spaces, a solution of the BVP for NRNT materials, is the triplet $(\boldsymbol{u}^\circ, \boldsymbol{E}(\boldsymbol{u}^\circ), \boldsymbol{T}^\circ)$ such that $\boldsymbol{u}^\circ \in \mathcal{K}$, $\boldsymbol{T}^\circ \in \mathcal{H}$, and $\boldsymbol{T}^\circ \cdot \boldsymbol{E}(\boldsymbol{u}^\circ) = 0$.

2.3 Regularity of stress and strain: singular fields

Concentrated strain and stress. For NRNT materials, it is possible to admit that strain and stress are bounded measures. Bounded measures can be decomposed into the sum of two parts

$$\boldsymbol{E} = \boldsymbol{E}^r + \boldsymbol{E}^s \ , \ \boldsymbol{T} = \boldsymbol{T}^r + \boldsymbol{T}^s \ , \tag{9}$$

where $(.)^r$ is the part that is absolutely continuous with respect to the area measure (that is $(.)^r$ is a density per unit area) and $(.)^s$ is the singular part.
On admitting singular strains and stresses, it is possible to admit that both the displacement $\boldsymbol{u}$ and the stress vector $\boldsymbol{s}$ be discontinuous. The stress vector is the contact force transmitted across a surface of unit normal $\boldsymbol{n}$, and, in Cauchy's sense, is related to the regular part of the stress through the relation $\boldsymbol{s} = \boldsymbol{T}^r\boldsymbol{n}$.

Displacement jumps. If the displacement vector exhibits a jump discontinuity across a regular curve Γ, on such a curve the strain is concentrated, namely is a line Dirac delta whose amplitude coincides with the value of the jump of $\boldsymbol{u}$ across Γ. Denoting $\boldsymbol{t}, \boldsymbol{n}$ the unit tangent and the unit normal to Γ, and calling Ω^-, Ω^+ the two parts on the two sides of Γ, Ω^+ being the part toward which $\boldsymbol{n}$ points, the jump of $\boldsymbol{u}$ on Γ can be denoted as follows

$$[\boldsymbol{u}] = \boldsymbol{u}^+ - \boldsymbol{u}^- \ , \tag{10}$$

and decomposed into tangential and normal components:

$$[\boldsymbol{u}] = w\,\boldsymbol{t} + v\,\boldsymbol{n} \ , \ w = [\boldsymbol{u}] \cdot \boldsymbol{t} \ , \ v = [\boldsymbol{u}] \cdot \boldsymbol{n} \ . \tag{11}$$

Denoting $\delta(\Gamma)$ the unit line Dirac delta with support on Γ, the concentrated strain on Γ, taking into account the relation defining the infinitesimal strain in terms of the displacement: $\boldsymbol{E} = \frac{1}{2}(\nabla\boldsymbol{u} + \nabla\boldsymbol{u}^T)$, and the material restrictions on strains for NRNT materials, takes the form

$$\boldsymbol{E} = v\,\delta(\Gamma)\,\boldsymbol{n} \otimes \boldsymbol{n}\ ,\ \ v \geq 0\ , \tag{12}$$

since, taking into account the restriction $\boldsymbol{E} \in Sym^+$, it must be

$$w = 0\ , \tag{13}$$

That is, the two parts Ω^-, Ω^+ may separate but cannot penetrate each other, and the sliding w along Γ must be zero.

Stress vector jumps. If the stress vector exhibits a jump discontinuity across a regular curve Γ, on such a curve the stress is concentrated, namely is a line Dirac delta whose amplitude P is related to the jump of $\boldsymbol{s}$ across Γ. Recalling the definition introduced above for $\boldsymbol{t}, \boldsymbol{n}$, on adopting the previous notation the jump of $\boldsymbol{s}$ across Γ can be denoted as follows

$$[\boldsymbol{s}] = \boldsymbol{s}^+ - \boldsymbol{s}^-\ , \tag{14}$$

and decomposed into normal and tangential components

$$[\boldsymbol{s}] = p\,\boldsymbol{t} + q\,\boldsymbol{n}\ ,\ p = [\boldsymbol{s}] \cdot \boldsymbol{t}\ ,\ q = [\boldsymbol{s}] \cdot \boldsymbol{n}\ . \tag{15}$$

Denoting $\delta(\Gamma)$ the unit line Dirac delta with support on Γ, the stress concentrated on Γ, taking into account the balance equations $div\boldsymbol{T} + \boldsymbol{b} = 0$, and the material restrictions for NRNT materials, takes the form

$$\boldsymbol{T} = P\,\delta(\Gamma)\,\boldsymbol{t} \otimes \boldsymbol{t}\ ,\ P' + p = 0\ ,\ P\rho + q = 0\ ,\ \ P \leq 0\ , \tag{16}$$

where ρ is the curvature of the line Γ and P' is the derivative of P with respect to its argument, namely the arc length along Γ. The amplitude P of the concentrated stress represents a concentrated axial contact force acting along the 1d substructure Γ. The last relation in (16) says that such a force must be compressive.

3 Energetical formulations of the BVP for NRNT materials

3.1 The kinematical problem and the equilibrium problem.

The BVP for NRNT materials can be decomposed into two parts: the search of a displacement field belonging to $\mathcal{K}$, and the search of a stress field belonging to $\mathcal{H}$. The first problem is named Kinematical Problem (KP) and the second problem is called Equilibrium Problem (EP). The two problems are coupled only through condition (6), and can be taken up independently.

If the solution of the BVP is attacked considering first the KP and taking as primal variable the displacement, then we say that a displacement approach is adopted. If, instead, the EP is considered first, by taking the stress as the primal variable, then we say that a force type approach is followed.

Compatibility of force and displacement data. First of all, it is to be pointed out that both the KP and the EP can be incompatible, in the sense that the displacement or the load data could be given in such a way that the set $\mathcal{K}$, or the set $\mathcal{H}$, are empty. In particular, the compatibility of the EP is an issue involved in the theorems of Limit Analysis. Such theorems, dealing with the possibility or the impossibility of collapse, can be viewed as follows: the safe theorem as a definition of compatible loads, and the kinematical theorem as an indirect way to assess the incompatibility of the loads.

3.2 Displacement approach: minimum of the potential energy.

Dealing with the solution of a BVP for the unilateral material that we consider with a displacement approach, under the preliminary assumption that both the KP and the EP are compatible and non-homogeneous, the problem arises of selecting, among the infinitely many admissible displacement fields, that (or those) to which a statically admissible stress field, such to satisfy the zero-dissipation condition (6), can be associated.

The idea is to seek, among all the kinematically admissible displacement fields, a possible solution of the BVP, by minimizing the total potential energy of the system. For NRNT materials the total potential energy reduces solely to the potential energy $\wp$ of the given contact and body loads.

Then the minimum problem can be formulated as follows:

"Find the displacement field $\boldsymbol{u}^{\circ} \in \mathcal{K}$ such that

$$\wp(\boldsymbol{u}^{\circ}) = \min_{\boldsymbol{u}\in\mathcal{K}} \wp(\boldsymbol{u}) \ , \tag{17}$$

where

$$\wp(\mathbf{u}) = -\int_{\partial\Omega_{\mathrm{N}}} \bar{\mathbf{s}} \cdot \mathbf{u}\, ds - \int_{\Omega} \mathbf{b} \cdot \mathbf{u}\, \mathrm{da} \ , \tag{18}$$

is the potential energy of the given external loads.

Minimum of $\wp$ and equilibrium. The proof of existence of the minimizer $\boldsymbol{u}^{\circ}$ of $\wp(\boldsymbol{u})$ for $\boldsymbol{u} \in \mathcal{K}$, is a complex mathematical question. Due to the poor regularity of the admissible functions, this proof requires sophisticated tools of mathematical analysis, and is well beyond the scopes of the present paper, devoted to more mechanical aspects of masonry equilibrium.

What it is possible to show, by using only elementary tools of calculus, by making the preliminary assumption that the settlements are compatible ($\mathcal{K} \neq \emptyset$), is that:

1. If the load is compatible (that is if $\mathcal{H} \neq \emptyset$), the functional $\wp(\boldsymbol{u})$ is bounded from below.

2. If the triplet $(\boldsymbol{u}^\circ, \boldsymbol{E}(\boldsymbol{u}^\circ), \boldsymbol{T}^\circ)$ is a solution of the BVP, it corresponds to a weak minimum of the functional $\wp(\boldsymbol{u})$.

Proofs.

1. If the load is compatible, then there exists a stress field $\boldsymbol{T} \in \mathcal{H}$, through which the functional $\wp(\boldsymbol{u})$, defined on $\mathcal{K}$, for each $\boldsymbol{u} \in \mathcal{K}$, can be rewritten as follows

$$\wp(\boldsymbol{u}) = -\int_{\partial\Omega_N} \bar{\boldsymbol{s}} \cdot \boldsymbol{u}\, ds - \int_\Omega \boldsymbol{b} \cdot \boldsymbol{u}\, da =$$

$$\int_{\partial\Omega_D} \boldsymbol{s}(\boldsymbol{T}) \cdot \bar{\boldsymbol{u}}\, ds - \int_\Omega \boldsymbol{T} \cdot \boldsymbol{E}(\boldsymbol{u}) da\,, \tag{19}$$

in which $\boldsymbol{s}(\boldsymbol{T})$ denotes the trace of $\boldsymbol{T}$ at the boundary. On assuming that the displacement assigned on the constrained part of the boundary are sufficiently regular (say continuous), since $\boldsymbol{s}(\boldsymbol{T})$ is a bounded measure, the integral $\int_{\partial\Omega_D} \boldsymbol{s}(\boldsymbol{T})\, \bar{\boldsymbol{u}}\, d\sigma$ is finite; and since $\boldsymbol{T} \in Sym^-$ & $\boldsymbol{E} \in Sym^+$, then the volume integral term in the right hand side of (19) is non negative and $\wp(\boldsymbol{u})$ is bounded from below.

2. If $(\boldsymbol{u}^\circ, \boldsymbol{E}(\boldsymbol{u}^\circ), \boldsymbol{T}^\circ)$ is a solution of the BVP, then, for any $\boldsymbol{u} \in \mathcal{K}$, one can write:

$$\wp(\boldsymbol{u}) - \wp(\boldsymbol{u}^\circ) = -\int_{\partial\Omega_N} \bar{\boldsymbol{s}} \cdot (\boldsymbol{u} - \boldsymbol{u}^\circ) ds - \int_\Omega \boldsymbol{b} \cdot (\boldsymbol{u} - \boldsymbol{u}^\circ) da =$$

$$\int_\Omega \boldsymbol{T}^\circ \cdot \big(\boldsymbol{E}(\boldsymbol{u}) - \boldsymbol{E}(\boldsymbol{u}^\circ)\big)\, da\,. \tag{20}$$

The result: $\wp(\boldsymbol{u}) - \wp(\boldsymbol{u}^\circ) \geq 0\ ,\ \forall \boldsymbol{u} \in \mathcal{K}$, follows from the dual normality condition (3). ■

The physical interpretation of the previous result is the following. Since the displacement solving the BVP corresponds to a state of weak minimum for the potential energy, then it is, at least, a state of neutral equilibrium (that is not unstable), in the sense that the transition to a different state requires a non-negative supply of energy.

Remark 1. On the basis of the minimum principle, if the EP is compatible and the KP is homogeneous, then the constant displacement field: $\boldsymbol{u} = \mathbf{0}$ is a possible minimizer. Indeed, in this case, one can write:

$$\wp(\boldsymbol{u}) = -\int_{\partial\Omega_N} \bar{\boldsymbol{s}} \cdot \boldsymbol{u}\, ds - \int_{\Omega} \boldsymbol{b} \cdot \boldsymbol{u}\, da \;=\; -\int_{\Omega} \boldsymbol{T} \cdot \boldsymbol{E}(\boldsymbol{u}) da\,, \quad (21)$$

$\boldsymbol{T}$ being a generic element of $\mathcal{H}$, certainly existing since, by assumption, $\mathcal{H}$ is not empty. Since the last member of (21) is always non-negative, then $\wp(\mathbf{0}) = 0$ is the infimum of $\wp$, and the displacement field $\boldsymbol{u} = \mathbf{0}$ is a minimizer of the potential energy. In this case, any $\boldsymbol{T} \in \mathcal{H}$ is a legitimate solution in terms of stress, since $\boldsymbol{T} \cdot \boldsymbol{E}(\mathbf{0})$ for any $\boldsymbol{T}$.

3.3 Force approach: minimum of the complementary energy.

Dealing with the solution of a BVP for the unilateral material that we consider, with a force approach, again under the preliminary assumption that both the KP and the EP are compatible and non-homogeneous, the problem arises of selecting, among the infinitely many admissible stress fields, that (or those) to which a kinematically admissible displacement field, such to satisfy the zero-dissipation condition (6), can be associated.

The idea is to seek, among all the statically admissible stress fields, a possible solution of the BVP, by minimizing the complementary energy of the system. For NRNT materials the form of complementary energy to be minimized is the sole complementary energy $\wp$c associated to the given settlements.

Then the minimum problem can be formulated as follows:

“Find the stress field $\boldsymbol{T}°$ ∈ $\mathcal{H}$ such that

$$\wp c(\boldsymbol{T}°) = \min_{\boldsymbol{T}\in\mathcal{H}} \wp c(\boldsymbol{T}) \quad ,\text{”} \quad (22)$$

in which

$$\wp c(\mathbf{u}) = -\int_{\partial\Omega_\mathrm{D}} \mathbf{s}(\mathbf{T}) \cdot \bar{\boldsymbol{u}}\, ds \ , \tag{23}$$

is the complementary energy associated to the given settlements.

Minimum of $\wp$c and compatibility. Leaving to more mathematical works the proof of existence of the minimum $\boldsymbol{T}°$ of $\wp c(\boldsymbol{T})$ for $\boldsymbol{T} \in \mathcal{H}$, what can be easily shown, on assuming preliminarily that the EP is compatible (i.e. $\mathcal{H} \neq \emptyset$), is that:

3. If the settlements are compatible (that is if $\mathcal{K} \neq \emptyset$), the functional $\wp c(\boldsymbol{T})$ is bounded from below.
4. If the triplet $(\boldsymbol{u}°, \boldsymbol{E}(\boldsymbol{u}°), \boldsymbol{T}°)$ is a solution of the BVP, then it corresponds to a weak minimum of the functional $\wp c(\boldsymbol{T})$.

Proofs.

3. If the given settlements are compatible, then there exists a displacement $\boldsymbol{u} \in \mathcal{K}$, through which the functional $\wp c(\boldsymbol{T})$, defined on $\mathcal{H}$, for any $\boldsymbol{T} \in \mathcal{H}$, can be rewritten as follows

$$\wp c(\boldsymbol{T}) = -\int_{\partial\Omega_\mathrm{D}} \mathbf{s}(\mathbf{T}) \cdot \bar{\boldsymbol{u}}\, ds =$$

$$= \int_{\partial\Omega_N} \bar{\boldsymbol{s}} \cdot \boldsymbol{u}\, ds + \int_\Omega \boldsymbol{b} \cdot \boldsymbol{u}\, da - \int_\Omega \boldsymbol{T} \cdot \boldsymbol{E}(\boldsymbol{u}) da\, , \tag{24}$$

   In which $\boldsymbol{s}(\boldsymbol{T})$ denotes the trace of $\boldsymbol{T}$ along the boundary. Taking into account that $\boldsymbol{u}$ is a function of Bounded Variation, on assuming that the given surface and body loads have enough regularity (say continuity) for the first two products in the last member of (24) to be summable, the integral $\int_{\partial\Omega_N} \bar{\boldsymbol{s}} \cdot \boldsymbol{u}\, ds + \int_\Omega \boldsymbol{b} \cdot \boldsymbol{u}\, da$ is finite; therefore, since $\boldsymbol{T} \in Sym^-$ & $\boldsymbol{E} \in Sym^+$, the volume term in the last member of (24) is non-negative, then $\wp c(\boldsymbol{T})$ is bounded from below.
4. If $(\boldsymbol{u}°, \boldsymbol{E}(\boldsymbol{u}°), \boldsymbol{T}°)$ is a solution of the BVP, then, for any $\boldsymbol{T} \in \mathcal{H}$, one can write:

$$\wp c(\boldsymbol{T}) - \wp c(\boldsymbol{T}^{\circ}) = -\int_{\partial\Omega_D}(\mathbf{s}(\mathbf{T}) - \mathbf{s}(\mathbf{T}^{\circ}))\cdot\bar{\boldsymbol{u}}\,ds =$$

$$\int_{\Omega}(\boldsymbol{T} - \boldsymbol{T}^{\circ})\cdot\boldsymbol{E}(\boldsymbol{u}^{\circ})da\,. \qquad (25)$$

The result $\wp c(\boldsymbol{T}) - \wp c(\boldsymbol{T}^{\circ}) \geq 0$, $\forall\boldsymbol{T} \in \mathcal{H}$, follows from the normality condition (2). ■

4 A trivial example

The two energy criteria introduced above provide tools for predicting the response of a structure, subject to non-vanishing loads and settlements. To illustrate the proposed method we consider the solution of the trivial benchmark problem described in Figure 1a. The problem is concerned with the non-homogeneous equilibrium and kinematical problem for a lintel, an element that can be considered as made up by many, conveniently arranged, small blocks (stones or bricks) or by a single monolithic piece. As shown in Figure 1a, The lintel is loaded along the upper side by uniformly distributed forces and suffers a symmetrical horizontal settlement of the two lateral constraints.

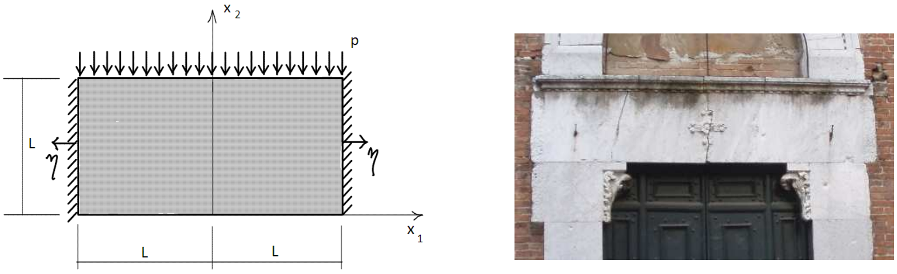

a b

Fig.1 - Masonry panel (lintel/wall beam) under given loads and settlements: (a). Stone lintel, cracked near the middle section due to a relative displacement of the abutments: (b).

An example of a similar structural element is shown in Figure 1b. This kind of lintels are often visible in the front façade of old Churches and Palaces, and is not rare to see that they are cracked in correspondence of their middle section.

The cracks which are visible in such real lintels are invariably produced by relative movements of the supporting structures. For such real structures, the load is different from that considered in Figure 1a, being actually the self-load of the lintel and a surface contact load transmitted by the hanging masonry. The last mentioned load is undoubtedly different from a uniform load, whilst, if the lintel does not crack horizontally, the self load can be transferred, by means of feeble tensile normal stresses, to the upper side of the lintel, becoming a uniformly distributed load.

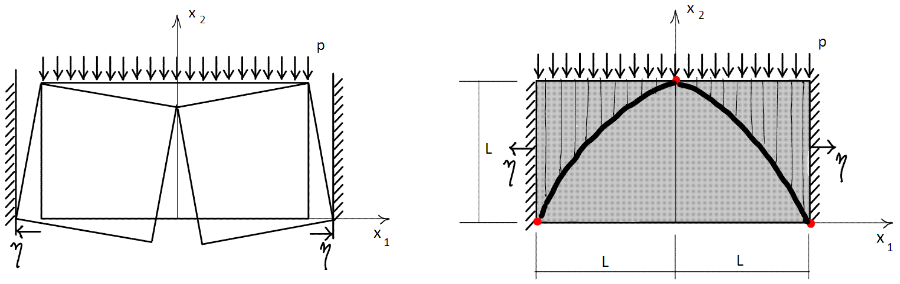

a b

Fig.2 - A possible kinematically admissible displacement field: (a) and a possible statically admissible stress field,: (b), for the BVP depicted in Figure 1a.

A possible solution. In Figure 2, a possible solution of the BVP described in Figure 1a, is reported graphically. In Figure 2a, a compatible displacement field and in Figure 2b a balanced stress field are reported. The displacement considered in Figure 2a is a piecewise rigid displacement with support on two rectangles, symmetrical with respect to the vertical axis x_2, and consists of a rigid block mechanism articulated on the three hinges indicated with dots in Figure 2b.The strain associated to such a compatible displacement is concentrated on three vertical lines of fracture, and is represented by uniaxial deformations of pure detachment, linearly variable along such lines. The stress field represented in Figure 2b consists of singular and regular parts. The regular part of stress, that is a uniaxial compressive stress directed vertically, produces a jump discontinuity of the stress vector across the curve represented with a solid black line in Figure 2 b. Such a discontinuity is balanced by the singular part of the stress, a concentrated uniaxial stress having the form $(16)^1$, tangent to such a curve, and satisfying the balance equations $(16)^2$, $(16)^3$: a concentrated axial stress of intensity P, acts along the curve, forming a so-called line of thrust. Such a line of thrust transmits concentrated forces to the hinges, producing a thrust force at the boundary and a horizontal force at the key hinge. The internal work of the statically admissible stress field depicted in Figure 2b, for the strain associated to the displacement field represented in Figure 2a, is zero, therefore these two fields represent a possible solution of the BVP.

Solution derived through the energy formulations. The solution of the trivial problem shown in Figure 1, is here reconsidered through the energy approach, as a way to show, on a simple example, how the energy criteria introduced in Section 3 can be used to generate approximate strategies to solve equilibrium problems for masonry-like structures. The analysis of this simple problems allows also to enlighten, within an easy context, some peculiar characteristics of the two approaches.

By attacking the problem with a displacement approach, an elementary approximation of the KP is obtained by considering a piecewise rigid displacement with support on two rectangular blocks. Restricting to the case in which the two blocks are fixed and coincide with the two rectangles obtained by dividing the domain along the vertical symmetry axis, the unknowns of the problem reduce to the six rigid displacement parameters of the two blocks. Choosing as poles of the rigid displacement the lower external vertices (A, C) of the two blocks, and restricting to symmetrical displacements, the kinematical conditions at the internal and boundary interfaces, accounting for the material kinematical restrictions, can be written, in terms of the components of horizontal translation u, vertical translation v and rotation ϕ about the pole A (say C for the assumed symmetry), as follows:

$$v = 0\,, u \geq 0\ , u \leq \eta\,, u - \phi L \geq 0\,, u - \phi L \leq \eta\ . \tag{26}$$

The potential energy (18), taking into account equation (26)[1], reads

$$\wp(u,\ \phi) = -\frac{pL^2}{2}\ \phi\ . \tag{27}$$

The minimization problem (17) reduces, in this approximated context, to a trivial minimization problem for the linear function (22) under the side linear constraints (26). Such a problem can be represented graphically as shown in Figure 3 a. From Figure 3a, it is deduced that the values $u=\eta$ and $\phi=\eta/L$ correspond to the minimum of the potential energy. Such values correspond to the mechanism depicted in Figure 2a.

For what concerns the force approach, restricting to stress fields of the type represented in Figure 2b, namely fields composed of a regular uniaxial part and of a singular part with support on a curve passing through three points A, B, A', the complementary energy can be written in terms of the position of these three points. Restricting to symmetric curves, denoting y_A, y_B the variable y-coordinates of the points A (A') and B having fixed abscissae L ($-L$) and 0 respectively, taking into account equations (16)[2], (16)[3], one obtains:

$$\wp c(y_A, y_B) = p\ L^2\ /\ 2\ (y_B - y_A)\ \ . \tag{28}$$

Such a function has to be minimized under the condition that the y-coordinates belong to the interval [0, L] and with the constraint $y_B > y_A$, ensuring that the axial force is finite and compressive. From the graph of Figure 3b it is deduced that the minimizer is $y_A = 0$, $y_B = L$, corresponding to a value of the complementary energy of $\frac{pL\eta}{2}$.

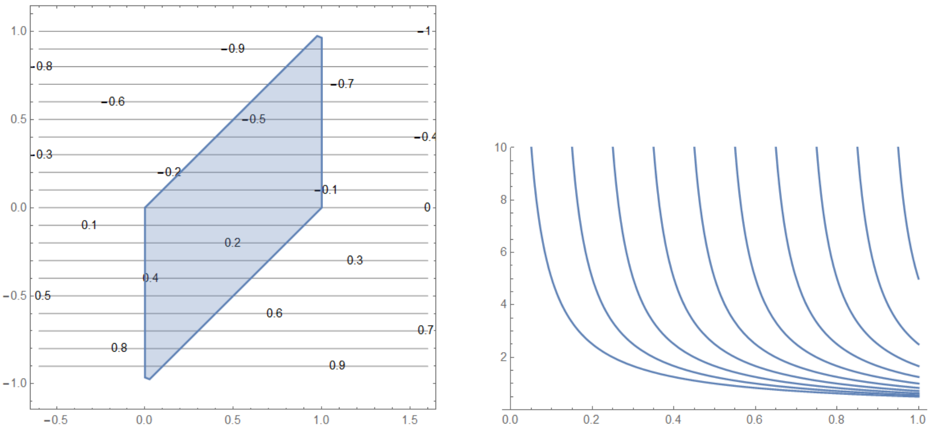

a b

Fig.3 - In (a): contour plot of the potential energy $\wp(u,\ \phi) = -\frac{\mathrm{pL}^2}{2}\ \phi$ normalized with respect to $\frac{\mathrm{pL}\eta}{2}$ as a function of the normalized variables $u° = \frac{u}{\eta}$ (horizontal axis) , $\phi° = \frac{\phi L}{\eta}$ (vertical axis). From the graph it is deduced that the minimizer is $u=\eta$ and $\phi=\eta/L$, corresponding to the value of energy $-\frac{\mathrm{pL}\eta}{2}$. In (b): plot of the complementary energy as a function of y_B (for $y_B > y_A$) for various values of y_A (from left to right: $y_A=\{0, 0.1, \dots, 0.9\}$). The positions y_A, y_B are normalized with respect to L and the value of energy is normalized with respect to $\mathrm{pL}\eta$. From the graph it is deduced that the minimizer is $y_A = 0$, $y_B = L$, corresponding to a value of complementary energy of $\frac{\mathrm{pL}\eta}{2}$.

In conclusion, both the displacement and force approaches indicate as the minimal solution the same state, that is the one depicted in Figure 2a and b.

5 Numerical approximation of the displacement approach: rigid blocks

The approximate solution of the minimum problem (17) generated by restricting the search for the minimum to the restricted class $\mathcal{K}_{pr}$ of piecewise rigid displacements, is considered. This infinite dimensional space is discretized on considering the partition

$$(\Omega_i)_{i\in\{1,2,..,M\}} \ , \tag{29}$$

of the domain Ω into a finite number M of rigid pieces, such that

$$\sum_{i=1}^{M} P(\Omega_i) < \infty \ , \tag{30}$$

$P(\Omega_i)$ denoting the perimeter of the piece Ω_i. In particular, on restricting to polygonal elements, the boundary $\partial\Omega_i$ of Ω_i, is composed by segments Γ, of length ℓ, whose extremities are denoted 0,1.

The segments Γ, which are either the common boundary between elements or between elements and the constrained part of the boundary, are called "interfaces".

On denoting $\mathcal{K}_{pr}^{M}$ the finite dimensional approximation of $\mathcal{K}_{pr}$ generated by the partition (29), the following minimum problem is considered

$$\wp(\widehat{\boldsymbol{u}}) = \min_{\boldsymbol{u}\in\mathcal{K}_{pr}^{M}} \wp(\boldsymbol{u}) \ . \tag{31}$$

To represent a generic displacement $\boldsymbol{u} \in \mathcal{K}_{pr}^{M}$, one can consider the vector $\widehat{\boldsymbol{U}}$ of $3M$ components represented by the $3M$ parameters of rigid displacement of translation and rotation of the M elements. These parameters are restricted by the assumption that the strain must be positive semidefinite. For piecewise rigid displacements the deformation is concentrated on the intefaces (that is on the segments Γ), and, recalling (12), assumes the form:

$$\boldsymbol{E} = v\, \delta(\Gamma)\, \boldsymbol{n} \otimes \boldsymbol{n} \ , \tag{32}$$

where

$$v = [\boldsymbol{u}] \cdot \boldsymbol{n} \ \geq 0 \ . \tag{33}$$

Therefore, on the segment Γ, besides the unilateral restriction (33), also the following condition

$$w = [\boldsymbol{u}] \cdot \boldsymbol{t} = 0 \ , \tag{34}$$

must be enforced.

Notice that conditions (33), (34), descending from the normality assumption (2), represent unilateral conditions of contact without sliding on the interfaces Γ.

The static counterpart of (33), (34) concerns the stress vector $\boldsymbol{s}$ acting on the interfaces (both the internal and the external).

Such a stress vector represents the reaction associated to the constraints (33) and (34), transmitted among the blocks and among the blocks and the soil. The stress vector coincides with the given tractions $\bar{\boldsymbol{s}}$, where the boundary of the blocks represents the loaded boundary. On denoting

$$\sigma = [\boldsymbol{s}] \cdot \boldsymbol{n} \ , \ \tau = [\boldsymbol{s}] \cdot \boldsymbol{t} \ , \tag{35}$$

The normal and tangential components of the stress vector along Γ, the condition to be imposed on $\boldsymbol{s}$ is

$$\sigma \leq 0 \ . \tag{36}$$

Notice that the tangential component τ of $\boldsymbol{s}$ is not restricted and can be non-zero also if on Γ one has: $\sigma = 0$.

Denoting N the total number of interfaces Γ, and $v(0), v(1), w(0), w(1)$ the normal and tangential components of the relative displacement across Γ , of the ends 0, 1 of the segment itself, the restrictions (33), (34) are equivalent to the $2N$ inequalities

$$v(0) \geq 0 \, , \ v(1) \geq 0 \ , \tag{37}$$

And to the $2N$ equalities

$$w(0) = 0 \, , \ w(1) = 0 \ . \tag{38}$$

The restrictions (37), (38) can be expressed in terms of the components of $\widehat{\boldsymbol{U}}$, and rewritten in the matrix forms

$$\boldsymbol{A}\,\widehat{\boldsymbol{U}} \geq 0 \ , \tag{39}$$

$$\boldsymbol{B}\,\widehat{\boldsymbol{U}} = 0 \ . \tag{40}$$

Finally, the minimum problem (26), approximating the minimum problem (17), takes the form

$$\wp\big(\widehat{\boldsymbol{U}}^{\boldsymbol{0}}\big) = \min_{\widehat{\boldsymbol{U}}\in\mathbb{K}^M} \wp\big(\widehat{\boldsymbol{U}}\big) \ , \tag{41}$$

in which $\mathbb{K}^M$ is the set

$$\mathbb{K}^M = \{\widehat{\boldsymbol{U}} \in \mathcal{R}^{3M} \,/\, \boldsymbol{A}\,\widehat{\boldsymbol{U}} \geq 0 \ , \ \boldsymbol{B}\,\widehat{\boldsymbol{U}} = 0\} \ . \tag{42}$$

Remark 2. The minimization problem (41) here proposed to approximate the minimum problem (17), transforms the minimum problem (17), formulated for a continuum, into a minimization problem for a structure composed by a finite number of rigid elements in mutual unilateral contact among each other.

Problem (41) is a standard problem of Linear Programming, since the function $\wp\big(\widehat{\boldsymbol{U}}\big)$ depends linearly on the 3M-vector $\widehat{\boldsymbol{U}}$ and the side constraints are linear. The existence of the solution of the approximate problem is trivially assured, if the exact functional is bounded from below (see (19)). For a limited number of variables (say less than 10^3) the problem can be solved effectively with the simplex method (see [13]), for larger size problems (up to 10^6/10^7 unknowns and sparse matrices $\boldsymbol{A}$ and $\boldsymbol{B}$) there exist a number of efficient approximation alternatives (see [14], [15]).

6 Application of the displacement approach to a real case

The numerical method based on the displacement approach proposed to approximate the BVP for NRNT masonry materials, implemented with the program of symbolic calculus Mathematica, is here applied to a simple example in order to simulate the fracture pattern in a real old building. This masonry construction, due to an evident foundation settlement, exhibits a widespread cracking on its main façade (Figure 4a).

In the simulation, the main façade, loaded by its self-weight, is discretized into 7364 triangular elements (Figure 4b).

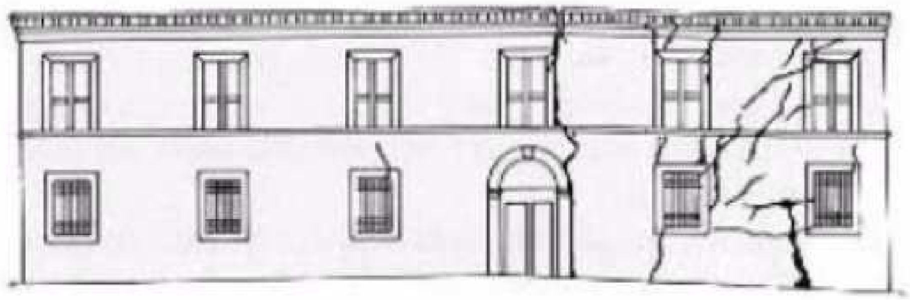

a

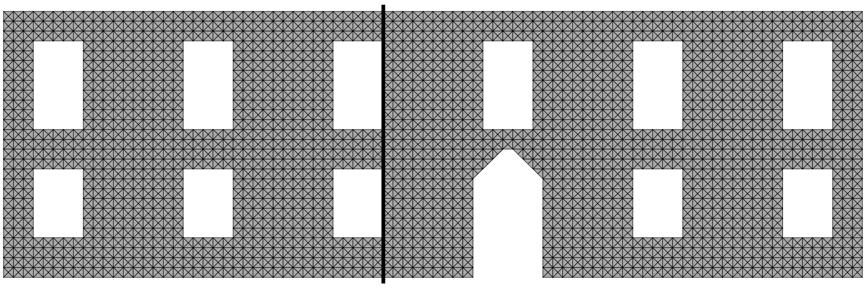

b

Fig.4 - Façade of a XVII century building in Bergamo, presenting an extensive cracking due to an evident differential settlement of the foundation. In (a) front view and crack pattern; in (b) discretization of the wall into triangular elements. (Redrawn from the site of the Fireworkers of Bergamo. Courtesy of Paolo Faccio)

The effect of a differential settlement of the right part of the foundation is considered. The analysis is restricted to the right part of the structure, on the right side of the vertical line depicted in Figure 4b, and represented in Figure 5a.

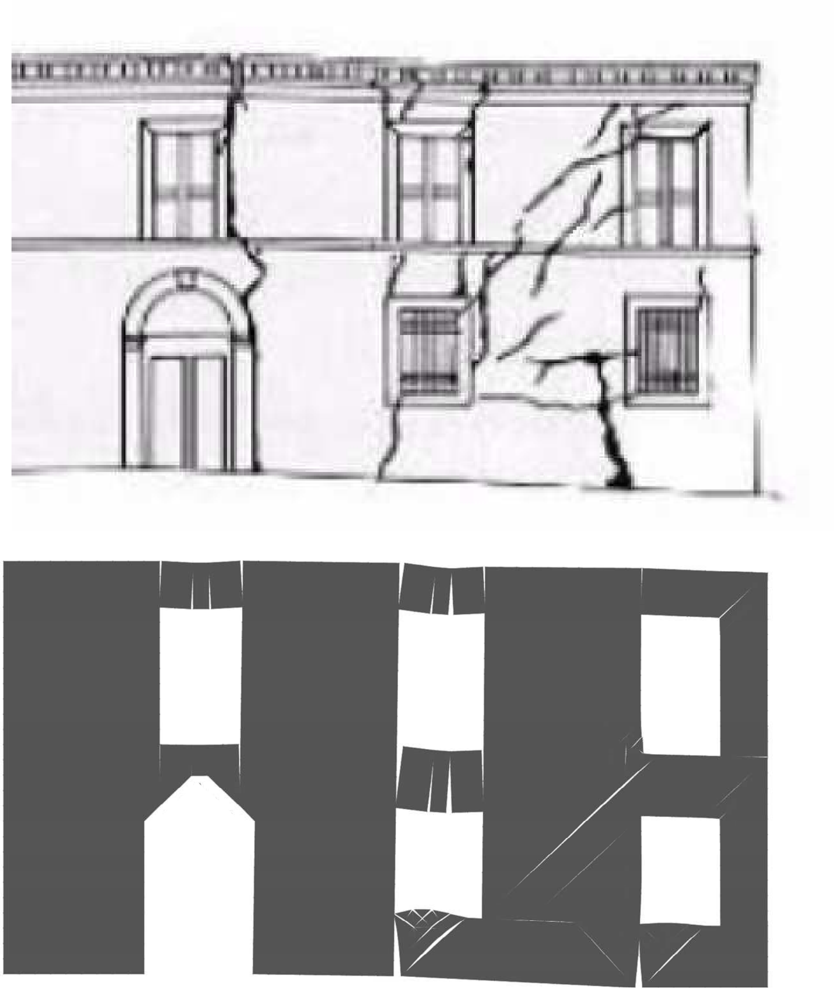

Fig.5 - Real crack pattern and result of the analysis.

The piecewise rigid displacement field, with support on the triangular elements, produced by the settlement is obtained by minimizing the potential energy $\wp(\widehat{\boldsymbol{U}})$ with respect to the generalized displacement $\widehat{\boldsymbol{U}}$, as described in Section 5.

Due to the high number of elements and conditions, to solve numerically problem (41), the approximate Linear Programming method known as "Interior-Point" method, has been adopted

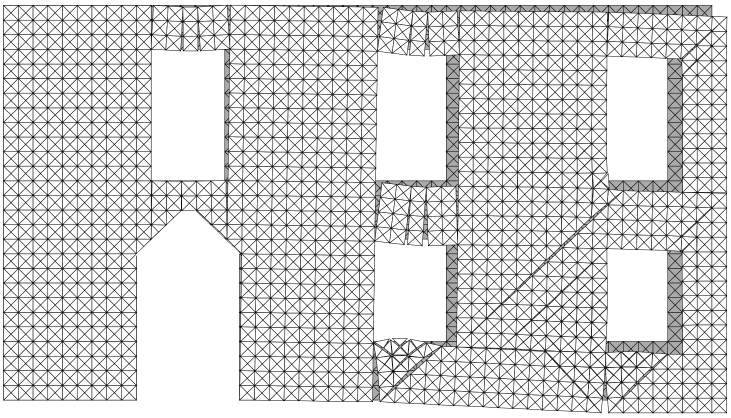

Fig.6 - Mechanism produced by a foundation settlement in the discretized structure of Figure 4b. The deformed and the original configurations are shown superimposed one on top of the other.

The optimal profile of the given settlement, controlled by three parameters, was obtained by executing a parametric analysis for various runs of the program on the grid of possible values of the parameters. In Figure 5, the solution corresponding to such optimal profile is shown for comparison, side by side, with the drawing of the real crack pattern. In Figure 6, the original and the deformed configuration, obtained by amplifying three times the magnitude of the displacements, are reported superimposed one on top of the other.

7 Conclusions

In the present work, a computer code for the prediction of fracture patterns produced by a given set of kinematical data (settlements/distortions) is proposed and developed.

In practical applications to real structures, the main critical issue of a fracture survey is identifying the particular form of foundation settlements producing the detected crack pattern.

The computer program here proposed, represents a deterministic tool enabling to find the mechanism and the fracture pattern due to known kinematical data, in a structure composed of rigid pieces in mutual unilateral contact.

In this work, we apply the method to two real examples. Based on the results we obtain for these two examples of different complexity, we can say that the method is able to reproduce satisfactorily the size, the number and the location of the rigid macro-blocks in which the structure decomposes when a mechanism forms due to known settlements. A lesser degree of correlation is detected concerning the crack path, in particular when the orientations of the real cracks are sensibly different from those of the element interfaces.

In the second example, since the exact settlements producing the mechanism are not known, we try to identify manually a specific combination of simplified settlements over a given set. A number of different runs of the program were performed, by varying the relative value of the settlements over a specified grid of individual values, choosing the combination which gave the “best fit”.

It goes without saying that a rational identification scheme, based on the code that we introduce in the present paper, should be implemented to make the method effective in practical applications. The development of such a task is outside the scopes of the present paper.

References

1. Angelillo, A., Cardamone, L., Fortunato, A. (2010) A numerical model for masonry-like structures. *Journal of Mechanics of Materials and Structures*, vol. 5 (*4*), pp. 583-615
2. Angelillo, M. (2014) Practical applications of unilateral models to Masonry Equilibrium. In *Mechanics of Masonry Structures* (Ed Angelillo M.) CISM International Centre for Mechanical Sciences 551, pp. 109-210. Springer Vienna
3. Angelillo, M., Fortunato, A., Montanino, A., Lippiello, M. (2014) Singular stress fields for masonry walls: Derand was right. *Meccanica*, vol. 49 (*5*), pp. 1243–1262
4. Brigante M., Ercolano, A. (1991) The dynamic analysis of multiblock structures with unilateral constraints. In: *Cheung Y.K., Lee Y.K., Leung A.Y.T. (eds), Proc. of the Asian Pacific Conference on Computational Mechanics (APCOM)*, Hong Kong, December 11-13, 1, pp. 601-606.
5. Dantzig, G.B., Orden, A., Wolfe, P. (1955) Generalized Simplex Method for Minimizing a Linear Form Under Linear Inequality Restraints. *Pacific Journal of Mathematics*, vol. 5 (*2*), pp. 183–195.
6. Dantzig, G.B., Thapa, M.N. (1997) Linear Programming,1: Introduction, Springer
7. Dorn, W.S., Greenberg, H.J. (1957) Linear programming and plastic limit analysis of structures. *Quarterly of Applied Mathematics,* vol. 15 (*2*), pp. 155-167.
8. Ercolano A. (1992) Seismic response of multiblock structures with unilateral constraints. *Proc. of the 10th World Conference on Earthquake Engineering (10 WCEE)*, Madrid, Spain, July 19-24, 1-10, pp. 3979-3982.
9. Ercolano A. (1997) Un metodo per l'analisi numerica di pannelli murari tramite la complementarità lineare. *XIII Convegno Nazionale del Gruppo Italiano Frattura,* Cassino, 27-28 maggio 1997.
10. Fortunato, A., Babilio, E., Lippiello, M., Gesualdo, A., Angelillo, M. (2016) Limit Analysis for Unilateral Masonry-like Structures. *The Open Construction and Building Technology Journal*, vol. 10 (Suppl 2:M12), pp. 346-362
11. Fortunato, A., Fraternali, F., Angelillo, M. (2014) Structural capacity of masonry walls under horizontal loads. *Ingegneria Sismica*, vol. 31 (*1*), pp. 41-51.
12. Heyman, J. (1995) *The stone skeleton*. Cambridge, UK: Cambridge University Press
13. Heyman,, J. (1966) The stone skeleton. *International Journal of Solids and Structures*, vol. 2 (*2*), pp. 249-279.
14. Huerta, S. (2006) Galileo was wrong. The Geometrical Design of Masonry Arches. *Nexus Network Journal*, vol. 8 (*2*), pp. 25-52.
15. Pasquino, M., Ercolano, A., D'Onofrio, C. (1993) Solution methods for framed structures with unilateral constraints. In: Brebbia C.A., Carlomagno C.M. (eds), *Proc. 6th International Conference on Computational Methods and Experimental Measurements*, Siena, May 1993, 2, pp. 115-130.

On the analysis of masonry arches

Nicola Maria Auciello[1]

[1]School of Engineering, University of Basilicata, Via dell'Ateneo Lucano 10,
85100 Potenza (PZ), Italy
nicola.auciello@unibas.it

Abstract. The behavior of masonry arches structures is studied through the homogenizing theory, applying the newest results of symbolic calculation. This procedure, based on the solution suggested in 1982 as an extension of Castigliano's theorem, takes advantage of considering the stony ashlar and mortar structure as an homogenous, non-tensile resistant body: as a consequence, a different reacting configuration will be needed for each load multiplier. Thus, it is urged to fix a modified structure, able to contain the arch funicular in determining the statically compatible solution to support traditional tensile stress methods. This work ends with an analysis on the behavior f a well-known existing monumental structure, Saint-Martin Bridge upon Lys.

Keywords: Wall arch, elastic approach, non-linear analysis.

1 Introduction

The study of stone arches may be pursued in two different ways. First method follows the tensile stress techniques, where simultaneous formation of numerous disjoints is assumed to be capable of originating a compatible mechanism, according to the second method, the behavior of the structure is considered in non-linear regime, through elastic approach. The latter, first suggested by Castigliano (1879) more than a century ago, has been considered little useful for many years, because of evident difficulty in numerical valuation, however, since automatic calculation tools are available, this technique was reconsidered, so that, by the end of last century, it led to significant numerical results, especially in terms of calculation velocity. Recently, thanks to wider employment of symbolic calculation programs, among which Wolfram Mathematica© (2014) is worth particular credit, calculation accuracy has been progressively increasing, so that non-linear-based problem resolution may be easily pursued. Basically, employing resolution procedures based on the method of stresses allows to combine the easiness of the mechanism method with non-linear elastic analyses, conducted on a modified and deformed structure. Hence, the arch is assumed as a set of stony ashlars, pulled together with no embodiment mortar intersection. In practice, the arc is assumed with regards to the usual hypotheses on a wall material, such as suggested by Heyman, long ago.

Thus, the following hypotheses are accepted:

1) Infinite stiffness;
2) sliding failure cannot occur
3) Stone has no tensile strength
4) Infinite compressive strength.

Under these hypotheses, failure may only arise due to instantaneous formation of such a number of hinges, so that the system becomes mechanism. In above mentioned works, Heyman proposed an assessment method based on progressive reduction of ashlar thickness. Basically, collapse load lowering may be achieved through kinematical admissible multipliers: this method suggested by Heyman employs hand-made calculations and tables, whereas many authors have introduced automatic calculation programs, which allow to draw the line of thrust, starting from the arch and following opening hinges positions.

Obviously, mechanism procedures, suggested by Heyman, were extended to cases where some hypotheses had been removed. In the following years, many researchers had been introducing new solutions to the arch problem, removing some of the previous hypotheses. One of the first results was pursued by Franciosi (1980) and Franciosi *et al.* (1981), where arches are studied by taking into account ashlar viscosity effects, or, were in Franciosi (1986) displacements of abutments. Recently, Smars (2008) proposed a method based on mechanism formation stability domains, under the hypothesis of finite displacements, whereas numerical solutions where suggested by employing finite brick-type elements methods, such as in Auciello and Ercolano (1997), Ochsendorf *et al.* (2001,2006), Cavicchi *et al.* (2004, 2005). In other words, many recent researches are able to cope with numerous and different practical situations. Anyway, changes provided in the elastic method suggested by Heyman are incapable of considering instability crises, and, more than that, do not provide information about the history of resisting section sharing, neither about position and wideness of fissured zones. To overcome these limits, Castigliano (1897) approach may be employed. In this work, by following the way led by Castigliano, his procedures were adapted and integrated with a well-known homogenization technique on the material, whose arch ashlars, together with their mortar embodiments, are assimilated to a non-elastic, non-pull-reacting body. The structure is so assumed to be made up of an homogenous material, where usual structural solution methods can be applied. One issue is to be mentioned: according to this procedure, a stiffness largerer than the real one is taken into account conceived. As a consequence, compression crisis stress so determined is bigger than the actual one, so that, as considering negligible pull stress under braking conditions, a safety advantage is originated. This method needs the step-by-step knowledge all of the geometrical and mechanical characteristics of the structure, so its behavior evolution may be monitored till the crisis, as first highlighted by Franciosi *et al.* (1982), Romano et al. (1984), Bridle et al (1990), Hughes et al. (1997).

2 Homogenization technique

Let us now consider an ideal stone arch structure, such as in the geometrical and loading scheme in Figure 1. The arch is made of a finite number of ashlars, linked to each other by mortar joints. Such a scheme is very close to reality, especially for monumental arches.

First operation consists in calculation under the hypotheses of linear-elastic and no-tension material. In this case, the behavior of the structure depends on the hyperstatic solution of the structure itself. If its material is assumed to be isoresistant to any set of three values of hyperstatic unknowns, then a statically compatible solution is yielded, as long as it respects the three congruence equations. However, in the case examined here, material is assumed to be no-tension , so that loads funicular polygon is subdued to set in the thickness of the structure, thus resulting into a statically compatible solution. No X_i triad may happen to be consistent with static compatibility, that's to say that the shape of the funicular allows no X_i triad to enclose it in the arch thickness.

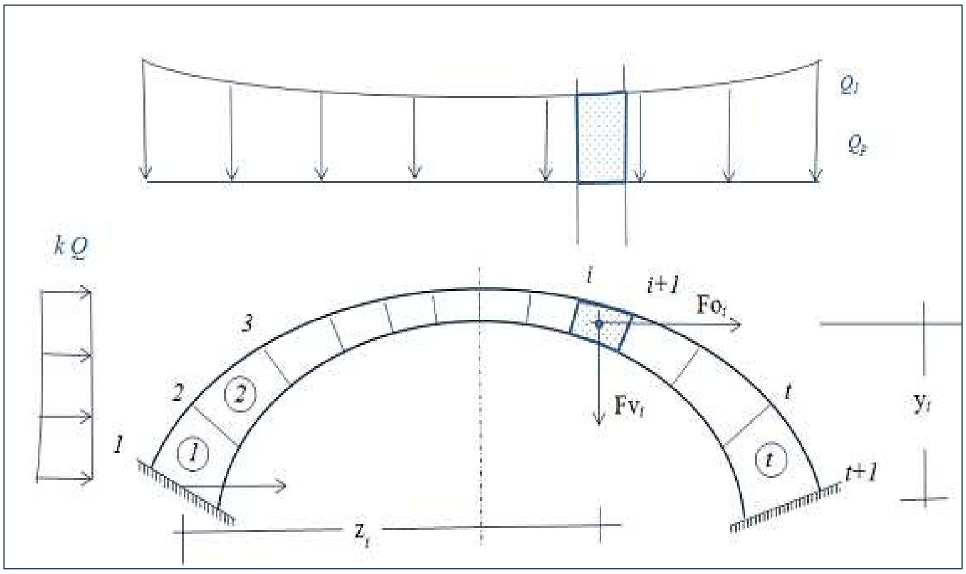

Fig. 1 - The masonry arch bridge.

Under this condition, problem solution may be achieved through numerics only, so that theoretical considerations linked to solution uniqueness and existence shall be left apart, whereas breaking multipliers, such as statically admissible coefficients, shall be determined.

2.1 Stonework material

A no-tension material may not exist. As a result, despite its intrinsic curves idealization, such a curve should be assumed to be tangent to axis τ, so that any Mohr circle, at τ≠0, would disrespect the intrinsic curve in 0. Thus, to a by saying “no-tension material”, an ideal behavior is imposed, according to which the relation defined in Figure 2 is respected.

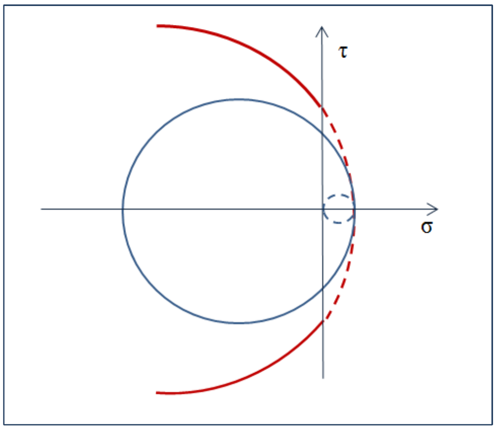

Fig. 2 - Intrinsic curves idealization, Mohr

Basically, such a material, just like mortar, requires cohesivity, although its pullout resistance is poor, and its breaking stretch is almost null.

2.2 Applied Loads

Applied actions on the structure are due to weights of the stony elements and possible abutments, beside accidental loads, such as load loads, wind, thermal variations and seismic actions.

Limit stresses due to seismic actions are fixed by regulations and determined through common procedures in structural dynamics (to which readers should refer) , depending on the acceleration imposed by the soil. Speaking of which, in order to produce a general as well as simple discussion, acting loads are here idealized and settled in two groups of forces, vertical ones and horizontal ones, whose specific calculations should be dealt by referring to codes.

As for the following analysis, in simple terms, the loading distribution is given by equation, Fig. 1:

$$F_{vi} = (Q_p + Q_1) - \frac{k}{2}(Q_p + Q_1), \qquad F_{oi} = k\,(Q_p + Q_1). \tag{1}$$

Particular attention should be paid to thermal variations, because of monumental structures remarkable stiffness, combined with actions due to quakes, as shown by Auciello and De Rosa (1985)

2.3 Structure resolution

To start with, valid solution for isorestistant material through congruence equations is assumed, and then supported by equivalent isostatic structure for hyperstatic unknown quantities calculations. The standard algorithm for virtual work is used, given it provides, since the beginning, the problem solution, by writing down the usual congruence conditions. In brief, unknown quantities are obtained through a linear system to be solved in X_i, such as in Figure 3.

Limit conditions are defined by taking into account the resulting equivalent isostatic structure in a formulation such as

$$\mathbf{A}\ \mathbf{X} = \mathbf{b} \tag{2}$$

Where **A** is the deformation matrix, and **b** the constant term, due to loads. A more detailed analysis is discussed in numerous structure mechanics textbooks, to which readers should refer.

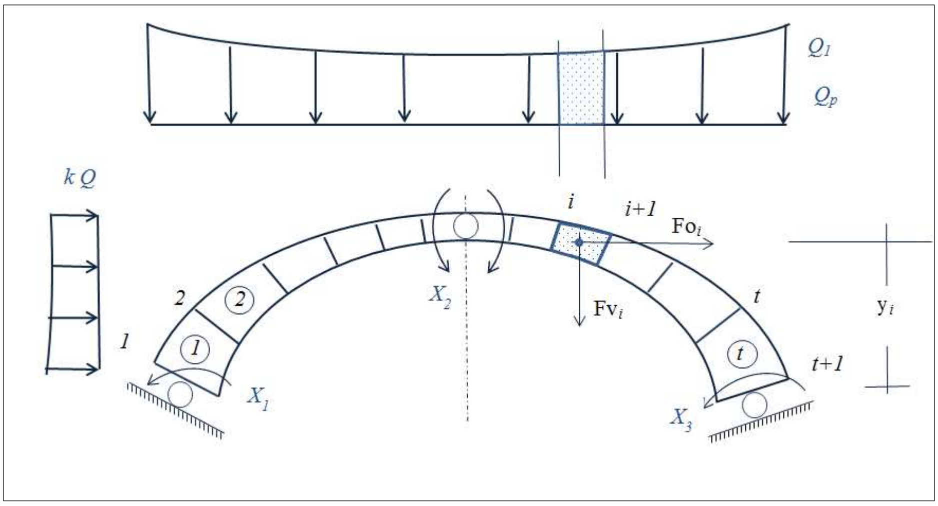

Fig. 3 – Structure resolution.

2.4 Iterative procedures in modified structure calculation

In the first phase, the system (Fig. 3) provides hyperstatic unknown quantities, and their stresses and tensions, by assuming an isoresistant, linear-elastic behavior. Thus, tensile areas are suppressed and a new reacting zone is obtained, modified from the former. Hence, congruence equations on the new structure are written and procedures are repeated to smooth structure variation the one from the other. After the first step, procedures require stresses to be known on each section and tensile areas suppression changes at each step, until a structure such as in Appendix A is obtained.

Obviously, non-linear procedures come to an end when ith cycle varies from the previous according to a tiny control parameter, as common sense; in practice, calculations stop when tensile stress reduce beneath a fixed value.

One of the most important issues in the process concerns integration methods when deformation matrix is calculated. Franciosi *et al.* (1982) and

Auciello and De Rosa (1985) employ a simple Euler-type integration method in their works. Such a choice imposed heavy numerical limitations, especially when discretization copes with high values. In this work, function integration, which is a cornerstone in congruence equations formulation, is easily overcome by employing Gauss integration, best fitting current program operative power, in particular employing symbolic calculation programs such as Mathematica (Wolfram, 2014).

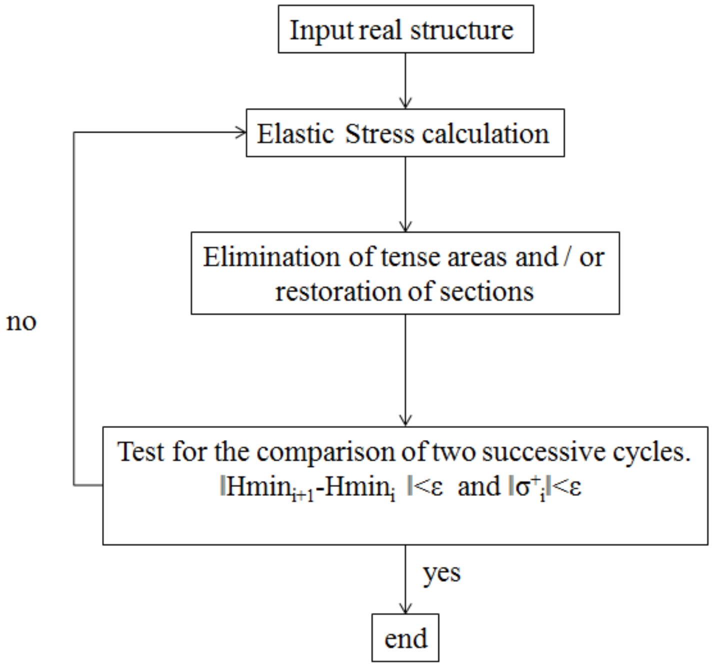

Fig. 4 - Flow-chart for the calculation of the reagent structure.

When iterations end, actual shape of the reacting arch is determined, by knowing all of the compressed arch sections. As a consequence, the following phase, consisting in reducing and restoring structure parts, is merely computational. Actual loads and geometrical dimensions are not modified, as well as acting loads are not changed. Each modified structure matches with a load k multiplier, and each value *k* is associated to a set of three hyperstatic unknown, to fit the actual reacting configuration of the arch, so that the funicular polygon may fit into the arch thickness. Such a study is then an useful and interesting way to develop new theories based on both load funicular shapes and changed thicknesses deriving from Heyman approach. In brief, Figure 4 reports the iterative procedures for a modified structure calculation, where tensile zones narrow at each step.

As suggested at the end of the procedures, the X_i triad results to be compatible, which means that X_i values may be used as a starting point for further stone arches, such as the one suggested by Franciosi *et al.* (1986), where tensions sharing process is not reproduced, whereas wedge distorsions are applied.

Employing the process shown in Figure 4, a computational approach may lead to obtain the crisis multiplier, by simple adapting the procedures to directly provide the non-linear trend of function $k-\sigma_{\min}$. In fact, it is easy to extend the process depicted in Figure 4 to higher values of multiplier k, as long as the crisis multiplier is determined and trend shown in Figure 5 is obtained. Numerical examples later discussed will demonstrate that increasing values of k produce increasing reduction of arch thicknesses, to which an increase in compression stress may be associated. At most, by following Heyman's hypotheses, a stress limit $\sigma_0'' \to -\infty$ may be admitted, which happens to be an impossible situation to be likely to happen, leading to a vertical asymptote coinciding with structure failure k value, as computed by Heyman (1966,1969).

These procedures allow to operate even when multiplers factor reach out to crisis values, and guarantee moderate time consumption in calculations.

3 Numerical results

3.1 A well-known example: Saint-Martin Bridge arch

The well known arch of Saint-Martin Bridge upon Lys arch is now examined. Its span is *L=31.4 m*, whereas its rise is *f=11.4 m*, already studied in the past by the author with other researchers in a work to which readers shall refer for geometrical and loading configurations (1982). Unlike the study here quoted, in this work, deformation matrix is taken into account, by calculating integrals through variable-sampling-point Gaussian method. This allows to decrease the discretization interval, resulting into a reduction of operative time. Unlike Franciosi *et al.* (1982) results, here the numerical solution will prove to converge even with a poor number of structural partitions. By following the flow chart in Figure 4, compatible triads X_i were determined, and their corresponding growing parameters *k*.

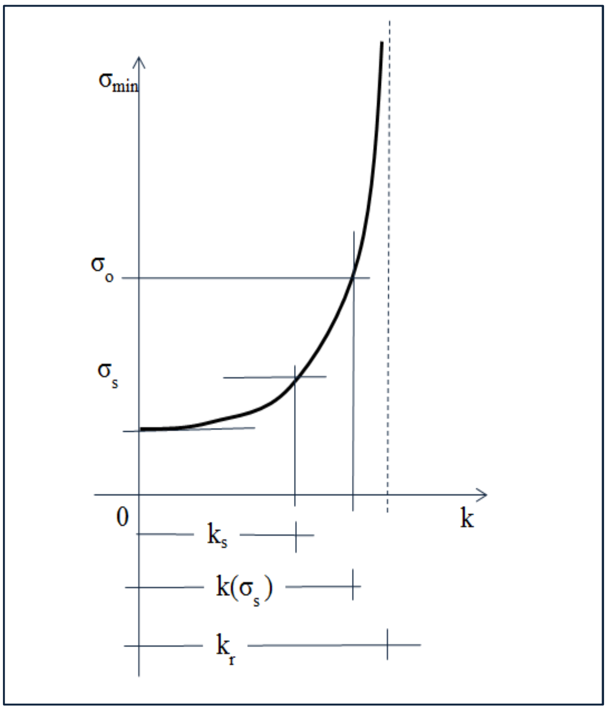

Fig. 5 - Graph $k - \sigma_{\min}$.

In Figure 6 reduced thicknesses for a 80-segment structure discretization are plotted. Automatic calculations produce collapse multiplier value kr=0,1405 , to which a vertical asymptote corresponds to $k \rightarrow \sigma_{\min}$.

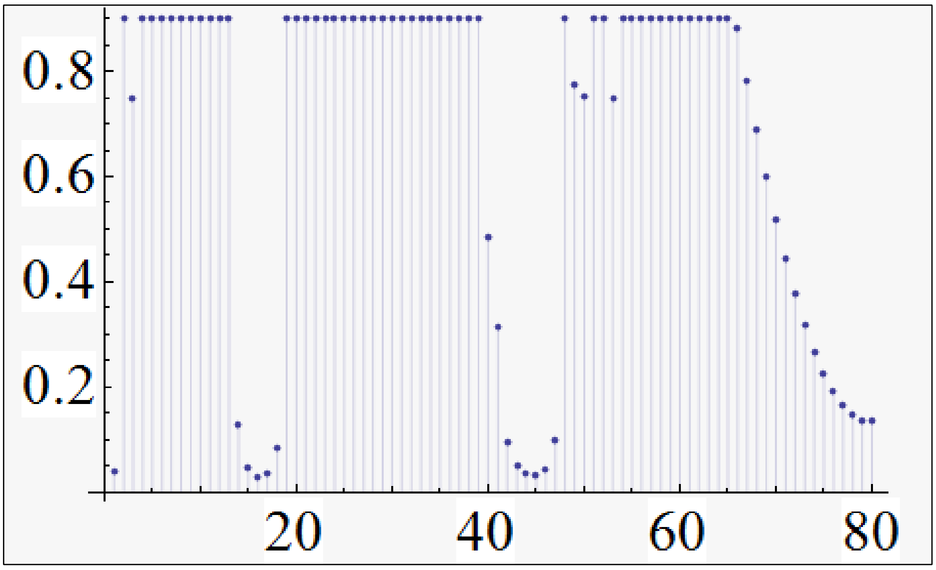

Fig. 6 - Reduced arc reagent thicknesses t=80; k=0,1405.

On the other hand, Table I reports top compressive stress values, compatible hyperstatic unknown quantities triads and minimum-thickness reacting section, as a function of loads multipliers. When k is poor, that's to say loads being due to weight only, it may be sensibly assumed that the arch had been specifically shaped in order to include the loading funicular, as well as the structure showing a poor sharing concentrated in several sections.

A particular issue shall be pointed out: such a circumstance does not avoid the reacting structure sharing, which, at the end of the cycle, results to be modified. In fact, being k=0, minimum thickness drops down from 0.9 to 0.6039 m, in several arch sections. Figure 7 plots the trend of $k \to \sigma_{\min}$ chart.

Table 1. Maximum Compression, minimum thicknesses for *k* increasing.

k	σmin [t/m^2]	X$_1$ [t m]	X$_2$ [t m]	X$_3$ [t m]	Hmin [m]
0	231,573	19,9166	-8,3740	-19,9166	0,6039
0,01	257,869	21,4096	-8,3400	18,3002	0,5390
0,02	285,793	22,6337	-8,4099	-16,5529	0,4778
0,03	319,664	23,7702	-8,5685	-14,7372	0,4220
0,04	355,488	24,6819	-8,8097	-12,4011	0,3751
0,05	393,196	25,4692	-9,1593	-9,8909	0,3354
0,055	412,341	25,8982	-9,3239	-8,6363	0,3180
0,06	452,476	26,2890	-9,5076	-7,1721	0,2881
0,065	478,905	26,5826	-9,7197	-5,5713	0,2706
0,07	514,089	26,9271	-9,9369	-3,9914	0,2506
0,08	589,493	27,5450	-10,3950	-0,4087	0,2161
0,09	681,229	28,0023	-10,9037	3,8447	0,1851
0,1	774,736	28,3365	-11,4522	8,8401	0,1611
0,11	923,298	28,7079	-11,9822	14,0570	0,1338
0,12	1154,660	29,0987	-12,5210	19,2813	0,1059
0,13	1599,150	29,5269	-13,0520	24,4584	0,0757
0,135	2034,120	29,7655	-13,3084	26,9977	0,0542
0,1405	3095,940	30,1020	-13,6092	30,0147	0,0294

Readers may easily notice that progressive reduction of the reacting cross section thickness may lead, at last, to completely determine the plastic hinge positions, due to which failure mechanics arise, once opening hinges position is known, limit design method produces the value of collapse multiplier, as a result of Heyman geometrical solution*; k=0.141*. This slight difference is mainly due to approximations adopted in these two methods. Credit shall then be given to the homogenous technique here introduced, for its remarkable computational stability, so that it should be preferred to Heyman geometrical-based procedures.

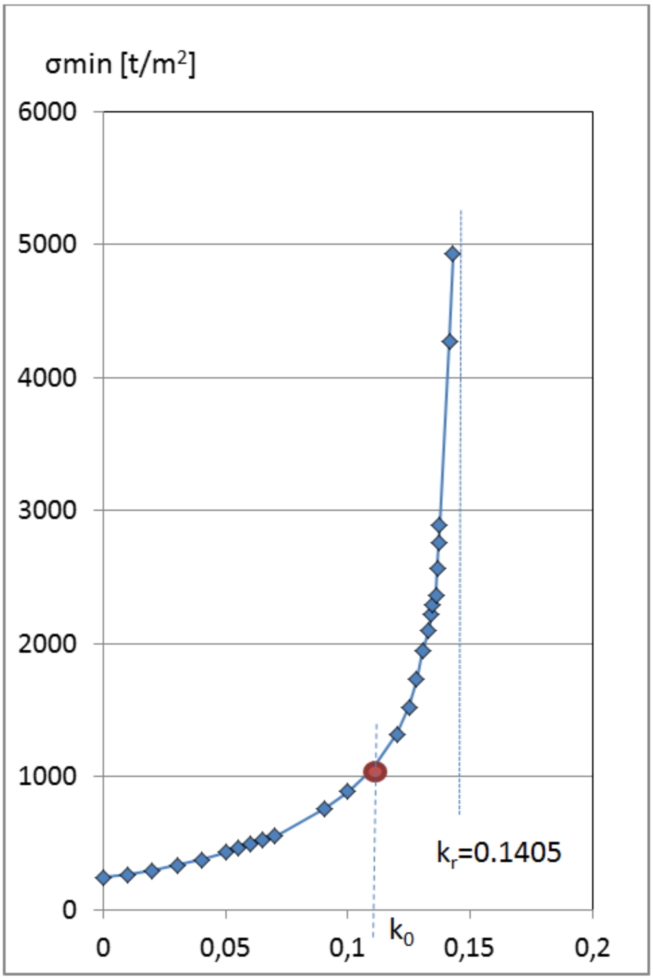

Fig. 7 – Graph $k \rightarrow \sigma_{\min}$; Saint Martin bridge.

3.2 Reinforcement technique

Franciosi *et al.* (1982) also analyze stone arch behavior in case of chains employment in a structural intervention, where structure sharing needs to be reduced. As exhaustively exposed, in seismic conditions, potential introduction of chains produces numerous benefits to the structure, and its elements. Obviously, such interventions are appreciated towards action which affect the arch-spirnger set, capable of interfering with failure mechanics, which tend to modify tie rods application points reciprocal displacements. In brief, due to the seism, chains do not modify the arch structural problem, but their presence affects springers behavior, on which their horizontal actions are applied.

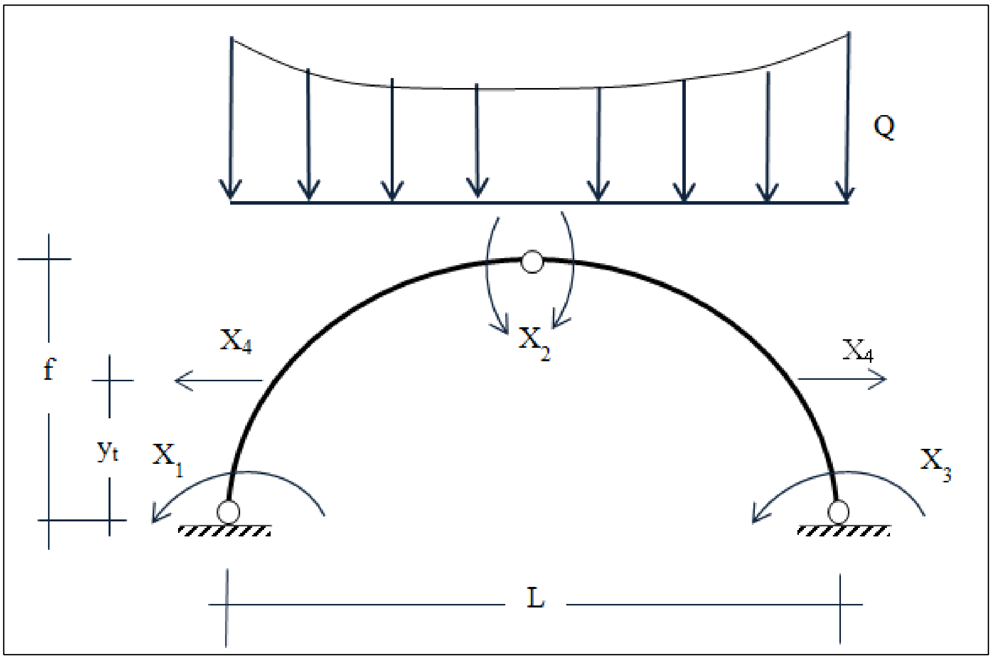

Fig. 8 - The reinforced structure; calculation scheme.

On the other hand, issued shall be considered about wheel ropes, placed in several spots of the arch and suitably fixed. In this case, springers effect is beneficial, as it increases failure multipliers for seismic cases only.

Despite neglecting merely technical issues, exhaustively discussed by Molise Region (2002), the behavior of an arch structure may anyway be analyzed, such as in Figure 8. Therein, the structural behavior of arch the rods is conceived as a result of springers actions concentrated in two different section, at height $y_t = a\,f$, being f the arch rise.

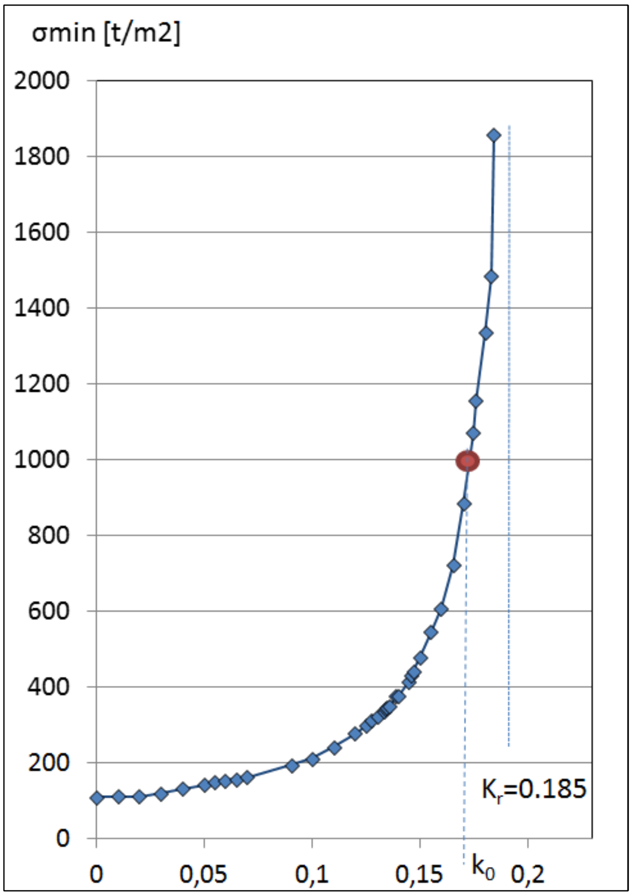

Fig. 9 – Graph $k \rightarrow \sigma_{\min}$.

By studying the same roman Saint-Martin Bridge, compatible hyperstatic unknown quantities were determined, wheel ropes being assumed to be placed on the arch haunches, X_i (i=1..4) being *a=1/3*. A remarkable increase may be noticed in failure multiplier, from k_r*=0,1405* in an unchained structure, to k_r*=0.185* that corresponds to the tie rod placing; Figure 9.

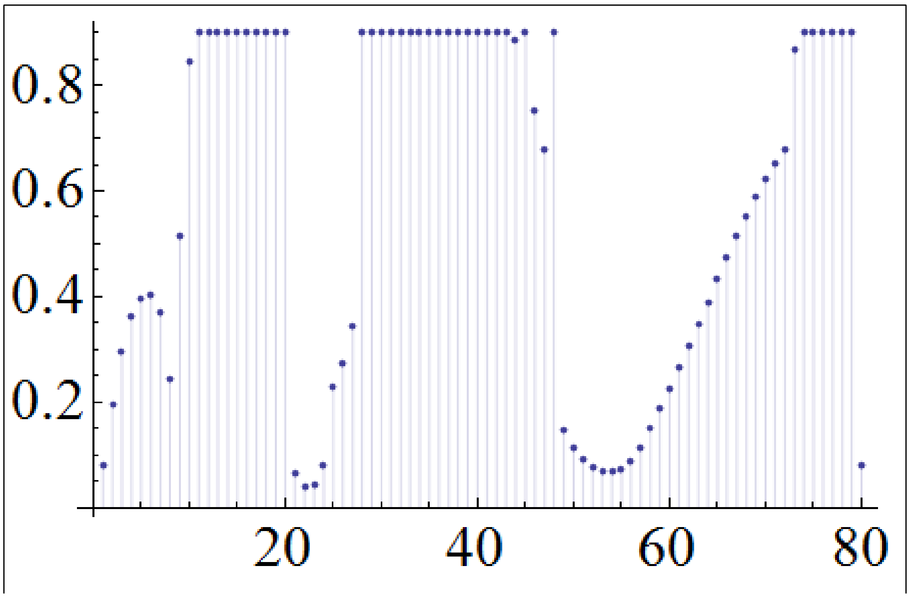

Fig. 10 - Reduced arch reagent thicknesses, t=80; k=0,185.

Except two opening hinges, the other two opening displace towards springers position, close to sections 23-25 and 50-55, Figure 10. Knowing opening hinges position allows to calculate kinetically admissible multiplier, according to Heyman's method.

4 Conclusions

Procedures here suggested seem to be preferable to different methods, especially since they employ valid processes and results in elastic regime. In fact, through successive iterations, arch structure is monitored until hinge formation, on which failure mechanics are based. Computationally speaking, stone arch homogenization technique enjoys numerous advantages if compared to usual failure calculation methods, since trial-and-error plastic hinges positioning is here avoided. At the same time, unlike "cunei" method suggested by Franciosi *et al.* (1986), according to the method here proposed, compatible hyperstatic unknown quantities do not represent a starting point in calculations. Moreover, as for deformation matrix calculation, on which the iterative method is based, the author esteems an original innovations lies in making up with a symbolic calculation program, which fully capitalizes Gaussian integration potential, in order to utterly reduce the structure discretization.

References

1. Albenga,G. (1953) *I ponti, la pratica*, pp. 99-173, UTET.
2. Auciello N.M., Ercolano A. (1997). Numerical simulation of masonry panels. *Engineering Transactions*, vol. 45 (*3-4*), pp. 375-394.
3. Auciello, N.M., De Rosa, M.A. (1985). Le variazioni termiche negli archi in muratura, *Atti Accademia Pontaniana*, Napoli, vol. 33, pp. 175-188.
4. Briccoli Bati, S. Paradiso M., and Tempesta, G. (1997). Archi in muratura soggetti a carichi e cedimenti delle imposte. *Costruire in Laterizio*, vol. 60, pp. 436-443.
5. Bridle, R.J., Hughes, T.G. (1990). An energy method for arch bridge analysis. Proceedings of the Institution of Civil Engineers, 89 (*3*), 375-385.
6. Castigliano, C.A. (1879). Theorie de l'equilibre des systems elastiques et ses applications. Torino, Italy: A.F. Negri, ed.
7. Cavicchi, A. (2004). Analisi limite agli elementi finiti di archi murari interagenti con il riempimento per la valutazione della capacità portante di ponti in muratura. Ph.D. thesis. *Department of Structural and Geotechnical Engineering, University of Genova, Italy.*
8. Cavicchi, A., Gambarotta, L. (2005). Collapse analysis of masonry bridges taking into account arch–fill interaction. *Engineering Structures,* vol. 27 (*4*), pp. 605–615.
9. Dejong, M., Ochsendorf, J.A. (2006). Analysis of vaulted masonry structures subjected to horizontal ground motion. In: *Structural Analysis of Historical Constructions*, P.B. Lourenço, P. Roca, C. Modena, S. Agrawal (eds.), vol. 2, New-Dehli.
10. Franciosi, V. (1980). Calcolo a rottura di strutture con materiale alla Coulomb. *Corso di istruzione permanente, Calcolo a rottura delle Strutture, Politecnico di Milano*.
11. Franciosi, V. (1980). L'attrito nel calcolo a rottura delle murature. *Giornale del Genio Civile*, vol. 8, pp. 215-234.
12. Franciosi, V. (1986). Su alcune questioni riguardanti la stabilità delle strutture lapidee monodimensionali. *Atti Accademia Pontaniana*, vol. XXXIV, pp. 205-253.
13. Franciosi, V., Auciello, N.M., De Rosa, M.A. (1982). Il procedimento delle tensioni ammissibili nella verifica degli archi e delle volte in muratura in zona sismica. *Autostrade*, vol. 9, pp. 35-47.

14. Franciosi, V., Auciello, N.M., De Rosa, M.A. (1986). L'uso sistematico delle distorsioni a cuneo; calcolo di stabilità e restauro conservativo. *Autostrade*, vol. 9, pp. 28-36.
15. Franciosi, V., Belli, P. (1981). La verifica, sotto sisma, delle strutture in muratura in presenza di attrito. *Convegno di Ingegneria Sismica in Italia*, Udine, May 29-31, CISM Courses and Lectures n. 271, Springer Verlag.
16. Heyman, J. (1966). The stone skeleton. *International Journal of Solids and Structures*, vol. 2 (*2*), pp. 249-279.
17. Baker J, Heyman J. (1969) Plastic Design of Frames. Applications. vol. 2. Cambridge University Press: Cambridge.
18. Heyman, J. (1969). The safety of masonry arches. *International Journal of Mechanical Sciences*, vol. 11 (*4*), pp. 363-385.
19. Hughes, T.G., Blackler, M.J. (1997). A review of the UK masonry arch assessment methods. *Proceedings of the Institution of Civil Engineers. Structures and buildings*, 122 (*3*), 305-315.
20. Ochsendorf, J.A. (2002). Collapse of masonry structures. Ph.D. dissertation, *Department of Engineering*, Cambridge University.
21. Ochsendorf, J.A. (2006). The Masonry Arch on Spreading Supports. *The Structural Engineer*, vol. 84 (*2*), pp. 29-36.
22. REGIONE MOLISE, L.R. Legge del 27 Dicembre 2002 n.286, Protocollo di Progettazione per la Realizzazione degli Interventi di Ricostruzione - EDIFICI IN MURATURA - Post-Sisma sugli Edifici Privati - Aggiornamento Marzo 2012.
23. Romano, G., Sacco, E. (1984). Materiali non resistenti a trazione equazioni costitutive e metodi di calcolo. Istituto di Scienza delle Costruzioni, Università di Napoli, Pubblicazione N. 350, Liguori Editore.
24. Smars, P. (2008). Influence of friction and tensile resistance on the stability of masonry arches, *Proceedings of the 6th International Conference on Structural Analysis of Historic Construction,* D. D'Ayala and E. Fodde, eds., Bath (UK), pp. 1199-1206.
25. Wolfram, S. (2014). Mathematica 10 version, *Wolfram Research.*

Appendix A

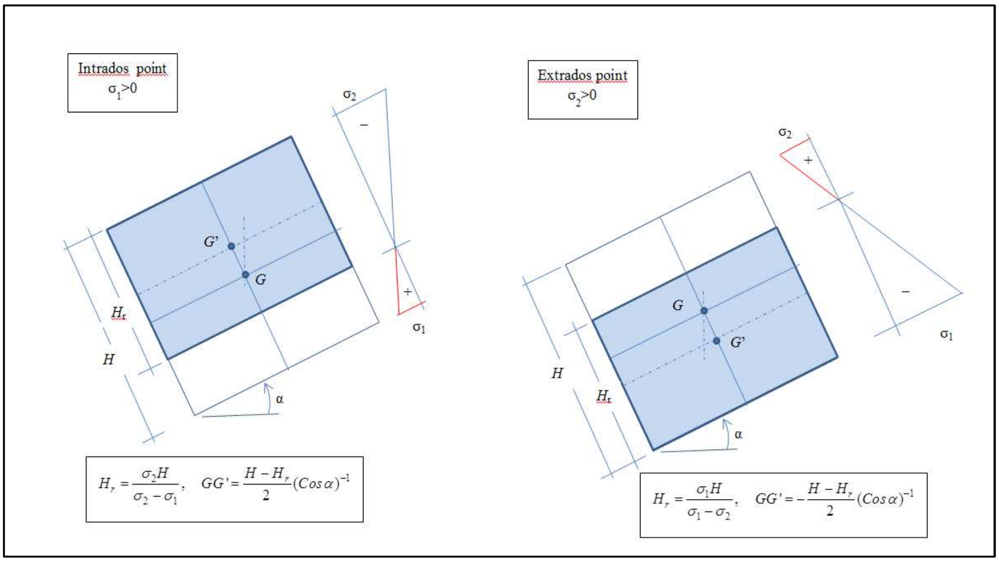

$$H_r = \frac{\sigma_2 H}{\sigma_2 - \sigma_1}, \quad GG' = \frac{H - H_r}{2}(Cos\,\alpha)^{-1}$$

$$H_r = \frac{\sigma_1 H}{\sigma_1 - \sigma_2}, \quad GG' = -\frac{H - H_r}{2}(Cos\,\alpha)^{-1}$$

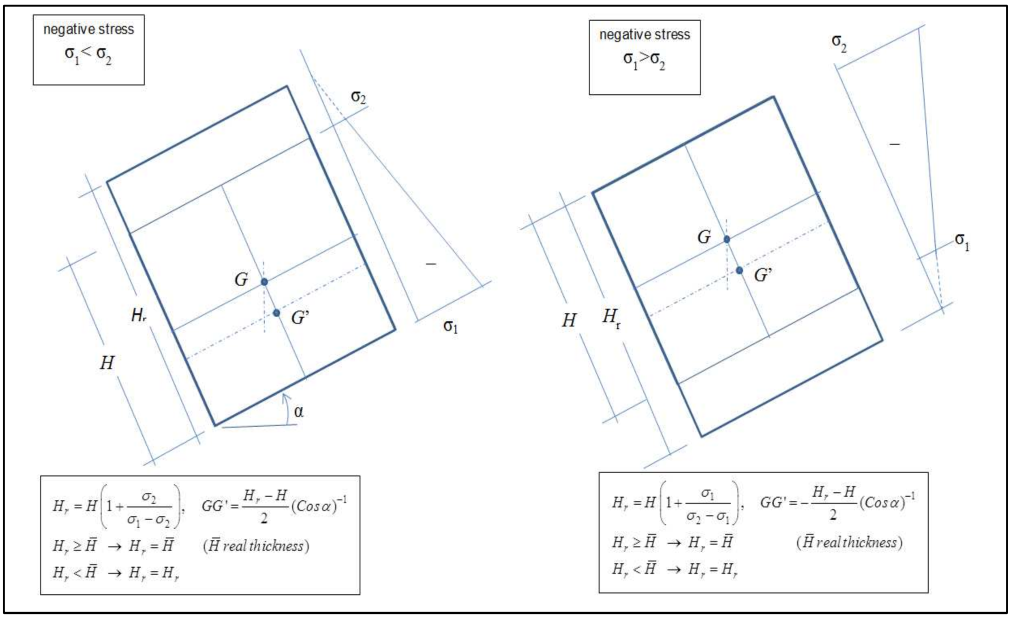

$$H_r = H\left(1 + \frac{\sigma_2}{\sigma_1 - \sigma_2}\right), \quad GG' = \frac{H_r - H}{2}(Cos\,\alpha)^{-1}$$

$$H_r \geq \bar{H} \ \rightarrow \ H_r = \bar{H} \qquad (\bar{H}\ real\ thickness)$$

$$H_r < \bar{H} \ \rightarrow \ H_r = H_r$$

$$H_r = H\left(1 + \frac{\sigma_1}{\sigma_2 - \sigma_1}\right), \quad GG' = -\frac{H_r - H}{2}(Cos\,\alpha)^{-1}$$

$$H_r \geq \bar{H} \ \rightarrow \ H_r = \bar{H} \qquad (\bar{H}\ real\ thickness)$$

$$H_r < \bar{H} \ \rightarrow \ H_r = H_r$$

The spandrel of masonry buildings: experimental tests and numerical analysis

Bruno Calderoni[1], Emilia Angela Cordasco[1], Gaetana Pacella[1], Paolo Simoniello[1]

[1] Università degli Studi di Napoli "Federico II",
80125 Napoli (NA), Italy
calderon@unina.it; emilia.cordasco@gmail.com;
pacellagaetana@gmail.com; ing.paolosimoniello@gmail.com;

Abstract: The interest of the scientific community for the seismic behavior of existing masonry buildings is continuously increasing in recent years. Initially it was directed mainly to the performance of masonry piers. The analysis of seismic damage, together with the development of nonlinear techniques, has led researchers to investigate the behavior of spandrels too. In recent years the authors have analyzed the structural behavior of spandrels in URM buildings by means of several experimental tests performed on specimens in reduced scale, made of different typologies of masonry or homogenous material. The results of this experimental campaign, carried out on both rectangular-shaped and H-shaped specimens, are reported in this paper. The different failure mechanisms and the different deformation capacities of the spandrels, strongly dependent on the slenderness ratio of the panel are highlighted too and compared with the results of several experimental tests on full scale masonry spandrels available in literature. The key-data and the set-up of the tests, the criteria adopted for testing and the results obtained are discussed, in order to underline their effectiveness in defining a theoretical interpretation of the actual mechanical behavior of spandrels in masonry buildings subjected to seismic actions. Then, some of the tests have been simulated by means of very refined FE models. The comparison between experimental and numerical results shows sensible variation depending on the material modeling and the geometrical properties of the panels.

Keywords: masonry building; spandrel; seismic behaviour; masonry shear strength; masonry tensile strength; non-linear FE analysis

1 Introduction

The seismic capacity of unreinforced masonry buildings is closely related to strength and deformability of the walls in their own plane whether they are effectively connected to the floor at each storey. Therefore, the structural characteristics of masonry spandrels and piers significantly influence the wall behavior. More specifically the spandrels play an important role in both resistance and deformability of the wall. Furthermore they may present different typological configurations with very different mechanical behavior. Indeed at least three classes of structural typologies can be defined for masonry spandrels: "weak spandrel"; "truss spandrel" and "beam spandrel" (Calderoni *et al.* 2007a). It has been already demonstrated that seismic vulnerability of existing masonry buildings is strongly influenced by the typology of spandrels (Calderoni *et al.* 2007a). Nevertheless, neither Italian nor International seismic codes (NTC08, EC8, FEMA 356, etc.) are sufficiently detailed with reference to both resistance and deformation of the spandrels. Furthermore, few experimental studies have been developed on this topic until now (Calderoni *et al.* 2008, Calderoni *et al.* 2010, Dazio and Beyer 2010, Gattesco *et al.* 2008, Graziotti *et al.* 2011, Parisi *et al.* 2010) and they refer to just a few of the possible structural typologies. In the recent past the authors have carried out an extensive experimental campaign on scaled-down spandrel specimens, simulating the "truss spandrel" typology and characterized by different slenderness and wall textures. The test results have shown different collapse mechanisms, shear strength and deformation capacities, depending on both slenderness ratio and material typology. Rectangular-shaped specimens, confined by the two rigid steel arms of the testing equipment, which simulate the very large stiffness of the masonry panel zone, have been tested. To investigate the influence of the deformability of the masonry panel zone on spandrel behaviour, H-shaped specimens, formed by a spandrel and part of the two adjacent piers, have been also tested. It is worth noting that the reduced scale can limit research field to some degree, as it is impossible to apply rigorous geometrical and mechanical similitude, particularly with regard to the thickness of the mortar joints. However, qualitative appraisal of the phenomenon is surely correct, while quantitative evaluation is possible to some extent making comparisons among the tested specimens. At present full-scale tests on masonry spandrels available in literature are very few in number, confirming the difficulties correlated to this kind of experimental activity. From the theoretical point of view, the behaviour of masonry piers and walls under seismic action has been extensively analyzed in the past, starting from the

'80s (Calderoni *et al.* 1984, Como & Grimaldi 1983). On the contrary, the structural behaviour of masonry spandrels has been investigated since only few years by a limited number of researchers (Corrêa *et al.* 2006, Betti *et al.* 2008, Cattari *et al.* 2008, Calderoni *et al.* 2007b, 2011, Milani *et al.* 2009; Beyer 2012; Rinaldin *et al.* 2014; Beyer and Mangalathu, 2014). The available theoretical models have been in general developed without a general approach to the problem, that appears very difficult to be stated because of the many different typologies of spandrels and masonry, which can be found in existing ancient masonry buildings particularly. Moreover the complex behavior of the masonry material, that involves a very low tensile strength, has enforced many authors to develop theoretical outcomes making direct reference to the results of their own experimental tests.

A review of the experimental tests performed by different researchers, including that by the authors, is presented and discussed in this paper, in order to underline the problems related to the behaviour of masonry spandrels in building subjected to horizontal loads. Furthermore a numerical sensitive analysis, taking into account different material models and yield criteria, is presented for some of the tests. The comparison between exp. and numerical findings demonstrates the difficulties in performing tests suitable to identify the actual behavior of the spandrels. Moreover the uncertainness and the limited reliability of FEM analyses performed on “complex” materials, like masonry, (often) without a deep knowledge of all the aspect of the problem to be analyzed, are shown and discussed in this paper.

2 Authors’ experimental activity on scaled-down specimens

2.1 Experimental tests on rectangular specimens

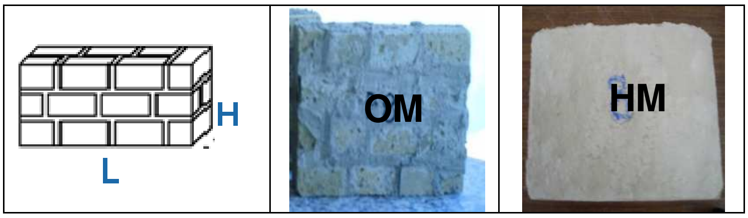

Fig. 1 - Scheme of specimen and picture of the two different specimens considered

Experimental tests have been carried out on scaled-down masonry spandrels (1:10), made up adopting different tuff masonry arrangements, typical of the Naples area (in Italy). Although the set of the tests performed by the authors is larger, for the scope of the paper the attention is focused only on the tests performed on specimens (named OM) made by ordinary masonry and the ones (named HM) made by mortar only, a homogeneous material characterized by low tensile strength (Figure 1).

All the specimens tested had the same length (L = 14 cm) and thickness (4.5 cm) but a different height (H), in order to obtain three different slenderness ratios (H/L): 0.5 (slender spandrels), 0.7 (intermediate spandrels), 1.07 (stocky spandrels).

The mechanical properties of the used material (reported in Table 1) have been experimentally obtained. In particular the compressive strength (f_h), for both OM and HM, and the tensile strength (f_t) for mortar only have been determined. The tensile strength of masonry material (OM) was not obtained by testing, but it has been assigned on the basis of literature data and considerations on the results obtained by the tests.

The samples were tested using a purposely-designed equipment, arranged to reproduce the behaviour of the "truss-spandrel" typology in a displacement controlled test (Calderoni *et al.* 2010, 2011).

Table 1. Mechanical properties of rectangular specimens [N/mm^2]

Ordinary Masonry		**Homogeneous Materials**	
f_h	f_t	f_h	f_t
2.50	0.092	4.30	0.43

The collapse mechanisms exhibited by the specimens, monotonically loaded, were quite different, depending on both slenderness ratio and masonry typology, as shown in Figure 2a. In the same picture the corresponding V-γ curves, being V the shear force acting at the end section of the spandrel and γ the chord rotation (shear deformation), are represented. More in details, OM specimens showed horizontal sliding at the interface between mortar joints and tuff stones for the slender spandrels, diagonal tensile cracking for the stocky spandrels and a sort of mixed failure for the intermediate spandrels. Mortar samples (HM) showed diagonal tensile cracking for both stocky and intermediate panels, while toe-crushing occurred at the edges of the panel for the slender ones.

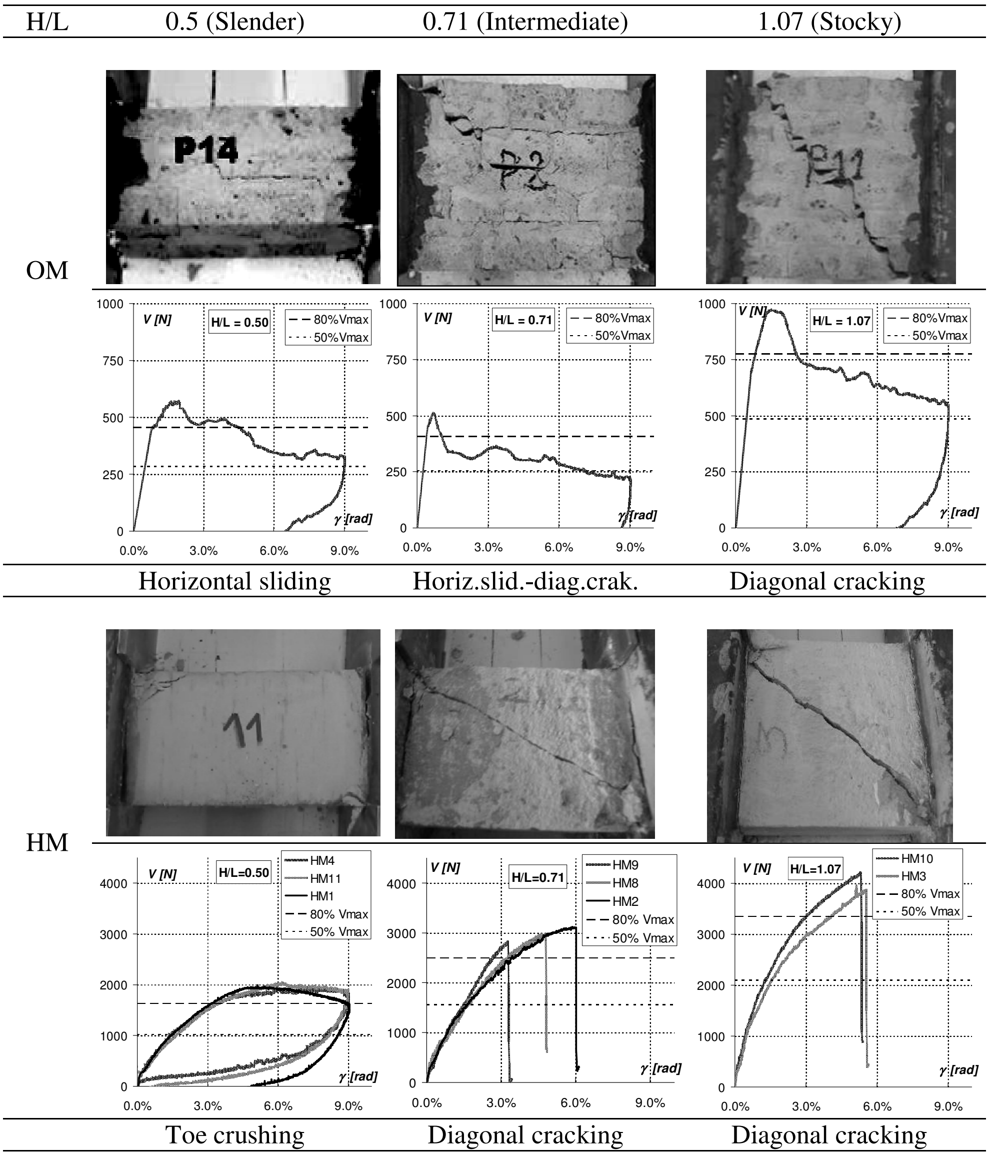

Fig. 2a - Collapse mechanism and deformation behaviour of tested spandrels

Finally the tested specimens showed a far from negligible deformation capacity in the post-elastic field, even if strongly connected with the collapse mechanism. Toe-crushing mechanism were characterized by a very ductile behavior. Horizontal sliding showed a reasonable deformation capacity, even if accompanied by some resistance reduction. On the contrary, diagonal cracking was related to a significant resistance reduction with a significant deformation capacity for masonry spandrels (OM) and to a sudden loss of resistance with a very brittle failure for HM spandrels (see V-γ curves in Figure 2a).

The different behaviors observed demonstrate that deformation and dissipative capacities of masonry are certainly related to the arrangement of stone blocks and also to the phenomena associated with their relative displacements at failure (interlocking, friction, etc.).

The significant differences in the collapse mechanism, deformation capacity and resistance level, highlighted the strong influence of both geometrical slenderness and masonry texture on spandrel structural behavior.

2.2 Experimental tests on H-shaped specimens

The experimental activity on rectangular specimens has evidenced some aspects:

a) the panel node was not a masonry element;
b) the surface between specimen and node was perfectly smooth;
c) the length of the effective (compressed) zone at the edges of the panel was not evident on the sample (Calderoni *et al.* 2011).

For these reasons enlarged H-shaped specimens, which include also part of the panel zone, have been tested (Calderoni *et al.* 2012, 2014). In this kind of specimens the cracking at the edges of the spandrel can also interest the masonry, so to evidence better the compressed zone.

Again the specimens (1:10 scaled down) were made of both homogeneous materials (HMH) and ordinary masonry (OMHA)) with three different slenderness of the spandrel (H/L=0.47, H/L=0.63, H/L=0.97). The mechanical properties of material are shown in Table 2, while pictures of the specimens are reported in Figure 2b.

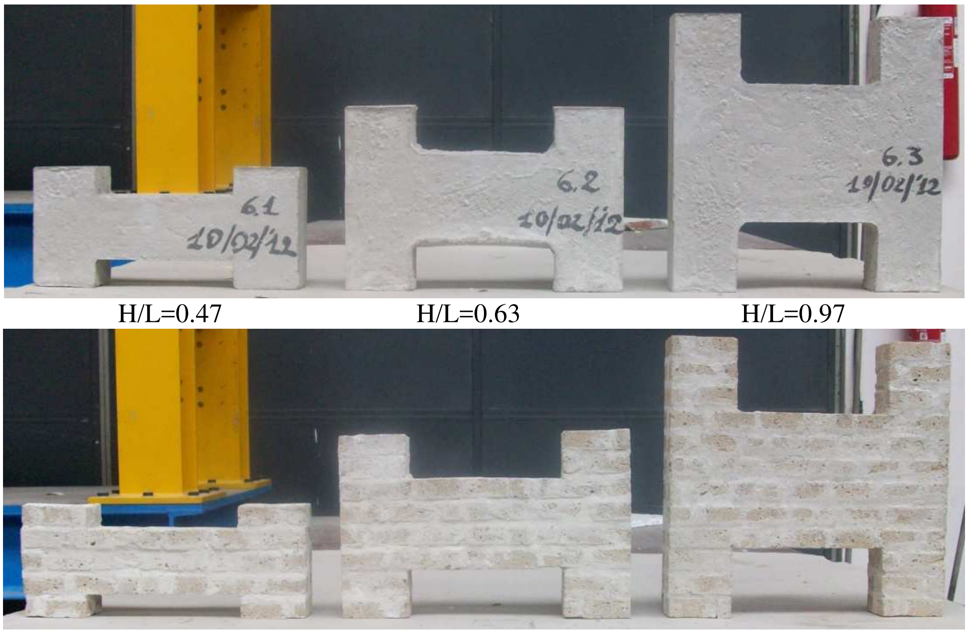

Fig. 2b - H-shaped specimens in homogeneous materials and ordinary masonry

When the first load was applied to the HMH specimen a partial separation (with an almost vertical crack) occurred at the interface between the spandrel and the node panel, so evidencing the effective compressed zone at the edges of the panel, which can be considered the end section of an active diagonal strut. This zone remains practically unchanged with increasing load (Figure 3). The failure mechanisms shown by the spandrels and the corresponding V-γ curves are reported in Figures 4 and 5 (respectively for OMHA and HMH samples).

When the first load was applied to the HMH specimen a partial separation (with an almost vertical crack) occurred at the interface between spandrel

Table 2. Mechanical properties of H-shaped specimens[N/mm^2]

Ordinary Masonry (OMH)		**Homogeneous Materials (HMH)**	
f_h	f_t	f_h	f_t
2.70	0.10	7.70	0.77

and node panel, so evidencing the effective compressed zone at the edges of the panel, which can be considered the end section of an active diagonal strut. This zone remains practically unchanged with increasing load (Figure 3).

The failure mechanisms shown by the spandrels and the corresponding V-γ curves are reported in Figures 4 and 5 (respectively for HMH and OMHA samples).

As the test went on, the crack pattern developed differently, depending on the slenderness ratio of the panel. The slender spandrels showed toe-crushing at both ends of the strut, with a quite good ductile behaviour. Nevertheless, in two cases diagonal cracking caused the final collapse, even if it occurred at a considerably large deformation ($\gamma = 8.3\%$).

The stocky spandrels showed a sudden and brittle failure: the fatal diagonal crack occurred at a lower level of deformation ($\gamma \approx 4.0\%$).

The intermediate spandrels showed an "intermediate" behaviour, characterized by toe-crushing at the edges, a ductile branch after the attainment of the maximum resistance capacity, followed by a brittle collapse due to diagonal cracking, which occurred at a significant deformation level ($\gamma \approx 7\%$).

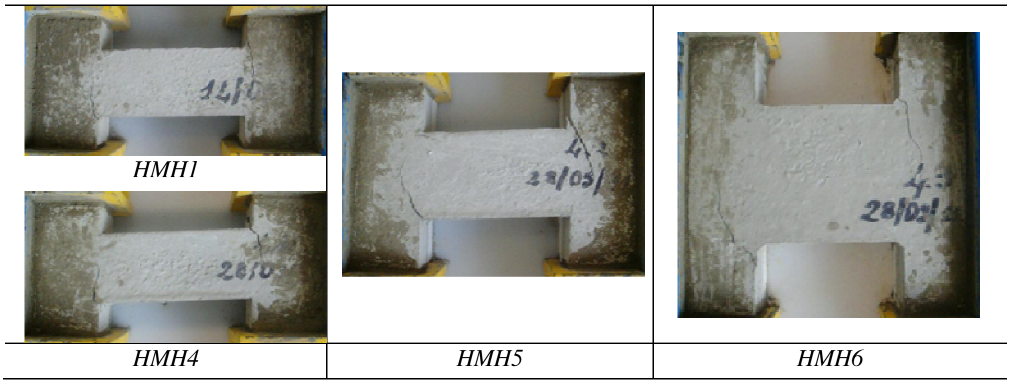

HMH1

HMH4

HMH5

HMH6

Fig. 3 - Homogeneous material spandrels (HMH): first crack patterns

Finally it can be observed that the collapse typologies shown by specimens, if related to the slenderness ratio of the spandrel, confirmed the results obtained by the tests on rectangular panels. The only significant difference is the evidence of the vertical cracks at the panel edges, extended inside the nodal panels: therefore the actual "static" slenderness ratio (H/L) of the spandrel is lower than the one corresponding to its pure geometry (the spandrel results more slender).

Also for the OMHA samples, as the load was applied to the specimens, vertical cracks arose between spandrel and node panels. The cracks developed along the mortar joint in some cases, or passed through the tuff blocks in other cases.

Differently from the HMH specimens, the cracks were limited to one masonry row only, both in the upper and in the bottom part of the spandrel. This means that the nodal panels give a contribution to the spandrel behaviour more significant than in the HMH cases, depending on the masonry texture and the assembling of the stone units.

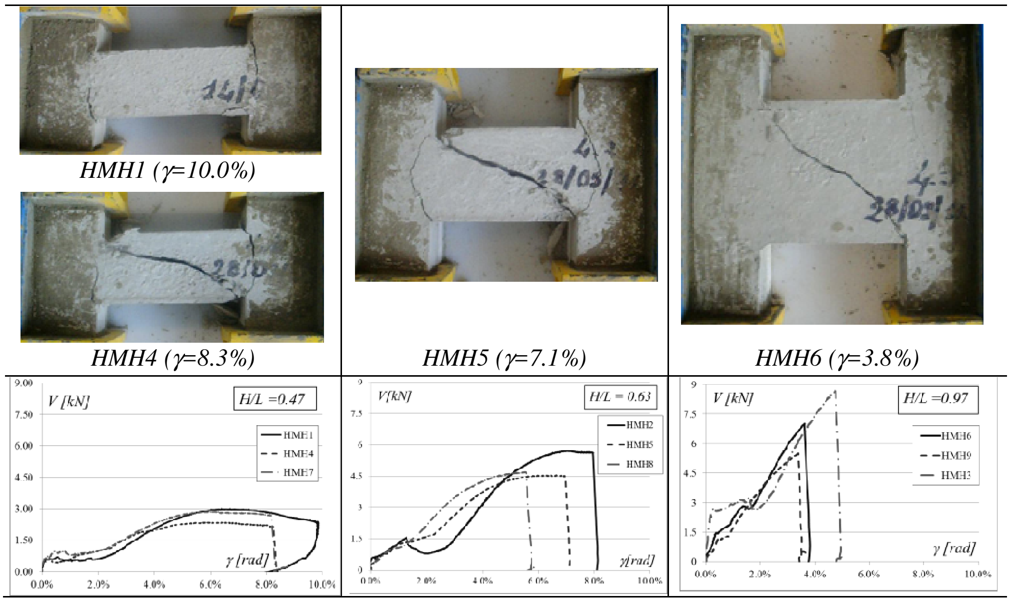
HMH1 (γ=10.0%)

HMH4 (γ=8.3%)

HMH5 (γ=7.1%)

HMH6 (γ=3.8%)

Fig. 4 - Spandrels in homogeneous material (HMH): failure mechanism and V-γ diagrams

It is confirmed that the actual slenderness ratio (H/L) of the spandrel is lower than the geometric one, even more that evaluated for spandrels in homogenous material.

The OMHA specimens showed a shear failure characterized by different crack patterns and evolution related to the slenderness ratio of the panel. In all cases the cracks formed initially in the central part of the panel and spread towards the corners as load increased, developing essentially in the mortar joints between the blocks.

The slender spandrels showed horizontal sliding between the block rows, while the stocky ones showed diagonal cracking widespread in the central part of the panel. The intermediate spandrels highlighted a sort of mixed failure, showing both horizontal sliding and diagonal cracking.

It is worth to notice that the tested OMHA spandrels never showed a brittle failure up to the very high deformation level reached in the test (10-20%). The stocky panels too experienced a very good deformation capacity in the post-elastic field, differently from the rectangular specimens.

In each curve three different branches can be observed: the first one corresponds to the elastic behaviour up to the formation of the cracks between spandrel and node, which is correlated to the low (but greater than 0) tensile resistance of masonry; the second one corresponds to the behaviour of a diagonal strut, up to the formation of cracks within the strut,

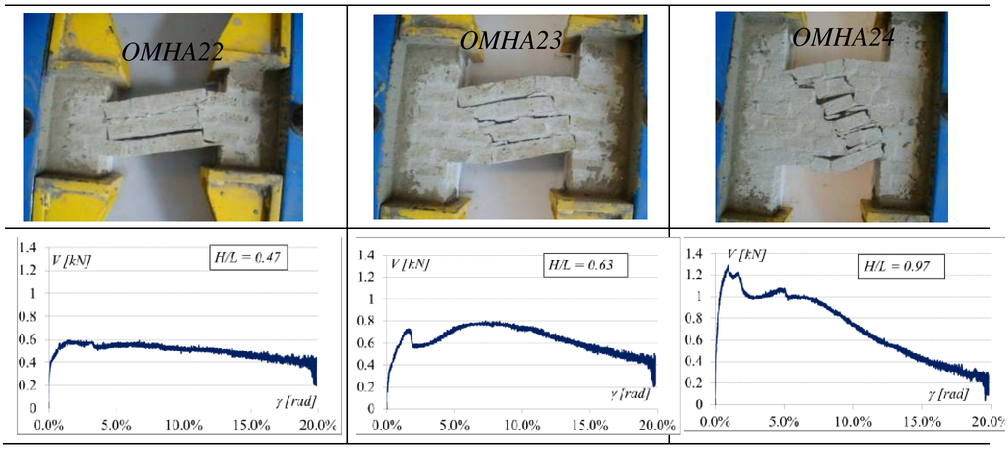

Fig. 5 - Spandrels in ordinary masonry (OMHA): failure mechanism and V-γ diagrams

when a sudden (but limited) reduction of resistance occurs; the third one represents the totally plastic behaviour of the cracked panel, which is able to hold the shear force without appreciable reduction of resistance up to high deformation level (γ=10% for slender and intermediate spandrels; γ= 5% for stocky panels). The decreasing branch shows a not negligible (but uniform) slope, which leads to the loss of resistance capacity when γ= 20% is reached, only for the stocky specimens.

3. Experimental tests available in literature

Due to the difficulties related to the identification of the actual behavior of masonry spandrels of URM buildings, the availability of a large database of experimental results can be a useful starting point for the development of theoretical models and formulations to evaluate the strength and the deformability of this structural element.
For this reason, in this section, the experimental tests performed on masonry spandrels reported in papers published in the period 2006-2015, are analyzed and classified.
In the following the key-data of the considered experimental campaigns are summarized, while in Table 3 the geometrical properties of the tested spandrels are reported. The corresponding test set-ups are shown in Figures 6 and 7.

Full scale tests:

Beyer et al. - H-shaped specimens:
full brick spandrels (with timber lintel or masonry arch) and hollow brick spandrel (with r.c. lintel). In every test horizontal tie rods were placed, even if applied in different way in each specimen.

Gattesco et al.: H-shaped specimens:
brick masonry spandrels with timber lintel and masonry arch (with or without horizontal tie rod); brick masonry spandrels reinforced with CFRP stripes (with shallow masonry arch); stone masonry spandrels with timber lintel (with or without reinforcing steel angle bars).

Magenes et al.: H-shaped specimens:
stone masonry spandrels with timber lintel, with or without horizontal tie rod; one spandrel without timber lintel and with tie rod. The presence of the tie rod is simulated by applying a horizontal axial stress to the spandrel

Parisi et al.: portal specimens:
tuff masonry specimens with timber lintel and with or without CFRP reinforcements; other specimens with masonry arch with or without r.c. curb. The set set-up reproduce for all specimens the scheme of spandrel with tie rod.

Scaled down 1:2 tests

Vignoli: H-shaped specimens:
single wythe brick masonry spandrels. Four types of specimens with three different aspect ratios were tested: simple masonry, masonry with timber lintel, r.c. lintel and steel chain.

Scaled down 1:10 tests

Calderoni et al.: Rectangular and H-shaped specimens:
rectangular specimens: tuff masonry spandrels in three different textures: ordinary masonry, XVIII cent. masonry, XIX cent. masonry, and homogeneous material (with or without reinforcement in FRP);
H specimens: ordinary tuff masonry panels and homogeneous material panels with or without reinforcement by means of FRP stripes o steel plates. Every test reproduces the scheme of spandrel with tie rod and weak lintel. Three different aspect ratios tested for every spandrel type.

It is worth noting that each research group has performed various tests on dissimilar specimens (often made of distinct material), using different testing-equipment and set-up and adopting different systems for loading the spandrel (in order to attempt to better simulate the actual behaviour of the panel within a masonry wall when subjected to horizontal actions). This depends on the fact that this topic is still not completely understood and there are many different typologies of masonry spandrels, which show different structural behavior. This has been observed in particular in the collapse mechanisms and consequently in shear and flexural resistance and in the deformation capacity. For these reasons the comparisons among different tests performed by distinct researcher groups is not simple and perhaps not at all useful.

Table 3. Geometrical properties of the tested spandrels

Authors	**Dimensions**			**Specimen typology**	**Scale**	**Typology of test**
	L **[cm]**	***H*** **[cm]**	***H/L***			
Beyer *et al.*	118	126	1.07	H-shaped	1:1	Ciclic/Monotonic
	150	105	0.70			
Magenes *et al.*	120	120	1.00	H-shaped	1:1	Ciclic
Gattesco *et al.*	100	120	1.20	H-shaped	1:1	Ciclic
	105	124	1.18			
Augenti *et al.*	170	100	0.59	Portal	1:1	Ciclic/Monotonic
Vignoli *et al.*	60	31.5	0.52	H-shaped	1:2	Ciclic
	60	57.5	0.96			
	60	44.5	0.74			
Calderoni *et al.*	14	7	0.5	H-shaped/ Rectangular	1:10	Ciclic/Monotonic
	14	10	0.7			
	14	15	1.07			

On the other hand the results of each experimental test, if correctly interpreted and analyzed, can be usefully adopted for verifying theoretical hypotheses or findings defined for the specific typology of spandrel corresponding to the tested one.

It is very important to take in mind that it is not possible, at the state of the knowledge in this field, to extrapolate from very few tests, performed necessarily on a specific spandrel typology, general results to be adopted for all the different situations. Many times the results are in fact strongly influenced by the testing conditions and the particularities of the performed tests, so leading easily to wrong interpretations.

It is worth to notice that the large part of the tested spandrels are stocky panels, while in existing buildings slender spandrels are frequent. This is not a detail if one would derive general rules from an experimental campaign, considered that the failure mechanism and the resistance capacity depend directly on the slenderness ratio.

Moreover, in all examined test campaigns almost only cyclic tests have been carried out, with the exception of the ones carried out by Calderoni *et al.*

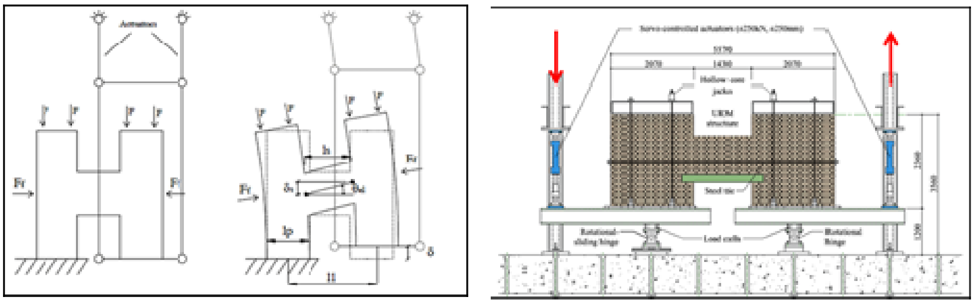

Magenes *et al.* Beyer *et al.*

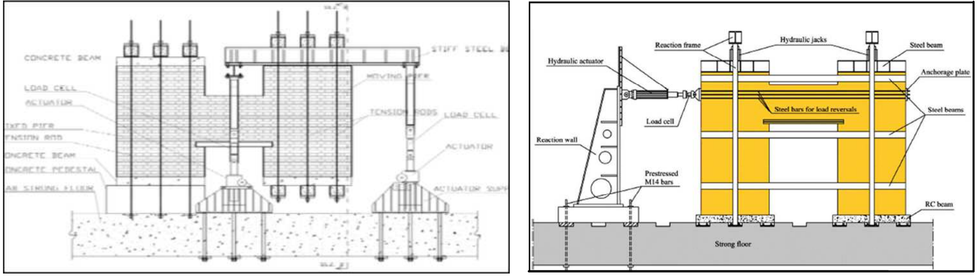

Gattesco *et al.* Augenti *et al.*

Fig. 6 - Test setup for full scale experimental tests

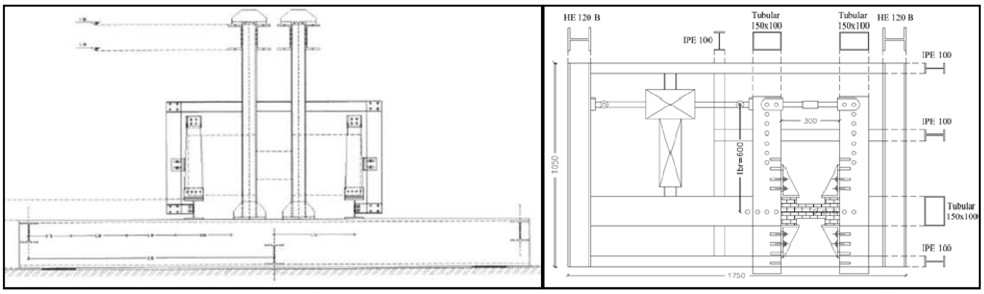

Vignoli *et al.* Calderoni *et al.*

Fig. 7 - Test setup for reduced scale experimental tests

It can be observed that a cyclic test, considered its intrinsic complexity, can be carried out in many different ways and is less controllable and more difficult to understand, so that its usefulness is strongly reduced if it is not related to monotonic tests.

Among the here classified experimental campaigns, besides the tests of the authors, the tests carried out by Beyer *et al.* on full bricks masonry specimens are described and analyzed more in details in the following section.

3.1 Experimental tests carried out by Beyer *et al.*

Beyer *et al.* (2012) performed, among the others, four tests on H-shaped specimens made of brick masonry, adopting the set-up represented in Figure 7. The four specimens had the same geometrical dimensions, but differed for the typology of the lintel and the dimension of the tie-rod: *i*) TUA had timber lintel and a ϕ13 mm steel-tie; *ii*) TUB had timber lintel and a ϕ10 mm steel-tie; *iii*) TUC had a masonry arch lintel and a ϕ13 mm steel-tie; *iv*) TUD had a masonry arch lintel and a ϕ32 steel-tie.

In addition, in TUA and TUC tests, tie-rods have been linked to the specimens in such a way to give a constant axial force to the spandrel, independently of the displacement applied to the specimen; instead, in TUB and TUD tests the axial force applied to the spandrel by tie-rod was not fixed a priori, depending on the deformation of the specimen during the test.

Cyclic controlled displacement loading histories were performed. Note that the compressive strength of masonry, evaluated by means of specific test, was 18 N/mm^2, while tensile strength has not been reported.

In Table 4 the main features of the tests have been summarized.

The failure mechanisms of spandrel in each test are shown in Figure 8, together with the corresponding shear-force vs. rotation curve.

It must be noted that, despite the significant differences among the four specimens, during the test all of them showed almost the same shear strength.

Moreover, contrary to expectation, the maximum shear strength has been reached by the specimen TUA, which is “reinforced” with a small- diameter and low-resistant tie-rod.

Table 4. Full bricks masonry spandrels tested by Beyer *et al.*

Test	Lintel type	Axial load in the piers	Axial load in the tie rod	Tie-rod diameter
TUA	Timber	0.33 MPa	Constant 80 / 40 kN	D13 mm
TUB	Timber	0.33 MPa	Variable	D10 mm
TUC	Masonry arch	0.43 MPa	Constant 80 kN	D13 mm
TUD	Masonry arch	0.43 MPa	Variable	D32 mm

Globally, the four tests presented by Beyer *et al.* led to the misleading (in the opinion of authors) sensation that the dimension (and the effectiveness) of the tie-rod does not influence the behaviour and the resistance of the spandrel and that the formation of a diagonal strut within the panel is not a key aspect for the masonry panel.

So, it is not astonishing that the researchers concluded that the shear resistance of a masonry spandrel is directly related to the tensile strength of the material (i.e. ruled by the first cracking bending moment), while it is well known that the tensile strength of masonry is not a reliable mechanical property and its value is very low and often already overpassed (and then nullified) when the URM building is loaded by seismic actions.

On the contrary, a deep analysis of the performed tests without any prejudice can lead to the observation that the failure mechanism occurred in all tests, except TUB, denotes clearly the activation of a strut in the spandrel, which suffered diagonal cracking widespread in the central part of the panel.

This behaviour is directly related to the geometrical slenderness of the spandrel, which corresponds to a stocky panel: for such panel the shear failure commonly is attained before the compressive strength of masonry is reached at the panel edges (toe-crushing failure) (Calderoni *et al.* 2011). Only TUB specimen showed a different failure pattern: total separation (with almost vertical crack) between the spandrel and the nodal panel at both edges occurred, so highlighting that the inclined truss did not activate in the panel.

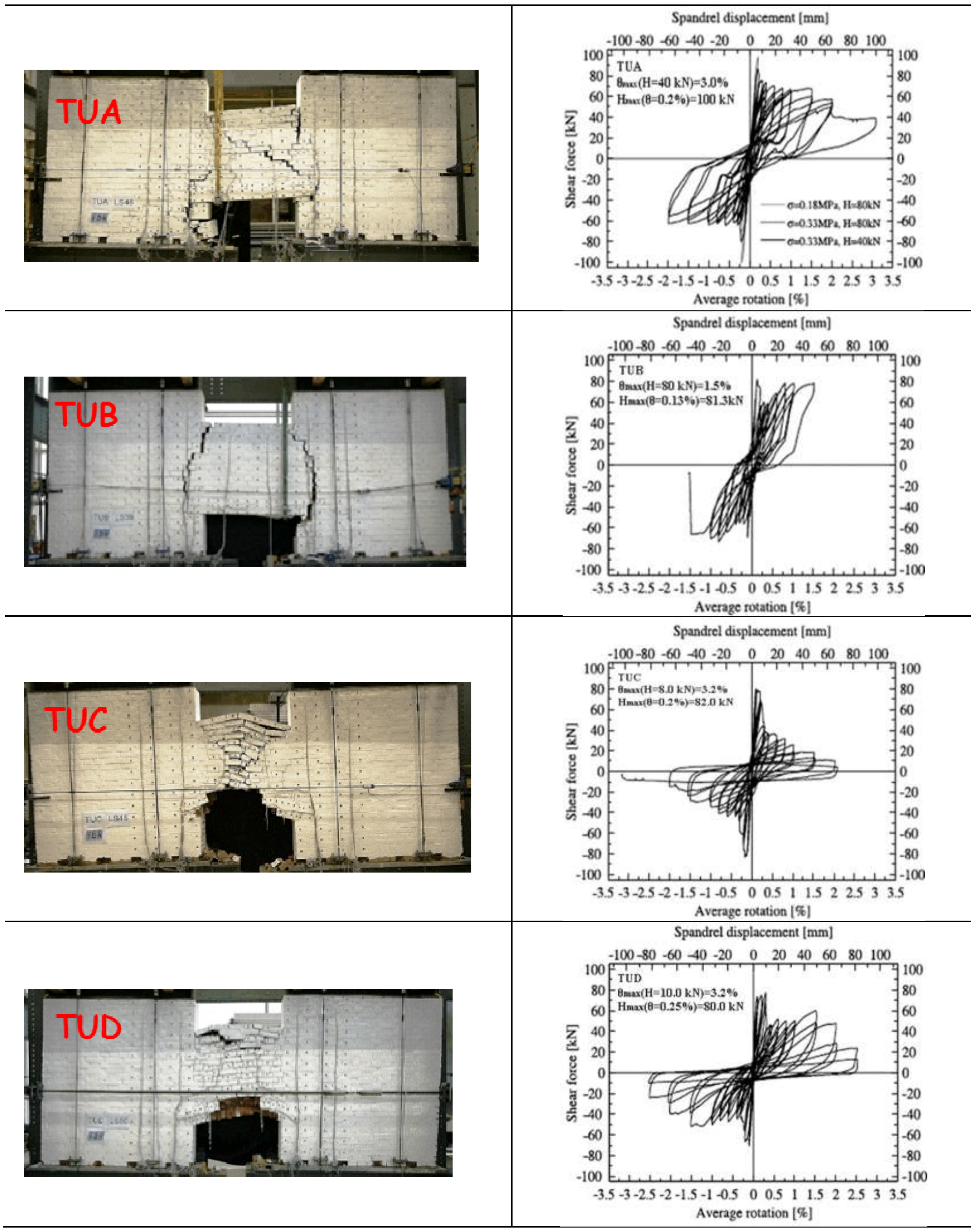

Fig. 8 – Failure mechanisms (left) and corresponding shear force vs rotation (right) (Beyer, 2005)

This fact was due to the very limited tensile resistance of the steel tie-rods, made of very small diameter bars (ϕ10), which resulted lower than the tensile strength of the masonry. Consequently the tie-rods yielded and collapsed soon and the spandrel behaved in flexure, facing the active bending moment by its low tensile resistance, which easily has been overpassed causing the vertical separations. In this case the shear diagonal failure could not be reached.

Finally, the above considerations confirm that few tests, even if carried out on similar (from the geometrical point of view) specimens, cannot give information easily usable for developing general rules on the structural behaviour of masonry spandrels.

On the contrary they are very useful and effective if used for confirming theoretical assumptions and/or for further deepening the problem.

4 Numerical analysis

In this section the results of FEM analyses, carried out for numerically simulating some of the tests reported before, are presented. The tests on rectangular specimens in homogenous material by Calderoni *et al.* and the tests (TU A-B-D) in brick masonry by Beyer *et al.* have been considered.

The aims of these analyses were: *(i)* to verify the effectiveness of different material models and yield criteria commonly adopted for 2D shell elements in order to simulate the masonry behaviour; *(ii)* to recover useful information, difficult to get by theory, as the extension of the effective (compressed) zone at the edges of the panel, the corresponding stress distribution consistent with the low (or null) tensile strength of masonry and the axial force acting in the spandrel; (iii) to better understand and interpret the failure mechanisms exhibited by the specimens.

Furthermore, once the validity of one material model and numerical schematization could be demonstrated by comparison with the experimental results, it should be possible to analyze (only numerically by adopting them) the behavior of further (non-tested) specimens, f.i. characterized by other slenderness ratios, made of different materials or restrained in other ways.

The well-known SAP2000 code has been used to carry out the numerical analyses. Particular attention has been paid in accurately reproducing the boundary conditions of the specimens in the test.

4.1 Analyses of the tests by Calderoni *et al.*

The rectangular panels in homogenous material have been modeled by means of 2D shell finite elements adopting a very refined squared mesh of 5mm x 5mm. The test equipment has been partially modeled too in order to correctly apply the load as in testing. Push-over (V-γ) curves have been obtained to compare with the experimental ones.

With reference to mechanical properties of masonry, compressive strength equal to 5.0 N/mm^2 and Young modulus equal to 340 N/mm^2 have been adopted.

The analyses have been carried out many times, by varying the yielding constitutive model of the non-linear material. The six different adopted material models differ each other in the way the null tensile strength has been accounted for and in the used yielding criterion for limiting (or not limiting) the shear stress.

In particular in the model 1A the horizontal stress (σ_{11} in SAP2000) acting on vertical plane has been considered elastic – perfectly plastic in compression (being 5 MPa the yield stress) and not limited in tension. The null tensile strength has been accounted for by iteratively "cutting" the model at the edges when σ_{11} got in tension. The shear stress (σ_{12}) has not been limited, while in the model 1C it has been considered limited by a full plastic criterion.

In the model 2A, only with reference to σ_{11}, a no-tension material behaving again elasto-plastically in compression (with 5 MPa limit) has been considered. Consequently, the extension of the non-compressed (partialized) zone is automatically defined. The shear stress (σ_{12}) has not been limited, while in the model 2C it has been considered limited by a full plastic criterion.

The models 3A and 3C are directly derived from 2A and 2C. The material behaviour is the same, but the spandrel model has been cut at the edges along the whole length of the no-tension zone, so avoiding the transferring of shear stresses in this zone (which should correspond to the edge-crack in the specimens).

In Figure 9a-b-c, 10a-b-c and 11a-b-c the σ_{11} and the σ_{12} stress patterns at a high shear deformation ($\gamma = 4.5\%$) are shown for slender, intermediate and stocky specimens respectively and for all the six models of material, which have been considered. It can be noted (Figure 9) that for slender spandrel the σ_{11} compressive stress resulted practically constant at the edges of the panel (equal to its yielding value) whatever be the material model considered. On the contrary the distribution of the σ_{12} shear stress is different on varying the material models, interesting only a part (the compressed one) of the edge cross sections for models 1 and 3 and the whole cross section for model 2. Even tough these differences, the obtained results, in terms of V-γ curve, are practically the same as varying the material models (Figure12a) and well correspond to the experimental ones.

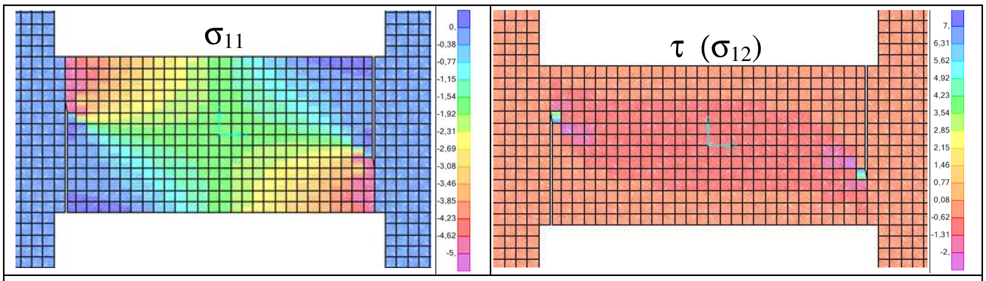

Material 1A: τ linear– γ=4.5%

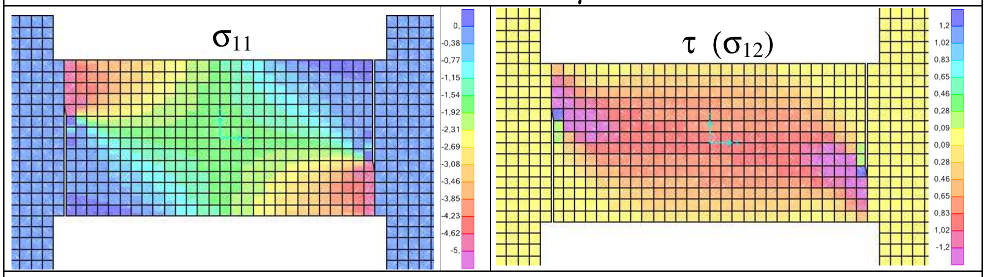

Material 1C: τ non-linear – γ=4.5%

Fig. 9a - Distribution of normal (left) and shear stresses (right) for slender spandrel; material model 1A and 1C.

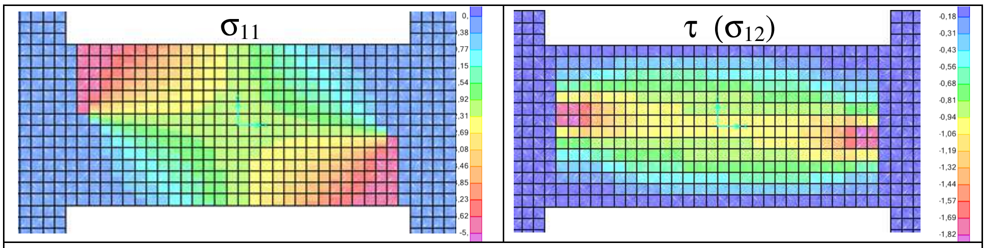

Material 2A: τ linear – γ=4.5%

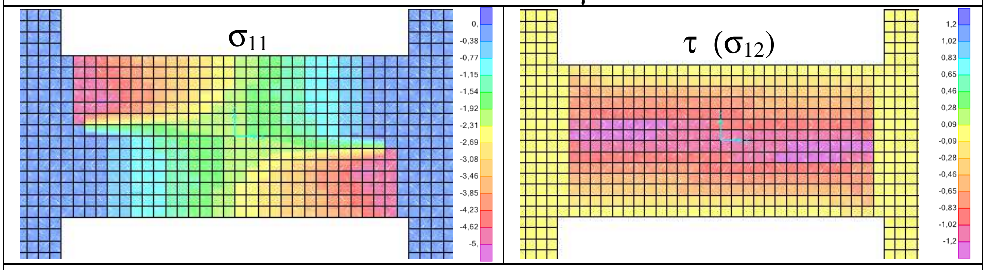

Material 2C: τ non-linear – γ=4.5%

Fig. 9b - Distribution of normal (left) and shear stresses (right) for slender spandrel; material model 2A and 2C.

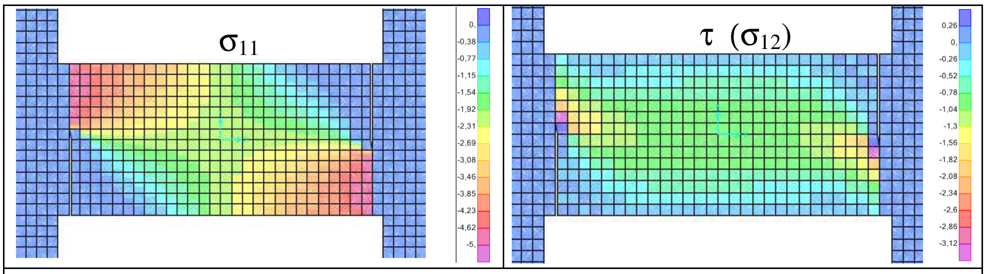

Material 3A: τ linear – γ=4.5%

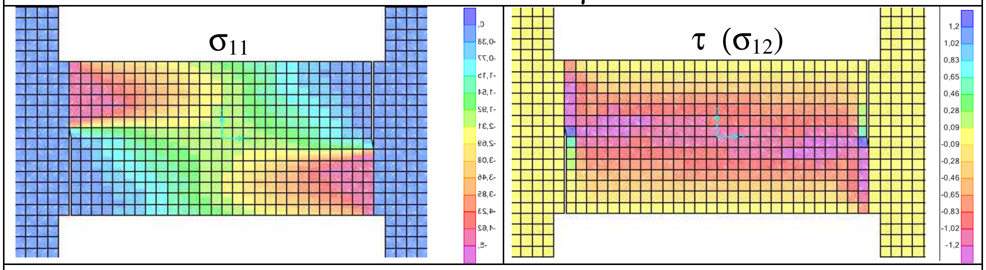

Material 3C: τ non-linear – γ=4.5%

Fig. 9c - Distribution of normal (left) and shear stresses (right) for slender spandrel; material model 3A and 3C.

This is due to the fact that the failure mechanism is commonly ruled in slender panel by the behaviour of the diagonal strut, which involves the compressive strength of masonry (toe-crushing). The differences in the σ_{12} shear stress are not significant because the failure does not involve the internal shear behaviour (no diagonal cracking in the tested specimens).

In the case of intermediate spandrel (Figure 10) far from negligible discrepancies appear in both the stress distribution and the extension of the compressed zones as varying the material model. This is confirmed in Figure 12b, where the corresponding numerical curves are drawn: no one of them follows well the experimental ones; the more correspondent are the 1A and 1C curves, which gives similar values of V_{max} even if with dissimilar elastic stiffness.

The discrepancies became very significant and not negligible (Figure11) in the case of the stocky spandrel, giving rise to V-γcurves (Figure12c) very spread and not coincident with the experimental ones.

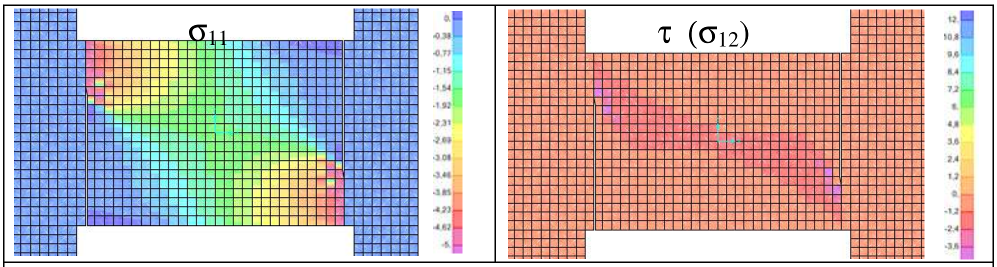

Material 1A: τ linear – γ=4.5%

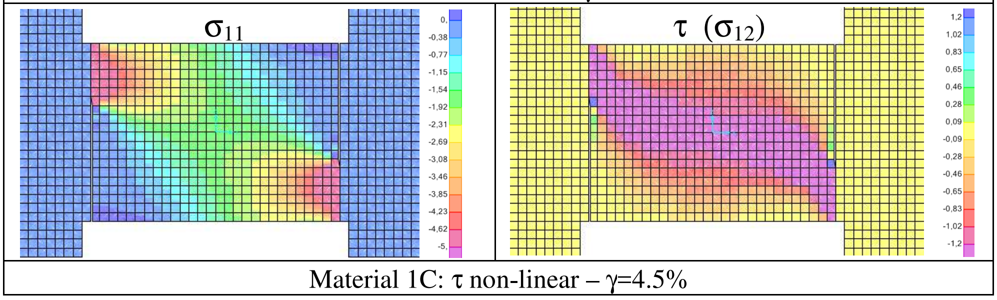

Material 1C: τ non-linear – γ=4.5%

Fig. 10a - Distribution of normal (left) and shear stresses (right) for intermediate spandrel; material model 1A and 1C.

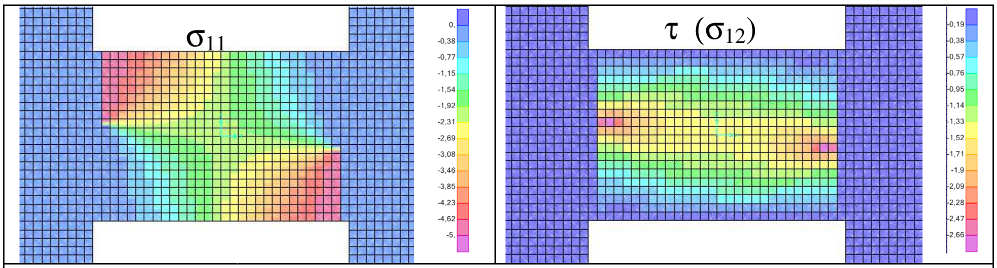

Material 2A: τ linear – γ=4.5%

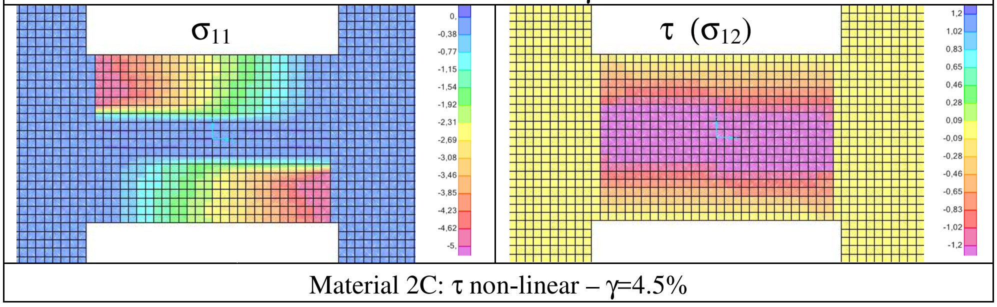

Material 2C: τ non-linear – γ=4.5%

Fig. 10b - Distribution of normal (left) and shear stresses (right) for intermediate spandre material model 2A and 2C.

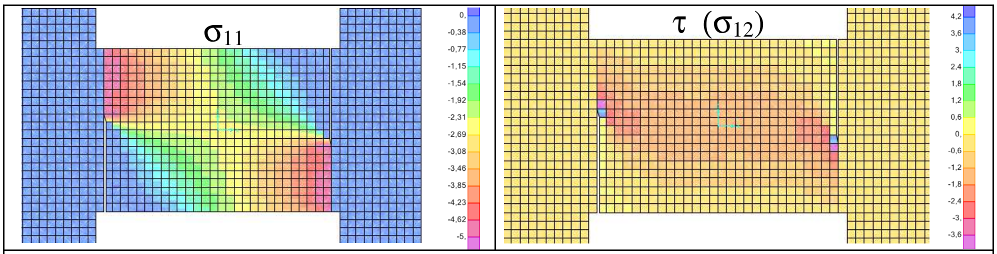

Material 3A: τ linear – γ=4.5%

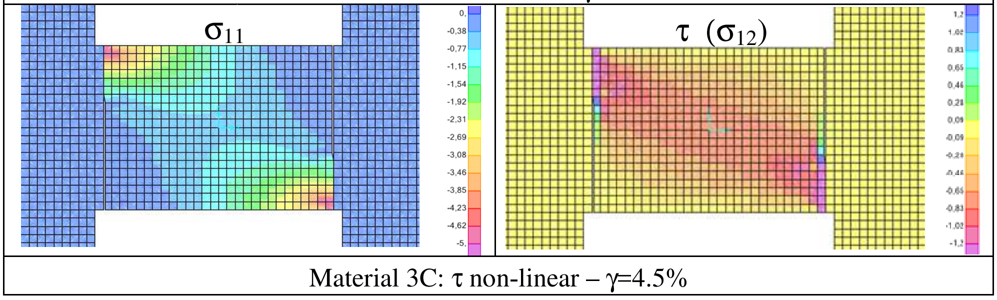

Material 3C: τ non-linear – γ=4.5%

Fig. 10c - Distribution of normal (left) and shear stresses (right) for intermediate spandrel; material model 3A and 3C.

Considered that the experimental tests on intermediate spandrels showed a mixed failure mode (both toe-crushing and diagonal cracking) and the ones on stocky spandrels showed diagonal cracking, i.e. governed also by shear stresses or only by shear stresses respectively, it is evident that all the constitutive model of material adopted in numerical analysis are not at all able to correctly simulate the shear behaviour. This is due to the fact that shear resistance is directly related to tensile strength, and consequently this last cannot be considered null, while it is sufficiently correct do not consider any tensile strength for normal stresses but for principal tensile stresses. Unfortunately, at now a sufficiently adequate constitutive model for masonry material suitable for FE numerical model does not yet exist, so making not at all affordable the numerical analyses performed on masonry structural elements, particularly for spandrels, whose behaviour is strongly related to shear.

4.2 Analyses of the tests by Beyer *et al.*

Three tests performed by Beyer *et al.* (TU A-B-D) have been modeled by means of 2D shell finite elements adopting a squared mesh of 100 mm x 100 mm for the TUA test and 25mm x 25mm for the other tests. Particular attention has been paid for correctly simulating restrains and loads used in each test. Only the material model 1A has been adopted: the horizontal stress (σ_{11}) acting on vertical plane has been considered elastic–perfectly plastic in compression (being 18.0 MPa the yield stress) and not limited in tension. The reduced tensile strength (set to 0.65 N/mm^2) has been accounted for as described after. The shear stress (σ_{12}) has not been limited too.

An iterative pushover analysis has been performed increasing at every step the rotation of the piers and progressively eliminating, along the boundary spandrel-pier, the shell elements showing horizontal tensile stress (σ_{11}) greater than 0.65 N/mm^2. So making the push-over curves (acting shear V vs. edge rotation φ) showed in Figure 13 has been obtained to compare with the experimental ones.

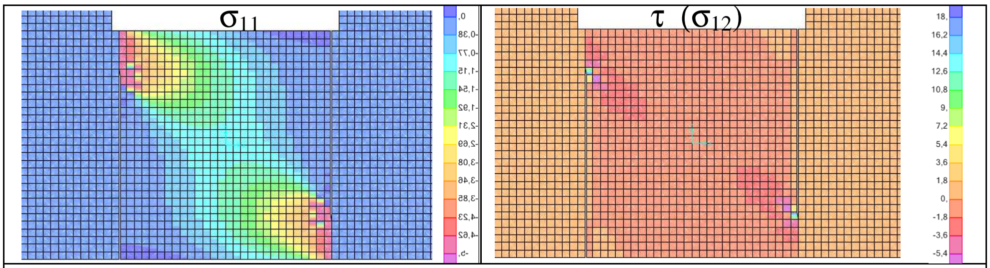

Material 1A: τ linear – γ=4.5%

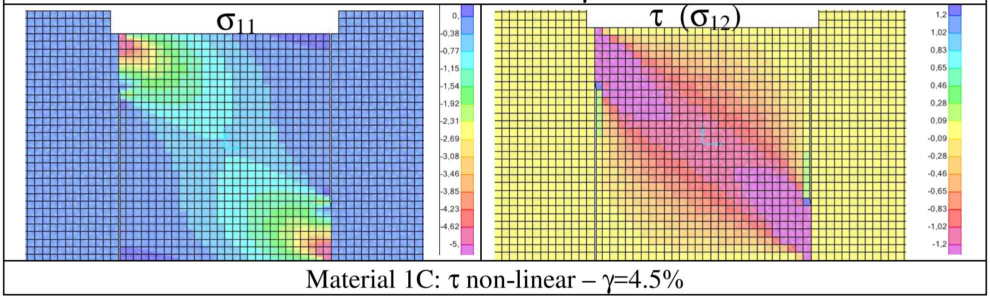

Material 1C: τ non-linear – γ=4.5%

Fig. 11a - Distribution of normal (left) and shear stresses (right) for stocky spandrel; material model 1A and 1C.

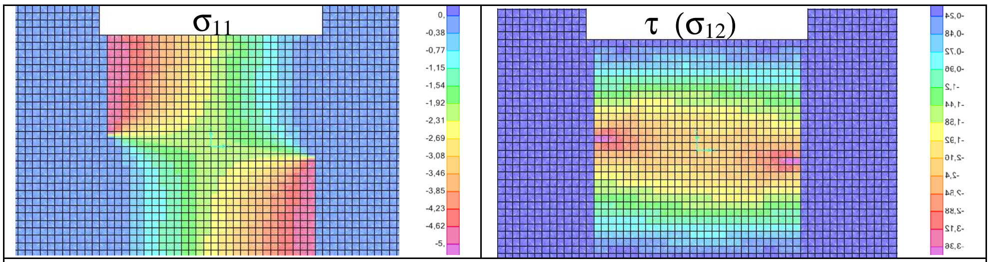

Material 2A: τ linear – γ=4.5%

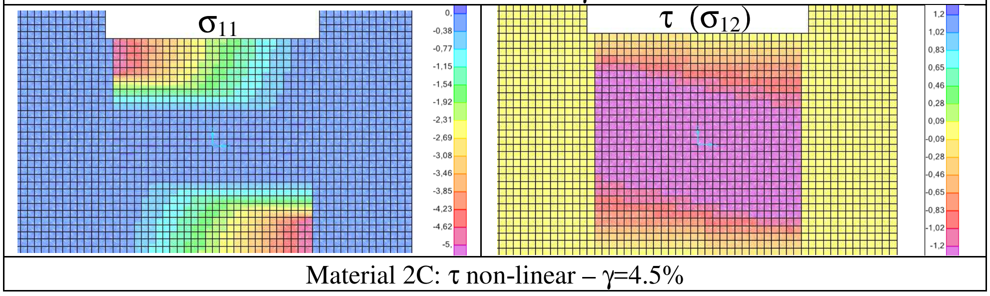

Material 2C: τ non-linear – γ=4.5%

Fig. 11b - Distribution of normal (left) and shear stresses (right) for stocky spandrel; material model 2A and 2C.

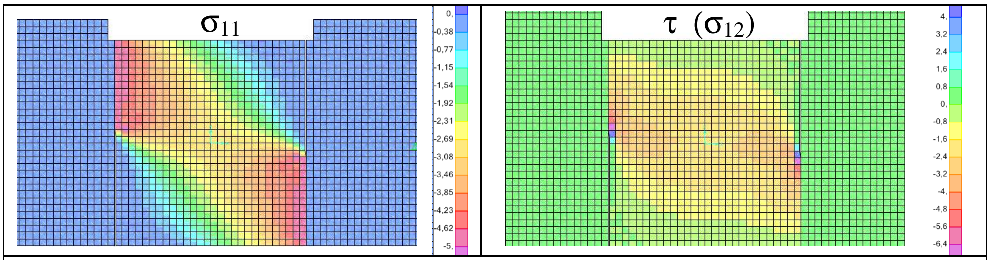

Material 3A: τ linear – γ=4.5%

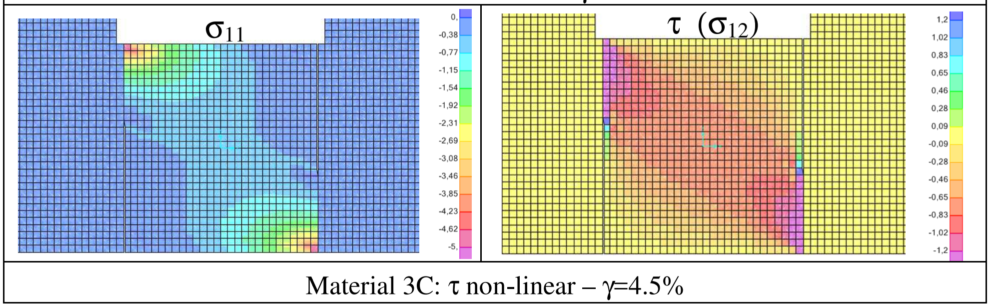

Material 3C: τ non-linear – γ=4.5%

Fig. 11c - Distribution of normal (left) and shear stresses (right) for stocky spandrel; material model 3A and 3C.

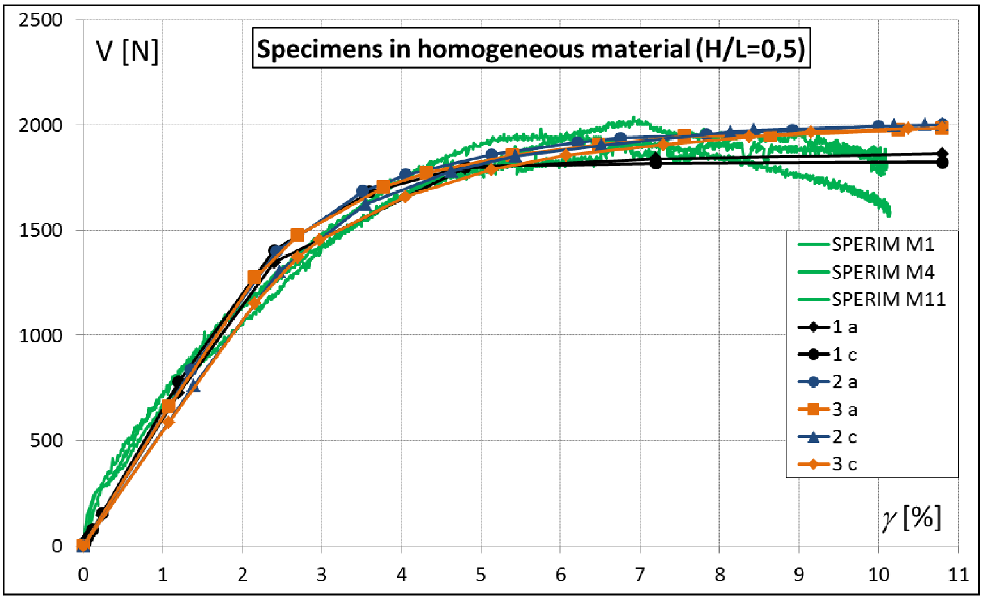

Fig. 12a - Comparison between numerical and experimental results for slender panels

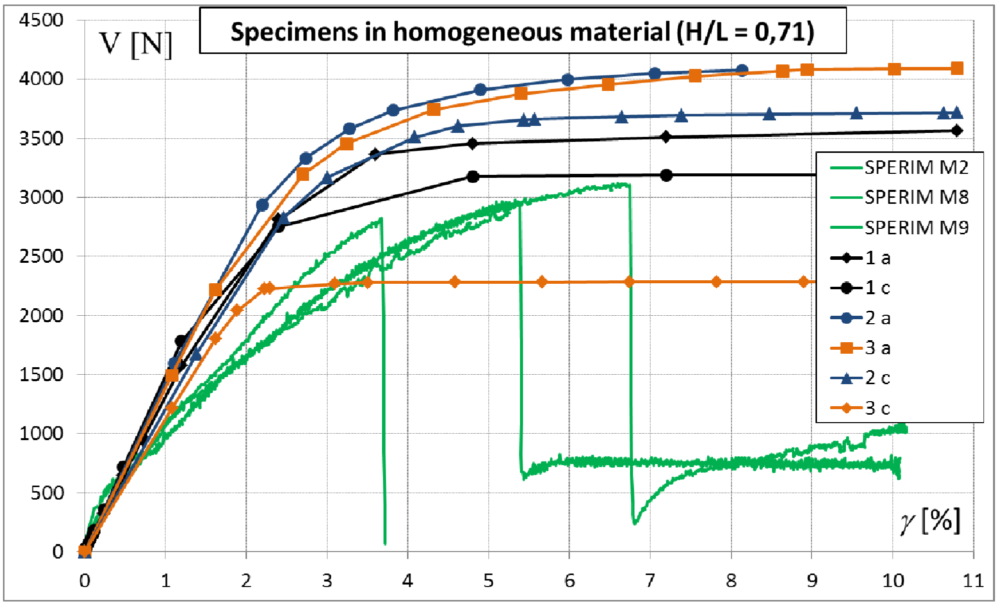

Fig. 12b - Comparison between numerical and experimental results for intermediate panels

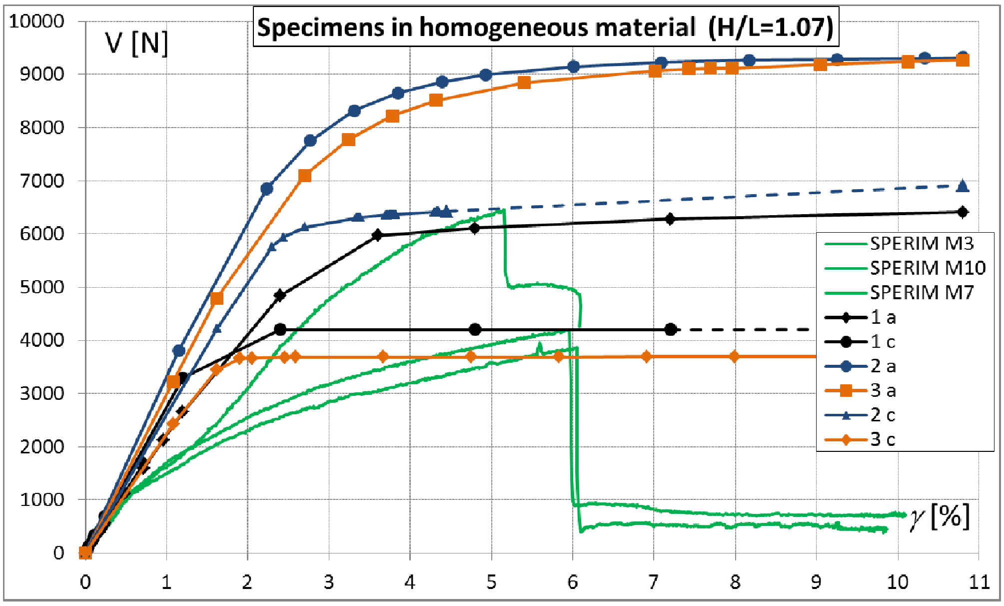

Fig. 12c - Comparison between numerical and experimental results for stocky panels.

The specimen TUB, at the rotation φ=0,0069%, reaches the maximum value of shear (about 85 kN), which is the resistance of the un-cracked spandrel, being the tensile strength of masonry just attained. As rotation is increased, the shear resistance practically falls to zero at φ=0,0078%, when tie-rod starts to be effective (the tie-rod is very small and has a high deformability). Consequently the spandrel can behave like a reinforced panel (the tie-rod provides tensile resistance to masonry): shear linearly increases as the rotation is increased, until the yield stress of the tie rod (75 kN) is reached for a shear force of only 65 kN. Note that this value is lower than that already reached by the un-cracked spandrel, so justifying the complete and sudden failure of the tie-rod (and then of the spandrel) at the attainment of the un-cracked resistance, as showed in the experimental test.

It is confirmed that very small ties are not able to allow the spandrel behaving as a more effective compressed diagonal strut and then to increase the spandrel shear resistance.

In the specimen TUA the tie-rod is pre-stressed at a very low tensile force (40 kN) in such a way this force cannot change as the rotation is increased. The maximum shear reached by the spandrel is slightly greater (95 kN at φ=0,0091%) than the one of TUB, because pre-stressing has increased the tensile strength of masonry in the lower part of the panel, so increasing the un-cracked resistance of the spandrel. As rotation increases the tensile strength of the masonry is overpassed and the shear in the spandrel goes down up to the value corresponding to the tensile stress given by the pre-stress of the tie-rod, which cannot be eliminated being given to the spandrel by means of external axial forces. In the experimental test, further increasing of rotation led the spandrel to suffer a diagonal cracking, but the model adopted for the material in this analysis cannot simulate this kind of failure.

The TUD specimen is similar to the TUB, but larger diameter steel bars (32 mm) have been used as tie-rods.

As for the TUB specimen, the maximum shear force of about 85 kN (at the rotation φ=0,0077%) has been reached, which again corresponds to the resistance of the spandrel at onset of cracking. Immediately after, being overpassed the tensile strength, the shear value falls down without significant increment of rotation, like in the TUB test. Then, as the rotation

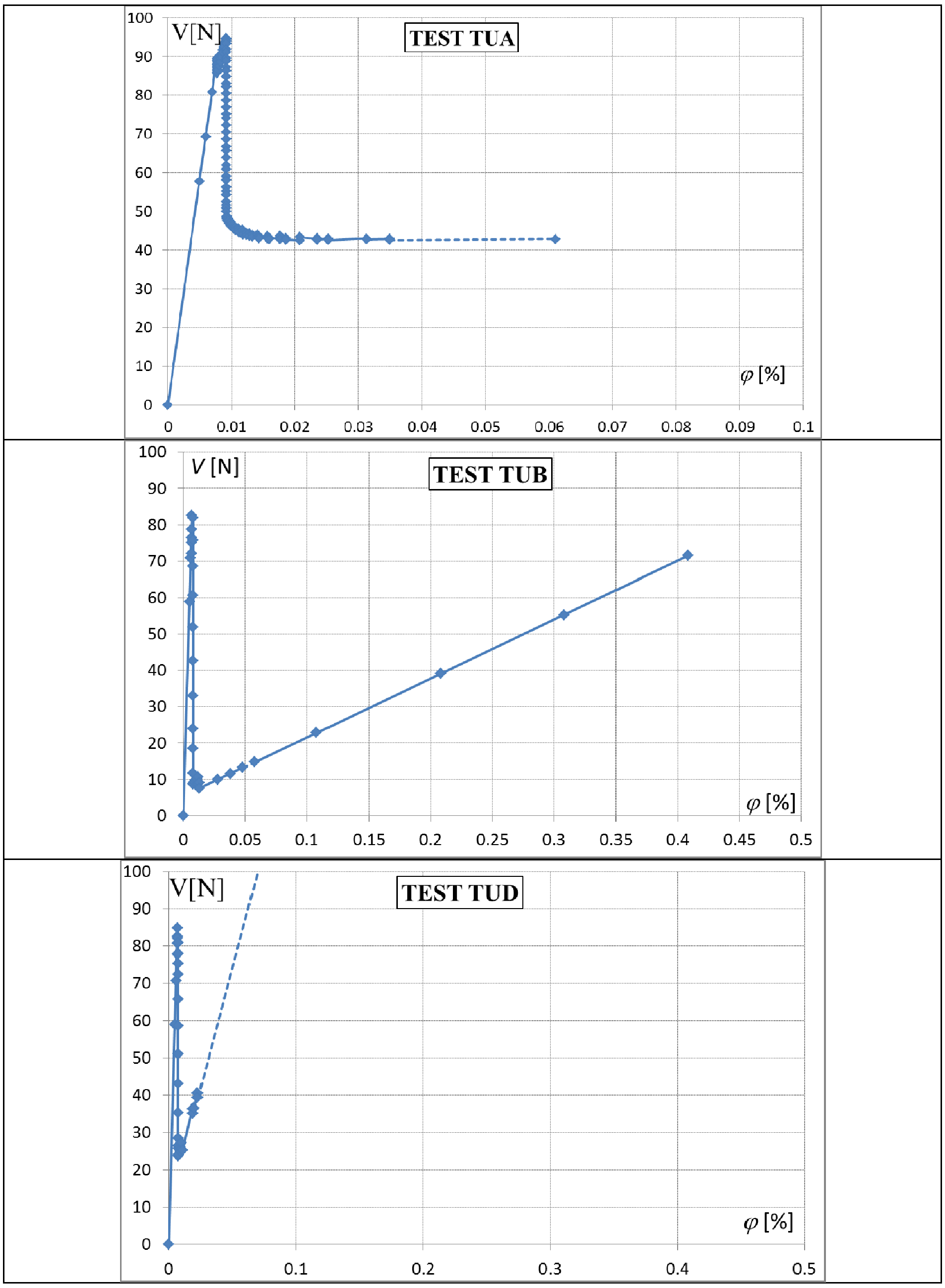

Fig. 13 - Numerical analyses for TUA, TUB, TUD tests by Beyer [Beyer *et al.* 2012]

is increased, the tie-rod can acts as reinforcement of the spandrel, giving it again the tensile strength and allowing the increasing of the shear resistance. In this case the large cross-section of the tie-rod could allow the spandrel to reach a very high shear force (related to the diagonal strut behaviour, i.e. to the compressive strength of masonry), as denoted by the numerical simulation. On the contrary, the actual tested specimen was not able to overpass the 85 kN shear force, because it experienced the diagonal cracking. This circumstance had to be expected, considered that the spandrel is a stocky panel, which is prone to diagonal cracking and cannot attain the higher resistance related to toe-crushing (Calderoni *et al.*, 2010).

In summary, numerical simulations are very useful for interpreting and well understanding the spandrel behaviour. But one has to keep in mind that the constitutive models for masonry, available at now for using in FEM analyses, are not able to catch all the possible failure mechanisms.

Anyway the performed analyses were very useful for highlighting the differences among the tested specimen, which experienced different failure mechanism even if they reached almost the same value of shear resistance.

Without this deepening, misleading conclusions could be attained, f.i. the one that the flexural (and shear) resistance of the spandrel is ruled directly (and only) by the first cracking bending moment, i.e. by the tensile strength of the material, and that it is not significantly affected by the presence of tie-rods.

5 Conclusions

This paper presents a discussion on the structural behaviour of masonry spandrels. This topic is very up to date and interesting, but from the theoretical point of view it is not completely understood, so that the phenomenological derivation of a structural model as well as the calibration of laboratory tests is somewhat difficult.

Nevertheless the experimental tests are an essential tool to improve knowledge, if they are calibrated according to the scope of the research. A correct experimental campaign should involve simple and clear tests with firstly monotonic loadings. Cyclic tests cannot be correctly designed and calibrated if the basic information are not derived from monotonic tests; further they are difficult to be interpreted.

It should be noted that the tensile strength plays an important role in the experimental tests, while in the real structures an unforeseen change in loading or use during their lifetime can influence or nullify the tensile strength, so that it cannot be taken into account in evaluating existing buildings.

The numerical analyses cannot easily be performed, since the procedures actually available, even the most accurate and sophisticated, are not completely reliable and give dissimilar results, depending also on the adopted constitutive model of the material and on the structural scheme to be modeled.

At this time every calibration should be based on a large set of experimental data and should be "guided" according to the structural scheme to be analyzed.

Acknowledgements

This study has been developed with the financial support of the Italian ReLUIS Consortium, within the research program (2013–2016) carried out for the Italian Agency for Emergency Management.

References

1. Betti, M., Galano, L., Vignoli, A. (2008). Seismic Response Of Masonry Plane Walls: A Numerical Study On Spandrel Strength. *Proceeding of Seismic Engineering Conference MERCEA 2008*, Reggio Calabria, Italy, pp. 787-794.
2. Beyer K, Dazio, A. (2012). Quasi-static monotonic and cyclic tests on composite spandrels. *Earthquake Spectra*, vol. 28 (*3*), pp. 885-906.
3. Beyer, K., Mangalathu, S. (2014). Numerical Study on the Peak Strength of Masonry Spandrels with Arches. *Journal of Earthquake Engineering*, vol. 18 (*2*), pp. 169-186.
4. Calderoni, B., Cordasco, E.A., Lenza, P. (2007a). Il ruolo della fascia di piano nel comportamento sismico degli edifici in muratura. *Ingegneria Sismica*, vol. 24 (*1*), pp. 26-40.
5. Calderoni, B., Cordasco, E.A., Lenza, P. (2007b). La capacità di accoppiamento delle fasce di piano nelle pareti murarie soggette a forze orizzontali. In: *Atti del Workshop WONDERmasonry2007*, Lacco Ameno (Ischia), October 2007, Firenze, Italy: Edizioni Polistampa, pp.147–160.

6. Calderoni, B., Cordasco, E.A., Lenza, P. (2008). Experimental Analyses of Yellow Tuff Spandrels of Post-medieval Buildings in the Naples Area. In: *Proceeding of Conference MERCEA 2008*, Reggio Calabria, pp. 824-831.
7. Calderoni, B., Cordasco, E.A., Lenza, P. (2010). Il comportamento strutturale delle fasce di piano degli edifici in muratura soggetti ad azioni orizzontali: indagine sperimentale. *Ingegneria sismica*, vol. 4, pp. 49-70.
8. Calderoni, B., Cordasco, E.A., Lenza, P., Pacella, G. (2011). A simplified theoretical model for the evaluation of structural behaviour of masonry spandrels. *International Journal of Materials and Structural Integrity*, vol. 5 (*2/3*), pp.192–214.
9. Calderoni, B., Cordasco, E.A., Lenza, P., Pacella, G. (2012). Ulteriori sviluppi dell’indagine sperimentale in scala ridotta su pannelli di fascia di piano. In: *Proceeding of Workshop on Design for Rehabilitation of Masonry Structures – WONDERmasonry*, Firenze: Edizioni Polistampa, pp. 98-112.
10. Calderoni, B., Cordasco, E.A., Lenza, P., Pacella, G.(2014). Experimental tests for the evaluation of shear strength of spandrels in ordinary masonry, In: *Proceedings of 9th International Masonry Conference*, July 7-9, Guimarães, Portugal.
11. Calderoni, B., Gulisano, M., Pagano, M. (1984). The method of bonded diagonals. In: *Proceeding of the III International CIB Symposium on Wall Structures*, Varsavia – Polonia, June 1984, pp. 269-277.
12. Cattari, S., Lagomarsino, S. (2008). A strength criterion for the flexural behaviour of spandrel in un-reinforced masonry walls. In: *Proceeding. of the 14th WCEE, October 2008*, Bejing, Cina, pp. 13-18.
13. Como, M., Grimaldi, A. (1986). Analisi limite di pareti murarie sotto spinta, Università di Napoli, In: *Atti Istituto di Tecnica delle Costruzioni*, n.456, Napoli.
14. Corrêa, M.R.S., Page, A.W., Han, Y., Masia, M. (2006). Experimental and theoretical study of the shear behaviour of URM walls with openings. *Masonry International*, vol. 19 (*1*), pp.1–14.
15. Dazio, A., Beyer, K. (2010). Seismic behaviour of different types of masonry spandrels. In: *Proceeding of The 14th European Conference on Earthquake*, September 2010, Skopje, Macedonia (CDrom).
16. Galano, L., Vignoli, A. (2006). Sulla caratterizzazione meccanica delle murature: prove in situ ed in laboratorio, tecniche di prova ed interpretazione dei risultati. In: *Proceeding of Workshop on Design for Rehabilitation of Masonry Structures – WONDERmasonry*, Firenze, April 2006, pp. 3-14.
17. Gattesco, N., Clemente, I., Marcorini L., Noè, S. (2008). Experimental Investigation on the Behaviour of Spandrel in Ancient Masonry Buildings. In: *Proceeding of the 14th WCEE*, October 2008, Beijing, China.
18. Graziotti, F., Magenes, G., Penna, A., Galasco, A. (2011). Comportamento ciclico sperimentale nel piano di fasce in muratura di pietra. In: *Proceeding of XIV Conference ANIDIS*, Bari, Italy, September 18-22, (CD-rom).
19. Milani, G., Beyer, K., Dazio, A. (2009) Upper bound limit analysis of meso-mechanical spandrel models for the pushover analysis of 2D masonry frames. *Engineering Structures*, 31 (*11*), pp. 2696-2710.

20. Parisi, F., Augenti, N., Balsamo, A., Prota, A., Manfredi, G. (2010). Lateral loading tests on a masonry system with and without external reinforcement. In: *Proceeding of the 14th European Conference on Earthquake*, September 2010, Skopje, Macedonia (CDrom).
21. Rinaldin, G., Amadio, C., Gattesco, N. (2014). Experimental and numerical characterization of the cyclic behaviour of unreinforced and reinforced masonry spandrels. In: *Proceedings of 9th International Masonry Conference*, July 7-9, Guimarães, Portugal.

Seismic vulnerability assessment of churches at regional scale after the 2009 L'Aquila earthquake

Gianfranco De Matteis[1], Giuseppe Brando[2], Valentina Corlito[1],
Emanuela Criber[2], Mariateresa Guadagnuolo[1]

[1] University of Campania "Luigi Vanvitelli",
Department of Architecture and Industrial Design, Aversa (CE), Italy
{gianfranco.dematteis, m.guadagnuolo}@unicampania.it, valentinacorlito@gmail.com
[2] University "G. d'Annunzio" of Chieti-Pescara,
Department of Engineer and Geology, Pescara (PE), Italy
[4]{e.criber, gbranco}@unich.it

Abstract. The extension of damage on churches observed after strong earthquakes evidences the necessity to plan, at regional scale, effective restoration, consolidation and preventive protection strategies. In this framing, the availability of suitable speedy methodologies for the assessment of the main structural fragilities and therefore of the seismic vulnerability of each church is the first fundamental step to be undertaken.

This paper presents a methodology for the seismic vulnerability assessment of churches based on a damage reconnaissance activity carried out after the 2009 L'Aquila earthquake on a population of 64 churches.

Firstly, the post-earthquake evaluation of damage is described with the aim of identifying both the recurrent damage mechanisms and the main local structural fragilities. As an important outcome, it has been observed that the occurred damage scenario, shown in terms of frequency of pre-established damage levels, can be represented by a binomial distribution, which depends on one parameter only, namely mean damage level.

Then, a literature predictive model able to give back the above parameter for several earthquake intensities is applied for outlining fragility curves related to the seismic risk of churches. These curves represent a powerful tool for the prediction of likely future damage scenarios.

Finally, some ongoing applications of the proposed analysis methodology to churches of different territorial areas are described.

Keywords: Seismic vulnerability, Cultural heritage, Old churches, Structural Damage, Fragility curves.

1 Introduction

Old masonry churches represent one of the most important assets of the Italian cultural heritage. The connection between seismic risk and conservation of such a type of structures is a topic of great importance in terms of both protection and losses prevention.

Earthquakes occurred in the last twenty years in the Apennines (i.e. Umbria e Marche earthquake,1997; L'Aquila earthquake, 2009; Emilia Romagna earthquake, 2012; Central Italy earthquake, 2016) evidenced the fragilities of old masonry churches and testified, once again, the importance of defining useful protection strategies to preserve their structural integrity, which often means historical identity of wide territories (Brandonisio *et al.*, 2013; Criber *et al.*, 2015). Indeed, the seismic protection of churches is not only a matter of cultural identity, but also a social and political issue, because, in an urban context, churches often represent the most important site of aggregation of people.

A meaningful example of how important is to protect churches from earthquake attacks is given by the partial collapses of the St. Francesco d'Assisi (PG) central vault (Umbria e Marche earthquake, 1997), shown in Figure 1, which caused not only human fatalities, but also losses of important and valuable frescoes.

Fig. 1 – St. Francesco d'Assisi basilica. Damages on the vault after the 1997 earthquake.

The importance of protecting churches in order to preserve inestimable assets was also underlined by more recent earthquakes. The collapse of the transept of the basilica of Collemaggio (Figure 2a) in L'Aquila, which is a meaningful example of Romanesque architecture, represented the loss of an important part of the Abruzzi cultural heritage. Likewise, the recent seismic event of Centre of Italy (2016) irremediably struck one of the most significant medieval basilica of Umbria, the St. Benedetto church in Norcia: today, the façade and the apse are the only parts of the church that survived to the earthquake (Figure 2b).

Fig. 2 – a) St. Maria di Collemaggio basilica (AQ) after L'Aquila earthquake (2009) and b) St. Benedetto basilica in Norcia (PG) after the Centre of Italy earthquake (2016).

On the other hand it has to be recognized that the correct and precise evaluation of the structural behaviour of churches, and more in general of monumental buildings, is very complex, due to specific issues related to the adopted constructional criteria. Due to the difficulty related to material modelling but also the geometrical complexity of the manufactures, the detailed specific analysis should be very elaborated and time consuming (Brando *et al.*, 2015) or should be based on specific approximated methodologies, for instance the one proposed in (Ercolano, 1994; De Luca *et al.*, 2004; Huerta, 2008), which are applicable is many but not all the situations.

All the above remarks emphasise the necessity to define suitable speditive vulnerability assessment methodologies at large scale, which are able to predict potential likely damages scenarios. These methodologies have to account for the recurrent damage mechanisms observed on churches after earthquakes of the past, as well as for possible protection devices (i.e. iron ties, buttresses, connecting elements across the walls, etc.) that have been already installed for removing or mitigating some structural fragility sources. For instance, the possibility to use simplified methods is shown in (Lourenço and Roque, 2006) where a geometric approach is used to retrieve back simplified safety indexes, with the aim to define an immediate screening of a certain number of historical buildings and to priorities more detailed numerical analysis.

In this paper, the vulnerability assessment at large scale of churches is dealt with. To this purpose, a methodology taken from existing literature and corroborated by post-earthquake observation carried out on a population of 64 three-naves churches after the 2009 L’Aquila earthquake in two of the most stricken dioceses of Abruzzi region is applied. In Section 2 the churches considered for the reconnaissance and the observed damage revealed after L’Aquila earthquake are described. Moreover, damage is classified in terms of severity and extension, in order to provide Damage Probability Matrices. These matrices provide a synthetic description of the occurred earthquake scenario corresponding to the occurred earthquake. In Section 3, the methodology for the vulnerability assessment is dealt with and used in order to provide fragility curves, which are able to predict damage scenarios for different earthquake intensity. In the following, the proposed methodology is referred to the population of 64 three nave churches identified in L'Aquila district. Finally, in Section 4, the ongoing research activity on churches belonging to a different territory is outlined, giving a first typological and structural description of identified buildings. It is worth noticing that issues provided in this paper has been presented by the authors also in previous studies, were the approach was mainly of observational type, i.e. aimed at evaluating by analytical procedure the damage scenario observed after the L'Aquila earthquake. Now the intention of the author is to check the possibility to apply the proposed methodology also for preventive purposes, by defining a specific vulnerability index (i_v) to assess structural capacity of a large population of churches for predicting possible damage scenarios due to future earthquakes in different regions (De Matteis *et al.*, 2016).

2 The churches of L'Aquila and Sulmona-Valva dioceses

2.1 General

L'Aquila is the capital city of Abruzzi and is located in the inner part of the region. The district extends on almost half of the regional territory and covers three ecclesiastical areas. In particular, the dioceses of L'Aquila and Sulmona-Valva, which are shown in Figure 3, together with the acronyms used in the following parts of the paper, were the most affected by the 2009 seismic event and for this reason they have been studied more in detail (Criber *et al.*, 2015; Brando *et al.*, 2015). In the investigated area, almost 640 churches, located in seventy-seven municipalities, were identified. Among these, the 10% (64) are three nave churches: they were identified as belonging to the most representative typology and therefore have been specifically considered for the reconnaissance activity; in fact their structural complexity provides more interesting information in terms of vulnerability sources and collapse mechanisms.

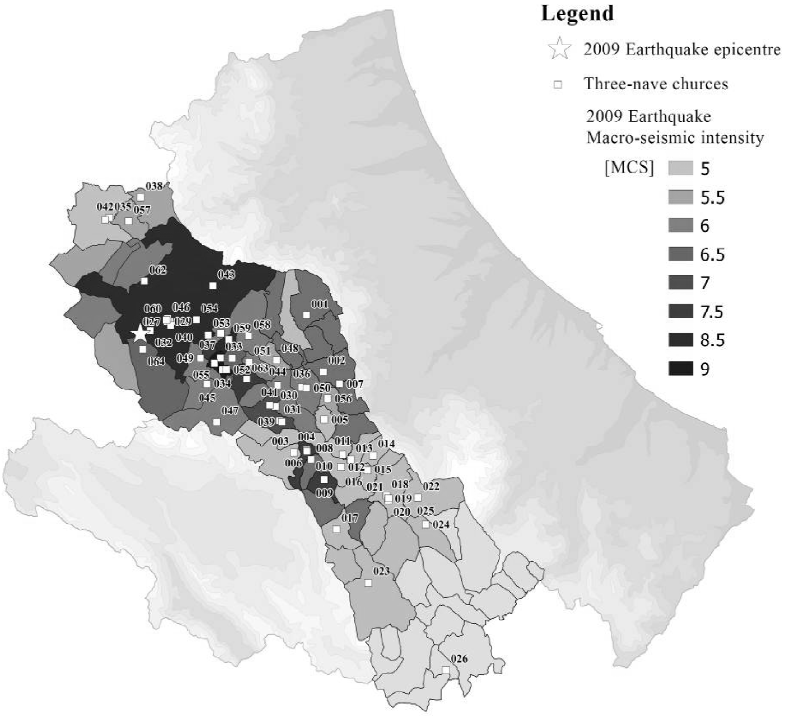

001	**SME**	San Marco Evangelista
002	**SMP**	Santa Maria della Pace
003	**SMA**	San Martino
004	**SFR**	San Francesco
005	**SBA**	San Benedetto Abate
006	**SGE**	San Giovanni Batt ed Ev.
007	**SPO**	San Pietro ad Oratorium
008	**SMS**	Santa Maria Assunta
009	**SGM**	Santa Gemma
010	**SMN**	Santa Maria Nova
011	**SMB**	Santa Maria del Borgo
012	**SMM**	Santa Maria Maggiore
013	**SPE**	San Pelino
014	**SMI**	San Michele Arcangelo
015	**MDL**	Madonna della Libera
016	**SPC**	San Pietro Celestino
017	**SGR**	Santa Maria delle Grazie
018	**SSA**	Santissima Annunziata
019	**SPA**	San Panfilo
020	**SDO**	San Domenico
021	**SMT**	Santa Maria della Tomba
022	**SMR**	Santa Maria Maggiore
023	**SMV**	Santa Maria delle Valle
024	**SSL**	San Salvatore
025	**SNB**	San Nicola di Bari
026	**SMC**	Santa Maria del Carmelo
027	**SBR**	Chiesa di San Bernardino
028	**SBM**	Chiesa di San Biagio d'Amit.
029	**SDM**	Chiesa di San Domenico
030	**CLM**	Basilica di S.Maria di Collem.
031	**SMG**	Chiesa dei Ss. Mass. e Giorgio
032	**SSV**	Chiesa di San Silvestro
033	**SBB**	Chiesa di San Benedetto Abate
034	**SAN**	Chiesa di Santa Maria Assunta
035	**SGI**	Chiesa di San Giustino
036	**SNM**	Chiesa dei Ss. Nican. e Marc.
037	**SGO**	Chiesa di San Gregorio Magno
038	**SLB**	Chiesa di San Lorenzo
039	**SFB**	Chiesa di San Flaviano
040	**SMX**	Chiesa di S. Maria di Pic. E.M.
041	**SLO**	Chiesa di Santa Maria del Loreto
042	**SFC**	Chiesa di San Flaviano
043	**SSS**	Chiesa di Santa Maria Assunta
044	**SGL**	Chiesa di San Giovanni Battista
045	**MPF**	Chiesa di S.Maria e S.Pietro
046	**SGT**	Chiesa di San Giovanni Battista
047	**SAS**	Chiesa di Santa Maria Assunta
048	**SPS**	Chiesa di Santa Maria in Pant.
049	**SSB**	Chiesa di San Sebastiano
050	**SMU**	Chiesa di Santa Maria in Cer.
051	**SPF**	Chiesa di San Panfilo d'Ocre
052	**SFM**	Chiesa di San Felice Martire
053	**SNC**	Chiesa di San Nicandro
054	**SLU**	Chiesa di Santa Lucia
055	**SPI**	Chiesa di San Pietro
056	**SDE**	Chiesa di San Demetrio
057	**SPT**	Chiesa di San Pietro Celestino
058	**SEU**	Chiesa di Sant'Eusanio Martire
059	**SGV**	Chiesa di San Giovanni Evang.
060	**SGG**	Santi Giusta e Giorgio
061	**SRO**	Chiesa di Santa Maria della R.
062	**SPN**	Chiesa di Santa Maria del Ponte
063	**SAR**	Chiesa di San Michele Arcang.
064	**SAG**	Chiesa di Sant'Agata

Fig. 3 – The three naves churches in L’Aquila and Sulmona-Valva dioceses: localization on the 2009 earthquake macro-seismic intensity map (MCS scale).

2.2 Typological classification of churches under investigation

The observed group of churches was classified according to the foundation period, as well as to the structural construction techniques. However, this classification was not always clear because churches of inner Abruzzi are strongly marked by significant stratifications, due to the several reconstructions and restorations carried out in the past (Rovida *et al.*, 2011), in particular after the earthquakes occurred in 1461 in L'Aquila (10 MCS), 1703 in the north of L'Aquila (10 MCS), 1706 near to Sulmona and 1915 in Avezzano (11 MCS).

In particular, for the sake of simplicity, three main different types of churches were identified: *medieval*, *post medieval* and *hybrid* churches.

The first group, including almost 20% of the whole population considered in the study, is composed by churches built from XI to XIV century, generally characterized by poorness of decorations (a typical feature of the churches built in this period in the central part of Italy (De Matteis and Mazzolani, 2010)) and by a low seismic vulnerability. This is mainly due to the plan simplicity, the absence of transept and dome, the presence of a light wooden roof and a masonry of good quality. For instance, the church of San Pietro ad Oratorium (SPO) in Capestrano in the Diocese of L'Aquila (Figure 4.a) is an important example of *mediaeval* church. Generally, the churches belonging to this group suffered low damage during the last L'Aquila earthquake.

The second group is composed by *post-medieval* churches (almost the 20% of the analysed stock), built between XV and XVII centuries (Renaissance and Baroque period), which is characterized by a medium seismic vulnerability. These churches are generally characterized by a rectangular plan with three naves crossed by a transept and surmounted by a dome at the intersection, as observed in Madonna della Libera (MDL) church in Pratola Peligna (Diocese of L'Aquila), which is shown in Figure 4.b. In these cases heavy vaults or mixed roofs are always present. The masonry is commonly made of rubble stones characterized by a chaotic texture.

The third group, namely the *hybrid* churches (almost the 60% of the whole analyzed population), is composed by churches characterized by many stratifications and structural variations, often following the main seismic events occurred in the past in a specific territory (Giannantonio, 1988 and 2000), implemented without effective structural design, leading sometimes to a worsening of the global structural response. The basilica di Santa Maria di Collemaggio (CLM) (Figure 4.c) in L'Aquila represents one of the most important example of *hybrid* churches.


a) b) c)

Fig. 4 – a) San Pietro ad Oratorium in Capestrano (AQ), b) Madonna della Libera in Pratola Peligna (AQ), c) Santa Maria di Collemaggio basilica in L'Aquila (AQ).

2.3 Survey of the main damage mechanisms

The most recurrent damage type is represented by cross diagonal cracks due to second mode mechanism type. This is associated to the in plane response of the wall, which is loaded by shear loads. Such type of mechanism has been frequently found on lateral walls, bell towers and domes, in particular when these elements were characterized by a poor masonry fabric (Figure

5). Vaults were characterized by significant damage, in particular for elliptical configurations, where fractures along both the diagonal directions and the circular spring-lines have been highlighted (Figure 6.a). Important damage has been observed also in barrel vaults, with longitudinal cracks generally localized along the key-stones (Figure 6.b).


a) b) c)

Fig. 5 – Diagonal cracks on wall after the 2009 seismic event. a) Bell tower of the St. Bernardino church (SBR) in L'Aquila; b) Lateral walls in St. Eusanio church (SEU) in Sant' Eusanio Forconese (AQ); c) Apse in St. Massimo and Giorgio church (SMG) in L'Aquila.

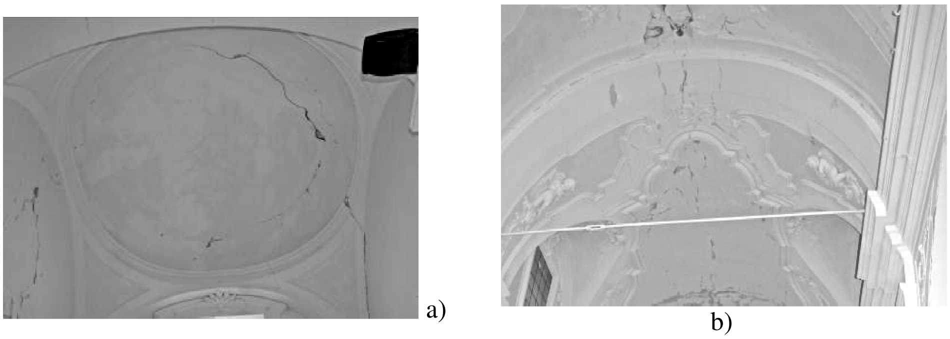
a) b)

Fig. 6 – Observed damages on a) elliptical vaults and b) barrel vaults of St. Maria Nova church (SMN) in Goriano Sicoli after the 2009 seismic event.

In pillars vertical cracks due to crushing phenomena have been sometimes relieved. These have been probably induced by the increasing compression stresses, due to the earthquake vertical component, which, even far from the epicentre, was often significant due to site effects (De Matteis *et al.*, 2016). The above failures are particularly evident on those columns made of rubble masonry (typical of *post-medieval* and *hybrid* churches), where cracks along the mortar have been observed (Figure 7).

Fig. 7 – Observed damages after the 2009 seismic event on rubble masonry pillars of St. Gemma church (SGM) in Goriano Sicoli (AQ).

An heavy damage has been observed on churches where reinforced concrete roof or beams have been added in recent years without effective connection with the vertical walls. The presence of these elements is evident in those churches affected by horizontal sliding cracks at the ring beams at the top of the walls.

Out-of-plane mechanisms have been identified when macro-elements resulted not correctly endowed with a proper number of well dimensioned ties. For the analysed churches, three main out-of-plane phenomena have been recognized: the rigid façade overturning, the façade top-corner overturning and the apse overturning. The first type of mechanism was evident, for example, in the St. Gemma church in Goriano Sicoli -SGM- (in the Sulmona-Valva Diocese). This church showed a fully developed mechanism, with a detachment between the façade and the lateral walls of about the thickness (Figure 8). The façade top-corner overturning has been detected when, even in presence of longitudinal ties that effectively constrained the rigid overturning of the whole façade, the corner connection was clearly inefficient due to the lack of restraining element (see Figure 9a).

Finally, the third type of overturning mechanism concerned the apse. It was generally due a bad connections or to the presence of wide openings. A meaningful example is the case of St. Martino church in Gagliano Aterno (SMA), where the diagonal cracks, typical of this mechanism, have been surveyed (see Figure 9.b).

Fig. 8 – Façade overturning in St. Gemma church (SGM) in Goriano Sicoli (AQ)

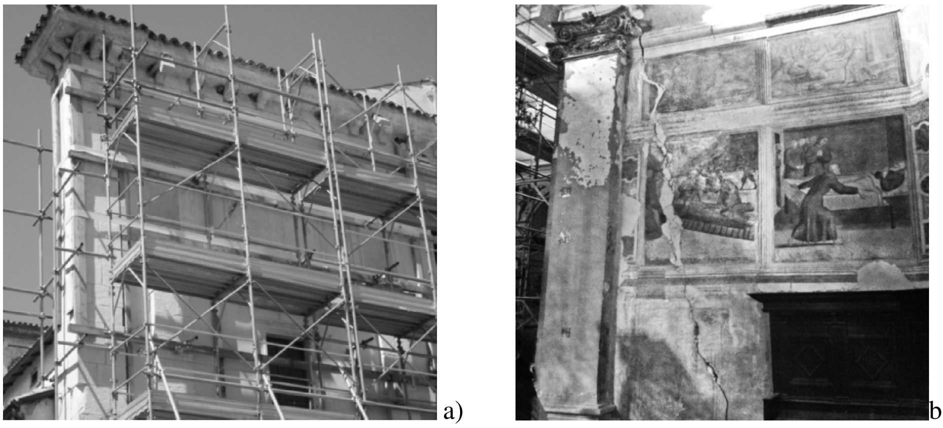

a) b)

Fig. 9 – a) Top-corner overturning on St. Maria della Pace church in Capestrano and b) Apse overturning on St. Martino church in Gagliano Aterno.

2.4 Damage classification

Consistently with the Italian Code "Guidelines for Cultural Heritage" (MiBACT, 2010), the classification of the observed damage has been carried out accounting for twenty-eight mechanisms referred to the main macro-elements (i.e. the façade, the colonnade, the vaults, the apse, the transept, the dome and the bell tower). For each mechanism, a specific level of damage d_k ($0 \leq d_k \leq 5$), has been defined according to the criteria introduced by Grunthal for the European Macroseismic Scale EMS-1998 (Grunthal, 1988). In Figure 10 the Grunthal definition of damage levels, proposed for residential buildings, is related to churches, according to the criteria described in (De Matteis *et al.*, 2016).

Then, according to equation (1) proposed in Guidelines, a global damage index (i_d), ranging from 0 (no damage) to 1 (full damage), has been calculated for each church belonging to the analysed stock. The results are given in Figure 11.

$$i_d = \frac{1}{5} \cdot \frac{\sum_{k=1}^{28} \rho_{k,i} \cdot d_{k,i}}{\sum_{k=1}^{28} \rho_{k,i}} \qquad (1)$$

In the above formula, ρ_k is an importance factor that weight the damage of the mechanism k (ranging from 1 to 28) according to the importance that the mechanism itself has for the global stability of the church. The considered values are given in (MiBACT, 2010). Each damage index i_d has been therefore related to a damage score D_k (ranging from 0 to 5), accounting for the criteria provided by Lagomarsino and Podestà (2004). For each church, the obtained score D_k is shown in Figure 12. The statistical elaboration of the damage scores D_k for churches as a whole and for the single macro-elements (in this case d_k coincides with D_k), allowed to determine the related Damage Probability Matrices (DPMs), shown in Figure 13, which provide the frequency of occurrence of the different levels of damage D_k.

Once the data on damage have been defined, it has been observed that a Binomial Probability Distribution Function (BPDF) fits suitably the related DPMs of both the whole churches and the single macro-elements, as shown in Figure 13. In particular, the adopted BPBDF is given in eq (2), where p_k represents the probability to have a certain level of damage D_k, k ranges from 0 to 5 and represents the damage level, while μ_d is the mean damage level. The latter represents the mean value of the damage evaluated for the whole stock of observed churches; it could be referred to the damage related to either the whole church considered as a whole, in such a case it has been calculated according to equation (3), or to the damage related a specific macro-elements of the church, according to eq. (4). In the case being, for the whole population of observed churches, while referring the damage to the whole church, the mean damage level μ_d, according to eq. (3) resulted equal to 1.734.

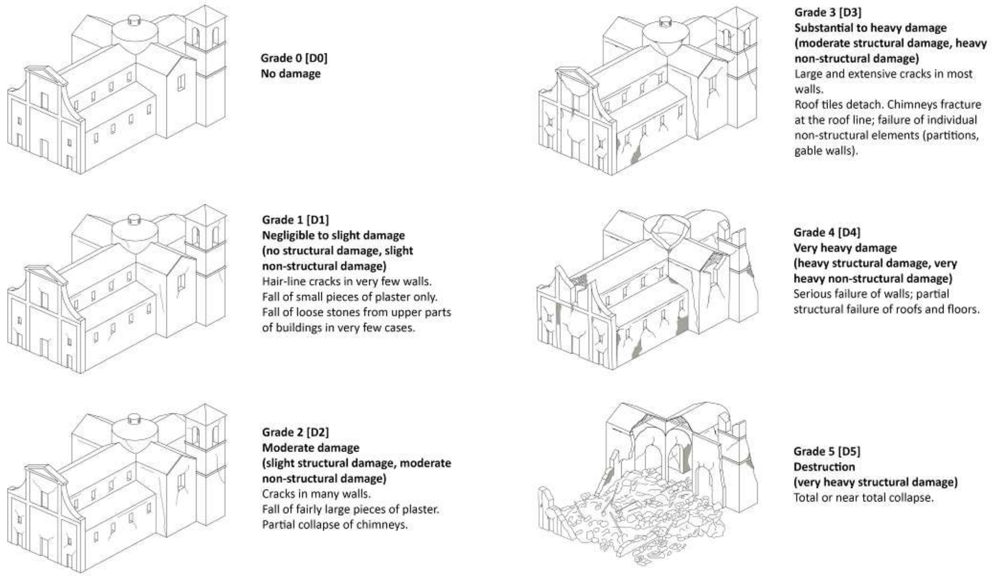

Fig. 10 – Damage classification for masonry churches according to the Grunthal approach

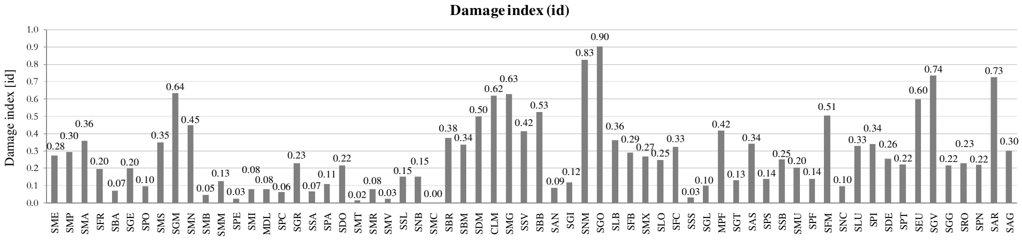

Fig. 11 – Damage index i_d for all the observed churches

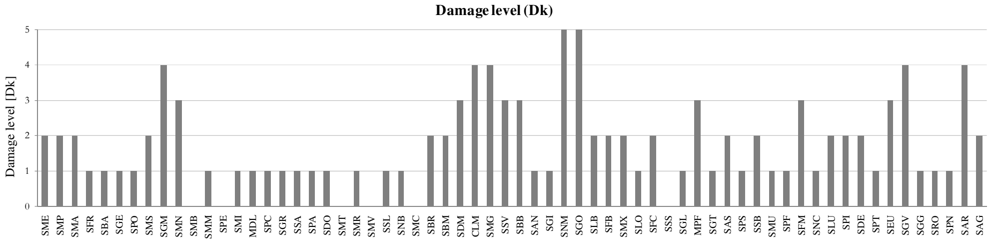

Fig. 12– Damage level D_k for all the 64 observed churches

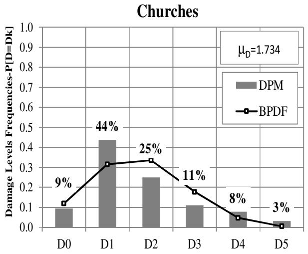

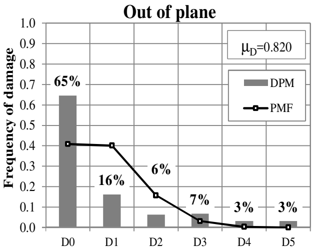

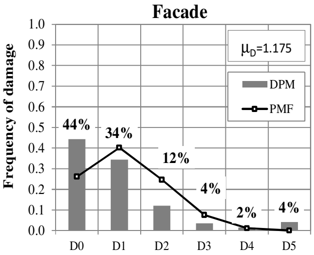

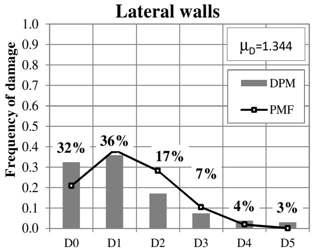

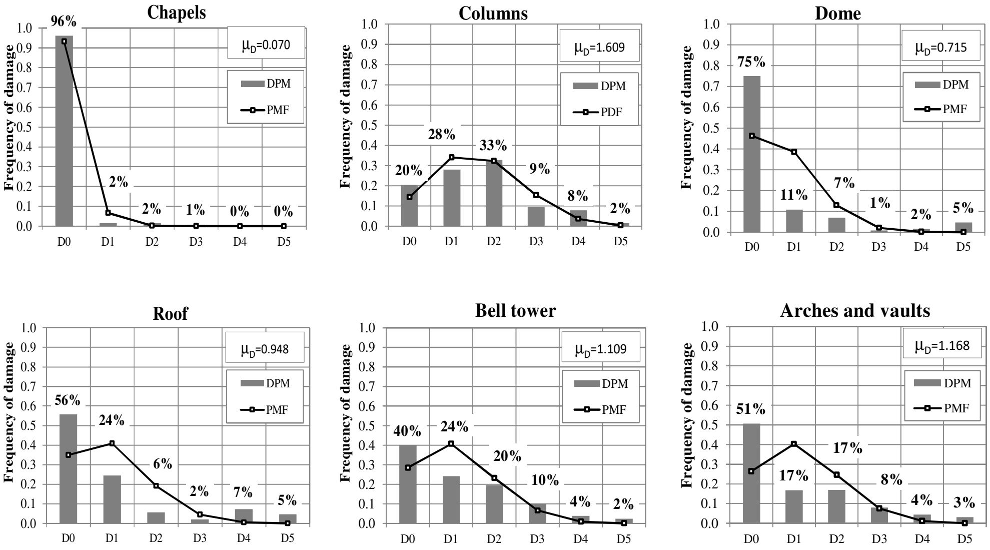

Fig. 13 – Damage Probability Matrix of the 64 observed churches vs binomial distribution

$$p_k = \frac{5!}{k!(5-k)!}\left(\frac{\mu_D}{5}\right)^k \left(1-\frac{\mu_D}{5}\right)^{5-k} \tag{2}$$

$$\mu_D = \frac{\sum_{i=1}^{n} D_{k,i}}{n} \tag{3}$$

$$\mu_D = \frac{\sum_{j=1}^{n}\sum_{i=1}^{m} d_{k,i,j}}{m \cdot n} \tag{4}$$

In the above equations, *n* is the number of churches and *m* the number of potential relevant mechanisms.

It can be observed that the binomial distribution is particularly able to retrieve back the probability of having a certain level of damage for a given earthquake. This is a significant outcome, as the above distribution depends on one parameter only, namely the mean damage μ_d. The latter could be preventively assessed based on the structural fragility of the analyzed churches, allowing the application of the above procedure as a predictive tool rather than as an observational analysis.

3 Seismic vulnerability assessment: definition and application

In order to define predictive models for predicting possible damage scenarios the expected mean damage μ_d should be preventively related to structural characteristics affecting the vulnerability of the churches of the analyzed population. To this purpose, a procedure based on the definition of vulnerability index of the church i_v given by the Italian Guidelines on Cultural Heritage (MiBACT, 2010) has been applied after a suitable modification. Therefore, each church has been partitioned into macro-elements, accounting the 28 likely mechanisms defined in the previous Section. Then, for each potential mechanism, fragility indicators and possible protection devices have been suitable defined and associated to a score ranging from 0 to 3. A score v_{ki}=0 applied to structural fragilities means that the mechanism itself does not represent a source of vulnerability for the building, whereas a score of 3 means that it is characterized by the maximum fragility and therefore it is prone to experience damage also for slight earthquakes. Similarly, a score $v_{k,pi}$=0 applied to a protection device related to the mechanism *i* means that it is absent or completely un-effective for the elimination of that collapse mechanism. On the contrary, a score of 3 indicates the maximum effectiveness of the protection device for the collapse mechanism under consideration.

In this study the evaluation of each score has been implemented by the definition of specific coefficients (i.e. z, w, f and η), which, for the sake of brevity are not fully provided in this paper, but are detailed in (De Matteis *et al.*, 2014) and are applied according to equations (5) and (6) for fragility indicators and anti-seismic devices scores, respectively:

$$v_{k,i} = \sum_{i=1}^{n} w \cdot z \cdot f \tag{5}$$

$$v_{k,p} = \sum_{i=1}^{n} w \cdot z \cdot \eta \tag{6}$$

In the above equations z is a Boolean coefficient, which can be equal to 1 or 0, depending on the presence/absence of the fragility indicator and protection devices, for eq. (5) and (6), respectively. The w coefficient is an importance factor ranging from 0 to 2. In eq. (5) it represents the potentiality of the fragility indicator in determining the vulnerability of the mechanism, as well as, in eq. (6), it is a measure of the capability of the applied protection device typology for inhibiting or limiting the mechanism development. For example, the vulnerability induced by irregularities has to be considered more important and influencing in those cases where there are irregularities both in elevation and in plan rather than in cases where only one irregularity is present. Similarly, constraining devices, as the buttresses or the ties, may have a different importance for out-of-plane mechanisms of a wall. The fragility coefficient f measures the effectiveness of the indicator and it ranges from 0 (in those cases for which the indicator does not influence the activation of the failure activation) to 1.5 (in case of fully vulnerability with respect to the onset of the failure). At the same manner, the efficiency coefficient η measures the effectiveness of the anti-seismic system that mitigated the possible failure. It also ranges from 0 to 1.5.

As an example, in the out of plane mechanism of the façade, the w coefficient for ties is set to 1, considering their effectiveness in overturning mechanism. If ties are actually present, the Boolean coefficient z is fixed equal to 1, whereas the efficiency coefficient η is set to 1.5 in case of totally effectiveness of devices. Similarly, the presence of opening at the corner has an important effect in the development of out of plane mechanism of façade. In this case, w is set to 1.5, z is fixed to 1 in case of presence, while the fragility coefficient f is set to 1.5 in case of large opening presence.

The scores described above have been used in order to obtain, for each building, the vulnerability index i_V given in eq. (7), according to the definition proposed in (MiBACT, 2010), which is calibrated in order to retrieve back values ranging from 0 to 1.

$$i_v = \frac{1}{6} \cdot \frac{\sum_{k=1}^{28} \rho_{k,i}(v_{k,i} - v_{k,p})}{\sum_{k=1}^{28} \rho_{k,i}} + \frac{1}{2} \tag{7}$$

In the above equation ρ_k is the importance factor already provided in eq. (1).

As a matter of example, in Figure 14, the vulnerability indices of the churches of the two Dioceses described in Section 2 are given.

Values ranging between i_V=0.376 (Madonna della Libera church, in the Sulmona Valva Diocese) and i_V=0.705 (St. Benedetto Abate church, in the L'Aquila Diocese) have been founded, with a mean value $\bar{i}_v$ of the obtained vulnerability indices equal to 0.53.

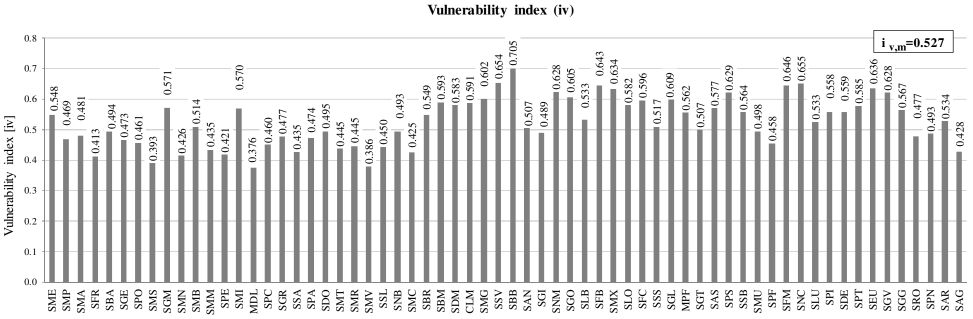

Fig. 14 - Vulnerability indexes for the 64 churches observed in the Sulmona-Valva and L'Aquila Dioceses.

The above mean value can be used for determining the expected mean damage for several earthquakes of macro-seismic intensity *I*, according to the eq. (8) already used in other studies, such as the ones described in (Lagomarsino and Podestà, 2004) and (Lagomarsino and Giovinazzi, 2006).

$$\mu_D = 2.5\left[1+\tanh\left(\frac{I+3.4375\cdot\bar{i}_v-8.9125}{3}\right)\right] \tag{8}$$

It is worth of being noticed that most of the 64 churches considered in this paper experienced a macro-seismic intensity *I* of about 6 (the average is 6.3, indeed). The mean damage that can be obtained for this earthquake intensity is equal to 1.75, which is almost equal to the mean value obtained downstream the damage reconnaissance activity (1.73), this meaning that the proposed methodology is quite reliable in reproducing the damage observed after L'Aquila Earthquake.

Obviously, this is a rough conclusion because a more precise evaluation of the reliability of eq. (8) should consider separate stocks of buildings for different earthquake intensity levels.

The methodology described above has been used in order to outline damage scenarios for several earthquake intensities, by getting out, for each damage level D_k, the related fragility curves. through the use of BPBDF, previously introduced and given in eq. (2). The outcome results allow to give back the probability of exceeding of a certain level of damage [$P\ (D \geq D_k) = \sum p_j$; with $1 \leq D_k \leq 5$], as a function of the macro-seismic intensity, considering the value of expected mean damage given by eq. (8).

The obtained fragility curves are shown in Figure 15. It is clear that the proposed fragility curves may represent a powerful tool to be used for outlining possible mitigation policies based on costs-benefits analyses and on the definition of acceptable risk for different levels of expected hazard. In addition, the proposed methodology allows to appreciate the reduction of seismic risk that can be pursued by applied strategically some retrofitting interventions on a stock of churches that can lead to a reduction of the vulnerability indices and, therefore, of the damage that they could undergo for a given earthquake intensity.

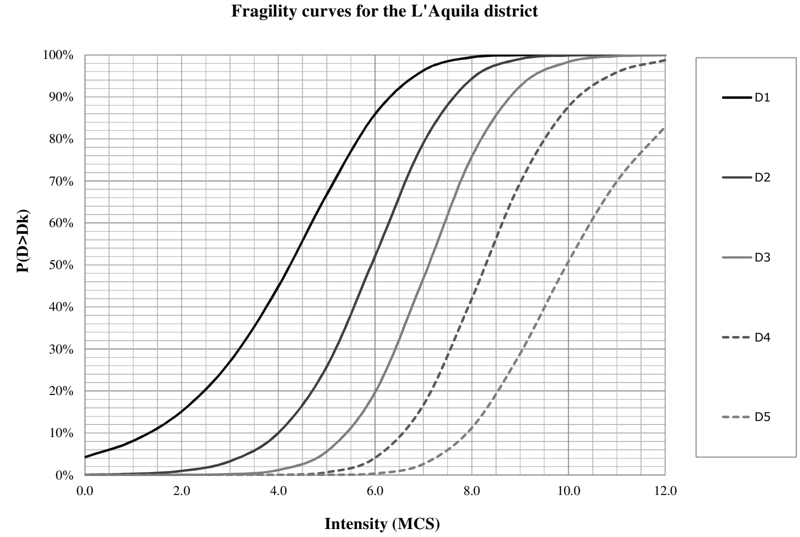

Fig. 15 – Fragility curves for three nave churches in the Sulmona-Valva and L'Aquila

dioceses.

4 Extension of the study: perspectives

It has been clearly proved that the above presented methodology, which is based on an approach similar to the one illustrated also in (MiBACT, 2016; Lagomarsino and Podestà, 2004) and (Lagomarsino and Giovinazzi, 2006), may be applied also for preventive purposes, through the use of eq. (2) and eqs. (5)-(8), rather than for assessing the damage scenarios observed after a specific earthquake by using eqs. (1)-(4). For this reason additional studies are in progress regarding different geographical areas. In particular two additional dioceses of Abruzzi have been identified, namely the Chieti-Vasto and the Lanciano-Ortona Dioceses (Figure 16).

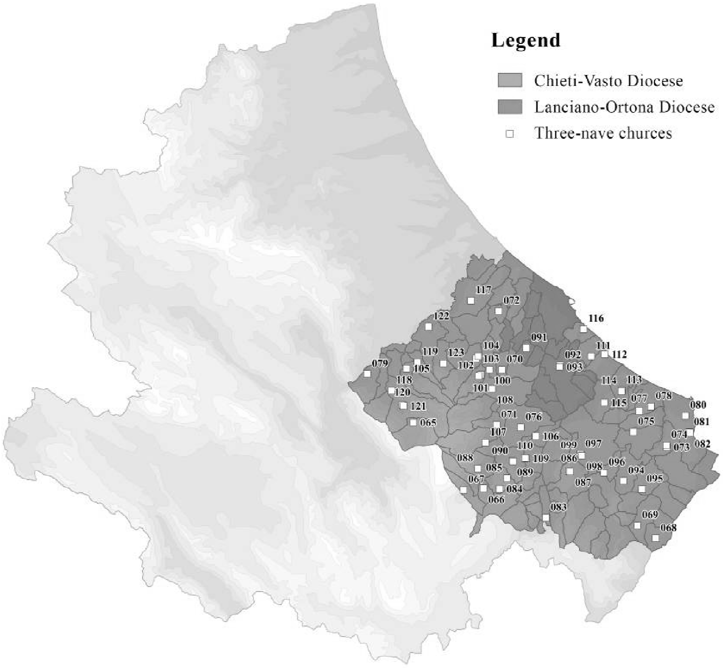

065	**SLM**	San Liberatore a Majella
066	**SMA**	Santa Maria Arabona
067	**SMM**	Santa Maria Maggiore
068	**SNB**	San Nicola di Bari
069	**SNB**	San Nicola di Bari
070	**STM**	Chiesa di San Tommaso
071	**SGT**	Chiesa di San Giustino
072	**CIM**	Chiesa dell'Immacolata C.
073	**MAC**	Santa Maria Assunta in Cielo
074	**MDL**	Chiesa Madonna di Loreto
075	**SLV**	Chiesa di San Salvatore
076	**SGV**	San Giovanni in Venere
077	**SMT**	San Matteo
078	**SPT**	San Pietro
079	**CED**	SS Cosma e Damiano
080	**SSV**	San Silvestro
081	**RMG**	San Remigio
082	**SMP**	Santa Maria del Popolo
083	**MEL**	Madonna dell'Elcina
084	**SLV**	San Salvatore
085	**MDP**	Madonna del Ponte
086	**SGV**	San Giovanni
087	**MDC**	Madonna di Carpineto
088	**SCZ**	San Cristinziano
089	**SDM**	San Domenico
090	**MDC**	Madonna della Cintura
091	**SCR**	Santa Croce
092	**SMM**	Santa Maria Maddalena
093	**SSV**	San Sabino Vescovo
094	**SMA**	Santa Maria assunta
095	**SMM**	Santa Maria Maggiore
096	**SNC**	San Nicola
097	**SMA**	San Michele Arcangelo
098	**MDR**	Santa Maria dei Raccomandati
099	**SMM**	Santa Maria Maggiore
100	**SNC**	Santi Nicola e Clemente
101	**MDC**	Madonna del Carmine
102	**SVT**	Santa Vittoria
103	**SGM**	San Giacomo
104	**SNC**	San Nicola
105	**MIB**	Madonna in Basilica
106	**SMM**	Santa Maria Maggiore
107	**SSA**	Santissimia Addolorata
108	**SMI**	Maria Santissima Incoronata
109	**SEU**	Sant'Eustachio
110	**MDM**	Madonna dei Miracoli
111	**SSL**	San Salvatore
112	**SSM**	Santa Maria Maggiore
113	**SPN**	San Panfilo
114	**SGB**	San Giovanni Battista
115	**MDG**	Madonna delle Grazie
116	**SMM**	Santa Maria Maggiore
117	**SMS**	Santa Maria della Serra
118	**SML**	Santa Maria della Libera
119	**SMG**	Santa maria delle Grazie
120	**SGS**	Santa Giusta
121	**SNB**	San Nicola di Bari
122	**SMM**	Santa Maria in Monteplanizio
123	**SBT**	San Bartolomeo

Fig. 16 – The three naves churches in Chieti-Vasto and Lanciano-Ortona dioceses

In such dioceses 59 three nave churches have been identified as shown in Figure 16. They represent the 18% of the whole religious heritage of the investigated area. These churches are quite different by the ones belonging to the inner Abruzzi discussed in the paper. In fact, the coastal part of Abruzzi is characterized by a low seismicity and, therefore, by churches with less significant stratifications, but also with more significant intrinsic vulnerability sources and less important anti-seismic systems. On the other hand, also the type of masonry is different with respect to the churches studied in this paper. In fact, fired clay bricks are widely used due to the presence of furnaces in the territory.

Also, the Campania region is characterized by very high seismic hazard and, above all, a considerable exposition factor. In fact, due to the geographical configuration and the cultural evolution of the Region, the population density is about four times larger than in Abruzzi. Moreover both the high presence and the different concentration of churches, due to the ancient history of the Campania region, reveals a potential very high seismic fragility of such area. For such a reason this territory represents an area of interest for the application of the above presented methodology.

In the whole, the Campania region is formed by 550 municipalities, 5 political districts and 24 ecclesiastical administrative boundaries, (i.e. the dioceses). In the Caserta district there are seven dioceses and about 300 parish churches have been identified (Figure 17). In such area churches are characterized by heterogeneous features in terms of geometric proportions and architectonic style and also structural typology.

In Figure 18 the relation between the location of some churches in Caserta (including both the main dioceses of the district, namely Caserta, Capua and Aversa, and the Alife-Caiazzo diocese, the latter nestled beneath the Matese massif) with population density in the area (a) and the seismic hazard (b) is shown. Despite the lower population density, the diocese of Alife-Caiazzo appears to be the most interesting one for the higher seismic hazard.

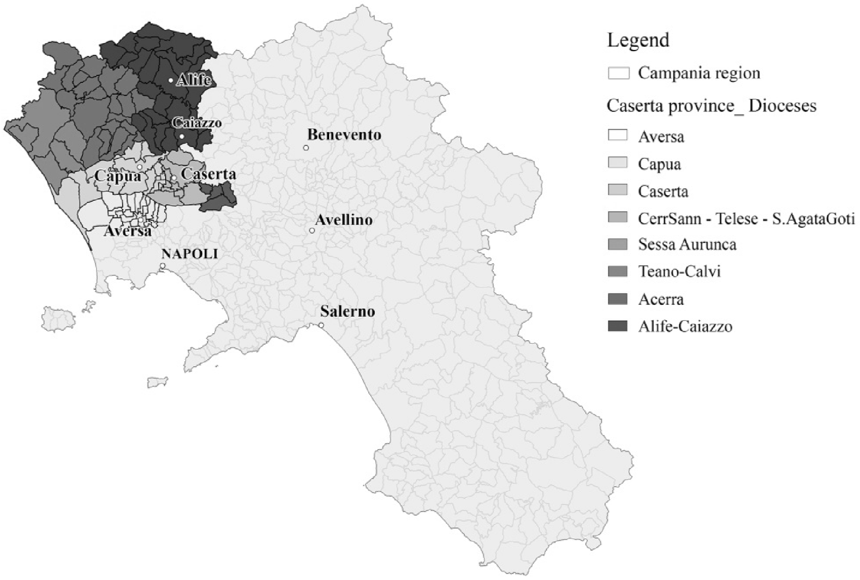

Fig. 17 –Dioceses localization of the Caserta political district.

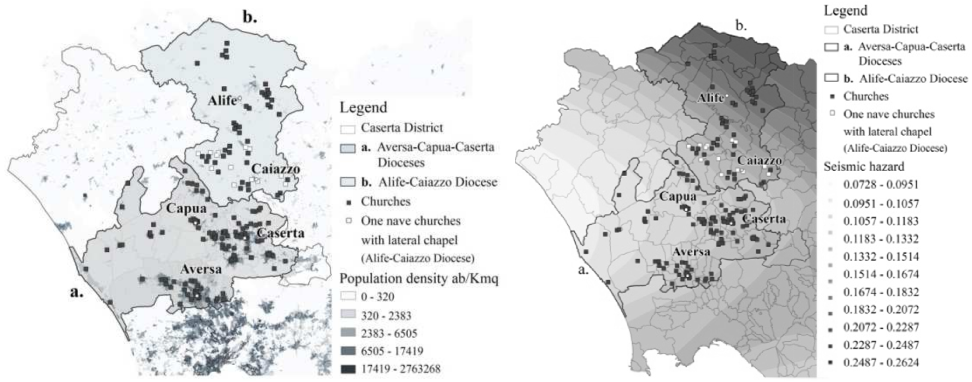

a) b)

Fig. 18 – Correlation between churches in Caserta with population density (a) and seismic hazard (b).

In this diocese more than 64 churches have been identified. Among them, about 45% are one nave with lateral chapel churches (Figure 19). Therefore, in such area, differently than in Abruzzi, one nave complex (with lateral chapels) churches seems to be the most interesting typology to be investigated.

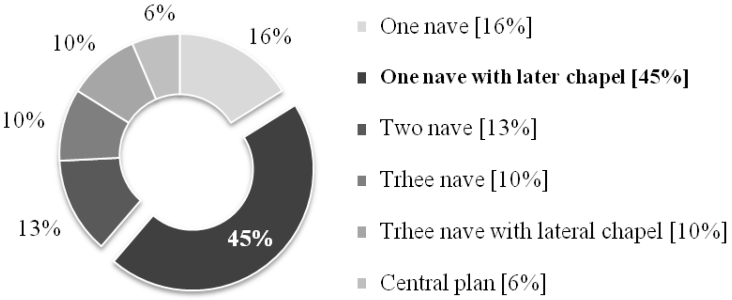

Fig. 19 – Churches typologies belonging to the Alife-Caiazzo diocese.

For such a church typology, the 57% has a single hall layout, characterized by a rectangular plan, a central nave and the lateral aisles with the same height. The transept is absent in 64% of cases; the 36% of churches has a Latin cross layout, with a transept crossing the main body. Finally, only the 7% has a basilica layout (Figure 20). Façades are often characterized by different structural and architectonic features with respect to other macro-elements, as they were usually erected after the construction of the main body of the church. For the same reason, generally, they are not structurally connected to the transversal walls. The most frequent façade layout is the salient façade (57%), which is characterized by a gable roof with tympanum on the central nave and two rakes upon the aisles. Façades with pitch roof characterize the 36% of the surveyed cases. Finally, only the 7% has a horizontal cornice, where the different height of the naves is concealed. The top of the façade is in 50% of cases sailing. They appear to be the most vulnerable typology, as the triangular elements at the top of both sides result very prone to develop overturning mechanisms due to the lack of restraining elements. Heavy thrusting (i.e. barrel and cross vaults) are present in the 71% of the analyzed cases, whilst light elements (i.e. visible timber truss and coffered ceiling or flat soffits) can be observed for the 29% of selected churches.

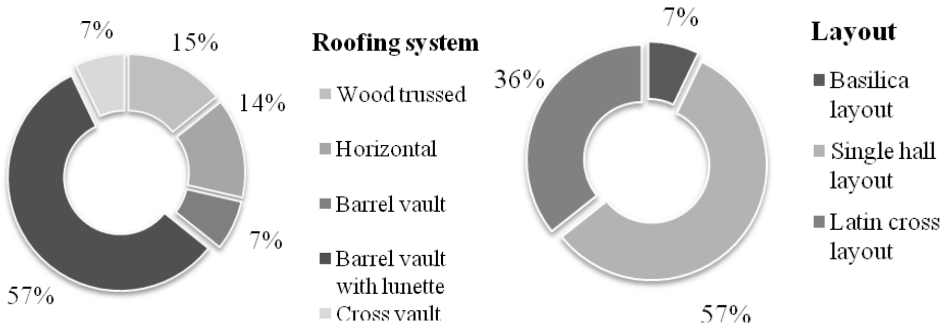

Fig. 20 – Layout (a) and roofing system (b) for one-nave with lateral chapel churches in the Alife-Caiazzo diocese.

5 Concluding remarks

This paper has dealt with the seismic vulnerability of masonry churches in light of the damage scenario observed after the 2009 L'Aquila earthquake. A reconnaissance activity focused on 64 three-naves churches, belonging to a wide territorial area hit by the earthquake, allowed to conclude that the frequency of pre-established damage levels, attained by churches in their entirety, can be well interpreted by a simple probabilistic distribution, that is the binomial probability function, which depends on one parameter only, namely the mean damage. On the other hand, it has been found that the binomial distribution is also able to well fit the frequencies of damage levels occurred for the single macro-elements.

Based on this outcomes, a methodology given by literature and suitably modified has been applied allowing the prediction of the aforementioned mean damage level and therefore for a preventive definition of fragility curves. In the whole, the proposed methodology appears to be effective for churches vulnerability assessment at regional scale; hence, it is worthy of being deepened more in details in future researches.

Provided the reliability of considered methodology, an underway research activity is now addressed to outline potential damage scenarios of churches of different Italian territories, focusing the attention on three additional diocese: 1) the Chieti-Vasto Diocese, 2) the Lanciano-Ortona Diocese and 3) the Alife-Caiazzo Diocese, in Campania. The results coming out from such studies could be used for defining appropriate strategies for seismic damage prevention at territorial scale.

References

1. Brando, G., Criber, E., De Matteis, G. (2015). The effects of L'Aquila earthquake on the St. Gemma church in Goriano Sicoli: Part II—fem analysis. *Bulletin of Earthquake Engineering*, vol. 13, pp. 3733–48.
2. Brandonisio, G., Lucibello, G., Mele, E., De Luca, A. (2013). Damage and performance evaluation of masonry churches in the 2009 L'Aquila earthquake. *Engineering Failure Analysis*, vol. 34, pp. 693-714.
3. Criber, E., Brando, G., De Matteis, G. (2015). The effects of L'Aquila earthquake on the St. Gemma church in Goriano Sicoli: Part I—Damage survey and kinematic analysis. *Bulletin of Earthquake Engineering*, vol. 13, pp. 3713–3732.
4. De Luca, A., Giordano, A., Mele, E. (2004). A simplified procedure for assessing the seismic capacity of masonry arches. *Engineering Structures*, vol. 26 (*13*), pp. 1915-1929.
5. De Matteis, G., Corlito, V., Criber, E., Guadagnuolo, M. (2016). Evaluation of earthquake damage scenario of churches at regional scale. Experiences in Abruzzi and perspectives in Campania, In: *Le Vie dei Mercanti, XIV International Forum*, World heritage and Degradation. Capri, June 17-18.

6. De Matteis, G., Criber, E., Brando, G. (2014). Seismic vulnerability assessment of masonry churches through the application of probabilistic methods". In: F. Peña, M. Chávez (eds.), *Proceeding of the 9th International Conference on Structural Analysis of Historical Construction (SAHC 2014)*, Mexico City, October 14-18.
7. De Matteis, G., Criber, E., Brando, G. (2016). Damage Probability Matrices for Three-Nave Masonry Churches in Abruzzi After the 2009 L'Aquila Earthquake". *International Journal of Architectural Heritage*, vol. 10 (*2-3*), pp. 120-145.
8. De Matteis, G., Mazzolani, F. M. (2010). The Fossanova Church: seismic vulnerability assessment by numeric and physical testing. *International Journal of Architectural Heritage*, vol. 4 (*3*), pp. 222-245
9. Ercolano, A. (1994). On a rigid-elastic model for monumental block structures", XI Congreso Nacional de Ingenieria De Mecanica, Valencia, Espana.
10. Giannantonio, R. (1988). Il terremoto del 1706 a Sulmona. La ricostruzione degli edifici sacri, OPUS, quaderno di storia architettura restauro, *Journal of the Department of Science and History of the Architectural*, Faculty of the University of Chieti-Pescara, n. I, Roma, 1988, pp. 119-144.
11. Giannantonio, R. (2000) Le chiese nel Settecento abruzzese, In: *L'Abruzzo nel Settecento*, Ediars, Pescara
12. Grunthal, G. (1998). European Macroseismic Scale. *Centre Européen de Géodynamique et de Séismologie*, Luxembourg, vol. 15.
13. Huerta, S. (2008). The analysis of masonry architecture: A historical approach. *Architectural Science Review*, vol. 51 (*4*), pp. 297-328.
14. Lagomarsino, S., Giovinazzi, S. (2006). Macroseismic and mechanical models for the vulnerability and damage assessment of current buildings, *Bulletin of Earthquake Engineering*, vol. 4 (*4*), pp. 415-443.
15. Lagomarsino, S., Podestà, S. (2004). Seismic Vulnerability of Ancient Churches: II. Statistical Analysis of Surveyed Data and Methods for Risk Analysis. *Earthquake Spectra*, vol. 20 (*2*), pp. 395–412.
16. Lourenço P.B, Roque J.A. (2006). Simplified indexes for the seismic vulnerability of ancient masonry buildings, *Construction and Building Materials*, vol. 20, pp. 200–208.
17. Ministry of Heritage and Cultural Activities MiBACT (2010). Circular n.26, Italian Code for protection of Cultural Heritage. Linee Guida per la valutazione e la riduzione del rischio Sismico del patrimonio culturale con riferimento alle norme tecniche per le costruzioni. Prot 10953 of 02/12/2010.
18. Rovida, R. Camassi, P. Gasperini and M. Stucchi (eds.), (2011). CPTI11, the 2011 version of the Parametric Catalogue of Italian Earthquakes. Milano, Bologna, http://emidius.mi.ingv.it/CPTI.

Palazzo Ducale in Parete: remarks on code provisions

Giorgio Frunzio[1], Luciana Di Gennaro[2], Mariateresa Guadagnuolo[1]
[1] Department of Architecture and Industrial Design, Università degli Studi della Campania
"Luigi Vanvitelli", Abbazia di San Lorenzo ad Septimum 81031 Aversa (CE), Italy
{giorgio.frunzio, m.guadagnuolo}@unicampania.it
[2] CO.GE.P.AR. Costruzioni Generali sas, Via delle Legioni 8/A - 80125 - Napoli, Italy
ing.lucianadigennaro@gmail.com

Sommario. The masonry have always been studied making reference to idealistic simplifications, that is to say basic and regular panels, made with homogenous techniques. To be realistic, getting to be confronted with a historical masonry of a centuries-old building, it is really difficult to apply the above said simplifications, the intriguing rules deduced from laboratory studies and also the numerical patterns more and more sophisticated.
Below are some considerations made in reference to a specific case study: Palazzo Ducale in Parete, of Caserta province. In this palace, it was quite impossible to imagine a model which could faithfully reflect the masonry history of over a thousand years. Some extremely simplified approaches are able to provide information about the capacity of the structure. Furthermore results from nonlinear static analyses are presented. Indications on the congruence between codes rules and results from numerical analyses performed according to the Italian seismic code are supplied. The results show that generally imposing the best approach for the generic case could not be satisfying for the particular one.

Keywords: Seismic Safety, Cultural Heritage, Masonry, Code provisions.

1 Introduction

Italian seismic codes issued until the Eighties did not explicitly require seismic-oriented calculations for masonry structures, but only to comply with some code requirements. Therefore several seismic codes devote a section to simplified dimensioning method for masonry buildings, for which the safety against collapse is deemed to be verified without explicit safety verification if buildings comply with some code provisions and rules. In fact, it is assumed that the respect of these requirements assures a suitable seismic behaviour, and thus an adequate safety. Such an exemption is usually applicable both to the new buildings and to the existing ones, if after possible retrofit they respect the code provisions.

Some requirements introduced in the new codes come from European legislation.

It needs a substantial certainty that the respect of code provisions and rules ensures a suitable building safety against earthquakes, without yielding confusion in the designers that employ the code.

Moreover, several code provisions drafted in Italy in past advised numerous limitations to the unreinforced masonry buildings to be retrofitted or built in seismic zones. A historical narration is presented below.

In recent years, several models characterized by different levels of complexity were developed and proposed for masonry structures, based on elements with different dimensionality (beam, shell or brick type) and aimed at different analysis types (Lourenço, 2002; Penna *et al.*, 2004; Chen *et al.*, 2008; Kappos *et al.*, 2002).

Among the simplified models advised in literature, frame type models based on the assemblage of beam elements are increasingly diffusing also for unreinforced masonry buildings (Magenes, 2006; Salonikios *et al.*, 2003; Sabatino *et al.*, 2011; Knox *et al.*, 2012). The models derive from other materials beam systems and then their extension to masonry structures is unavoidably affected by approximations, whose reach is somehow tricky to assess.

This paper focuses the attention on the seismic response of Palazzo Ducale in Parete, Caserta province, unreinforced masonry structure. The analyses are mainly aimed at evaluating the congruence between simplified dimensioning methods, as well as at comparing the Italian code provisions (NTC/08) with the ones provided by Eurocode 8 (EC8), and numerical results of analyses performed according to the procedure advised by Italian seismic code NTC/08.

2 Code provisions

It is possible to neglect the seismic valuation if some provisions are respected when masonry buildings are made up of regular stone blocks. The requirements to be complied to differ in each national code and with respect to European codes also.

First, it is necessary to point out that the Parete municipality was not considered seismic according to the classification made after the code 2-2-1974, n. 64 (L/74). Therefore, static analysis could be carried out with D.M.LL.PP. 20/11/1987 - Technical standards for the design, execution and testing of masonry buildings and for their consolidation (DM/87).

At the same time, D.M.LL.PP. 24/01/1986 - Technical standards related to buildings earthquake-proof (DM/86) was issued for seismic zones.

Afterwards, the code tool to be used in the seismic zones is D.M.LL.PP. 16/01/96 - Technical standards for construction in seismic areas (DM/96) and then NTC/08.

A concise comparison among rules of DM/96, EC8 and NTC/08 for simple masonry buildings is contained in (Guadagnuolo *et al.*, 2009). The NTC/08 provisions are similar to the ones of Eurocodice 8, but less restrictive, and are more severe than the DM/96 ones, above all for what concerns building and wall geometry.

Particularly EC8 limits the exemption of the explicit safety verification to the only ordinary buildings belonging to lower importance categories, located in zones of low and medium seismicity and satisfying the provisions and the rules specified in detail in the Section 9.7. Therefore, the code subordinates the exception to the building use, excluding both the buildings whose integrity during earthquakes is of vital importance (e.g. hospitals and fire stations) and the buildings whose seismic resistance is important in consideration of the consequences associated with collapses (e.g. schools and assembly halls).

Furthermore, the acceleration at site must be lower than $0.15 \cdot k \cdot g$, where k is a corrective factor depending on the shear walls length.

The NTC/08 requires instead the general criteria for regularity in plan and in elevation and with some specific provisions in terms of building geometry, masonry stress and constructive rules, detailed in the Section 7.8.1.9 for the new buildings, and integrated in the Section C8.7.1.7 of the related Instructions for the existing ones (Circolare/09, n. 617 - Instructions for the Application of the "New Technical Standards for Buildings"). No limitation dependent on the building importance category is introduced, whereas the building must not be located in zone 1, even though the acceleration at site is not limited.

Although NTC/08 have rules analogous to EC8, it is remarkable to note a smaller limitation on the length of resisting walls and on the allowable number of storeys in relation to the acceleration at site $S\cdot a_g$.

The specific provisions provided by the two above seismic codes are rather similar, but EC8 is more demanding for what concerns the shear walls length. In fact, a minimum of two walls in two orthogonal directions, each having length greater than 30% of the building length in the direction under consideration, is required in EC8 (except in cases of low seismicity), whereas in NTC/08 the required wall length (greater than 50% of the building dimension) may be provided by the cumulative length of the piers separated by openings.With regard to the exemption of the seismic verification it can be noticed that the code requirements that define the simple buildings must be absolutely suitable for structures of smaller importance and complexity also. Specifically, it needs a substantial certainty that the respect of code provisions and rules ensures a suitable building safety against earthquakes, without yielding confusion in the designers that employ the code. This means, for instance, that a large percentage of the buildings held simple from the seismic code, if subjected to numerical seismic verification, must provide a result congruent with the assumption. The above considerations assume special importance by considering that a great share of the Italian one-story and two-story masonry buildings are “simple” (more than 50% according to recent ratings).

3 Palazzo Ducale

The Palazzo Ducale in Parete, of Caserta province, is located in the historical centre, next to the ancient San Pietro Apostolo Church (Figure 1).

Palazzo Ducale is composed of a central rectangular nucleus (defensive tower), built probably between XI and XII century, and other blocks added in the following centuries. In particular, the palace, in its actual appearance, has a star-shaped structure with four angular and four connecting units, which represent the four principal fronts, shorter than the central tower. The building is made up by three stories and is in reinforced masonry (Figures 2 and 3). It is similar to many historic buildings frequently found in seismic areas of Southern Italy.

When the complex was built, it is quite probable that the roof was planar and the last level was the Noble floor. As a consequence, the existing configuration of the trussed roof should be dated back to the XVIII century.

This hypothesis firstly derives from the discovering of a rocky gargoyle in the South-West tower on the attic floor. Its pavement is characterized by remarkable grades towards the gargoyle, confirming the ancient hip of the rainwater. Furthermore in the historical map of the Feud of Parete, dated back to the XVII century and shown at the offices of the District, the palace is clearly of a level shorter than the one now existing (Figure 4).

Fig. 1 – Palazzo Ducale: Aerial photography

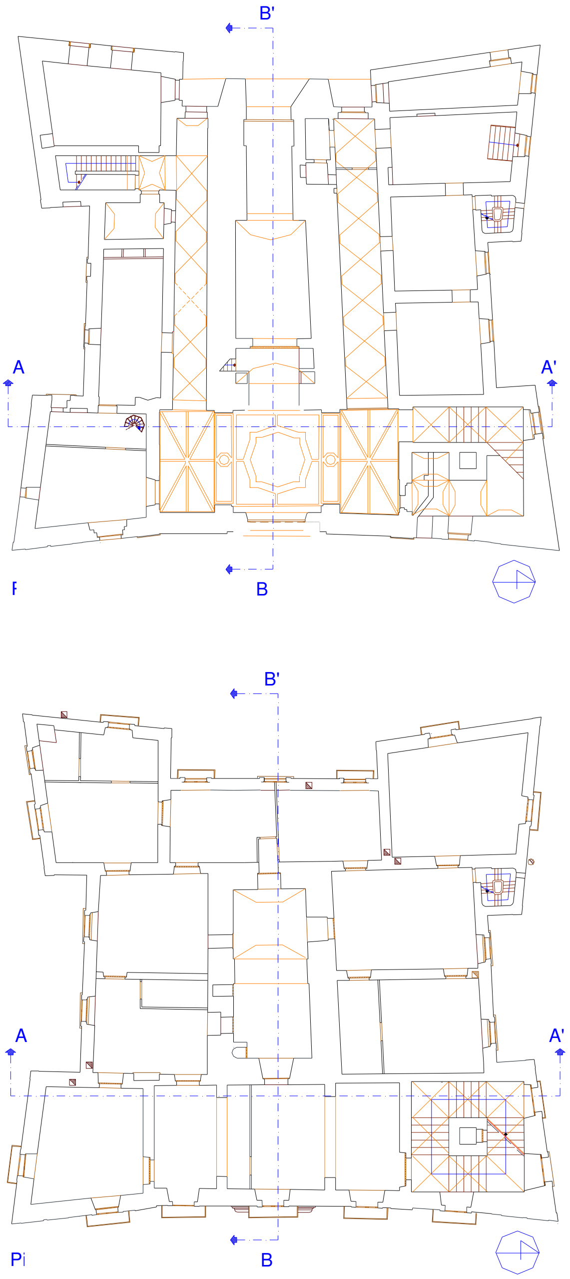

a)

b)

Fig. 2 – Palazzo Ducale: Ground (a) and Noble (b) floor map

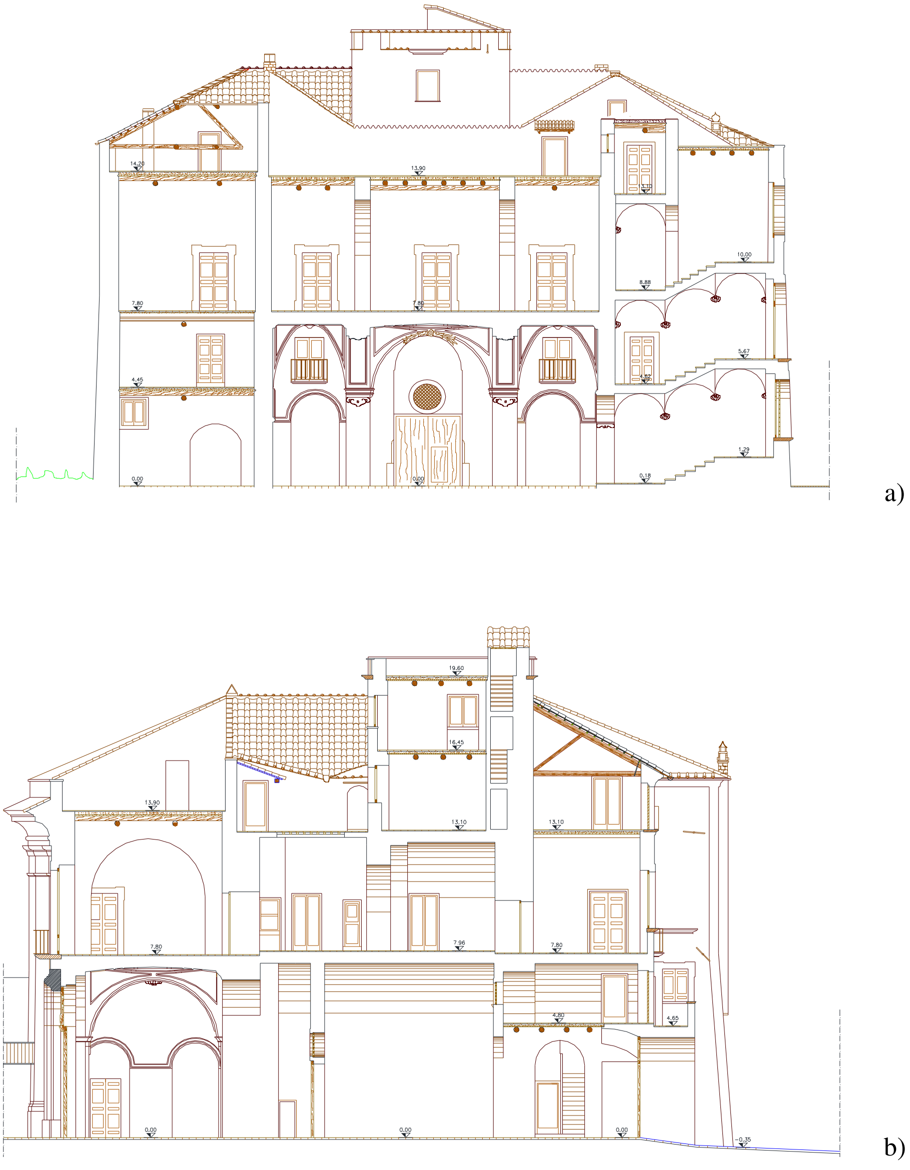

Fig. 3 – Palazzo Ducale: Section A-A' (a) and B-B' (b)

The whole structure is composed of grey tuff masonry of great quality made of squared blocks of average dimensions. The vertical load bearing masonries are of variable dimensions between 2 and 0.7 m for the central defensive tower, and 1 and 0.6 m for the structures of the palace (Figure 2).

Masonry with compression strength fm= 2.93 MPa, shear strength ft= 0.2 MPa, Young's modulus E = 3677 MPa, shear modulus G = 1202 MPa and weight w = 16 kN/m^3 were taken into account. The properties of the materials were obtained by laboratory tests on masonry samples taken in situ and non-destructive tests carried out in situ (Faella *et al.*, 2012).

The actual damage to the Ducal Palace, before the restoration intervention (Figure 5), after almost a thousand years since its construction, actually does not detect signs of seismic damage, despite the structural discontinuities, the negligence to which it was subjected, the presence of pushing elements and superfluous architecture still present until a few years ago.

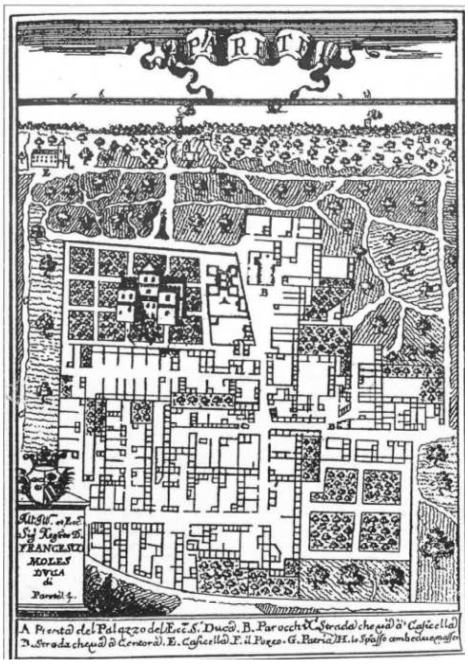

Fig. 4 – Parete Feud: cartographic excerpt (XVII sec)

Over the years, the building was undergoing operations such as bed joint reinforcement and repair cracks. Therefore, in general, every reinstatement operation carried out on the masonry has allowed to make masonry mechanical properties uniform within the structural analysis. The horizontal structures on the first level have been built with masonry cross vaults and barrel vaults, whereas the ones on the other levels have been made with

Fig. 5 – Palazzo Ducale: a) Principal front (Est); b) Internal view

wooden deckings of recent restoration, with a primary frame of chestnut wood beams, most of them originals, and secondary frame made of a double crossed planking of chestnuts and connectors of stainless steel.

The box-behaviour is entrusted to the use of steel tie rods partly ancient (recognizable because of bolted end-sticks) and partly of recent installation.

The roof is built with trusses of chestnut, a secondary structure made of chestnut binding rafters, a chestnut planking and functional package whose aim is to guarantee the water proofing, the thermal insulation and microcirculation of air under the mantle of bent tile (Figure 6).

4 Simplified dimensioning methods

In the DM/87, a simplified method to verify the masonry structures in precise hypothesis was proposed since there were not complex instruments

Fig. 6 – Palazzo Ducale: Principal front after restoration

available.

> *For buildings made by masonry composed of resistant elements, it is possible to neglect the static valuation if some provisions are respected:*
>
> *a. the building is made of three or less levels in or outside the ground;*
> *b. the plan of the building can be inscribed in a rectangle with a ratio between shortest and largest side not lower than 1/3;*
> *c. the slenderness of the masonry, in any case major than 12;*
> *d. the area of the section of the masonry resisting to the horizontal actions, mentioned in percentage compared to the total surface of the plan of the building, is not less than 4% in both the main directions except for the overhanging parts. The walls, shorter than 50 cm (length measured net of the opening), are not to be taken in consideration with reference to the percentage of the resistant masonry. These provisions must also show that:*
>
> $\sigma = N / (0,65\, A) \leq \sigma_m$
>
> *in which*
> *N: vertical total load at the base of the lower floor of the building*
> *A: total area of the load bearing walls of the masonry;*
> σ_m: mean value of masonry normal stress.

In the specific case of Palazzo Ducale:

a) the building is composed of three levels on the ground;
b) the rectangle in which the building is inscribed has the following dimensions: L_1=33.6 m and L_2=32.15 m, then the ratio between shortest and largest side is about 0.96 (>1/3);
c) the major measure observed of the ratio h/t is 10.17<12;
d) the resistant masonry in the parallel direction of x is, in percentage, 17.4%, while it is 23.82% in the parallel direction of y. Moreover, N=90429560 N, A=347300000 mm^2, f_k=2.05 N/mm^2, σ=0.40 N/mm^2 < σ_m=0.41 N/mm^2.

Therefore Palazzo Ducale satisfies all the required requirements, according to DM/87 it is possible to neglect the static valuation.

According to DM/86 for the masonry buildings in seismic zone some provisions must be respected; not pushing horizontal structures, effective toothing, insertion of reinforced concrete beams; size of the openings; resistant walls distance ($d \leq 7$ m); masonry characteristics and walls width.

These requirements were confirmed in the DM/96, some further requirements to neglect verification were introduced: Provisions about structural symmetry, about resistant walls distance ($d \leq 7$ m), about walls width, foundations, floor height ($h \leq 5$ m) and also about floor overcharge.

Attention was paid on mural portions above doors and windows openings, are therefore needed concrete or steel beams effectively linked in masonry and the openings have to be vertically aligned.

The resistant masonry area, expressed as percentage of the total building area is put in relation to seismic zoning and the tension validation is replaced by the:

$$\sigma = N/(0.50\ A) < \bar{\sigma}_m$$

Therefore Palazzo Ducale don't satisfies all the requirements, according to DM/96 is not possible to neglect the seismic evaluation.

In NTC/08 the regulation requirements are referred to building geometry, masonry, floors and joints characteristics and also to loads and strain states (Guadagnuolo *et al.*, 2008).

Referring to masonry characteristics, Palazzo Ducale is made of block masonry with effective toothing according to NTC/08.

Concerning geometric characteristics, the building is made of three floors in a seismic zone is where $S\ a_g < 0.35g$ (Figure 4). Floor height is above 3.5 m. This requirement was not present in EC8 and was 5 m in DM/96. Palazzo Ducale shows a symmetric plan in both x and y directions, with not relevant projections, complying the regulation requirements (projection length L_s < 25% overall length in that direction L_i).

In each direction there are at least two walls of neat length above the 50% of the overall length in the same direction. The requirements are met also by the perimeter alignments whose relative distance is more than 75% of the overall length in the perpendicular direction. The requirements in EC8 are not satisfied because only in the y direction the building shows the presence of two piers (the central tower walls) having length of 30% of the Li dimension. Another not satisfied requirement is the NTC/08 maximum walls distance (7m).

The openings are regular and aligned on all floors complying the vertical requirements. Floors can be considered as rigid because consolidation interventions on wooden ones are planned. Vaults can be considered not pushing due to presence of tie rods in both directions and on every floors.

The 75% of vertical loads is supported by the same system resisting the lateral loads. The ratio between the walls resisting section area and the total plan area is above the 5,5% in both directions referring to $0{,}15g<S \cdot a_g<0{,}20g$.

Finally the mean strength value on the ground floor piers is greater than the limit value of $0.25 \cdot (f_m/F_C)/\gamma_m$.

Palazzo Ducale don't satisfy all the required requirements, according to NTC/08, is then necessary to carry out the seismic verification as presented below.

5 Modelling and analyses performed

Nonlinear static analyses have been performed using a masonry-type frame model in 3MURI software. This modelling considers each masonry wall as an assemblage of beam/column-type elements, with rigid end offsets to reproduce the high stiffness and strength of the joint regions. Figure 7 shows the masonry-type frame model of the building.

In the pushover analysis, piers are assumed to have elastic-perfectly plastic behaviour. Hinges are located at both ends of each element and have strength threshold values deriving from both flexural and shear failure mechanisms. The failure criteria taken into account in the new Italian seismic code are considered. Likewise to the pier elements, an elastic-perfectly plastic behaviour is assumed for the spandrel beams, but lower strengths and limited ultimate displacements are assumed. The model is updated each time an element achieves a limit condition (resisting bending moment at one end, shear strength, axial strength).

However, many elements of uncertainty arising from this approach are due both to the pristine and intrinsic nature of the same methodology, and to the number of approximations and choices the engineer must make. These choices can arbitrarily conduct to a specific result, more than another one. To sum up, these uncertainties can be outlined as follows:

1. The horizontal spandrel is an element lacking in tensile strength, then it is really difficult to model them as components that react to bending moment stress;
2. The beam is considered homogeneous but this aspect is more likely a stretch taking in consideration that the masonry nature itself is often very varied;
3. The impossibility of valuing in a precise way the behaviour of all the vaults;
4. The local flexible behaviour of the deckings and the out-of-plane response of the walls cannot be considered in masonry-type frame model, which only analyzes the global response of the building.

It is also remarkable to say that the above examination turns out to be

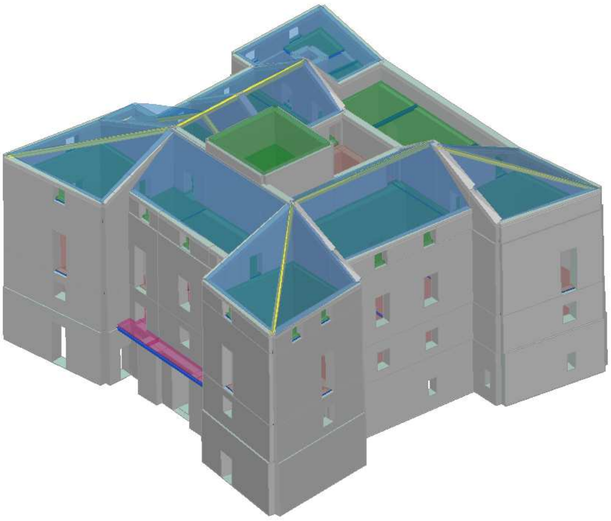

Fig. 7 – Palazzo Ducale: Structural frame type model

stressed during the analysis of the non-linear phase of the structure, which is also necessary to obtain believable results. The main resulting approximations are examined in (Guadagnuolo *et al.*, 2017).

5.1 Results

The non-linear static analysis procedure adopted in the EC8 and in the Italian seismic code, both for design and assessment, is based on a maximum displacement prediction, which depends on the definition of an equivalent elastic perfectly plastic s.d.o.f. structure, derived from a capacity curve obtained by a pushover analysis.

The maximum displacement capacity of masonry elements is a crucial parameter as significantly constrains the ULS safety verification in non-linear static analyses (Magenes *et al.*, 2009); it mainly depends on type of masonry, failure mode (shear failure mechanisms generally provide minor deformation capacity) and level of axial load (in general, the greater the axial load, the lower is the capacity in displacement of walls).

Nowadays, the check is always performed using the capacity spectrum method comparing the capacity of a structure with the demands of earthquake ground motion on it. In this context, the computed failure mechanism is definitely a discriminating factor in the displacement capacity of structures.

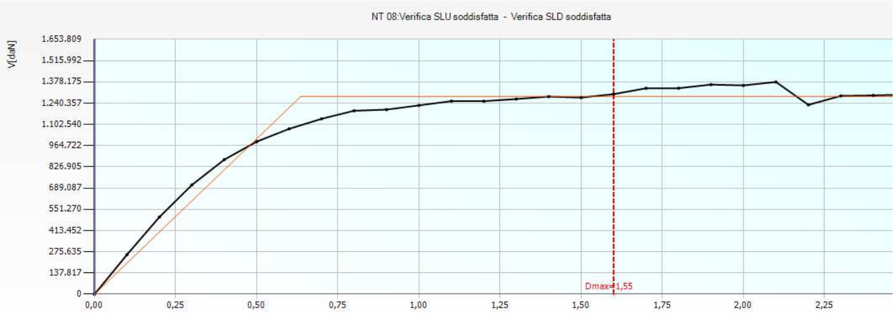

Fig. 8 – Code verification in X-direction by the capacity spectrum method

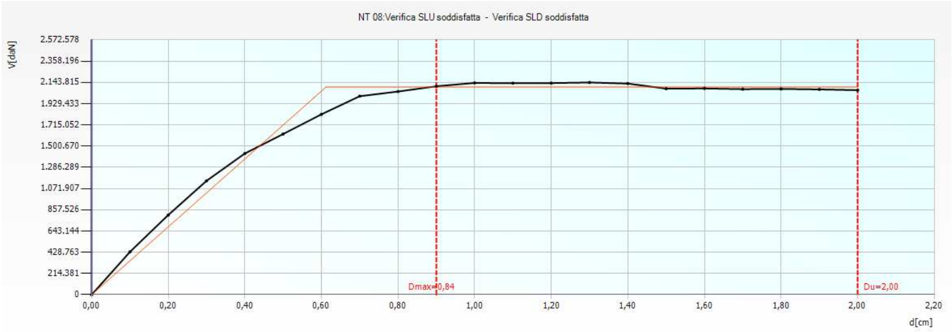

Fig. 9 – Code verification in Y-direction by the capacity spectrum method

In the pushover analysis the height-wise lateral load distribution proportional to the product of the displacements of the first vibration mode times the floor tributary masses (distribution d1) and the invariant height-wise lateral load distribution (d2) were assumed. No accidental eccentricity was considered in performing the pushover analysis, that is the lateral forces were applied at the mass center of the floors. The mass center at the roof was assumed as control point. The safety verification was performed according to the capacity spectrum method, applying the response spectrum shaped for Parete at the life safety limit state, (soil type B, topographic category T_1, nominal life V_n = 100 years, class of use C_u = 3, peak ground acceleration a_g = 0.189g, F_o = 2.52, soil coefficient S = 1.2, T_B = 0.17 sec, T_C = 0.52 sec, T_D = 2.36 sec).

Each analysis was performed until the building lateral capacity is reduced of 20% with respect to the maximum strength, due to the loss of contribution of the piers that achieve the limit failure displacement, or until any further increment in lateral load is impossible.

The safety verification has been performed in terms of displacement in the case of pushover analysis, according to the NTC/08 provisions.

The Figures 8 and 9 show the code verification (distribution d1) in X-direction and Y-direction respectively by the capacity spectrum method.

The Ducal Palace was verified according to the spectrum capacity model, while it did not meet the requirements for the simplified verification of

DM/96, NTC/08 and EC8. So these more stringent requirements might exclude many historical masonry buildings in our area.

6 Conclusions

The seismic response of Palazzo Ducale in Parete, Caserta province, unreinforced tuff masonry building is presented in the paper. The Parete municipality was not considered seismic according to the classification made after the code L/74. Therefore, static analysis could be carried out with DM/87. Afterwards, the code tool to be used in the seismic zones is DM/96 and then NTC/08. A historical narration has been presented.

Furthermore some extremely simplified approaches and results from nonlinear static analyses has been presented.

This paper focuses on how it is difficult to find a scientific approach which provides a complete response to the questions that a specialist asks about on homogeneous, incoherent and different from case to case material, such as masonry.

The studies of the scientific community, and their developments, make us able to get more and more in-depth information but it is necessary no to ignore the simplicity. The possibility of using simple methods based on the previous experience (when technicians did not disposed of modern instruments of calculus) allows to compare results with different approaches in order to be sure of the accuracy of the methodology chosen.

References

1. Alessandri, C., Mallardo, V. (2012). Structural assessments of the Church of the Nativity in Bethlehem. *Journal of Cultural Heritage*, vol 13 (*4*) pp. 61 - 69.
2. Benedetti, A., Cennamo, C, Monaco, M. (1999). Evoluzione del concetto di consolidamento delle strutture murarie attraverso le innovazioni tecnologiche, In: *Atti del III Convegno Nazionale Arco, Manutenzione e Recupero della Città Storica, Conservazione e Sicurezza*, Roma, Italy: Gangemi Editore.

3. Calderoni, B. (2013). La sicurezza di murature esistenti in relazione alla resistenza a compressione: considerazioni con riferimento ad un caso reale "Ingegneri Napoli" - *Notiziario dell'Ordine degli Ingegneri della Provincia di Napoli*, n. 3, pp. 6 -13.
4. Calderoni, B., Cordasco, E.A., Lenza, P., Pacella, G. (2011). A simplified theoretical model for the evaluation of structural behaviour of masonry spandrels. *International Journal of Materials and Structural Integrity*, vol 5 (*2-3*), pp. 192-214.
5. Cante, M. (1997). Il Palazzo Ducale di Parete. La storia, le vicende, i personaggi ...il future, Naples, Italy: Arte Tipografica Editore.
6. CEN European Committee for Standardization (2003). Eurocode 8: Design of structures for earthquake resistance - prEN 1998-1. Final Draft.
7. Cennamo, C., Chiaia, B., Di Fiore, M. (2010). Consideration about damage and retrofit of the SS. Rosario Church in Gesualdo (AV). In: Mazzolani F.M. (ed.) *International Conference Urban Habitat Constructions under Catastrophic Events*, CRC Press.
8. Chen, S.Y., Moon, F.L., Yi, T. (2008). A macroelement for the nonlinear analysis of in-plane unreinforced masonry piers. *Engineering Structures*, vol. 30 (*8*), pp. 2242-2252.
9. Corrado, G. (1912) Parete – Ricerche storiche e cenni descrittivi Parete – Ristampa del 1988.
10. D'Agostino, S. (2015). Between Mechanics and Architecture: the quest for the rules of the art, In: *Masonry Structures: Between Mechanics and Architecture*, pp. 1-19. Springer International Publishing.
11. De Chiara, N. (2011). Aversa e i suoi casali nel Settecento. La Carte di Fioravanti, Cuneo, Italy: NerosuBianco Editions.
12. De Guglielmo, F., Angelillo, M., Ribera, F. (2014). Masonry walls between art and science: historical building techniques and structural analysis according to Heyman's assumptions. In: F. Peña & M. Chávez (eds.) *SAHC 2014 - 9th International Conference on Structural Analysis of Historical Constructions*, Mexico City, October 14 – 17, pp.1-10.
13. Esposito, G., Frunzio, G., Monaco, M. (1993). Il tufo giallo napoletano. Caratteristiche meccaniche In: *Atti del Convegno Internazionale "Le pietre da costruzione: il tufo calcareo e la pietra leccese"*, pp. 705 - 713.
14. Faella, G., Frunzio, G., Guadagnuolo, M., Donadio, A., Ferri, L. (2012). The Church of the Nativity in Bethlehem: non-destructive tests for the structural knowledge, *Journal of Cultural Heritage*, vol 13 (*4*), pp. 27 - 41.
15. Frunzio, G., Gesualdo, A., Monaco, M. (2001). Constitutive behaviour of masonry In: Lourenco, P., Roca, P. (eds.), Historical Constructions, vol. 1, pp. 585- 590. University of Minho, Portugal: Multicomp Lda.
16. Frunzio, G., Monaco, M. (1997). Catene metalliche: interventi di restauro e di presidio. In: G. Mascolo, Materiali e tecniche per il restauro, vol. 1, pp. 283- 291. Cassino (FR), Italy: Idea Stampa Edizioni.
17. Gesualdo, A., Monaco, M. (2011). Seismic retrofitting techniques for existing masonry buildings, *Journal of Civil Engineering and Architecture*, vol. 5 (*11*), pp. 1011 - 1018.

18. Guadagnuolo, M., Faella, G. (2009). Risposta sismica di edifici “semplici” in muratura. *Ingegneria Sismica*, vol. 3, pp. 35-46.
19. Guadagnuolo, M., Faella, G. (2008). Seismic safety of simple masonry buildings, In: *Proc. Mercea – Seismic Engineering International Conference*, Reggio Calabria e Messina, Italy, July 8-11, Melville, New York, USA: American Institute of Physics.
20. Guadagnuolo, M., Faella, G., Donadio, A., Ferri, L. (2014). Integrated evaluation of the Church of S.Nicola di Mira: Conservation versus safety, *NDT & E International*, vol. 68, pp. 53-65.
21. Guerriero, L., Chiaccio, N. (2015). Il restauro del palazzo Ducale di Parete In: Terra Laboris 27 pp. 1 – 58 Armando Caramanica Editore, Marina di Minturno (LT), Italy.
22. Kappos, A.J., Penelis, G.G., Drakopoulos, C.G. (2002). Evaluation of simplified models for lateral load analysis of unreinforced masonry buildings, *Journal of Structural Engineering*, 128 (*7*), pp. 890-897.
23. Knox, C.L., Ingham, J.M. (2012). Non-linear equivalent frame modeling: Assessment of a two storey perforated unreinforced masonry wall, *NZSEE Annual Technical Conference & AGM*, 13-15, Christchurch, New Zealand.
24. Lourenço, P.B. (2002). Computations on historic masonry structures, *Progress in Structural Engineering and Materials*, vol. 4 (*3*), pp. 301-319.
25. Magenes, G. (2006). Masonry building design in seismic areas: recent experiences and prospects from a European standpoint, In: *Proc. First European Conference on Earthquake Engineering and Seismology* (13th ECEE and 30th General Assembly of ESC), Geneva, Switzerland, September 3-8.
26. Magenes, G., Modena, C., da Porto, F., Morandi, P. (2009). Seismic behavior and design of new masonry buildings: Recent developments and consequent effects on design codes, In: *Proc. of the Workshop “Eurocode 8 Perspectives from the Italian Standpoint”*, Napoli, Italy.
27. Ministero delle Infrastrutture e dei Trasporti (2008). Norme Tecniche per le Costruzioni, D.M. 14.01.2008, Official Bulletin n. 29, February 4 (in Italian).
28. Ministero delle Infrastrutture e dei Trasporti (2009). Circolare 2 febbraio 2009, n. 617 - Istruzioni per l’applicazione delle “Nuove norme tecniche per le costruzioni” di cui al D.M. 14 gennaio 2008.
29. Ministero dei Lavori Pubblici (1987). Norme tecniche per la progettazione, esecuzione e collaudo degli edifici in muratura e per il loro consolidamento. D.M.LL.PP. 20/11/1987.
30. Ministero dei Lavori Pubblici (1989). Circolare 4 gennaio 1989 N. 30787, Istruzioni in merito alle norme tecniche per la progettazione, esecuzione e collaudo degli edifici in muratura e per il consolidamento.
31. Ministero dei Lavori Pubblici (1996). Norme tecniche per le costruzioni in zone sismiche, D.M.LL.PP. 16.01.1996, Gazzetta Ufficiale n. 29 del 5 Febbraio 1996.
32. Penna, A., Resemini, S., Falasco, A., Lagomarsino, S. (2004). Non linear seismic analysis of masonry structures, In: *Proc. 13th World Conference on Earthquake Engineering*, Vancouver, Canada, August 1-6.

33. Rapone, D., Brando, G., Spacone, E., De Matteis, G. (2014). Seismic vulnerability assessment of the old historic centre of Scanno. In: *HERITAGE 2014 4th International Conference on Heritage and Sustainable Development*, Green Lines Institute.
34. Ribera, F., Angelillo, M., De Guglielmo, F. (2016). Criteri e Interventi per il Consolidamento degli Edifici in Muratura: La Chiesa della Pietà dei Turchini a Napoli. In: Colloqui AT.e 2016. MATER(i)A. Materials | Architecture | Technology. Energy/Environment | Reuse. (Interdisciplinary) | Adaptability Matera 12-15 Ottobre 2016 Roma Gangemi Editore Pag.1-10.
35. S.T.A. Data srl (2015). Manuale di utilizzo del software 3Muri, Torino.
36. Sabatino, R., Rizzano, G. (2011). A simplified approach for the seismic analysis of masonry structures. *The Open Construction and Building Technology Journal*, vol. 5 suppl 1-M7, pp. 97-104.
37. Salonikios, T., Karakostas, C., Lekidis, V., Anthoine A. (2003). Comparative inelastic pushover analysis of masonry frames. *Engineering Structures*, vol. 25 (*12*), pp.1515-1523.

Thrust network analysis of masonry vaults

Francesco Marmo[1], Daniele Masi[1], Daniele Mase[1], Luciano Rosati[1]

[1] Dipartimento di Strutture per l'Ingegneria e l'Architettura,
Università di Napoli Federico II
{f.marmo, daniele.masi, rosati}@unina.it, danielemase@gmail.com

Summary. We illustrate the assumptions underlying a recent reformulation of the Thrust Network Analysis (TNA), a methodology that allows one to model internal forces within masonry arches and vaults by means of a network of thrusts. The proposed version of the TNA allows for analysis of structures of complex geometry, with openings or free edges, subjected to the combined action of vertical and horizontal loadings. Several numerical examples are reported to show how the method can be applied to evaluate the limit geometric proportions, e.g., minimum thickness, or the horizontal load bearing capacity of masonry arches and vaults.

Keywords: Masonry, Arch, Vault, Limit thickness, Load bearing capacity

1 Introduction

Stresses in masonry arches or vaults at failure are usually considerably lower than those required to cause material failure; hence stability of such kind of structures is basically due to their shape and self-weight magnitude and distribution (Heyman, 1995). This peculiarity has been an advantage prior to the development of structural analysis since stability of a full scale structure could be assessed on a scale model: the real structure was erected by scaling up the dimensions of a prototype or an existing structure while keeping constant the relative proportions (Huerta, 2008).

One of the first rational approaches to the stability of masonry arches was found in the analogy between the shape of masonry arches in equilibrium and that of hanging cables in tension. Such an analogy (or catenary principle) is known since the 17th century and was first presented by Robert Hooke (Hooke, 1676) in a famous anagram; the analogy was ultimately motivated by Heyman thanks to the limit analysis principles (Heyman, 1982).

The Thrust Network Analysis (TNA) is a methodology based on Heyman's principles and is used for modeling stresses in masonry vaults as a discrete network of forces in equilibrium with gravitational loads. It was recently contributed by O'Dwyer (O'Dwyer, 1999) and fully developed by Block and coworkers in recent times (Block, 2009; 2014). Alternative approaches can be found in (Ercolano, 1994; 1995; Angelillo et al., 2010; Fraternali, 2010; Tralli et al., 2014).

Reducing the bias by the quoted authors in favor of a graphical interpretation of the method, Block's version of the TNA has been recently reformulated by discarding the dual grid and focusing only on the primal grid, thus significantly enhancing the computational performances of the method (Marmo and Rosati, 2017). Such a reformulation of the TNA also includes horizontal forces in the analysis as well as holes or free edges in the vault. The coefficient matrices entering the solution scheme have been obtained by assembling the separate contribution of each branch, thus avoiding the ad-hoc node numbering and branch orientation required by Block's approach.

Numerical examples, regarding the application of the method to the evaluation of limit thickness or horizontal bearing capacity of some vaulted structures are illustrated to show the effectiveness and robustness of the TNA in assessing the safety conditions of existing masonry vaults.

2 Thrust network analysis

Equilibrium of vaulted structures can be studied by considering a network of thrusts, i.e. compressive forces acting within the structure in equilibrium with the applied loads. Such a network, from now on denominated *thrust network*, is described by means of N_n nodes and N_b branches connecting pairs of nodes.

The thrust network is not used to geometrically model the volume occupied by the vaulted structure, as it happens, e.g., in finite element modelling; rather it is representative of the thrust forces that equilibrate the external load-

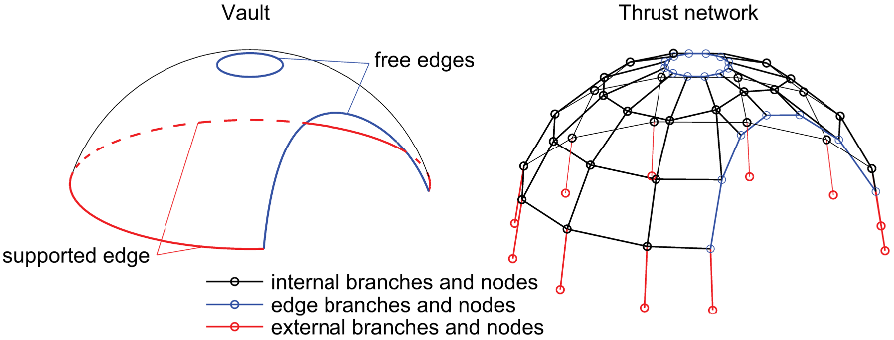

Fig. 1 – Restrained and free edges of a vault and their representation by external and edge branches and nodes

ings. Accordingly, branches of the network represent the direction of the thrust forces, similarly to the branches of a funicular polygon.

The n-th node of the network is characterized by its position (x_n, y_n, z_n), in a three-dimensional Cartesian reference frame in which z is the vertical direction. The generic branch b of the network is identified by two end nodes and the corresponding value of the thrust force, denoted as $\mathbf{t}^{(b)} = (t_x^{(b)}, t_y^{(b)}, t_z^{(b)})$.

Nodes are loaded both by an external force $\mathbf{f}^{(n)} = (f_x^{(n)}, f_y^{(n)}, f_z^{(n)})$, whose value depends on the region of influence of the node, and by the thrust forces pertaining to branches connected to the node; being compressive by assumption, these thrust forces are oriented towards node n. Branches can be labelled as *internal*, if they represent a thrust force that is interior to the network, *edge* if they represent forces that are on a free edge or *external* if they represent the support reactions, see, e.g., Figure 1. Following the same logic, the set of nodes is split into N_i internal nodes, N_e edge nodes and N_r external (restrained) nodes, where only one external branch converges. Hence one has $N_n = N_i + N_e + N_r$.

While the horizontal position of internal and external nodes is assigned, the coordinates of the edge nodes are unknown. This is due to the fact that relevant edge branches, i.e. branches connected by edge nodes, will be funicular, in both the horizontal and vertical directions, of the internal thrusts and of the applied loads converging to edge nodes.

Equilibrium conditions are employed in order to evaluate branch thrusts, heights of internal and external nodes and the coordinates of boundary (edge) nodes. Such equations are written only for internal and edge nodes, while external nodes are used uniquely as endpoints of external branches that, in turn, represent support reactions. Accordingly, external nodes and branches are used to model the constraints of the vaulted structure.

2.1 Equilibrium of nodes

Following the approach illustrated in (Marmo and Rosati, 2017), the horizontal equilibrium of internal nodes is enforced by the $2N_i$ equations

$$\begin{cases} \mathbf{C}_i \hat{\mathbf{t}}_h + \mathbf{f}_{x,i}\, r = \mathbf{0}_i \\ \mathbf{S}_i \hat{\mathbf{t}}_h + \mathbf{f}_{y,i}\, r = \mathbf{0}_i \end{cases} \tag{1}$$

where $\mathbf{C}_i$ and $\mathbf{S}_i$ are coefficient matrices containing the cosine directors of the horizontal projections of the network branches; the subscript i indicates that only equilibrium of internal nodes is considered. The vector $\hat{\mathbf{t}}_h$ appearing in (1) collects branch reference thrusts $\hat{t}_h^{(b)} = r t_h^{(b)} = r\sqrt{t_x^{(b)2} + t_y^{(b)2}}$, while r is an unknown parameter and $\mathbf{0}_i$ is a vector of N_i zeros.

The coefficients $\mathbf{C}_i$ and $\mathbf{S}_i$ in (1) are obtained by selecting the rows relevant to the internal nodes from two coefficient matrices $\mathbf{C}$ and $\mathbf{S}$ that, in turn, contain the cosine directors of all branches of the network and are constructed by assembling branches' contributions for all N_i nodes of the network. In particular, the generic branch b, which connects nodes n and $m^{(b)}$, contributes to the b-th column of the matrices $\mathbf{C}$ and $\mathbf{S}$ by the terms

$$\mathbf{C}^{(b)} = \frac{1}{\ell_h^{(b)}} \begin{bmatrix} x_n - x_m^{(b)} \\ x_m^{(b)} - x_n \end{bmatrix} \qquad \mathbf{S}^{(b)} = \frac{1}{\ell_h^{(b)}} \begin{bmatrix} y_n - y_m^{(b)} \\ y_m^{(b)} - y_n \end{bmatrix} \tag{2}$$

that are assembled into rows n and $m^{(b)}$, being

$$\ell_h^{(b)} = \sqrt{\left(x_n - x_m^{(b)}\right)^2 + \left(y_n - y_m^{(b)}\right)^2} \tag{3}$$

Also the vertical equilibrium is enforced for all internal nodes of the network, so as to obtain a system of N_i linear equations that can be expressed in matrix form as

$$\mathbf{D}_i\mathbf{z} + \mathbf{f}_{z,i}\, r = \mathbf{0}_i \tag{4}$$

The entries of $\mathbf{D}_i$ are a combination of the reference thrust densities of the network branches and the subscript i is used to indicate that only the equilibrium of internal nodes is considered. The entries of $\mathbf{D}_i$ are computed by assembling the thrust densities of all branches. Specifically, for a generic branch b connecting nodes n and $m^{(b)}$ of the network, the coefficients

$$\mathbf{D}^{(b)} = \frac{\hat{t}_h^{(b)}}{\ell_h^{(b)}} \begin{bmatrix} 1 & -1 \\ -1 & 1 \end{bmatrix} \tag{5}$$

are evaluated and assembled in rows n and $m^{(b)}$ of columns n and $m^{(b)}$ of a coefficient matrix $\mathbf{D}$. Thus, the entries of the matrix $\mathbf{D}_i$, appearing in equations (4), are obtained by selecting the rows of $\mathbf{D}$ corresponding to internal nodes.

The vector $\mathbf{z}$ collects unknown heights of all nodes, while $\mathbf{f}_{z,i}$ is the vector of the vertical loads applied to the internal nodes.

The parameter r in formula (4) is used to obtain several solutions to the same vertical equilibrium equation. In particular, it is clear from this equation that, keeping $\mathbf{f}_{z,i}$ constant, lower values of r are associated with lower values of $\mathbf{z}$ and vice versa. Additionally, r is used to transform the reference horizontal thrusts to actual horizontal thrusts, according to the above mentioned relation $\hat{t}_h^{(b)} = r t_h^{(b)}$. Hence, such a parameter can be used to obtain an equilibrated configuration of the network characterized by higher values of thrust, i.e. maximum thrust solution, corresponding to a shallower thrust network, i.e. lower values of $\mathbf{z}$, and vice versa.

2.2 Solution procedure for networks subjected to horizontal and vertical loads

In presence of horizontal nodal forces equations (1) and (4) expressing in turn horizontal and vertical equilibrium of nodes are coupled by means of the unknown r so that their solution is more cumbersome to achieve. However if one sets a tentative value for r, say it $r^{(j)}$, the corresponding reference thrusts $\hat{\mathbf{t}}_h^{(j)}$ are evaluated by solving the linear optimization problem

$$\min_{\hat{\mathbf{t}}_h}\left(\mathbf{i}_b\cdot\hat{\mathbf{t}}_h^{(j)}\right)\ \text{such that}\ \begin{cases}\begin{bmatrix}\mathbf{C}_i\\ \mathbf{S}_i\end{bmatrix}\hat{\mathbf{t}}_h^{(j)}=-\begin{bmatrix}\mathbf{f}_{x,i}\,r^{(j)}\\ \mathbf{f}_{y,i}\,r^{(j)}\end{bmatrix}\\ \hat{\mathbf{t}}_h^{(j)}\geq\hat{\mathbf{t}}_{h,\min}\end{cases}\tag{6}$$

obtained from the horizontal equilibrium equations (1). In formula (6) $\mathbf{i}_b=(1,1,...,1)$ has N_b entries so that the product $\mathbf{i}_b\cdot\hat{\mathbf{t}}_h^{(j)}$ represents the sum of all components of $\hat{\mathbf{t}}_h^{(j)}$. This particular choice for the objective function is useful to obtain a solution $\hat{\mathbf{t}}_h^{(j)}$ that is as close as possible to the assigned minimum values $\hat{\mathbf{t}}_{h,\min}$.

The reference thrusts $\hat{\mathbf{t}}_h^{(j)}$ obtained from the solution of (6) can be used to evaluate the x and y coordinates of the edge nodes by means of the equations

$$\begin{aligned}\mathbf{x}_{i+e}^{(j)}&=-\left[\mathbf{D}_{i+e\,i+e}^{(j)}\right]^{-1}\left[\mathbf{D}_{i+e\,r}^{(j)}\mathbf{x}_r+\mathbf{f}_{x,i+e}\,r^{(j)}\right]\\ \mathbf{y}_{i+e}^{(j)}&=-\left[\mathbf{D}_{i+e\,i+e}^{(j)}\right]^{-1}\left[\mathbf{D}_{i+e\,r}^{(j)}\mathbf{y}_r+\mathbf{f}_{y,i+e}\,r^{(j)}\right]\end{aligned}\tag{7}$$

Depending on the geometry and connectivity of the network, the procedure above described modifies the positions of internal and edge nodes. In general this effect is negligible for internal nodes but, should their position be significantly modified by the application of formula (7), external loads need to be recomputed.

Once the j-th estimate of the horizontal position of all nodes is assigned, nodal heights and a new $(j+1)$ estimate of r are evaluated from (4) by solving the linear optimization problem

$$\min_{\mathbf{z},r}\pm r^{(j+1)}\ \text{such that}\ \begin{cases}\left[\mathbf{D}_i^{(j)}\ \mathbf{f}_{z,i}\right]\begin{bmatrix}\mathbf{z}^{(j)}\\ r^{(j+1)}\end{bmatrix}=\mathbf{0}_i\\ \begin{bmatrix}\mathbf{z}_{\min}\\ 0\end{bmatrix}\leq\begin{bmatrix}\mathbf{z}^{(j)}\\ r^{(j+1)}\end{bmatrix}\leq\begin{bmatrix}\mathbf{z}_{\max}\\ +\infty\end{bmatrix}\end{cases}\tag{8}$$

where $\mathbf{z}_{\min}$ and $\mathbf{z}_{\max}$ are the lower- and upper-bounds imposed by the designer to the nodal heights of the network. Usually, for internal nodes they can be set equal to the heights of the intrados and extrados of the vault; alternatively, to reach a full compression of the vault section, they can be set equal to the heights corresponding to the lower and upper third of the vault thickness.

The objective function $\pm r$ is set equal to $+r$ if one looks for a solution that minimizes r, thus obtaining the shallowest configuration of the network. Conversely, one sets $-r$ to obtain a solution that maximizes r, which is relevant to the deepest network. In both cases, positive values of r are estimated since the constraint $0 \leq r \leq +\infty$ is imposed in (8).

If the difference between two successive estimates of r is lower than a given tolerance, i.e.

$$\left| \frac{r^{(j+1)} - r^{(j)}}{r^{(j)}} \right| < tol \tag{9}$$

the procedure is terminated. If the previous condition is not fulfilled, the procedure is reiterated by solving (6), (7) and (8), and verifying again the fulfilment of (9).

Once solution is reached, actual branch's thrusts are evaluated by composing the horizontal and vertical reference thrusts of each branch, according to

$$t^{(b)} = \sqrt{\left[t_h^{(b)}\right]^2 + \left[t_z^{(b)}\right]^2} = \frac{\hat{t}_h^{(b)}}{r} \frac{\ell^{(b)}}{\ell_h^{(b)}} \tag{10}$$

where $\ell^{(b)}$ is the length of the b-th branch.

2.3 An optimized iterative solution procedure in absence of edge nodes

In case the network is lacking of edge nodes, an optimized procedure can be employed. Actually, since the conditions in (6) are linear, the generic solution $\hat{\mathbf{t}}_h^{(j)}$, corresponding to a given value of $r^{(j)}$, can be expressed as

$$\hat{\mathbf{t}}_h^{(j)} = \hat{\mathbf{t}}_h^{(0)} + \frac{r^{(j)}}{r^{(1)}} \left[\hat{\mathbf{t}}_h^{(1)} - \hat{\mathbf{t}}_h^{(0)}\right] \quad \text{if} \quad r^{(j)} \geq r^{(1)} \tag{11}$$

where $\hat{\mathbf{t}}_h^{(0)}$ and $\hat{\mathbf{t}}_h^{(1)}$ are the reference thrusts returned by the linear optimization (6) in which it has been set $r = r^{(0)} = 0$ and $r = r^{(1)} = r_1$, r_1 being an arbitrary positive scalar.

It is straightforward to verify that (11) fulfils both the equality and the inequality conditions on the right-hand side of (6), provided that $r^{(j)} > r_1$; hence thrusts associated with $r^{(j)}$ can be assumed as a solution that fulfils horizontal equilibrium of nodes and the linear optimization problem (6) can be solved only twice.

Once $\hat{\mathbf{t}}_h^{(0)}$ and $\hat{\mathbf{t}}_h^{(1)}$ have been evaluated, the reference thrusts $\hat{\mathbf{t}}_h^{(1)}$ are used in (8) to obtain the nodal heights and the tentative value $r^{(j+1)}$. This estimate of r is used in (11) to obtain a new value of reference thrusts that, in turn, is used again in (8) to obtain a new estimate of r. The procedure is iterated until the convergence condition (9) is fulfilled. Finally, at convergence, formula (10) is applied to evaluate actual values of thrust in each branch of the network.

3 Numerical examples

Four numerical examples are reported below. The first two of them concern the analysis of a three centred arch while the last two address the full three-dimensional analysis of two spherical domes that only differ for the presence of a circular opening at the top. For all examples two solutions are shown, corresponding to the deepest and shallowest configurations of the network, respectively. Indicating by r_d the value of r associated with the deepest configuration of the network and by r_s the one associated with the shallowest configuration, it is shown that the ratio r_s/r_d is related to the safety factor of the arch or vault and it can be used to characterize a limit condition for the structure.

3.1 Minimum thickness of a three-centred arch

Let be considered the three-centred arch of Figure 2 having centres $C_1 \equiv (-2m, 0m)$, $C_2 = (0m, -4m)$, $C_3 = (2m, 0m)$, radii $R_2 = 6m$, $R_1 = R_3 =$

$R_2 - \sqrt{2^2+4^2} \approx 1.53\,m$ and springing angles $\alpha = \beta = \pi/10$. The arch has thickness $t = 0.4\,m$ and is subjected only to self-weight, this is evaluated by considering a weight per unit area equal to $\rho = 8\,kN/m^2$. The corresponding deepest and shallowest configurations of the thrust network are reported in Figure 3.

Thus is clear how the two network configurations are visibly different. This is confirmed by the value of the ratio $r_s/r_d = 1.6585$ that, being different from unity, emphasizes that forces within the arch have the possibility to adapt to changes in the loading condition or to settlements of the structure.

A second analysis has been carried out by progressively reducing the thickness of the arch to the value $t = 0.234\,m$, which corresponds to a unit value of the ratio r_s/r_d. Indeed, as shown in Figure 4, the deepest and shallowest configurations of the network are indistinguishable, so that the minimum

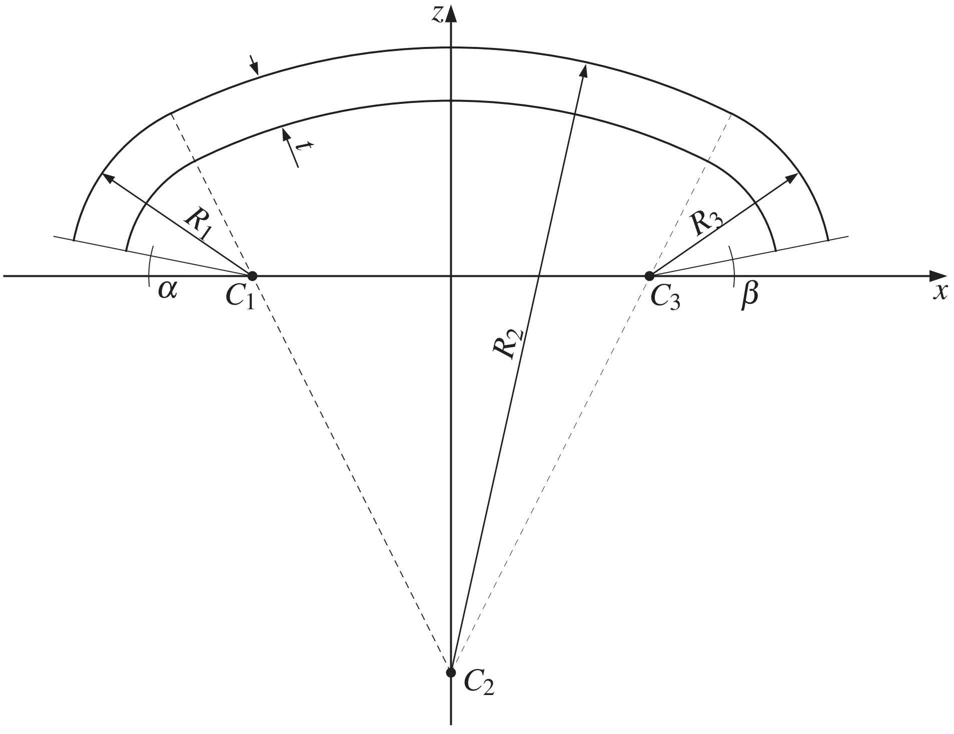

Fig. 2 – Three-centred arch

limit value of the arch thickness has been reached.

3.2 Maximum horizontal load of a three-centred arch

The same approach used for determining the minimum arch thickness can be exploited to evaluate the horizontal load bearing capacity of the arch. The arch under consideration is the same described earlier and has thickness $t = 0.4m$. Horizontal forces are kept proportional to the vertical ones so that the analysis has been carried out by progressively increasing the value of the ratio f_h/f_z until the deepest and shallowest configuration of the network become coincident as in Figure 5. Such a condition is characterized by $r_s/r_d = 1$ and,

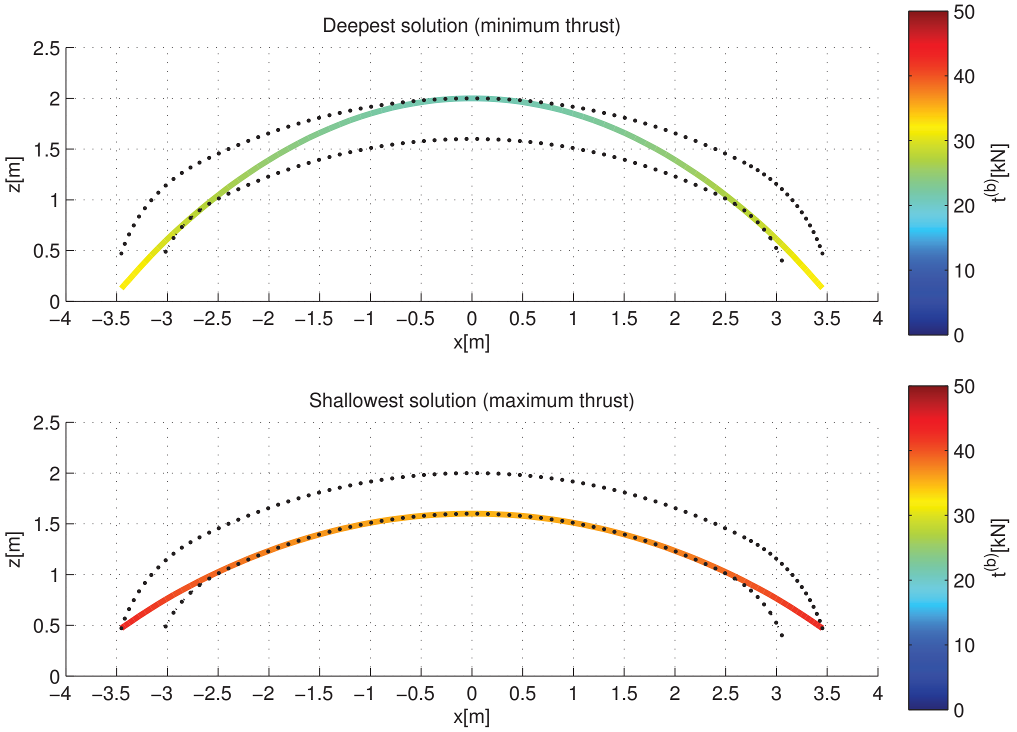

Fig. 3 – Three-centred arch: deepest and shallowest network configurations for the arch of thickness $t = 0.4m$ subjected to self weight

in this case, it is attained when the ratio between the horizontal and vertical loads reaches the limit value $f_h/f_z = 0.821$.

3.3 Maximum horizontal load of a hemispherical dome

In order to show how this approach can also be applied to three-dimensional networks, we consider a hemispherical dome of diameter $D = 4\,m$ and thickness $t = 0.2\,m$. Branches of the network are directed along the meridians and parallels of the dome, converging to a node placed at the top.

Both vertical and horizontal forces are applied at the nodes of the network

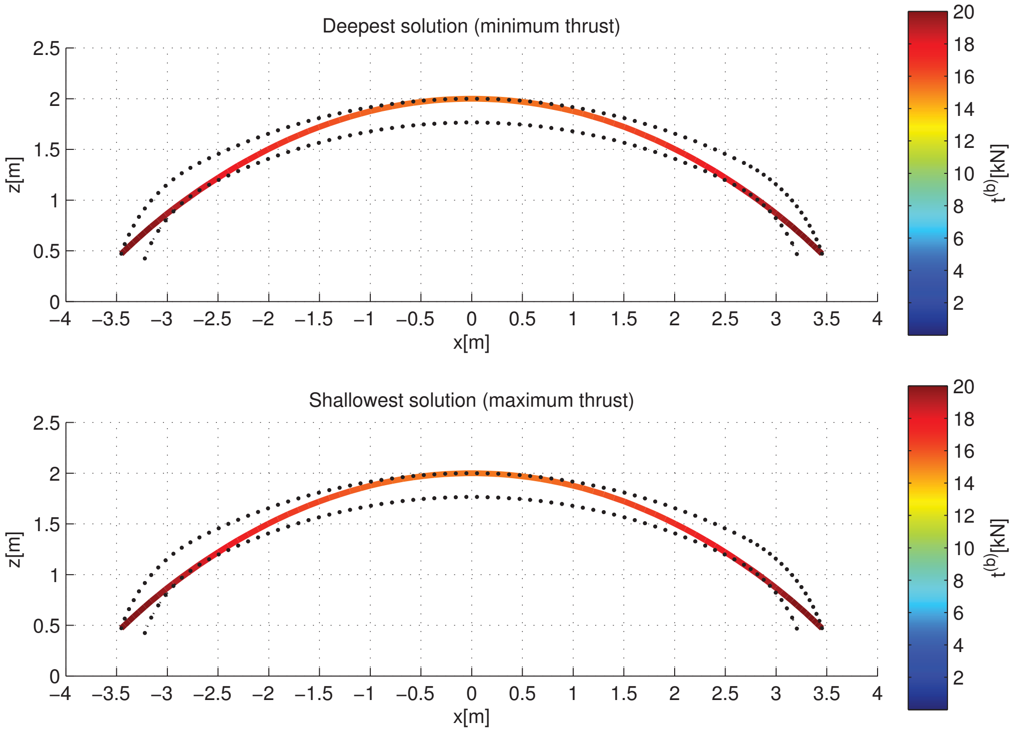

Fig. 4 – Three-centred arch: coincidence of the deepest and shallowest network configurations for the arch subjected to self weight emphasizes that the minimum thickness ($t = 0.234\,m$) has been attained

proportionally to the self-weight of the dome. In particular, vertical forces applied at the top node is $f_z = 6\,kN$, nodes of the first parallel, i.e. the one closer to the top node, is $f_z = 4\,kN$, while the forces $f_z = 6\,kN$, $f_z = 8\,kN$ and $f_z = 12\,kN$ are applied at the nodes of the second, third and fourth parallel, respectively. Horizontal forces act along the x axis and are kept proportional to the vertical ones.

The ratio r_s/r_d attains the value 1.4029 if horizontal forces are ignored, confirming the visible difference between the deepest and shallowest configuration of the thrust network, see, e.g. Figure 6.

The analysis of the dome subjected to the combined action of vertical and

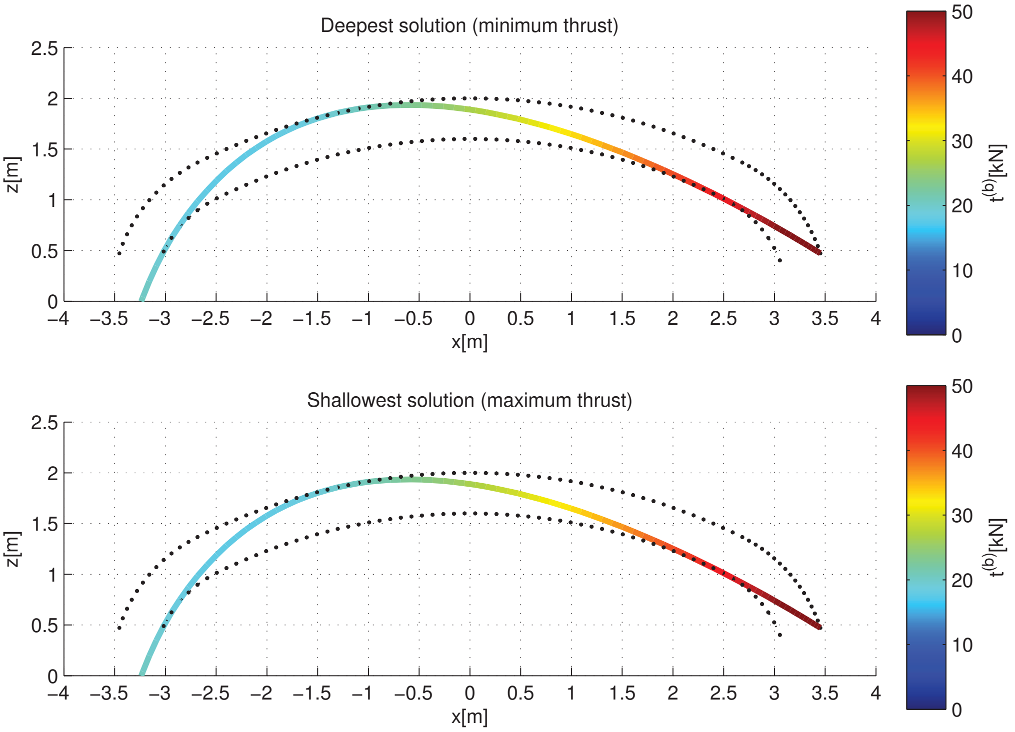

Fig. 5 – Three-centred arch: deepest and shallowest network configurations for the arch having thickness $t = 0.4\,m$ subjected to vertical and horizontal loads applied according to the ratio $f_h/f_z = 0.821$

horizontal loads has been carried out by progressively increasing the value of the ratio f_h/f_z till the attainment of the limit condition $r_s/r_d = 1$. As shown in Figure 7, an intermediate solution, corresponding to $f_h/f_z = 0.08$, still exhibits a visible difference between the deepest and shallowest configurations of the thrust network, confirmed by the value attained by the ratio $r_s/r_d = 1.3215$.

Finally, the limit value of the horizontal forces, corresponding to $r_s/r_d = 1$, is attained when $f_h/f_z = 0.159$; in this case the deepest and the shallowest configurations of the network, reported in Figure 8, become indistinguishable.

3.4 Maximum horizontal load of a hemispherical dome with oculus

As a final example, the dome analysed in the previous subsection in which a circular opening (oculus) of diameter $d = 0.8\,m$ is present at the top is considered. The corresponding network is obtained from the one used for the previous example by deleting the top node and all branches converging to it. Loadings are also equal to the ones considered in the previous example, except for the force applied to the top node.

Thrust network configurations corresponding to the network subjected to self-weight is reported in Figure 9, in which the difference between the deepest and shallowest configurations of the thrust network is quantified by the ratio $r_s/r_d = 1.5195$. Such a ratio reduces as the horizontal forces are applied. In particular, for a value of horizontal forces corresponding to the ratio $f_h/f_z = 0.08$, the deepest and shallowest configurations of the network, plotted in Figure 10, are still sensibly different; this is witnessed by the value of the ratio $r_s/r_d = 1.4355$. Conversely, when the limit value of horizontal loads is attained, i.e. when $f_h/f_z = 0.171$, the deepest and shallowest configuration of the network are coincident, see, e.g., Figure 11, and the ratio r_s/r_d attains a unit value.

By comparing Figure 8 and Figure 11, and the corresponding limit values of the ratio f_h/f_z, associated with a ratio $r_s/r_d = 1$, that amount respectively to 0.171 and 0.159, one infers that the seismic safety of the dome with oculus is greater than the one pertaining to the hemispherical dome.

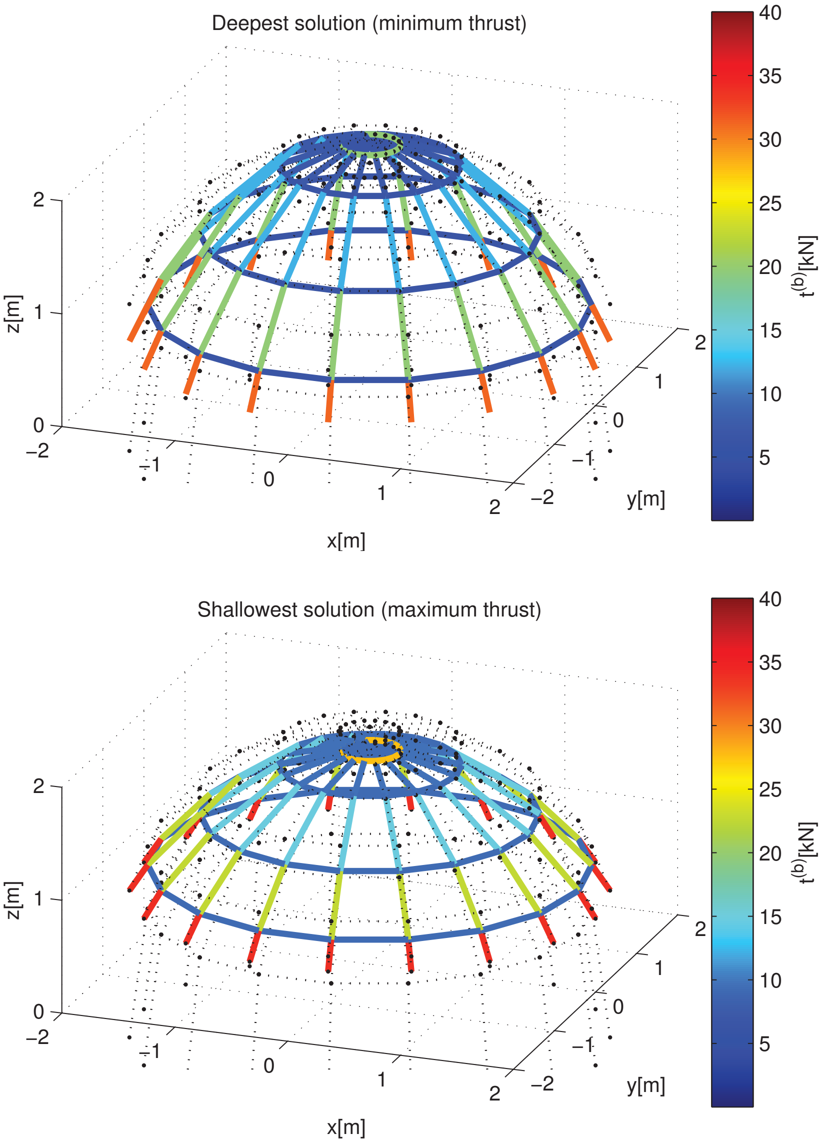

Fig. 6 – Hemispherical dome: deepest and shallowest network configurations for dome subjected to self-weight

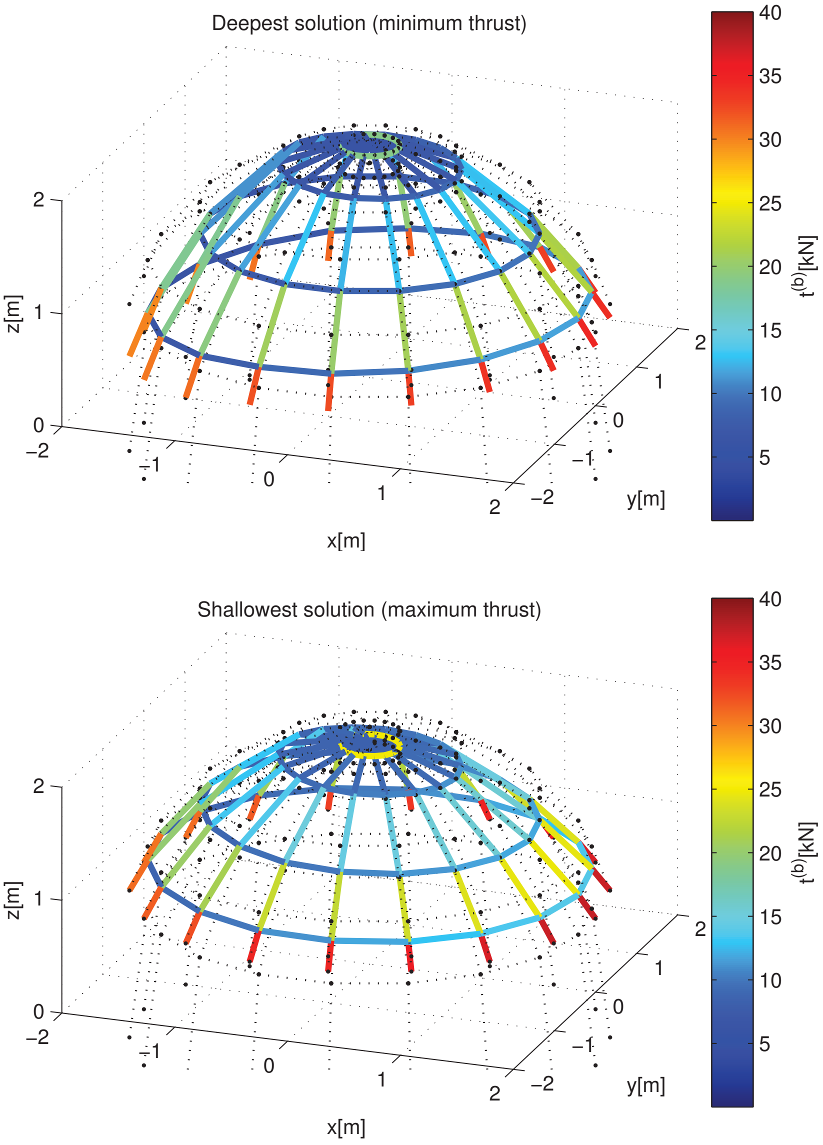

Fig. 7 – Hemispherical dome: deepest and shallowest network configurations for dome subjected to self-weight and horizontal loads applied according to the ratio $f_h/f_z = 0.08$

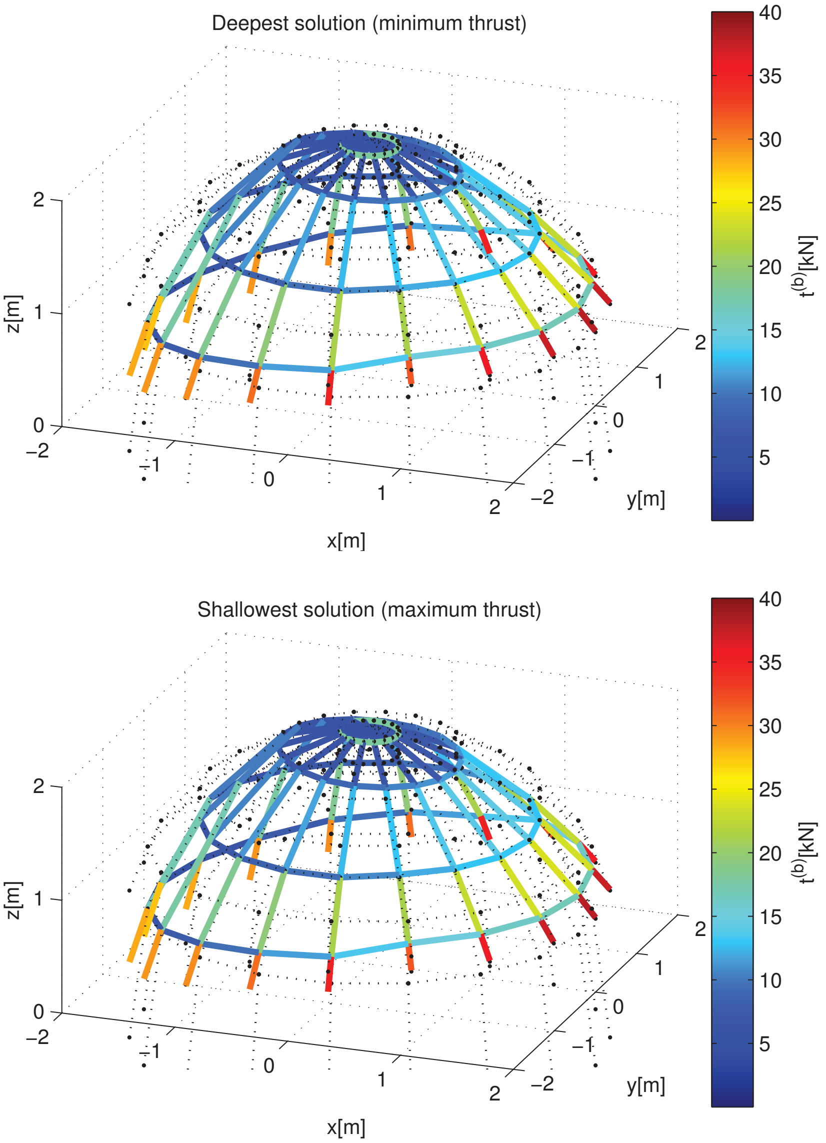

Fig. 8 – Hemispherical dome: deepest and shallowest network configurations for dome subjected to self-weight and horizontal loads applied according to the ratio $f_h/f_z = 0.159$

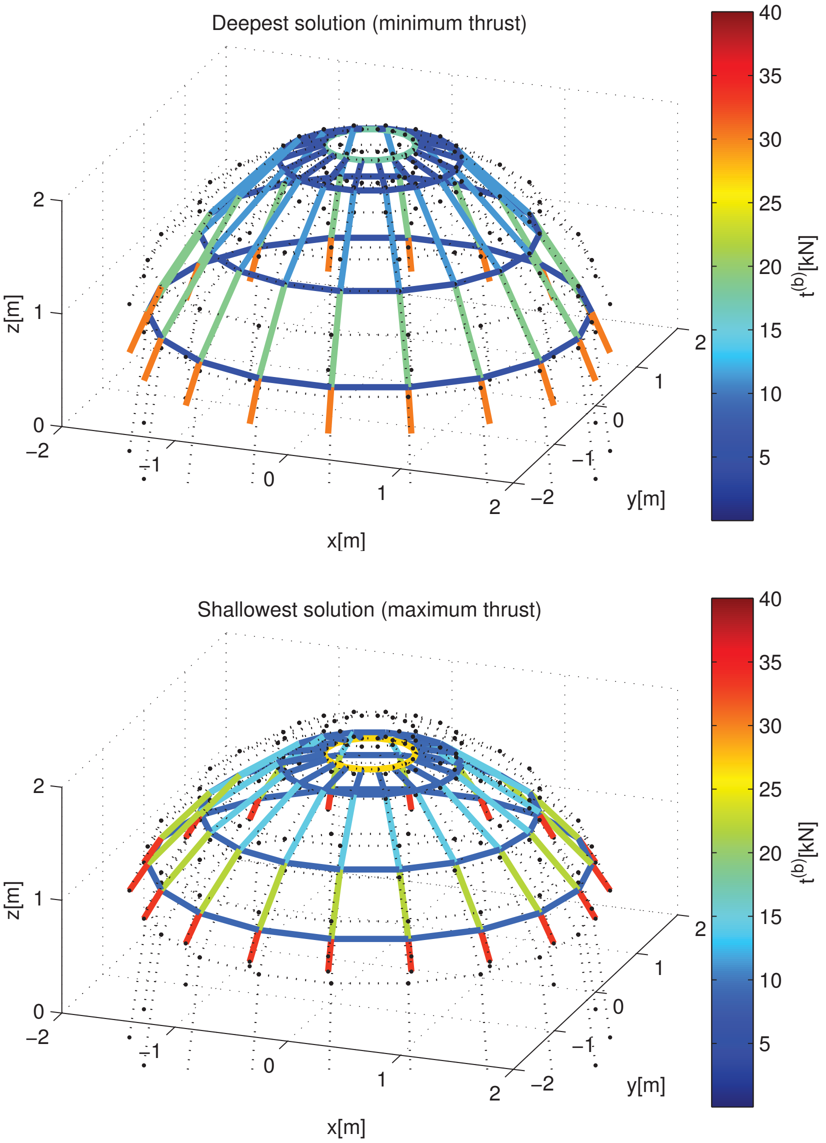

Fig. 9 – Dome with oculus: deepest and shallowest network configurations for dome subjected to self-weight

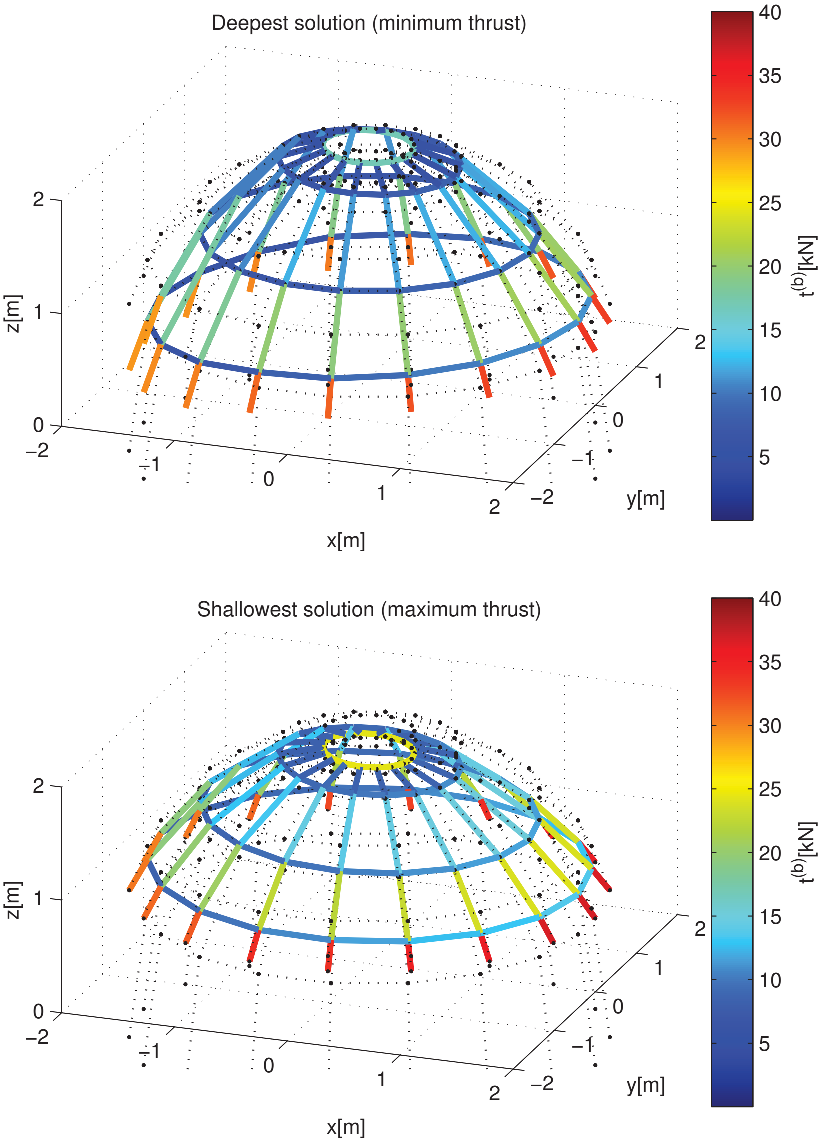

Fig. 10 – Dome with oculus: deepest and shallowest network configurations for dome subjected to self-weight and horizontal loads applied according to the ratio $f_h/f_z = 0.08$

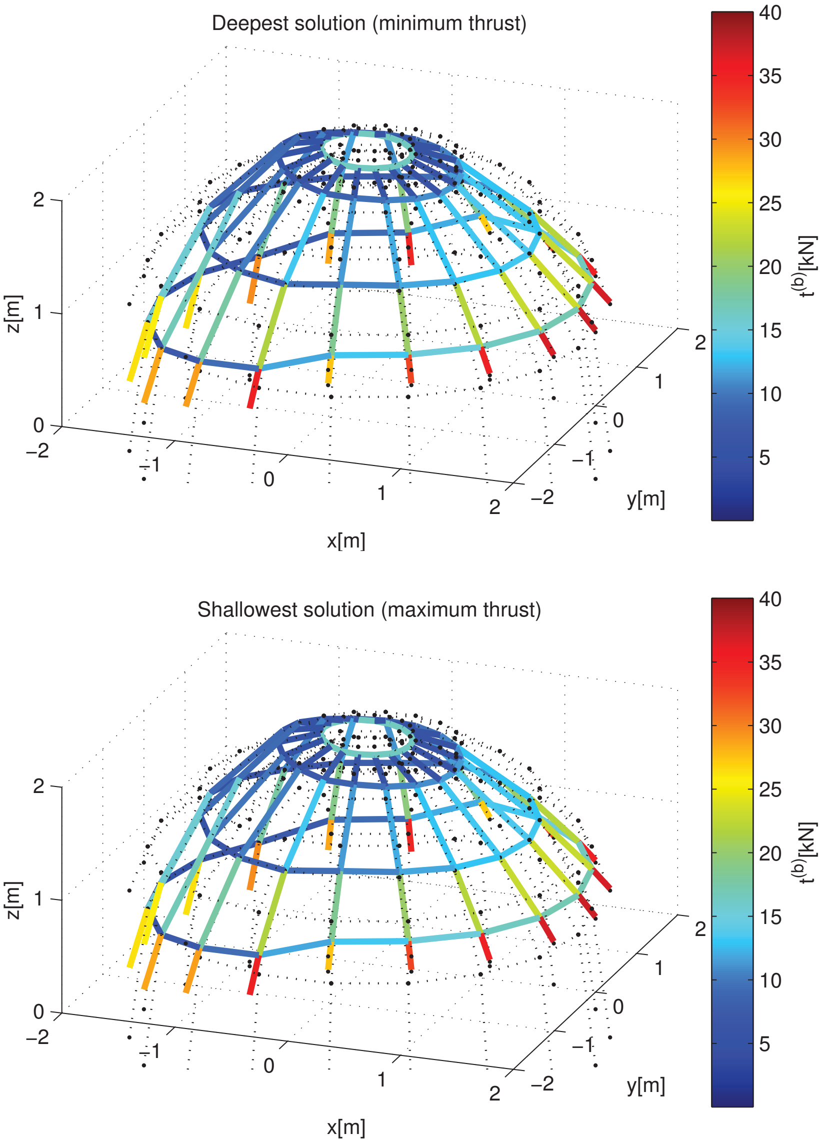

Fig. 11 – Dome with oculus: deepest and shallowest network configurations for dome subjected to self-weight and horizontal loads applied according to the ratio $f_h/f_z = 0.171$

4 Conclusions

The version of the Thrust Network Analysis proposed by Marmo and Rosati (2017) has been described and applied to the equilibrium analysis of arches and vaults subjected to vertical and horizontal loads. The approach contributed by Block in his PhD Thesis (Block, 2009) has been reformulated and extended in order to obtain a computationally efficient method capable of analysing thrust networks, possibly characterized by the presence of holes or free edges, subjected to the combined action of vertical and horizontal loads.

To be more specific, the computational efficiency of the method by Block (2009) has been enhanced by avoiding unnecessary complications. In particular, the optimization problem summarized in formula (6) involves much less equality conditions with respect to the original formulation by Block, yet providing the same final solution. This is due to the fact that the first two sets of equations reported in formula (4.32) of (Block, 2009) can be easily inverted and substituted in the subsequent two sets of equations. This significantly reduces the total size of the resulting optimization problem (6) and enhances the computational performances of the proposed TNA reformulation.

Furthermore, in the original formulation of the method the entries of the matrices **C** and **S** used to express horizontal equilibrium of nodes, see, e.g., formula (1), are assigned by assuming a specific node numbering and branch orientation; in particular, internal nodes are numbered first, while the external ones are numbered at last so that all branches are oriented towards nodes with lower index. Conversely, since the entries of **C** and **S** are obtained by assembling the branch contributions, which are given by formulas (2), no assumption about the node numbering is required in the proposed reformulation of the method.

Computational efficiency of the method is also enhanced by ruling out the determination and employment of the so called *dual grid*. Actually, we recall that the reference thrusts $\hat{t}_h^{(b)}$, are used by Block (2009) to define the branches' lengths of a *dual grid* that is reciprocal to the one referred to as *primal grid*, composed by the horizontal projection of the thrust network. Such a dual grid represents the graphic visualization of nodes' equilibrium in the horizontal plane. In particular, increase or decrease of the branches' thrust can be visualized by increasing or decreasing the corresponding length of the dual grid's branches.

In the presented version of the method we allow for a different value of the thrust lower bound to be assigned to each branch of the network so that the duality relationship between reciprocal grids can be avoided; moreover this graphical representation becomes of difficult interpretation when horizontal forces are applied to nodes.

References

1. Angelillo, M., Cardamone, L., Fortunato, A. (2010) A numerical model for masonry - like structures. *Journal of Mechanics of Materials and Structures*, vol. 5, pp. 415-583.
2. Block, P. (2009) *Thrust Network Analysis*. PhD thesis, Massachusetts Institute of Technology.
3. Block, P., Lachauer, L. (2014) Three-dimensional equilibrium analysis of gothic masonry vaults. *International Journal of Architectural Heritage*, vol. 8, pp.1-24.
4. Ercolano, A. (1994) On a rigid-elastic model for monumental block structures, *XI Congreso Nacional De Ingenieria De Mecanica*, Valencia, Spain.
5. Ercolano, A. (1995) Simulazione di strutture murarie, *XII Congresso Nazionale dell'Associazione Italiana di Meccanica Teorica ed Applicata (AIMETA)*, Napoli, Italy.
6. Fraternali, F. (2010) A thrust network approach for the equilibrium problem of unreinforced masonry vaults via polyhedral stress functions. *Mechanics Research Communications*, vol. 37, pp. 198-204.
7. Heyman, J. (1982) *The masonry arch*. Ellis Horwood, Chichester.
8. Heyman, J. (1995) *The Stone Skeleton: Structural Engineering of Masonry Architecture*. Cambridge University Press, Cambridge.
9. Huerta, S. (2008) The analysis of masonry architecture: a historical approach. *Architectural Science Review*, vol. 51, pp. 297-328.
10. Hooke, R. (1676) *A description of helioscopes and some other instruments*. T.R. for John Martyn, London.
11. Marmo, F., Rosati, L. (2017) Reformulation and extension of the thrust network analysis. *Computers and Structures*, vol. 182, pp.104-118.
12. O'Dwyer, D. (1999) Funicular analysis of masonry vaults. *Computers and Struc-*

tures, vol. 73, pp. 187-197.

13. Tralli, A., Alessandri, C., Milani, G. (2014) Computational methods for masonry vaults: a review of recent results. *The Open Civil Engineering Journal*, vol. 8, pp. 272-87.

Lateral torsional buckling of compressed open thin walled beams: experimental confirmations

Ida Mascolo[1], Marcello Fulgione[1], Mario Pasquino[1]

[1] Università degli Studi di Napoli, Federico II, Via Claudio 21
80125 Napoli, Italy
{ida.mascolo, marcello.fulgione, pasquino}@unina.it

Summary: This paper provides an approximate solution for the differential equations that govern the buckling of beams with a gradually changing of the thin-walled C cross section. This is a coupled problem of flexural and torsional buckling, whose exact solution is hard to get. We have therefore chosen to use an energy approach through the Dirichlet's principle. It allows, using the Ritz- Rayleigh algorithm, the quick implementation of a solution close to the real value of the critical load. Because of the complexity of the problem, it was considered appropriate to provide an experimental validation of the theoretical results with proper laboratory tests.

Keywords: Buckling analysis; theorem of minimum total potential energy; Dirichlet's principle; Ritz-Rayleigh method; variable cross section beam; coupled flexural-torsional buckling; shear centre position; imperfection sensitivity.

1 Introduction

In the design of compressed members, it generally takes into account the failures due to simple flexural buckling (Eulerian). In the case in which the moment of inertia of the cross section varies according to the power of the distance along the bar we have to take in account the possibility of further equilibrium modes. Owing the dependence of the shear centre position from the applied loads and because of the low torsional stiffness of the open thin walled sections the bar may twist, or even worse it may twist and bend simultaneously.

The differential equations that govern the problem of bending and torsion were derived by Euler. They are coupled and so it's very difficult to achieve a closed solution of the problem.

The stability problem in bars with varying cross section has a considerable practical importance in many fields of the engineering applications: mechanical, structural an aeronautical. In fact, by removing a portion of the material in a proper chunk of the bar we can increase the stability or the economic performances. On the other hand, recent history is full of dramatic examples of failures due to lateral torsional buckling. For this reason, to date, many authors continue to address this subject, researching the most appropriate approach: Method of initial parameters (Vlasov, 1959); Energy Method (Timoshenko and Gere, 1961; Franciosi, 1967); Finite Difference Method (Bazant, 1965); Exact Element Method (Eisenberger and Cohen, 1995); Variational Iteration Method (Coşkun and Atay, 2009); FEM Approach (Trahair, 2014; Kováč, 2015).

In this work the solution is obtained through an energy approach using the Dirichlet's theorem. The accuracy of the energy method is related to the buckled shape assumed. If the guessed shape is close to the true shape, the buckling load calculated is quite close to the true value; however, it should be pointed out that in this case the method provides an upper bound to the true critical load. The buckling shape guessed is obtained by using limited trigonometric series and the solution is given by Ritz-Rayleigh algorithm.

The theoretical results thus obtained were then validated by proper experimental investigations.

2 Problem definition

The position of the shear centre in a constant cross section beam is univocally determined by cross section geometry. As already shown in a previous work (Mascolo and Pasquino, 2016), this is no longer true when the cross section varies according to a power of the distance along the beam. In this case, the shear centre position also depends on the applied stress. Take a C cross section as an example, symmetric with respect to the centroidal axis x, the laws that govern the shear centre position along the beam are:

$$x_c(z) = -\frac{B'^2 H'^2 \delta}{4I_x} + \frac{H'}{I_x}\left(\frac{N\delta}{2A^2}\frac{dB'}{dz} - \frac{M_x}{\delta}\frac{d}{dz}\left(\frac{6B'H'}{6B'H'^2 + H'^3}\right)\right)\frac{B'\delta}{2}$$

$$y_c(z) = 0$$

where M_x e I_x are, respectively, the bending moment and the moment of inertia with respect to the x axis, A is the cross section area. The meaning of the other terms can be obtained from Fig. 1.

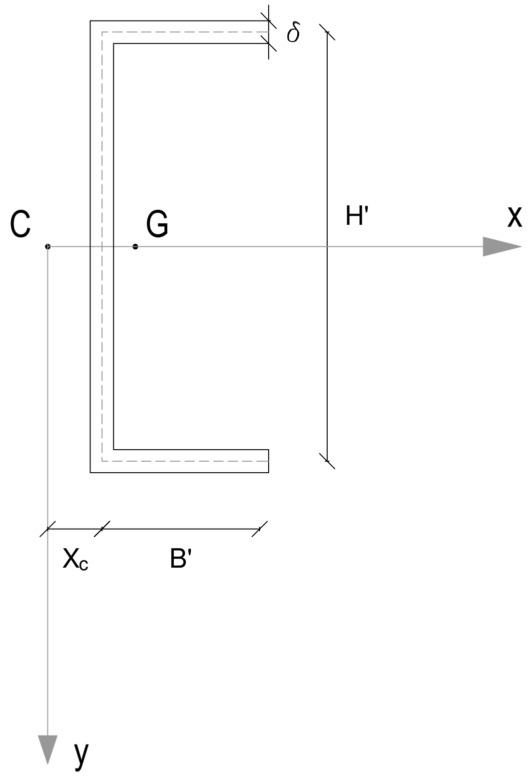

Fig. 1 – Cross-section geometry

Euler derived the differential system of equations that governs the deflection curve of the beam:

$$\begin{cases} \left(EI_\eta u''\right)' - Nu' + Ny_G\vartheta' = 0 \\ \left(EI_\xi v''\right)' - Nv' - Nx_G\vartheta' = 0 \\ C_2\vartheta'''' + C_2'\vartheta''' - \left(C_1 + \dfrac{NI_c}{A}\right)\vartheta'' - \left(C_1 + \dfrac{NI_c}{A}\right)'\vartheta' + Nu''y_G - Nv'x_G = 0 \end{cases}$$

where EI_ξ and EI_η are the flexural rigidity of the beam with respect to the principal centroidal axes; *N(z)* is the axial compressive force to the generic abscissa *z*; *u* and *v* are the deflection of the centroid in *x* and *y* directions; ϑ' is the rate of change of the cross section twist angle about the shear centre; *E* and *G* are the Young's and shear modules; I_c is the polar moment of inertia of the cross section about the shear centre;
C_1 is the warping rigidity:

$$C_1 = G\frac{\int \delta^3 ds}{3}$$

C_2 is the warping constant that depends from the sectorial area ω_s:

$$C_2 = E\int \omega_s^2 \delta ds$$

In this system, the equations of bending and twist are coupled so it is quite difficult to get an exact value of the true critical load. Thus we do not look for a closed solution of the problem, choosing an approximate way by the Dirichlet variational method. It states that a position of stationary total potential is an equilibrium position.

Making use of this theorem, moving from one configuration assigned to another one, infinitely close and kinematically admissible, we can establish that it is also balanced depending on the first variation of total potential energy, in terms of displacement functions *u*, *v*, *w*. In this way, the Dirichlet's theorem gives *n* necessary and sufficient conditions of equilibrium:

$$\frac{\partial Ept}{\partial c_i} = 0 \qquad i = 1,...,n$$

where Ept is the total potential energy and c_i are n Lagrange multipliers. Then, the total potential energy is a functional of the deflection components *u(x)*, *v(y)*, *w(z)*. Choosing as suitable buckling shape a limited trigonometric series, the deflection shape can be reviewed as the sum of *n* natural deformation modes:

$$s_j = \sum_{i=1}^{n} c_{j,i} \Psi_{j,i} \qquad j = 1,2,3 \qquad i = 1,..,n$$

where $\Psi_{j,i}$ represents the partial sum of the first *n* terms of the Taylor series expansion. In this way, the total potential energy become a quadratic function of the *3n* parameters $c_{j,i}$:

$$Ept = f(c_{j,i}, F_{cr})$$

This strategy has therefore allowed a transition from continuous to discrete, assimilating the continuous system to a holonomic one.
By imposing stationarity with respect to the *n*-th parameters $c_{j,i}$, it leads to a linear eigenvalue problem:

$$\frac{\partial Ept}{\partial c_{j,i}} = \left[K_{j,i} - F_{cr} G_{j,i} \right] \partial c_{j,i} = 0$$

The solution of this linear problem gives the value of the studied critical load. The solution as will be closer to the real value as the number of chosen Lagrangian parameters will be greater.

3 Case study

It is analyzed an open thin wall C cross section *S420* steel beam; the width of the flanges and the height of the web is linearly variable along the *z* axis.

The beam was obtained from a single sheet of steel formed onto a press brake.

As can be seen in Fig. 2, the static scheme is a pinned-pinned beam, subjected to an axial compression force centered in the centroid of the section.

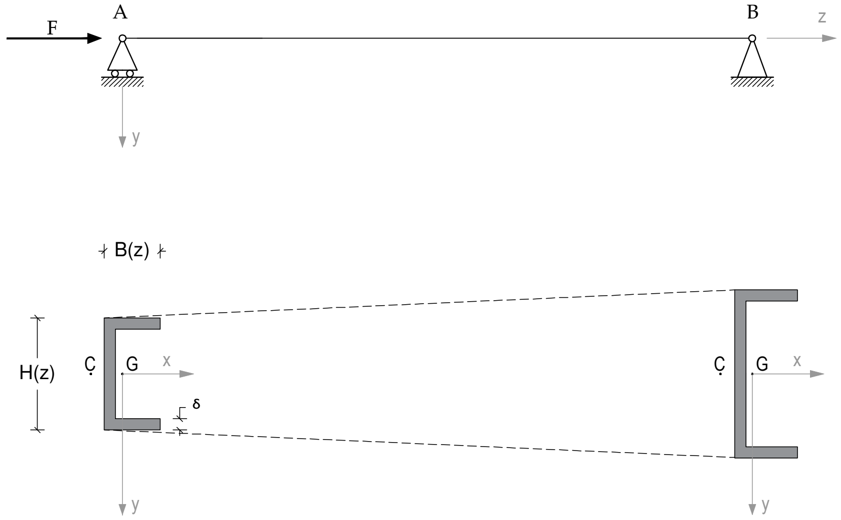

Fig. 2 – Beam geometry

The supports allow only the rotations around *y* axis and preventing the translations in the *x*, *y* directions; in *B* are, moreover, prevented the translations in the *z* direction.

The kinematically admissible class of displacements that we have chosen for the theoretical resolution of the problem is the partial sum to the first *n* terms of the Taylor series expansion:

$$u = \sum_{i=1}^{n} u_i sen\left(\frac{n\pi z}{l}\right)$$

$$v = \sum_{i=1}^{n} v_i \left(1 - \cos\left(\frac{2n\pi z}{l}\right)\right)$$

$$\vartheta = \sum_{i=1}^{n} \vartheta_i sen\left(\frac{n\pi z}{l}\right)$$

We tested two beams with the same geometrical and mechanical characteristics, using MTS 810 universal testing machine of the 550 kN load range. As can be seen in Fig. 3, the constraints have been designed and manufactured specifically to ensure the required kinematic conditions. The tests were conducted in standard conditions of pressure and temperature; during the tests we registered time, compressive force, displacements of the web and the flanges in some representative points of the beams and strains in other representative points. The sampling frequency of all parameters was 5 Hz.

Fig. 3 – Tested beam: pre and post buckling

Furthermore, for the purpose to ensure the invariability of the section shape, we have introduced appropriate transverse stiffening plates along the beams.

For the purpose of gauging stress and strain of the beams, we have used, in the most representative points, displacement transducers of the WA type series and strain gauges sticked along 0° and 90° directions on both sides of the beams.

In order to check the subcritical, critical and post critical behaviour of the tested beams, the tests were stopped when the stress of a representative point of the beams has reached the plastic region.

Fig. 4 shows the obtained experimental stress-strain curve.

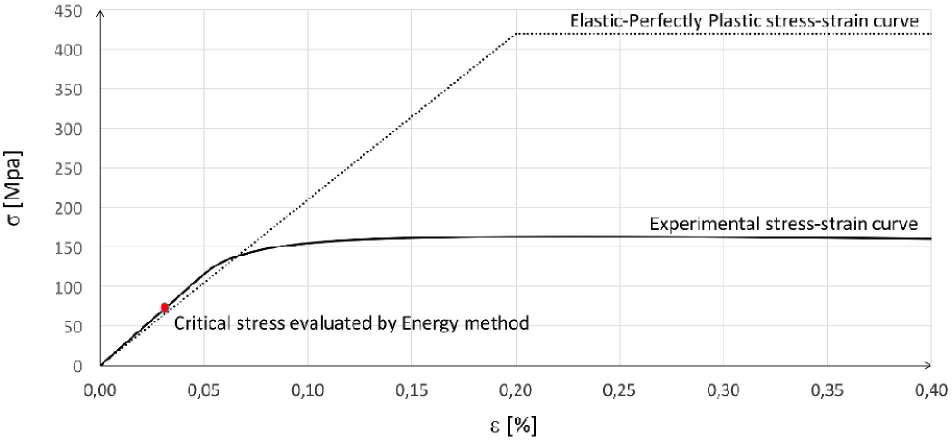

Fig. 4 – Comparison of experimental and theoretical results

The comparison with elastic-perfectly plastic curve of material highlighted how the stress that caused beam to buckle is appreciably lower than the yield strength. Above all, it appears clear that the implemented energy method has provided conserved values of critical load.

4 Conclusions

By the amount of data obtained from the experimental tests, it was possible to detect a satisfactory correspondence between the theoretical and experimental values of the critical load. The energetic method proves to be a powerful means of investigation, it is reliable and easy to be implemented. However, it should be emphasized that the critical load values obtained in the experiments are rather different from one another.

Furthermore, as shown in Fig. 5, once the tested beams have reached a maximum value of strength F_m, they have exhibited a softening with plastic deformations; this appears to violate the hypothesis of elastic buckling.

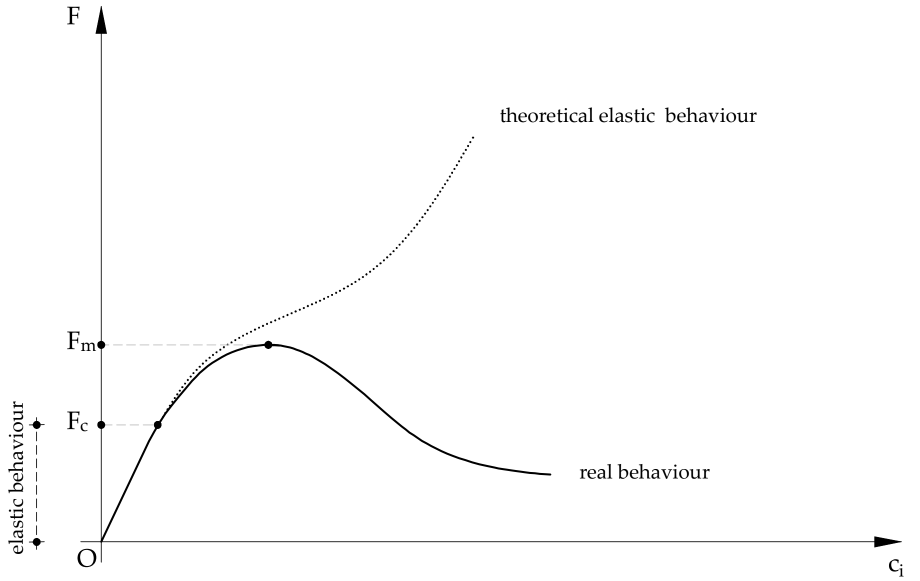

Fig. 5 – Subcritical, critical and post critical behaviour

However, the conviction of the authors is that the buckling has occurred in the elastic field. Once the stress draws the critical value, the beam suddenly bends and this causes the variation of the shear centre position and then additional torsional stresses. Because of the bending and the twist of the beam, any small load increments cause high stresses in the material and quickly the strain reaches the yield strength values. Indeed, the Koiter's post-buckling theory (Hutchinson and Koiter, 1970) has shown that whether the post-buckling path of the loaded structure has a limit point, the buckling load is sensitive to initial imperfections. In this case, the results of repeated buckling tests can exhibit noticeable scatter.

References

1. Bazant, Z. (1965). *Non-uniform torsion of thin-walled bars of variable section*, IABSE publications, vol. 25, pp. 17-39.
2. Coşkun, S. B., Atay, M. T. (2009). Determination of critical buckling load for elastic columns of constant and variable cross sections using variational interation method. *Computers and Mathematics with Applications*, vol. 58 (*11*), pp. 2261-2266.
3. Eisenberger, M., Cohen, R. (1995). Flexural-torsional buckling of variable and open cross section members. *Journal of Engineering Mechanics*, vol.121 (*2*), pp. 244-254.
4. Franciosi, V. (1967). *Scienza delle costruzioni, vol. V, Stabilità dell'equilibrio*, Napoli, Italy: Liguori.
5. Hutchinson, J. W., Koiter, W. T. (1970). Postbuckling Theory. *Applied Mechanics Reviews*, vol. 23 (*12*), pp. 1353-1366
6. Kováč, M. (2015). Elastic Critical Force for torsional-flexural buckling of metal members with mono-symmetric cross sections. *Applied Mechanics and Materials*, vol. 769, pp. 36-42.
7. Mascolo, I., Pasquino, M. (2016). Lateral-torsional buckling of compressed and highly variable cross section beams. *Curved and Layered Structures*, vol. 3 (*1*), pp. 146-153.
8. Timoshenko, S. P., Gere, J. M. (1961). *Theory of elastic stability*, New York: McGraw Hill, Book Company.
9. Trahair, N.S. (2014). Bending and buckling of tapered steel beam structures. *Engineering Structures*, vol. 59, pp. 229-237.
10. Vlasov, V. Z. (1961). *Thin-walled elastic beams*, Washington, D.C., U.S.A.: National Science Foundation.

Wall structure finite-element by BEM coupling

Vincenzo Minutolo, Eugenio Ruocco

Dipartimento di Ingegneria Civile Design Edilizia Ambiente
Università degli Studi della Campania "Luigi Vanvitelli",
81031 Aversa (CE), Italy
{vincenzo.minutolo, eugenio.ruocco}@unicampania.it

Abstract. The calculation of structures made of the assembly of several walls requires finite element modeling, henceforth it gives raise to a large number of degrees of freedom. The actual work shows that the number of parameters is reduced by using Boundary Elements to derive the stiffness matrix of the element. The proposed technique gives origin to positive definite and symmetrical matrix due to the use of constant boundary elements. Moreover, the resulting matrix can be assembled together with Finite Element ones in order to obtain the description of complex three dimensional structures. Substructuring and multi region modeling are possible and continuity relaxation between elements as well as interface and non linear constitutive laws can be comprised. Some examples are reported in order to verify the accuracy and the feasibility of the procedure for the elastic case.

Keywords: Boundary Element, Finite Element, mixed coupling, masonry wall.

1 Introduction

Worldwide, the main part of cultural heritage buildings are made by masonry structures.

The mechanical characterization of those structures is done by means of plane walls assembled within a three-dimensional framework. The plane walls present both in plane and out of plane behavior. The main criteria for calculating such wall bearing structures is to assume that vertical and horizontal loads are transferred to the foundation through the walls by means of the in plane mechanism. On the other hand, the collapse and the failure of the structure seem to involve out of plane mechanism for the majority of the cases. However, it is of great importance to evaluate the in plane response at first (Auciello and Ercolano 1997, Caliò *et. al.* 2002, Galasco *et al.* 2004, Solonikios 2003).

Starting from the above considerations, simplified methods are often used for the structural analysis of masonry assembly. For instance, the structure, actually made of interconnected plates and shells, can be analyzed with reference to equivalent frame, i.e. it is analyzed as one dimensional beam element assembly, sometimes considering shear strain effects and rigid links.

The finite element method, conversely, is a powerful tool to calculate the response of plane walls, but it requires great amount of computer space. Consequently, in practical engineering simplified methods are preferred and the FEM is restricted to the analysis of complex structural systems or to check the accuracy of simplified methods (Ercolano 1995, Ercolano 1997).

In the paper, a suitable and effective method for calculating element stiffness matrix by coupling of Boundary Element Method (BEM) and FEM is proposed. The method allows performing the two-dimensional elastic analysis of masonry wall. Moreover, it allows considering voids and inclusions of different materials by means of substructures.

The structural response is calculated by a displacement-based FEM that uses a set of finite macro-elements (Macro Boundary Finite Elements MBFE) connected each other.

The stiffness matrix of the elements is obtained by means of variational Boundary Element Method (Polizzotto 2000). In a sense the BEM kernels are used as a shape function for the element. The duality in term of energy of the nodal tractions and displacements is enforced by using constant Boundary Elements. It ensures that the Boundary Integral Equation governing the element equilibrium can be discretized into a positive definite matrix.

Henceforth, the resulting wall element is treated like any finite element and assembled into classical routine (Vodička *et al.* 2011).

The Boundary Integral Equations are formulated considering that the wall is homogeneous and undergoing to plane stress. Even if heterogeneity could be considered with a little effort (Minutolo *et al.* 2009), the analysis is limited to the homogeneous case. The wall is modeled as a plane surface whose boundary lines are discrerized into straight segments with only one node at the middle, so that the shape function of the BEM is constant.

2 Formulation

Let us consider a plate element that occupies the plane domain Ω, the plate is made of linearly elastic material and exhibits plane stress. Forces b_k are applied in internal points of the structure body and tractions t_k on its boundary $\Gamma = \partial\Omega$. On the elastic plane the vectors t_{lk}^* and u_{lk}^* represents the Green’s functions for the displacement and the traction at the boundary point x in the k direction due to a unit load applied at y, where y is an internal point in the l direction. By these definitions, the following Somigliana's identity can be written (Aliabadi Wrobel 2002, Brebbia Dominguez 1992):

$$\begin{aligned} u_l(y) &= \\ &-\int_\Gamma t_{lk}^*(x,y)u_k(x)d\Gamma(x) + \int_\Gamma u_{lk}^*(x,y)t_k(x)d\Gamma(x) + \\ &+\int_\Omega u_{lk}^*(x,y)b_k(x)d\Omega(x). \end{aligned} \tag{1}$$

The identity (1) gives the displacements at internal points, u_l, as a function of the boundary values u_k and t_k.

Boundary Integral Equation (BIE) involving only boundary values of the unknowns is obtained by collocating equation (1) on boundary points of the plate, provided that discontinuity of the kernels of the equation (1) is accounted. The resulting BIE is:

$$\begin{aligned} & c_{lk}(\xi)u_k^i(\xi) = \\ & -\int_\Gamma t_{lk}^*(x,\xi)u_k(x)\,d\Gamma(x) + \int_\Gamma u_{lk}^*(x,\xi)t_k(x)\,d\Gamma(x) + \\ & +\int_\Omega u_{lk}^*(x,\xi)b_k(x)\,d\Omega(x). \end{aligned} \tag{2}$$

where the integral concerning t_{lk}^* has to be considered in the sense of Cauchy principal value and c_{lk} are numerical coefficients depending on the boundary regularity at the point ξ.

In order to numerically evaluate eq. (2), the plate boundary is divided into linear boundary elements, where the traction and the displacement are represented only by the value assumed at the node at the center of the element. The body forces have to be accounted by performing volume integration, although no unknown quantity is defined on the internal points. However, plate interior has to be described by plane elements too. Hence, let us assume that N is the number of boundary elements and M the number of internal cells: the equation (2) is discretized performing both the collocation of the equation on each boundary point i, and integrating the kernels on each boundary element k and on internal cell:

$$\mathbf{c}^i\mathbf{u}^i + \sum_{j=1}^{N}\left[\int_{\Gamma_j}\mathbf{t}^*\,d\Gamma\right]\mathbf{u}^j = \sum_{j=1}^{N}\left[\int_{\Gamma_j}\mathbf{u}^*\,d\Gamma\right]\mathbf{t}^j + \sum_{k=1}^{M}\left[\int_{\Omega_k}\mathbf{u}^*\mathbf{b}\,d\Omega\right]. \tag{3}$$

After reordering of the equation with respect to the nodal values of displacement and traction, the following linear algebraic equation system is obtained,

$$\mathbf{Gt} = \mathbf{Hu} - \mathbf{b} \tag{4}$$

where $\mathbf{H}$ and $\mathbf{G}$ are 2Nx2N matrices. Moreover, $\mathbf{u}$, $\mathbf{t}$ and $\mathbf{b}$ are vectors collecting nodal values of displacement, traction and equivalent nodal force corresponding to body loads.

The nodal force is defined by the resultant of the traction on the left hand side of equation (4):

$$\mathbf{Lt} = \mathbf{LG}^{-1}\mathbf{Hu} - \mathbf{LG}^{-1}\mathbf{b} \tag{5}$$

where

$$\mathbf{L} = \begin{pmatrix} L_1 & 0 & 0 & 0 & 0 \\ 0 & L_1 & 0 & 0 & 0 \\ 0 & 0 & \ddots & 0 & 0 \\ 0 & 0 & 0 & L_N & 0 \\ 0 & 0 & 0 & 0 & L_N \end{pmatrix} \tag{6}$$

is a diagonal matrix containing the lengths of the boundary elements.

It is well known (Polizzotto 2000) that the collocation method leads to a fully populated, unsymmetrical and not positive definite matrix:

$$\mathbf{A} = \mathbf{LG}^{-1}\mathbf{H}. \tag{7}$$

The matrix (7) is unsuitable for the characterization of the macro element's stiffness matrix.

To obtain such a result, let us take into account the discretized form of Total Potential Energy of the plate (Reissner 1950, Washizu 1982, Panzeca *et al.* 2009),

$$\Pi = \frac{1}{2}\mathbf{u}^T\mathbf{Au} - \mathbf{u}^T\mathbf{f}^e \tag{8}$$

where

$$\mathbf{f}_e = \mathbf{L}\left(\mathbf{t} + \mathbf{G}^{-1}\mathbf{b}\right) \tag{9}$$

and calculate its variation

$$\begin{gathered} \partial\Pi = \frac{1}{2}\left[\delta(\mathbf{u})^T\mathbf{Au} + \mathbf{u}^T\mathbf{A}\delta(\mathbf{u})\right] - \delta\left(\mathbf{u}^T\right)\mathbf{f}^e = 0 \rightarrow \\ \delta(\mathbf{u})^T\left(\frac{1}{2}\left[\mathbf{A} + \mathbf{A}^T\right]\mathbf{u} - \mathbf{f}^e\right) = 0, \quad \forall\delta(\mathbf{u}). \end{gathered} \tag{10}$$

Then, it is possible to set up a fully populated and symmetric system of linear equations for the computation of unknown boundary displacements and generalized forces, where the coefficient matrix $\mathbf{K}$ is a symmetric and positive definite stiffness matrix. Notice that $\mathbf{K}$ is coincident with the symmetric part of matrix $\mathbf{A}$.

It follows that the characteristic relationship between the forces acting on the macro element nodes and the corresponding displacements assumes the form:

$$\mathbf{f} = \mathbf{K}\,\mathbf{u} \tag{11}$$

where the symbols have to be considered as in Finite Element Method, namely $\mathbf{f}$ is the equivalent nodal force vector, $\mathbf{u}$ the nodal displacement and $\mathbf{K}$ the stiffness matrix of the element.

3 Results

In this section the validity and the accuracy of the proposed element is presented, and some results calculated by means of the proposed element are compared with numerical and analytical ones available in literature.

In the first example, the overall response of the in-plane walls (Figure 1a) is investigated by utilizing macro-element subdivision reported in Figure 1b. Constant BEM elements, with size h = 100 mm, are used for boundary discretization of the single macro element. The horizontal and vertical loads are distributed along the horizontal slabs (Figure 1a).

The wall element has plane stress with thickness $t = 500\,mm$, Young Modulus $E = 1260\,MPa$ and Poisson's ratio $\nu = 0.2$. The global assembly is obtained considering the presence of the reinforced concrete riddles and architraves. These parts are treated like macro-elements with different stiffness depending on the homogenized material.

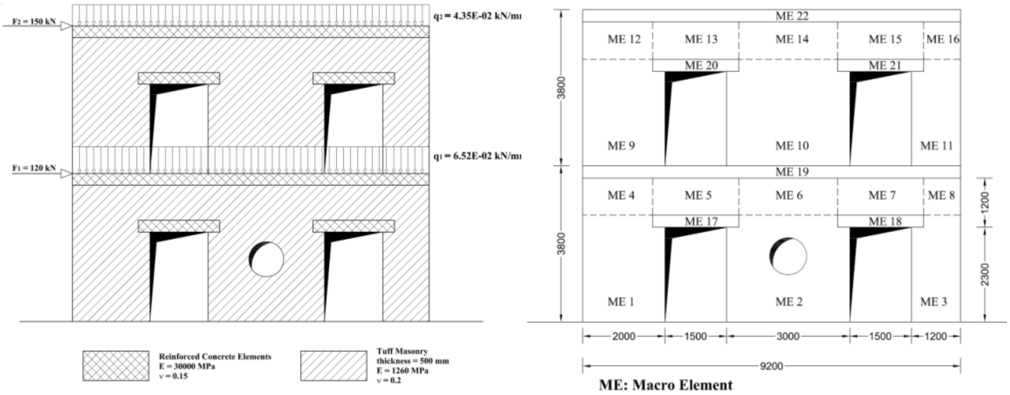

(a) (b)

Fig. 1 – Masonry wall example: a) geometry and loads; b) macro-element subdivision

The results are compared with numerical ones, obtained by the commercial FEM software package Ansys ©, which uses a displacement based FEM formulations.

The normal and tangential stresses along the Path 1 and displacement components along Path 2 and 3 are plotted in Figure 2.

The stress at the foundation of the wall on the left is characterized by bending and axial stress combination since the horizontal forces, the displacement in vertical direction is almost constant due to the prevalence of vertical load. In Figure 2, the results from commercial FEM program are reported and the good agreement between proposed model and FEM calculation can be appreciated. FEM calculation has been performed using quadrilateral elements that on the boundary coincide with the boundary element. However, FEM requires the discretization of the whole surface of the wall, whereas Macro Boundary Element requires only line element along the interfaces.

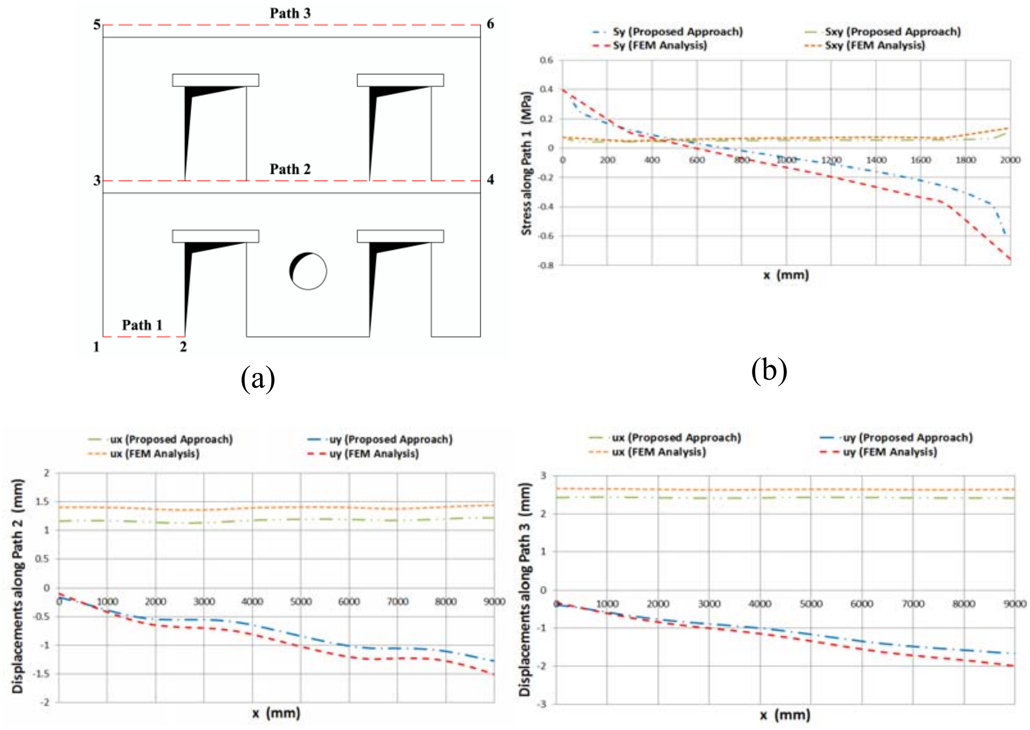

(a) (b)

(c) (d)

Fig. 2 – Results: a) horizontal paths for the plot results; b) stress along path 1; c) displacements along path 3; d) displacements along path 2

4 Conclusions

An accurate and efficient derivation of element stiffness by means of Boundary Integral Equation has been discussed. The obtained stiffness matrix can be used in conjunction with Finite Elements in two-dimensional elastic analysis of masonry wall with voids and inclusions of different materials. The element is described in term of nodal displacement. The number of nodes can be arranged in accordance with the desired accuracy and the connectivity of the walls constituting the structure.

The use of constant BEM elements gives a greater rigidity to the structure with respect to a conventional FEM model and tends to FEM with decreasing size. The results show that the proposed approach is capable of simulating with good approximation the in-plane response of unreinforced masonry.

The work can be extended to the case of discontinuous interfaces and heterogeneous wall panels. The Boundary Integral derivation is, indeed, suitable of modification by introducing heterogeneous 2D elastic kernels. The assembly of the stiffness matrix of the MBFE can be performed by using unilateral coupling or interface constitutive law.

References

1. Aliabadi M. H. (2002) *The Boundary Element Method. Applications in Solids and Structures*. Chicester, U.K.: Wiley.
2. Auciello N.M., Ercolano A. (1997) *Numerical simulation of masonry panels.* Engineering Transactions. *Engineering Transaction*, vol. 45 (*3-4*), pp. 375-394.
3. Brebbia C.A., Dominguez J.(1992) *Boundary Elements, An Introductory Course*, Southampton, U.K.: Computational Mechanics.
4. Caliò I., Marletta M., Pantò B. (2002). A new discrete element model for the evaluation of the seismic behavior of unreinforced masonry buildings. *Engineering Structures*, vol. 40, pp. 327-338.
5. Ercolano A. (1995) Simulazioni di strutture murarie. In: *Proc. XII Cong. Naz. Associazione Italiana di Meccanica Teorica e Applicata, vol 1, Meccanica delle Strutture, Napoli,* pp. 377-382.
6. Ercolano A. (1997) *Un metodo per l'analisi di pannelli murari tramite complementarietà lineare, In: Proc. XIII Cong. Naz. Associazione Gruppo italiano della Frattura, Cassino*, pp. 27-28.
7. Galasco A, Lagomarsino S, Penna A, Resemini S. (2004). Non-linear seismic analysis of masonry structures. Paper no. 843. In: *Proc. 13th world conference on earthquake engineering.*
8. Leung K. L., Zavareh P. B., D. E. Beskos (1995). 2-D elastostatic analysis by a symmetric BEM/FEM scheme. *Engineering Analysis with Boundary Elements*, vol. 15 (*1*), pp. 67-78.
9. Minutolo V., Ruocco E., Ciaramella S., (2009) Isoparametric FEM vs. BEM for Elastic Functionally Graded Materials. *Computer Modelling in Engineering and Science*, vol. 489 (*1*), pp.1-21.

10. Panzeca T., Milana V., Salerno M. (2009) A symmetric Galerkin BEM for plate bending analysis. *European Journal of Mechanics - A/Solids*, Vol.28, 1, pp. 62-74.
11. Polizzotto C. (2000) A symmetric Galerkin boundary/domain element method for finite elastic deformations. *Computer Methods in Applied Mechanics and Engineering*, vol. 189 (*2*), pp. 481-514.
12. Reissner, E., (1950) On a variational theorem in elasticity. *Journal of Mathematics and Physics*., Vol. 29, pp.90-95.
13. Salonikios T, Karakostas C, Lekidis V, Anthoine A. (2003).Comparative inelastic pushover analysis of masonry frames. *Engineering Structures* ; vol.25 (*12*), pp. 1515–1523.
14. Ruocco E., Minutolo V., Ciaramella S.(2011) A generalized analytical approach for the buckling analysis of thin rectangular plates with arbitrary boundary conditions. *International Journal of Structural Stability and Dynamics*, vol. 11 (*1*), pp.1-21
15. Ruocco E., Minutolo V. (2012) Buckling of composite plates with arbitrary boundary conditions by a semi-analytical approach. *International Journal of Structural Stability and Dynamics,* Vol. 12 (*5*)
16. Vodička,R. Mantič, V. París, F. (2011). Two variational formulations for elastic domain decomposition problems solved by SGBEM enforcing coupling conditions in a weak form. *Engineering Analysis with Boundary Elements*, vol. 35 (*1*), pp. 148-155
17. Washizu, K., (1982) *Variational Methods in Elasticity and Plasticity*, Oxford, UK: Pergamon Press.

On the shape optimization of the force networks of masonry structures

Giuseppe Rocchetta, Mariella De Piano, Valentino P. Berardi, Fernando Fraternali

Department of Civil Engineering, University of Salerno, Via Giovanni Paolo II, 132
84084 Fisciano (SA), Italy
giusepperocchetta@gmail.com, {mdepiano, berardi,f.fraternali}@unisa.it

Abstract. A novel lumped stresses network approach for the analysis of the mechanical behavior of masonry structures is presented. It is formulated through a network of lumped stresses, making use of polyhedral stress functions and a variational approximation of the continuous equilibrium problem. The proposed method allows for modelling masonry structures as no-tension elements and gives, in the case of curved masonry members, the optimized surface through a predictor-corrector procedure and the stress function describing the membrane stress. The given approach offers a useful tool for predicting the crack pattern of unreinforced masonry structures and the associated stress fields. It is validated against some benchmark case studies dealing with a hemispherical dome, a groin vault, a cloister vault and a masonry beam.

Keywords: Lumped stress approach, Masonry structures, No-tension model, Polyhedral stress function, Crack pattern, Mesh adaption

1 Introduction

Masonry buildings realized in the last centuries are a significant part of the international architectural heritage. The evaluation of structural vulnerability of these constructions is the first step to evaluate their safe and to preserve them over time.

From historical point of view, the first models for the stability analysis of curved masonry structures were formulated with reference to arches, by introducing the funicular curves (Hooke, 1675; Poleni, 1748; Heyman, 1966); the slicing technique (Wittman, 1879; Ungewitter, 1890; Heyman, 1966, 1977; Boothby, 2001; Foraboschi, 2004; Como, 2009); physical or virtual hanging chain models (Tomlov *et al.*, 1989; Kilian and Ochsendorf, 2005; Andreu, 2007; Kilian 2007); and the limit analysis of no-tension structures (Heyman, 1966, 1995; Del Piero, 1998: Huerta, 2001).

In the last few years, the Heyman limit analysis approach has been extended by several authors for the evaluation of the mechanical behavior of vaulted and plane masonry structures, by developing analytical, computational and graphical methods capable to search for at least one purely compressive state of thrust in equilibrium with the applied loads. Most of them approximate the thrust surface as a force network (O'Dwyer, 1999; Fraternali, 2001; Fraternali *et al.*, 2002 (1,2); Block and Ochsendorf, 2005, 2007; and Ochsendorf and Block, 2009). In this way discrete loads and structural discontinuities can be incorporated easily in the modelling.

Recent contributions to the ongoing research have optimized the search the thrust surface by using polyhedral stress potentials to generate equilibrated lumped stress networks (Fraternali *et al.*, 2002 (1,2); Adriaenssens *et al.* 2009).

The present work deals with a novel lumped stresses network approach for the analysis of the equilibrium problem of unreinforced masonry structures. Such an approach is developed through a network of lumped stresses, making use of polyhedral stress functions and a variational approximation of the continuous equilibrium problem. A constrained lumped stress method LSM is proposed for the analysis of curved members, by enforcing that a compressive membrane state of stress "condensed" across a material surface S (thrust surface), contained in a bounded region of the 3D space, is in equilibrium with the external loads. The membrane behavior is modelled by means of a discrete network of compressive forces, which allows us to approximate the no-tension model of masonry (Giaquinta and Giusti, 1985; Del Piero, 1989; Heyman, 1995). The membrane equilibrium problem is solved via an iterative procedure based on a variational formulation, under the assumptions of polyhedral test functions for the thrust surface and membrane stress potential.

The proposed LSM has been generalized for the elastic problem of a wall that incorporates ENT elements by means of a mixed LSM-displacement method (LSDM).

Case studies of curved structures (hemispherical dome, groin vault and cloister vault) and plane members (masonry beams) are analyzed in depth.
The numerical results highlight the efficacy of the proposed approach in predicting equilibrated lumped stress networks and associated crack patterns.

2 Equilibrium problem of masonry structures

The elastic problem is analyzed with reference to masonry curved structures and walls.

2.1 Vaulted structures

We introduce the thrust surface S of a masonry vault, as a no tension membrane contained in a design domain, and its shape function $f = f(x_1, x_2)$ (Figure 1).

Let Ω denote the horizontal projection of the thrust surface and let $\{x_1, x_2, x_3\}$ be Cartesian coordinates with unit base vectors $\{\mathbf{e}_1, \mathbf{e}_2, \mathbf{e}_3\}$, such that x_3 is perpendicular to Ω.

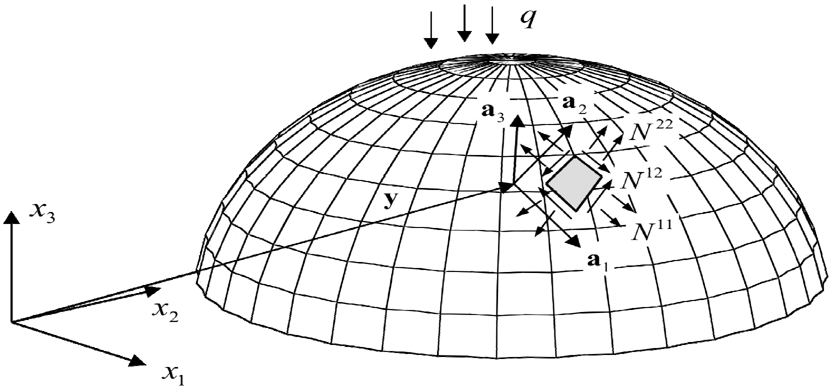

Fig. 1 – Thrust surface S

The covariant base vectors can be easily obtained by regarding x_1 and x_2 as curvilinear coordinates over S (Monge's coordinates), as follows:

$$\mathbf{a}_1 = \mathbf{e}_1 + \partial f / \partial x_1 \, \mathbf{e}_3, \qquad \mathbf{a}_2 = \mathbf{e}_2 + \partial f / \partial x_2 \, \mathbf{e}_3, \qquad \mathbf{a}_3 = 1/J \, \mathbf{a}_1 \times \mathbf{a}_2, \tag{1}$$

where:

$$J = \sqrt{1 + (\partial f / \partial x_1)^2 + (\partial f / \partial x_2)^2}. \tag{2}$$

The equilibrium equations of S are conveniently formulated with reference to the non-orthogonal basis $\{\mathbf{e}_1, \mathbf{e}_2, \mathbf{a}_3\}$:

$$\frac{\partial P^{\alpha\beta}}{\partial x_\beta} + q_{(\alpha)} = 0, \quad \frac{\partial^2 f}{\partial x_\alpha \partial x_\beta} P^{\alpha\beta} - \frac{\partial f}{\partial x_\alpha} q_{(\alpha)} + q_{(3)} = 0 \quad (\text{summation on } \alpha, \beta). \tag{3}$$

Here, $q_{(i)}$ $(i = 1,2,3)$ denote the external forces per unit area of Ω acting on S, while $P^{\alpha\beta} = J N^{\alpha\beta}$ $(\alpha, \beta = 1,2)$ denote the projections of the membrane stress resultants $N^{\alpha\beta}$ (Figure 1) onto Ω.

The $P^{\alpha\beta}$ stresses can be derived from the Airy potential (or stress function) φ, assuming pure vertical loading ($q_{(1)} = q_{(2)} = 0$):

$$P^{11} = \partial^2\varphi / \partial x_2^2,\ P^{22} = \partial^2\varphi / \partial x_1^2,\ P^{12} = -\partial^2\varphi / \partial x_1 \partial x_2, \tag{4}$$

The equation (3) can be rewritten by substituting equ. (4), as follows:

$$a_{\alpha\beta}\partial^2\varphi / \partial x_\alpha \partial x_\beta - q = 0 \text{ in } \Omega, \tag{5}$$

where:

$$a_{11} = \partial^2 f / \partial x_2^2,\ a_{22} = \partial^2 f / \partial x_1^2,\ a_{12} = -\partial^2 f / \partial x_1 \partial x_2,\ q = -q_{(3)}.$$

Once the surface tractions along the boundary of S are prescribed, the equation (5) can be solved by considering the boundary condition:

$$\varphi = \mu(s) \text{ on } \partial\Omega, \tag{6}$$

where s is a curvilinear coordinate measured along the arc-length of $\partial\Omega$, and $\mu(s)$ (*Dirichlet problem*) is the moment of all support forces about a vertical axis through the point s.

The stress function φ is obtained via the following variational formulation of (5)-(6):

$$\int_\Omega a_{\alpha\beta} \frac{\partial\varphi}{\partial x_\alpha} \frac{\partial\delta\varphi}{\partial x_\beta}\, d\Omega \ + \ \int_\Omega q\, \delta\varphi\, d\Omega = 0. \tag{7}$$

The equation (7) has to be satisfied for each $\delta\varphi$ vanishing on $\partial\Omega$.
It is well-known that the no-tension constraint for the masonry implies that φ in addition must be concave (Giaquinta and Giusti, 1985).

The Airy stress function φ is evaluated by using the Constrained LSM approach below presented.

2.1 Walls

The mechanical behavior of masonry walls can be analyzed within the field of stress plane problem. The members is modelled as a plane body Ω, subject to kinematical boundary conditions $\mathbf{u} = \overline{\mathbf{u}}$ on a given portion Γ_u of its boundary $\Gamma \equiv \partial\Omega$, and surface tractions $\mathbf{p}$ over $\Gamma_p = \Gamma \setminus \Gamma_u$. Within the proposed procedure no body forces are considered. The plane body Ω is assumed to be polygonal and simply-connected and then is discretized by a triangulation $\Pi_h = \{\Omega_1, ..., \Omega_M\}$ (primary mesh), characterized by a fixed mesh size, $h = \sup_{m \in \{1,...,M\}} \{diam(\Omega_m)\}$, and a dual tessellation $\hat{\Pi}_h = \{\hat{\Omega}_1, ..., \hat{\Omega}_N\}$ (dual mesh). The primary mesh is extended outside the portion Γ_p of Γ, considering an "extended mesh" Π'_h (Figure 1).

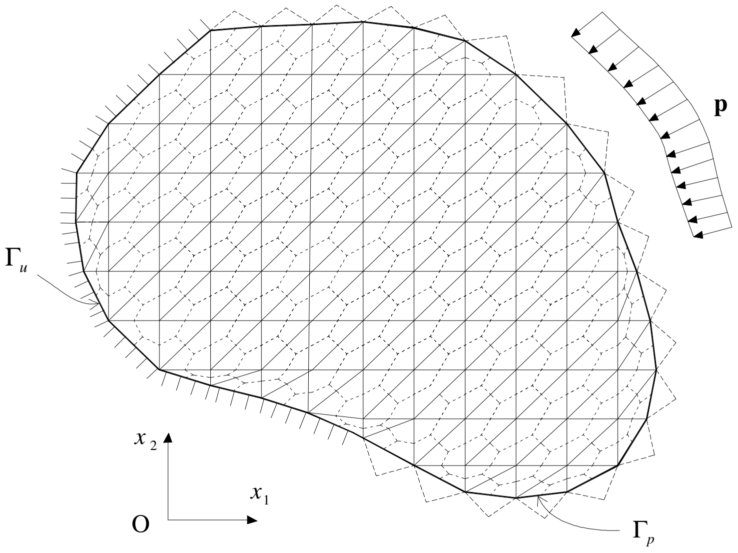

Fig. 2 – Primary and secondary meshes of a plane body.

The stress field of the body is derived from a single-valued scalar potential or Airy stress function φ, by using the mixed LSM-displacement approach below presented.

3 Lumped stress method

The Lumped Stress Method presented in Fraternali (2001) and Fraternali *et al.* (2002) approximates the Airy stress function φ through piece-wise linear functions $\hat{\varphi}$ defined over either the shape function, in the case of curved structures, or the plain body, in the case of walls.

The method has been originally developed for curved surfaces, starting from a partially non-conforming scheme (cf. Ciarlet, 1978) formulated under the assumption of C^0 approximations to both f and φ, (i.e. polyhedral test functions $\hat{f}$ and $\hat{\varphi}$ defined on a triangulation Ω_h of Ω) (Figure 3).

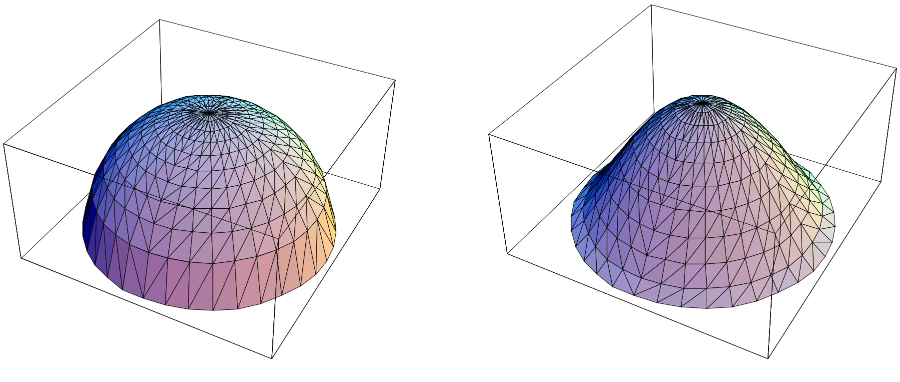

Fig. 3 – Polyhedral approximations to f (left) and φ (right).

Such an approximation scheme leads to the following discrete version of (7):

$$\sum_{edges} \hat{A}_i^j \frac{\hat{\varphi}_j - \hat{\varphi}_i}{h_i^j}(\delta\hat{\varphi}_j - \delta\hat{\varphi}_i) + \sum_{nodes} Q_i \delta\hat{\varphi}_i = 0 \ , \qquad (8)$$

where:

h_i^j is the length of the edge of Ω_h connecting nodes i and j;
$\hat{\varphi}_1,\dots,\hat{\varphi}_N$ are the nodal values of $\hat{\varphi}$;
$\hat{A}_i^j$ is the jump of the derivative $\partial\hat{f}/\partial n$ along the normal to the edge i-j;
Q_i is the resultant vertical force in correspondence with node i.

Starting from (8), the following system of linear algebraic equations can be obtained:

$$R_i = \sum_j \hat{P}_i^j \frac{\hat{f}_i - \hat{f}_j}{h_i^j} - Q_i = \sum_{j,k} U_{ijk} \hat{\varphi}_j \hat{f}_k - Q_i = 0, \quad i = 1,\dots,N, \qquad (9)$$

In (9), $\hat{P}_i^j$ represents the jump of the normal derivative $\partial\hat{\varphi}/\partial n$ across the edge i-j of Ω_h; U_{ijk} are coefficients depending only on the geometry of the mesh; the summations are extended to all the nodes connected to the node i; and N is the total number of nodes forming Ω_h. Quantities $\hat{P}_i^j$ are the axial forces carried by the bars of a planar truss structure having the same geometry of the skeleton of Ω_h.

One can regard the quantities $\hat{P}_i^j(\hat{f}_j - \hat{f}_i)/h_i^j$ as the axial forces carried by the spatial truss S_h, which is obtained from Ω_h through the mapping $x_3 = \hat{f}(x_1, x_2)$. Eqns. (9) represent the nodal equilibrium equations of S_h in the vertical direction, associating a unique polyhedral stress function $\hat{\varphi}$ to a given polyhedral shape function $\hat{f}$, and vice-versa. A concave polyhedral stress function $\hat{\varphi}$ gives rise to all compressive forces in the bars of S_h and Ω_h. It is worth noting that the modeling of a continuous membrane through a pin-jointed bar network actually corresponds to a non-conforming (or external) variational approximation of the membrane equilibrium problem.

The LSM above described can be extended to masonry walls (Figure2).

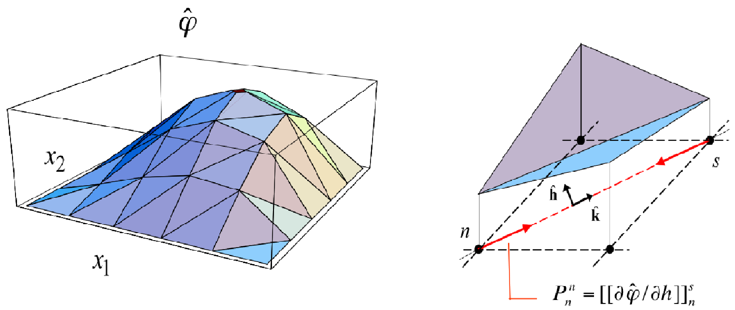

Fig. 4 – Polyhedral approximation of the Airy stress function and current lumped stress P_n^s.

Let introduce the "relaxed" version of the complementary energy of the body (Figure4):

$$E_h(\hat\varphi) = \frac{1}{2}\sum_{n=1}^{N}\sum_{s,t=1}^{\mathsf{S}_n}\hat{A}_n^{st}\, P_n^s(\hat\varphi)\, P_n^t(\hat\varphi) - \sum_{n\in U}\mathbf{R}_n(\hat\varphi)\cdot\bar{\mathbf{u}}_n\ , \tag{10}$$

where:

$$\hat{A}_n^{st} = \frac{\ell_n^s\,\ell_n^t\,\mathbf{A}\,[\hat{\mathbf{h}}_n^s\otimes\hat{\mathbf{h}}_n^s]\cdot\hat{\mathbf{h}}_n^t\otimes\hat{\mathbf{h}}_n^t}{4\,|\,\hat\Omega_n\,|} \tag{11}$$

In (10)-(11), N is the total number of nodes of Π_h; S_n indicates the number of nearest neighbors of the generic node n; ℓ_n^s is the length of the edge $n-s$; $\hat{\mathbf{k}}_n^s$ and $\hat{\mathbf{h}}_n^s$ are the tangent and normal unit vectors to such an edge, respectively; $P_n^n = [[\partial\hat\varphi/\partial h]]_n^s$ is the jump of $\nabla\hat\varphi\cdot\hat{\mathbf{h}}_n^s$ across $n-s$ (i.e., the normal derivative of $\hat\varphi$ through this edge).
It is not difficult to show that:

$$\mathbf{R}_n(\hat{\varphi}) \;=\; -\sum_{s=1}^{S_n} P_n^s(\hat{\varphi})\hat{\mathbf{k}}_n^s \;. \qquad (12)$$

The quantities P_n^s represents the axial forces carried by the bars of an *ideal truss* B_h, which has the same geometry of the skeleton of Π'_h (Figure 4). Similarly, the quantity $\mathbf{R}_n$ can be regarded as the total force acting at node *n* of such a truss. Due to the assumption of zero body forces, $\mathbf{R}_n$ will be nonzero only at the boundary (support reaction). The discrete functional (10) defines a non-conventional complementary energy of the truss B_h, which is defined per dual elements $\hat{\Omega}_n$, and not per elements (as in an ordinary truss).

Let φ_o denote the minimizer of the "exact" complementary energy of the body, and $\hat{\varphi}_h$ the minimizer of (10). It is not difficult to show that $\hat{\varphi}_h$ strongly converges to φ_o as h tends to 0, under suitable smoothness assumptions on φ_0 and the primal and dual meshes.

The smoothness of meshes can be satisfied by modelling Π_h as a structured core and by assuming that $\hat{\Pi}_h$ is made up of polygons connecting the middle points of the edges of Π_h with the barycenters of the primal triangles ("barycentric" dual mesh, cf. Figure 2).

A Γ–convergence proof of the LSM for the biharmonic problem of isotropic elasticity is given in Davini (2002), considering families of triangulations that are regular in the sense of Ciarlet (1978).

3.1 Constrained LSM approach to the analysis of curved structures

Lumped stress approach is used to predict the mechanical behavior of vaulted structures by means of a shape optimization procedure, which assumes that the vertical load q and the boundary values of $\hat{f}$ and $\hat{\varphi}$ are prescribed on $\partial\Omega_h$. The search for the corresponding thrust surface consists of seeking a couple ($\hat{f}$, $\hat{\varphi}$) such that the discrete equilibrium equations (9) are satisfied, under geometry constraints of the form

$$\hat{f}_i^{lb} \leq \hat{f}_i \leq \hat{f}_i^{ub} \quad (i = 1,\ldots,N), \tag{13}$$

and the concavity constraint on $\hat{\varphi}$. Limitations (13) require that the thrust surface is contained in a given 3D domain D, coinciding either with the region comprised between the extrados and the intrados of an existing vault, or with a suitable design space. A constrained lumped stress approach (CTNA) can be formulated as follows, assuming that an in initial guess $\hat{f}^0$ of $\hat{f}$ is available:

1) compute $\hat{\varphi}^0$ from the linear system $\left(U_{ijk}\hat{f}_k^0\right)\hat{\varphi}_j^0 = Q_i$;
2) compute the "concave hull" $\hat{\varphi}^{'}$ of $\hat{\varphi}^0$;
3) raise the vertices of $\hat{\varphi}^0$ to the upper portion of ∂C (concave surface), obtaining a new estimate $\hat{\varphi}^{'}$ and a new mesh topology ;
4) compute a new shape function $\hat{f}^{'}$ from the linear system $\left(U_{ijk}\hat{\varphi}_j\right)\hat{f}_k^{'} = Q_i$;
5) if $\hat{f}^{'}$ satisfies the geometry constraints (13) stop with $\hat{f} = \hat{f}^{'}$ and $\hat{\varphi} = \hat{\varphi}^{'}$; otherwise correct $\hat{f}^{'}$ so as to verify (13), set $\hat{f}^0 = \hat{f}^{'}$ and go back to 1.

Overall, the CTNA admits the quantities $Q_i, \hat{f}_i^{lb}, \hat{f}_i^{ub}$ $(i = 1,\ldots,N)$, and the nodal values of $\hat{f}$ and $\hat{\varphi}$ on $\partial\Omega_h$ as input. It produces the quantities $\hat{f}_i, \hat{\varphi}_i$ at the inner nodes of Ω_h as output, according to the elastic no-tension model of masonry (cf. Giaquinta and Giusti, 1985; Del Piero, 1989). It is worth noting that the concave-hull construction of step 2) provides topological adaption of the current force network, while steps 3), 4) and 5) perform geometrical adaption (see the results of the next section). The CNTA allows one to obtain a statically admissible, purely compressive lumped stress network, and ensures the satisfaction of the master 'safe' theorem of no-tension materials (Heyman, 1966, 1995; Del Piero, 1998), if the geometrical constraints (13) are verified. Once the solution ($\hat{f}$, $\hat{\varphi}$) of the CNTA is known, one can predict the portions of S_h and Ω_h exposed to fracture, localized in regions where the material is subject either to zero stress, or uniaxial compressive stress, as it will be shown in the next section. The continuum limit φ of the polyhedral stress function $\hat{\varphi}$ will exhibit either a flat (zero stress) or single-curvature (uniaxial stress) profile in correspondence with such regions. Cracks will run at the extrados if the thrust surface lies towards the intrados, and vice-versa.

3.2 Mixed LSM-displacement approach to the analysis of masonry walls

A Mixed LSM-displacement approach based on the Lumped stress approach above described is applied to masonry walls.

Let introduce the interelement and boundary nodes that are not subject to kinematical constraints, named *pivot*, and let utilize the LSM above presented by assuming that arbitrary nodal forces are applied to the pivot nodes. Under such hypotheses, the equilibrium problem of the wall can be expressed into the following variational form:

$$\min_{\hat{\varphi} \in R^n} E_h(\hat{\varphi}) = \frac{1}{2}\mathbf{P}(\hat{\varphi}) \cdot \mathbf{A}\,\mathbf{P}(\hat{\varphi}) \; - \; \mathbf{R}(\hat{\varphi}) \cdot \bar{\mathbf{u}} \tag{14}$$

$$\textit{such that:} \quad \begin{cases} \mathbf{S}\hat{\varphi} - \mathbf{q} = \mathbf{0} \\ \mathbf{P}(\hat{\varphi}) \le \mathbf{0} \quad \textit{in ENT elements} \end{cases}$$

where:

$\hat{\varphi}$	*is the vector collecting the nodal values of the Airy stress functions of each element;*
$\mathbf{P}(\hat{\varphi})$	*is the vector collecting the lumped stresses* $P_n^s = [[\partial\hat{\varphi}/\partial h]]_n^s$*;*
$\mathbf{A}$	*is the compliance matrix defined through (8);*
$\mathbf{R}(\hat{\varphi})$	*is the vector collecting the support reactions;*
$\bar{\mathbf{u}}$	*is the vector of the imposed nodal displacements;*
$\mathbf{q}$	*is the vector collecting the nodal forces applied to the pivot nodes;*
$\boldsymbol{S}$	*is the coefficient matrix of the equilibrium equations of the pivot nodes.*

In order to solve (14), we introduce the augmented Lagrangian given by

$$L_A\left(\hat{\varphi},\mathbf{u},\rho\right) = E_h\left(\hat{\varphi}\right) - \mathbf{u}\cdot\left(\mathbf{S}\hat{\varphi}-\mathbf{q}\right) + \frac{\rho}{2}\left(\mathbf{S}\hat{\varphi}-\mathbf{q}\right)^2 \tag{15}$$

where $\mathbf{u}$ denotes the vector collecting the displacements of the pivot nodes (*Lagrange multipliers*), and ρ is a penalty parameter (Nocedal and Wright, 2006).

The proposed LSDM admits nonzero nodal forces only in correspondence with pivot nodes (active nodal forces), and kinematically restrained nodes (support reactions).

An iterative solution method for the minimum problem of (15) is as follows:

a) given a tentative solution ($\hat{\varphi}^k$,$\mathbf{u}^k$, ρ^k), compute $\hat{\varphi}^{k+1}$ through the quadratic programming problem:

$$\min_{\hat{\mathbf{j}}\in R^n} L_A\left(\hat{\mathbf{j}},\mathbf{u}^k,\rho^k\right) \textit{ such that } \mathbf{P}\left(\hat{\varphi}\right) \leq \mathbf{0} \quad \textit{in ENT elements}; \tag{16}$$

b) update the Lagrange multipliers through:

$$\mathbf{u}^{k+1} = \mathbf{u}^k - \rho^k\left(\mathbf{S}\hat{\varphi}^{k+1} - \mathbf{q}\right); \tag{17}$$

c) update the penalty parameter, by $\rho^{k+1} > \rho^k$, if the norm of the residual vector $\mathbf{R}^{k+1} = \mathbf{S}\hat{\varphi}^{k+1} - \mathbf{q}$ increases with respect to the previous step;

d) return to point a) with $\hat{\varphi}^k \leftarrow \hat{\varphi}^{k+1}$; $\mathbf{u}^k \leftarrow \mathbf{u}^{k+1}$; $\rho^k \leftarrow \rho^{k+1}$, until the norm of the residual vector gets lower than a given tolerance.

The solution of problem (16) is not affected by lack of feasible solutions, due to the appropriate triangulations of the ENT members (Fraternali, 2007).

The numerical procedure starts by considering an initial triangulation of the wall and elastic solutions $\hat{\varphi}^0$ in each element, ignoring no-tension constraints, and then the convex-hull $conv\left(\hat{\varphi}^0\right)$ of $\hat{\varphi}^0$ is evaluated in the ENT members (Avis and Fukuda, 1992) and $\hat{\varphi}^1 = conv\left(\hat{\varphi}^0\right)^+$ is set in such elements, where $conv\left(\hat{\varphi}^0\right)^+$ is the concave face of $conv\left(\hat{\varphi}^0\right)$. In the next step $conv\left(\hat{\varphi}^0\right)^+$ is assumed as the *concave hull* of $\hat{\varphi}^0$. The projection of $conv\left(\hat{\varphi}^0\right)^+$ onto the platform defines a new triangulation of the current ENT element, which is associated with a suitable, statically admissible, stress function (cf.

Angelillo and Rosso, 1995). The concave-hull driven remeshing of the elastic no-tension members may remove nodes from such elements and, eventually, create gaps between them and the neighbor elements, as we shall see in the next section (example 2). In the elastic elements we simply assume $\hat{\boldsymbol{\varphi}}^1 = \hat{\boldsymbol{\varphi}}^0$, without remeshing.

Such a method could be easily coupled with standard finite element and boundary element models.

The LSDM update (17) of the pivot displacements can be rewritten as:

$$\Delta \mathbf{u}^k = \mathbf{u}^{k+1} - \mathbf{u}^k = \left(\mathbf{K}^k\right)^{-1} \Delta \mathbf{q}^k, \tag{18}$$

where:

$$\mathbf{K}^k = diag\left\{1/\rho^k, \ldots, 1/\rho^k\right\}; \quad \Delta \mathbf{q}^k = \mathbf{q} - \mathbf{S}\hat{\boldsymbol{\varphi}}^k. \tag{19}$$

The association of LSDM elements with finite elements and/or boundary elements simply requires the assembly of the diagonal matrix $\mathbf{K}^k$ into the global stiffness matrix of the overall discrete model, and the insertion of the load vector $\Delta \mathbf{q}^k$ into the incremental load vector, at each update of the nodal displacements. The update of the stress function vector will be performed locally in the LSDM elements, via step a).

5 Numerical examples

The proposed constrained LSM method has been applied to some benchmark examples, examining the equilibrium problems of a hemispherical dome, a groin vault, a cloister vault and a masonry beam.

More specifically, Figure 3-left shows the examined hemispherical dome (co-latitude opening equal to 0.9 π), while Figure 3-right illustrates the stress function $\hat{\varphi}$ obtained by letting $\hat{f}$ coincide with the middle surface, and applying a uniform vertical load per unit area of the platform. The above stress function assumes a convex shape towards the basis of the structure, which is associated with not-admissible circumferential tensile stresses. The concave-hull construction is able to transform the initial guess of Figure 3-left into the concave profile shown in Figure 5-left, which corresponds to the no-tension lumped stress network depicted in Figure 5-right. The latter predicts biaxial compression towards the crown of the dome, and uniaxial meridian compression towards the basis, and then allows us to predict a meridional crack pattern near the basis of the structure ("orange-slice" cracking mode), accordingly to what is observed in many real masonry domes of similar shape (cf. e.g. Heyman, 1995).

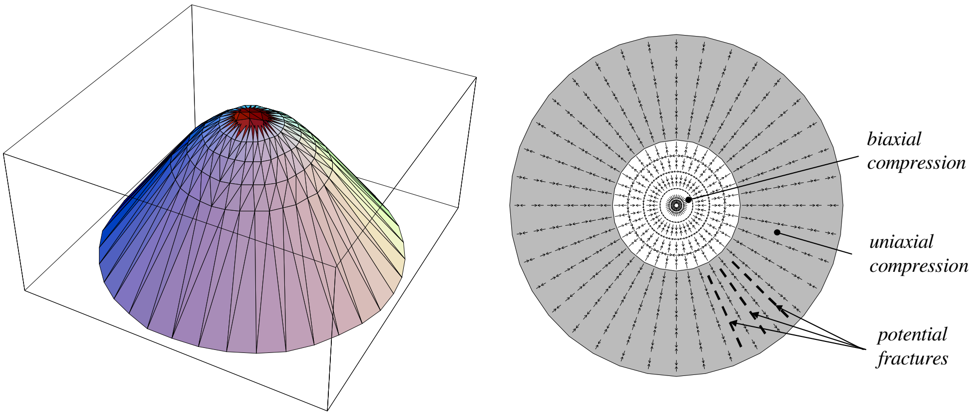

Fig. 5 – Stress function (left), lumped stress network and potential crack pattern (right) of a hemispherical dome under uniform vertical loading.

The second example deals with a groin vault with base dimensions 7.5 m × 7.5 m, parabolic web panels of thickness 20 cm, diagonal ribs of thickness 40 cm, and maximum rise equal to 3.2 m. The vault has self-weight of 20 kN/m^3, and bears a material with weight of 6 kN/m^3 filling the space in between the extrados and the horizontal plane through the vertex (Figure 6).

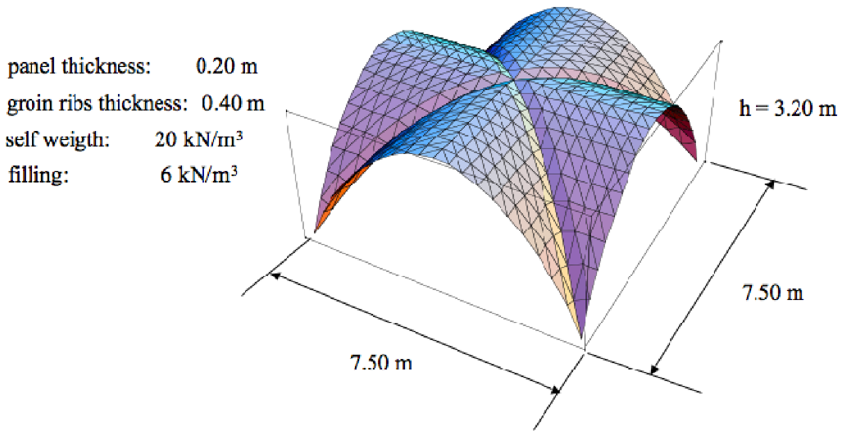

Fig. 6 – Geometry and loading data for a groin vault.

At the first step, $\hat{\varphi}$ is assumed to be null and $\hat{f}$ corresponding to the middle-surface on $\partial\Omega_h$. The quantities $\hat{f}$, $\hat{\varphi}$, $\hat{P}_i^j$ and the potential crack pattern obtained for the present example are reported in Figs. 7 and 8. One observes from Figure 8 that cracks may run parallel to the wall ribs at the extrados ("Sabouret" cracks), along the groin ribs, and near the crown at the intrados of the examined vault, which is in good agreement with the cracking "pathology" frequently observed in real quadripartite vaults (cf. Heyman, 1995; Como, 2009). As a matter of fact, the final profile of the stress function shown in Figure 7 bottom-right, and the associated lumped stress network depicted in Figure 8-right, indicate that the no-tension state of stress is uniaxial in such regions. The topology of the final thrust network is illustrated in Figure 8-left.

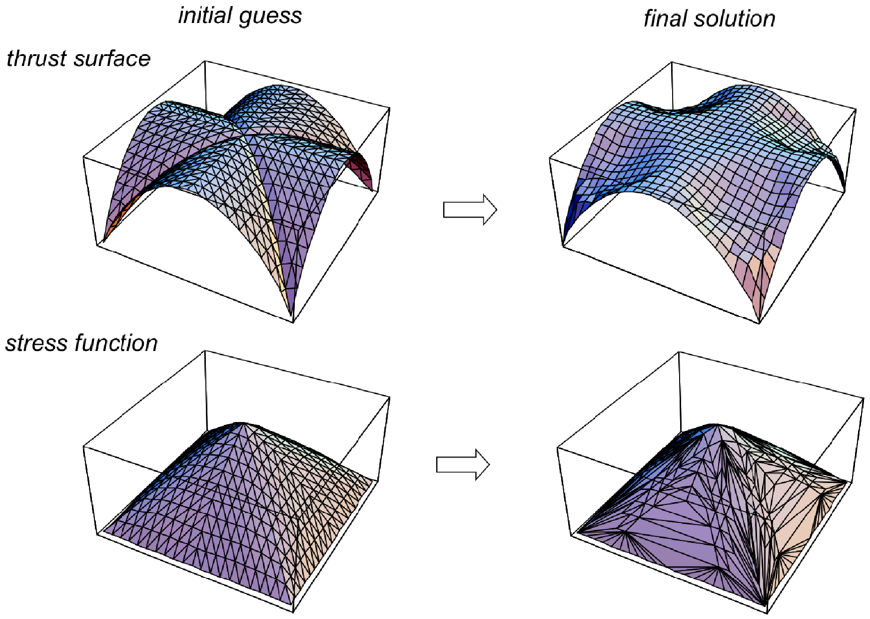

Fig. 7 – Thrust surface and stress function of an unreinforced groin vault under vertical loading.

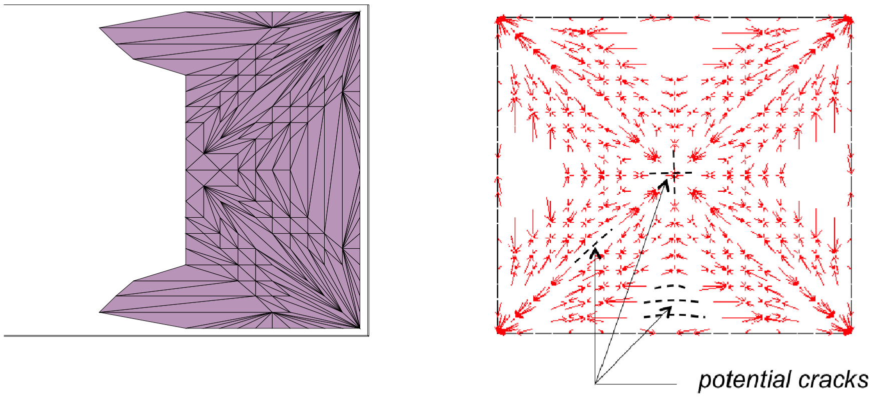

Fig. 8 – Final meshing (left) and force network (right) of a groin vault under vertical loading.

We examined the cloister vault shown in Figure 9, which has a 3.5 m × 3.5 m wide platform, and maximum rise of 1.2 m. The vault is made of tufe bricks with unit weight of 18 kN/m^3, and thickness varying from 37 cm to 17 cm. It carries the self-weight, a filling of 10 kN/m^3, and a dead load of 5 kN/m^2 per unit area of the platform (cf. Figure 9).

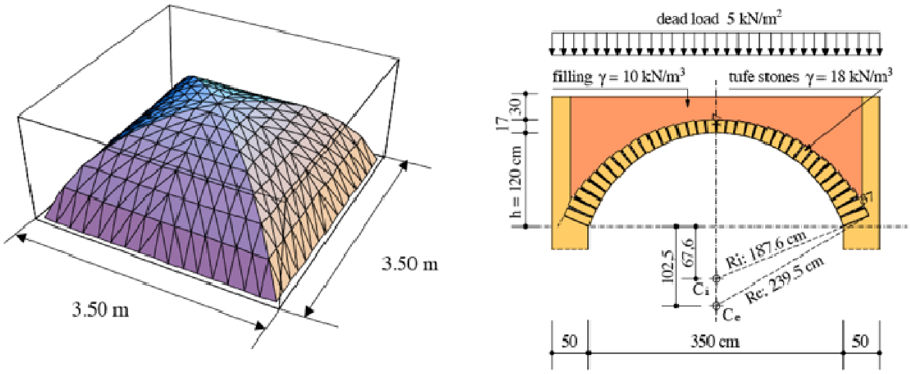

Fig. 9 – Geometry and loading data for a cloister vault.

The thrust surface $\hat{f}$, the stress function $\hat{\varphi}$, and the forces $\widehat{P}_i^j$ obtained for such a vault through the CLSA are illustrated in Figs. 10 and 11. In this case, we assumed $\hat{\varphi} = \hat{\mu}$ on $\partial\Omega_h$, with $\hat{\mu}$ computed from a finite element analysis of the vault under simply supported boundary conditions (Formato, 2007). The results shown in Figs. 10, 11 underline that the crack pattern of the vault under examination may include diagonal fractures along the web joints and radial fractures along the walls at the extrados, in conjunction with crown cracks at the intrados (we refer e.g. to Tomasoni, 2008 for typical cracking mechanisms of cloister vaults). We analyzed the cloister vault also under the combined action of vertical loads and upward/downward movements of the base supports, in correspondence with a corner of the supporting perimeter. For this case, we compared the CLSA predictions with an experimental study carried out on a real scale sample of the structure (Formato, 2007).

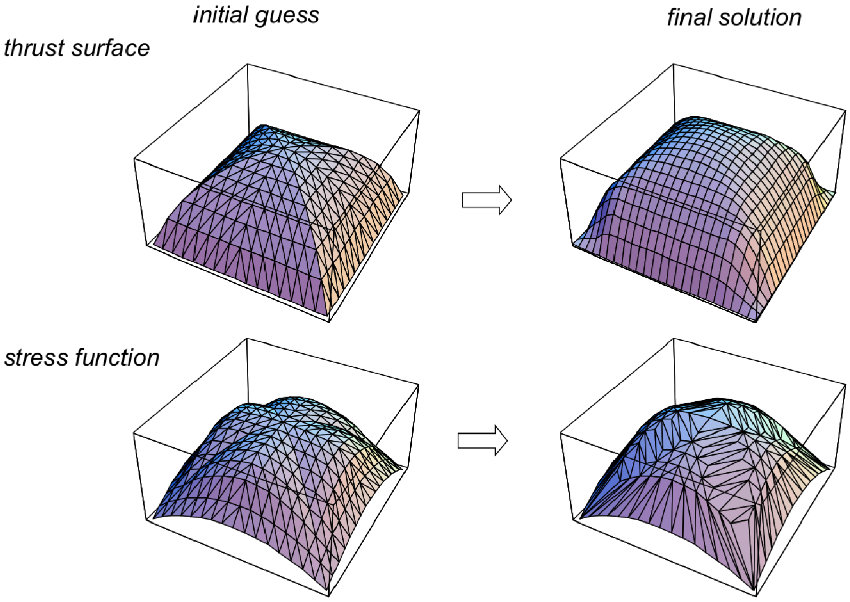

Fig. 10 – Thrust surface and stress function of an unreinforced cloister vault under vertical loading.

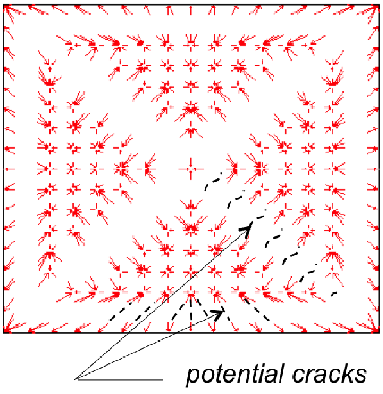

Fig. 11 – Potential crack pattern of a cloister vault under vertical loading.

Figure 12-left shows the schematic model of the vault subject to cycles of lifting and release in a corner of the supporting perimeter after the

numerically computed lumped stress network and the associated crack patter. Figure 12-right illustrates the experimentally detected cracking mechanism of the vault sample, after few 55 cycles of lifting and release of the corner supports with a variable pressure from 0 to 120 bar to produce a significant damage of the vault. One notices a rather good matching between the CNTA predictions and the experimentally observed damage.

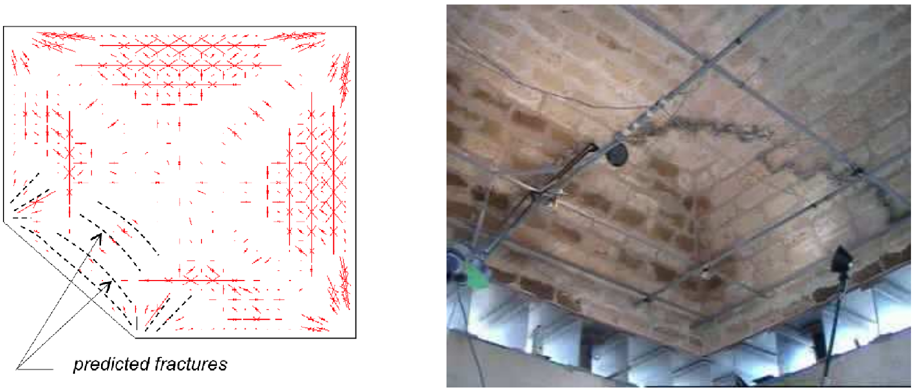

Fig. 12 – Comparison between predicted (left) and experimentally observed (right) fracture damage of a cloister vault under the combined action of vertical loads and vertical movements of corner supports.

Two case studies of masonry beam are analyzed: in the first one there is no reinforcement of the beam; in the second one the beam is strengthened with a steel profile at the bottom edge. The same examples were analyzed in Fraternali (2007) by means of a pure LSM approach (no displacement computation). We assume an orthotropic ENT constitutive model for the masonry. Regarding the steel reinforcement (second example), we instead assume an isotropic elastic behavior. One immediately recognizes it predicts an "arch-type" load resisting mechanism within the beam. The LSDM solution for the second example is illustrated in Figure 14. In the present case, the lumped stress network exhibited by the beam partially interests the lower edge (differently from the first example, cf. Figure 13, left), and migrates into the reinforcing steel element towards the edges (Figure 14, left). The latter is interested by alternating tensile (red) and compressive (black) stresses, as expected in a clamped beam that reacts in tension. Concerning the deformed shape, we observe that the LSDM solution predicts the debonding of the masonry beam from the steel element nearby the mid-span (Figure 14, right). This is due to the fact that the central lower portion of the masonry beam is essentially under zero stress (Figure 14, left), as in the previous example (Figure 13, left). According to the ENT model, such a region is expected to be heavily cracked and not contributing to the equilibrium of the remaining portion of the body (cf. Giaquinta and Giusti,1985; Del Piero, 1989).

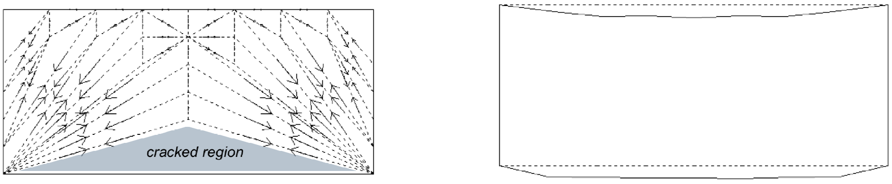

Fig. 13 – LSDM solution for a clamped masonry beam. Left: lumped stress network. Right: deformed shape.

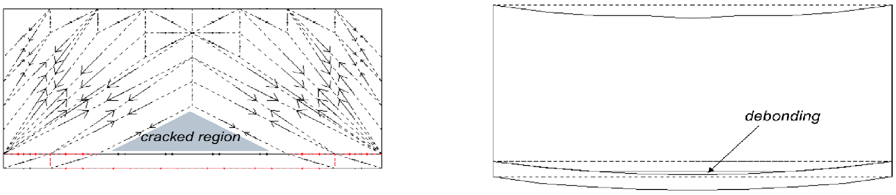

Fig. 14 – LSDM solution for a clamped masonry beam strengthened with a steel profile at the bottom edge. Left: lumped stress network. Right: deformed shape.

The final example a shear wall subject to relative horizontal displacements of the edges. In this case, we modeled the masonry as an isotropic ENT material with zero Poisson ratio. The LSDM solution for the present problem is illustrated in Figure 15. It is worth noting that the lumped stress pattern shown in Figure 15, left closely reproduces the distribution of compression rays obtained in Fortunato (2010) through an analytical approach. The ENT model predicts that the wall under consideration can be affected by cracks along such directions (Giaquinta and Giusti,1985; Del Piero, 1989; Fortunato, 2010).

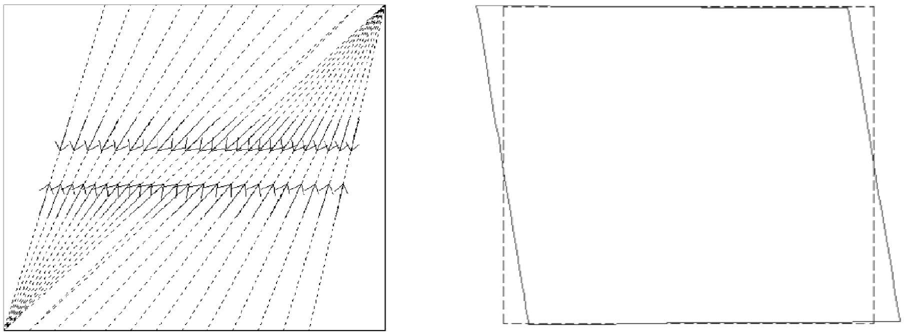

Fig. 15 – LSDM solution for a shear wall. Left: lumped stress network. Right: deformed shape.

6 Concluding remarks

A novel lumped stresses network approach to the equilibrium problem of masonry members has been presented. The given approach searches for the regions exposed to fracture damage according to the no-tension model of the masonry.

By modeling of the membrane state of stress carried by masonry structures through a polyhedral stress function, an adaptive, predictor-corrector technique has been formulated to generate statically admissible force networks for vaulted geometry. It has been shown that Lumped stress approach provides statically admissible force network according with no-tension constraints.

The proposed LSA has been generalized for the elastic problem of a wall that incorporates ENT elements by means of a mixed LSM-displacement method (LSDM).

The analyzed case studies have illustrated the reliability of the proposed approach in predicting the equilibrium configuration and the crack pattern of real masonry structures.

The generalization of the masonry model proposed in the present work to substructures, mixed structures, and strengthened masonry is addressed to future work. Stress approaches to ENT (or “masonry-like”) structures exhibit some peculiar advantages, since one can prove the uniqueness of the solution of the ENT boundary value problem in terms of the stress field. Such a generalization may usefully employ a tensegrity approach to the lumped stress network describing the state of stress of a masonry vault (Fraternali *et al.*, 2015; Carpentieri *et al.*, 2016).

References

1. Andreu, A., Gil, L., Roca, P. (2007). Computational analysis of masonry structures with a funicular model. *Journal of Engineering Mechanics ASCE*, vol. 133 (*4*), pp. 473-480.
2. Avis, D., Fukuda, K. (1992). A pivoting algorithm for convex hulls and vertex enumeration of arrangements and polyhedra, *Discrete and Computational Geometry*, vol. 8 (*3*), pp. 295-313.
3. Block, P., Ochsendorf, J. (2005). Interactive thrust line analysis for masonry structures. In: G. Mochi (Ed.). *International Seminar on Theory and Practice of Construction: Knowledge, Means, and Models*, Ravenna, Italy, pp. 13-24.
4. Block, P., Ochsendorf, J. (2007). Thrust Network Analysis: A new methodology for three-dimensional equilibrium. *Journal of the International Association for Shell and Spatial Structures*, vol. 48 (*3*), pp. 167-173.
5. Block, P. (2009). Thrust network analysis – Exploring three-dimensional equilibrium. *PhD dissertation*, Massachusetts Institute of Technology, USA.
6. Boothby, T.E. (2001). Analysis of masonry arches and vaults. *Progress in Structural Engineering and Materials,* vol. 3 (*3*), pp. 246-256.
7. Carpentieri, G., Modano, M., Fabbrocino, F., Feo, L, Fraternali, F. (2016). On the minimal mass reinforcement of masonry structures with arbitrary shapes. *Meccanica*, vol. 52 (*7*), pp. 1561-1576.
8. Ciarlet, P.G. (1978). *The Finite Element Method for Elliptic Problems*. North-Holland, Amsterdam.
9. Como, M. (2009). *Statica delle costruzioni in muratura*. Aracne Editrice, Roma.
10. Del Piero, G. (1989). Constitutive equations and compatibility of the external loads for linear elastic masonry-like materials. *Meccanica,* vol. 24 (*3*), pp. 150–162.
11. Del Piero, G. (1998). Limit analysis and no-tension materials, *Int. J. Plasticity*, vol. 14 (*1-3*), pp. 259-271.
12. Formato, F. (2007). A theoretical and experimental study on the statics of masonry vaults. *PhD dissertation*, University of Salerno, Italy.

13. Fraternali, F. (2001). Complementary energy variational approach for plane elastic problems with singularities. *Theoretical and Applied Fracture Mechanics*, vol. 35 (*2*), pp. 129-135.
14. Fraternali, F., Angelillo, M., Fortunato, A. (2002). A lumped stress method for plane elastic problems and the discrete-continuum approximation. *International Journal of Solids and Structure*, vol. 39 (*25*), pp. 6211-6240.
15. Fraternali, F., Angelillo, M., Rocchetta, G. (2002). On the stress skeleton of masonry vaults and domes. *PACAM VII*, January 2-5, Temuco, Chile, pp. 369-372.
16. Fraternali, F., Carpentieri, G., Modano, M., Fabbrocino, F., Skelton, R.E. (2015). A tensegrity approach to the optimal reinforcement of masonry domes and vaults through fiber-reinforced composite materials. *Composite Structures*, vol. 134, pp. 247-254.
17. Giaquinta, M., Giusti, G. (1985). Researches on the equilibrium of masonry structures. *Archive for Rational Mechanics and Analysis*, vol. 88 (*4*), pp. 359–392.
18. Heyman, J. (1966). The stone skeleton. *International Journal of Solids and Structure,* vol. 2 (*2*), pp. 249-279.
19. Heyman, J. (1977). Equilibrium of Shell Structures. *Oxford Engineering Science Series*, Clarendon Press, Oxford.
20. Heyman J. (1995). The stone skeleton. *Cambridge University Press*, Cambridge.
21. Huerta, S. (2001). Mechanics of masonry vaults: The equilibrium approach. In P. B. Lourenço and P. Roca (Eds.). *Proceedings of Historical Constructions, Guimarães*, pp. 47-69.
22. Kilian, A., Ochsendorf, J. (2005). Particle-spring systems for structural form finding. *Journal of the International Association for Shell and Spatial Structures,* 46 (*2*), pp. 77-85.
23. Kilian, A. (2007). Steering of form. *Journal of the International Association for Shell and Spatial Structures,* vol. 48 (*4*), pp. 17-21.
24. Lucchesi, M., Padovani, C., Pasquinelli, G., Zani, N. (2008). Masonry constructions: mechanical models and numerical applications. Lecture Notes in: *Applied and Computational Mechanics*, vol. 39, Springer-Verlag, Berlin Heidelberg.
25. Milani, G., Milani, E., Tralli, A. (2008). Limit analysis of masonry vaults by means of curved shell finite elements and homogeneizzation. *International Journal of Solids and Structure,* vol. 45 (*20*), pp. 5258-5288.
26. Ochsendorf, J. and Block, P. (2009). Designing unreinforced masonry. In: E. Allen and W. Zalewski (Eds.). *Form and Forces: Designing Efficient, Expressive Structures*, Chapter 8. John Wiley Sons, New York, USA.
27. O'Dwyer, D. (1999). Funicular analysis of masonry vaults. *International Journal of Solids and Structure,* vol. 73 (*1*), pp. 187-197.
28. Poleni G. (1991). *Memorie istoriche della gran cupola del Tempio Vaticano*. Edizioni Kappa, Rome, Italy, (Anastatic reprint of the original edition of 1748)..
29. Tomasoni, E. (2008). Le volte in muratura negli edifici storici. *Tecniche costruttive e comportamento strutturale*, Aracne Editrice, Roma, Italy.
30. Tomlow, J., Graefe, R., Otto, F., Szeemann, H. (1989). Das Modell / The Model / El Modelo. Number 34. In: *Mitteilungen des Instituts for Leichte Flchentragwerke (IL).* Stuttgart: Universität Stuttgart.
31. Ungewitter, G. (1890). Lehrbuch der gotischen Konstruktionen *(III. Auflage neu bearbaitet von K.Mohrmann ed.).* Leipzig: T.O. Weigel Nachfolger.
32. Wittmann, W. (1879). Zur Theorie der Gewölbe. *Zeitschrift für Bauwesen,* vol. 29, pp. 61-74.

The Editors

Elio Sacco is full professor of Solid and Structural Mechanics at the University of Cassino and Southern Lazio. He is Associate Editor of "Meccanica" and Editorial Board member of several international journals. His research field and activity concern: Mechanics of masonry materials and structures, Material Constitutive Modelling, Micromechanics and Homogenization Techniques, Multiscale Analysis of Heterogeneous Structures, Analysis of Plate and Shells.

Michela Monaco is Irpine, Tenured Assistant Professor in Structural Mechanics and Experimental Mechanics at University of Campania "Luigi Vanvitelli" since December 2002. Author and reviewer of papers in the field of Structural Mechanics. Member of Evaluation Units of both European and Italian Funds and Grants. Her research field and activity concern: Mechanics of Masonry Constructions, Dynamics, Experimental Mechanics, Solid Mechanics.

The Editors

Elio Sacco is full professor of Solid and Structural Mechanics at the University of Cassino and Southern Lazio. He is Associate Editor of “Meccanica” and Editorial Board member of several international journals. His research field and activity concern: Mechanics of masonry materials and structures, Material Constitutive Modelling, Micromechanics and Homogenization Techniques, Multiscale Analysis of Heterogeneous Structures, Analysis of Plate and Shells.

Michela Monaco is Irpine, Tenured Assistant Professor in Structural Mechanics and Experimental Mechanics at University of Campania “Luigi Vanvitelli” since December 2002. Author and reviewer of papers in the field of Structural Mechanics. Member of Evaluation Units of both European and Italian Funds and Grants. Her research field and activity concern: Mechanics of Masonry Constructions, Dynamics, Experimental Mechanics, Solid Mechanics.